Université Fédérale
Toulouse Midi-Pyrénées

THÈSE

En vue de l'obtention du

DOCTORAT DE L'UNIVERSITÉ DE TOULOUSE

Délivré par l'Université Toulouse 3 - Paul Sabatier

Présentée et soutenue par

Franziska Maria STAMM

Le 25 janvier 2019

Caractérisation expérimentale du fractionnement isotopique à l'équilibre entre les espèces aqueuses et solides naturels : les systèmes Si aqueux - silice amorphe et Mg aqueux - brucite

---

Ecole doctorale : **SDU2E - Sciences de l'Univers, de l'Environnement et de l'Espace**

Spécialité : **Sciences de la Terre et des Planètes Solides**

Unité de recherche :
GET - Geosciences Environnement Toulouse

Thèse dirigée par
ERIC OELKERS et Jacques SCHOTT

Jury

M. Jérôme GAILLARDET, Rapporteur
Mme Sophie OPFERGELT, Rapporteure
M. Martin DIETZEL, Rapporteur
M. Franck POITRASSON, Examinateur
M. Eric OELKERS, Directeur de thèse
M. Jacques SCHOTT, Co-directeur de thèse

Experimental characterization of the equilibrium isotopic fractionation between aqueous species and natural solids:
the systems aqueous Si - amorphous SiO_2 and aqueous Mg - brucite

Extended Abstract

Silicon (Si) and Magnesium (Mg) are major elements in rock-forming minerals, biological systems and seawater. Characterizing the isotopic composition of these elements in inorganic and organic environments makes it possible to better constrain their geochemical cycle and to interpret the geologic record. The accurate interpretation of these natural isotopic signatures requires knowledge of the equilibrium isotope fractionation between Si or Mg bearing solids and the main inorganic and organic Si and Mg species present in natural waters. At present, these data are scarce and not reliable.

In this thesis laboratory experiments were performed at *bulk chemical* equilibrium to determine the equilibrium isotopic fractionation factor between Si or Mg bearing solids and aqueous solutions with various pH, temperature, and in the presence or absence of organic (catechol, citrate or EDTA) and inorganic ligands (sulphate) at 25° and 75°C.

The 'three-isotope method' was applied to unambiguously determine the equilibrium fractionation factor Δ_{eq} of such two-component solid-solution system. The advantage of this method is that in the case where the two-component system does not reach full isotopic equilibrium, the isotopic composition at equilibrium can still be determined by extrapolation. Additionally the three-isotope method provides information into isotope exchange rates, and thus insight into the mechanism of isotopic exchange. Fur this purpose, after attaining bulk chemical equilibrium the aqueous solutions were spiked with ^{29}Si or ^{25}Mg and then placed together with new amorphous SiO_2 or brucite powder to equilibrate isotopically. Isotopic measurements were performed on fluids and solids collected at selected times during the experiments with an MC-ICPMS.

Equilibrium fractionation factors between solids and distinct aqueous species were obtained by coupling the experimental results with the results of aqueous speciation calculations performed using PHREEQC. All experimental determined equilibrium fractionation factors were compared with results of corresponding *ab initio* calculations. Among the noteworthy results of this thesis one should highlight the strong impact that can have Si and Mg complexation with some organic ligands on the isotopic composition of coexisting Si and Mg solids and aqueous species (i.e. $\Delta^{30}Si_{Sicatechol\text{-}H_4SiO_4^\circ} = -19.05 \pm 0.49$ ‰ and $\Delta^{26}Mg_{Mg^{2+}\text{-}MgEDTA^{2-}} = 2.17 \pm 0.19$ ‰.). The results of this study can be used to model paleoclimate conditions and may provide a new insight into the isotopic records of sedimentary rocks, and biological systems.

Résumé

Le silicium (Si) et le magnésium (Mg) sont deux éléments majeurs abondants dans les minéraux, les systèmes biologiques, les eaux douces et les océans. La caractérisation de leurs compositions isotopiques dans la biosphère et les milieux terrestres inorganiques permet une meilleure compréhension de leurs cycles géochimiques et facilite l'interprétation de certains enregistrements géologiques. L'interprétation des signatures isotopiques naturelles requiert dès lors la connaissance précise des fractionnements isotopiques à l'équilibre survenant entre les principaux solides porteurs de silicium et magnésium et les principales espèces inorganiques et organiques de Si et Mg présentes dans les fluides naturels. A ce jour, ces données restent encore trop rares et peu fiables.

Les travaux de cette thèse s'appuient principalement sur des expériences de laboratoires conduites à *l'équilibre chimique* en vue de déterminer le fractionnement isotopique à l'équilibre entre des solides porteurs de Si ou Mg et des solutions aqueuses de différents pH, contenant ou non un ligand organique (catéchol, citrate ou EDTA) ou inorganique (sulfate) à des températures de 25 et 75°C.

La méthode des « trois isotopes » a été employée afin de déterminer sans ambiguïté le fractionnement à l'équilibre dans ces systèmes à deux composants « $\Delta_{eq\ fluide\text{-}solide}$ ». Cette méthode présente comme avantage de pouvoir déterminer des compositions isotopiques par extrapolation, même si l'équilibre isotopique n'est pas atteint. Elle permet également de fournir des informations sur les vitesses d'échanges isotopiques et donc sur les mécanismes de l'échange isotopique lui-même. Dans ce but, après avoir atteint l'équilibre chimique entre silice amorphe et solution ou brucite et solution, un spike de ^{29}Si ou de ^{25}Mg a été ajouté à la solution aqueuse. Cette solution ensuite été mélangée à une nouvelle poudre de SiO_2 amorphe ou de brucite afin d'atteindre l'équilibre isotopique. Les mesures isotopiques ont été effectuées par MC-ICPMS sur les solutions et les solides, recueillis à des moments choisis au cours des différentes expériences.

Les fractionnements isotopiques à l'équilibre entre les solides et les espèces aqueuses et entre les différentes espèces aqueuses d'un même élément ont été obtenus en couplant les résultats expérimentaux avec les résultats des calculs de spéciation aqueuse effectués à l'aide du code géochimique PHREEQC. Tous les facteurs de fractionnement à l'équilibre entre solide et espèce aqueuse d'un élément ou entre deux espèces aqueuses d'un même élément ainsi obtenus ont été comparés aux résultats de calculs *ab initio* menés sur les mêmes systèmes. Parmi les résultats les plus remarquables, on retiendra l'impact très important que

peut avoir la complexation du silicium et du magnésium avec certains ligand organiques sur la composition isotopiques de leurs espèces aqueuses et des solides en équilibre, avec, par exemple, $\Delta^{30}Si_{Sicatechol\text{-}H_4SiO_4^\circ}$ = -19.05± 0.49 ‰ et $\Delta^{26}Mg_{Mg^{2+}\text{-}MgEDTA^{2-}}$= 2.17 ± 0.19 ‰. Les résultats de cette étude, qui fournissent un éclairage nouveau sur des données isotopiques de roches sédimentaires et de systèmes biologiques, peuvent être utilisés afin de reconstituer certains paléo-environnements.

Preface

This thesis presents the research carried out by the author from February 2015 to September 2018 at the Laboratoire Géosciences Enviornement Toulouse / Centre National de la Recherche Scientifique (CNRS UMR 5563 GET) in Toulouse, France. The work is composed of six chapters.

Chapter 1 presents an extended general introduction to the thesis, addressing the aim and motivation of this study. Chapter 2 describes the theoretical background of the experiments, the materials and methods used during the experimental work. A general conclusion of the thesis is provided in Chapter 6, as well as, an outlook on future research possibilities in this field.

The main results of this thesis are described in Chapters 3, 4, and 5. These are included as three scientific manuscripts, which are either submitted or in preparation for submission to international peer-reviewed journals. These chapters are prepared so that they can be read individually, therefore some material is repeated within these chapters.

Chapter 3 is comprised of the manuscript submitted to *Geochimica et Cosmochimica Acta* on the 8th October 2018 and titled "The experimental determination of equilibrium Si isotope fractionation factors among $H_4SiO_4°$, $H_3SiO_4^-$ and amorphous silica ($SiO_2 \cdot 0.32\ H_2O$) at 25 and 75°C using the three isotope method", authored by Franziska M. Stamm, Thomas Zambardi, Jérôme Chmeleff, Jacques Schott, Friedhelm von Blanckenburg, and Eric H. Oelkers. The experimental and analytical work was performed by myself, with suggestions of Jacques Schott, and if needed with assistance of the corresponding technicians. Measurements on the Neptune MC-ICP-MS were carried out by myself with assistance of Thomas Zambardi, Jérôme Chmeleff, and the working group of Friedhelm von Blanckenburg. Data evaluation was carried out by myself, Thomas Zambardi and Jérôme Chmeleff. The data interpretation was performed by myself, Jacques Schott and Eric H. Oelkers. The manuscript was written by myself and the co-authors, notably Jacques Schott and Eric H. Oelkers provided comments and suggestions and critically reviewed the manuscript.

Chapter 4 describes the content of the manuscript: "Extreme silicon isotope fractionation between silicic acid and the aqueous organosilicon complexes: Implications for silica biomineralization", authored by Franziska M. Stamm, Merlin Méheut, Thomas Zambardi, Jerome Chmeleff, Jacques Schott, and Eric H. Oelkers, with the following contributions: The experimental work was performed by myself, with remarks and ideas of Jacques Schott. Analytical procedures were performed by myself with assistance of the

corresponding technicians if needed. Measurements on the Neptune MC-ICP-MS and data evaluation were carried out by myself with assistance of Thomas Zambardi and Jérôme Chmeleff. Ab initio calculations were performed by Merlin Méheut. The manuscript was written by myself and the co-authors, notably Jacques Schott and Eric H. Oelkers, who also provided input on data interpretation.

Chapter 5 describes the content of the completed manuscript: "Determination of the equilibrium magnesium isotope fractionation factors between brucite and aqueous inorganic and organic species", authored by Franziska M. Stamm, Thomas Zambardi, Jerome Chmeleff, Jacques Schott, and Eric H. Oelkers, with the following contributions: The experimental work was performed by myself, with input of Jacques Schott. Analytical procedures were performed by myself with assistance of the corresponding technicians. Measurements on the Neptune MC-ICP-MS and data evaluation were carried out by myself with assistance of Thomas Zambardi and Jérôme Chmeleff. The manuscript was written by myself and the co-authors. Jacques Schott and Eric H. Oelkers provided input on data interpretation and helped finalize the manuscript.

The Appendix is composed of tables of the electronic supplement material of chapters 3,4, and 5.

To Gisela, Hermann & Moritz

Acknowledgements

There are many people I would like to thank for their help and support during the past years.

First of all, I would like to thank my advisors Eric Oelkers and Jacques Schott for their support, inspiring discussions and guidance throughout my thesis. Thank you for your mentorship, the continuous encouragement, and making sure I stayed on the right path.

I would also like to thank the reviewers and jury members for taking the time to evaluate this thesis.

This work was funded by the European Union through the IsoNose People Programme and I am very grateful to be part of this network.

Special thanks go to Jérôme Chmeleff for his advice and patience in teaching me, together with Thomas Zambardi everything I know about the Neptune. I also want to thank Merlin Méheut for many interesting discussions and sharing his knowledge about ab initio calculations.

I am thankful to the academic staff at the GET, especially Pascale Bénézeth, Sebastian Fabre, Vasileios Mavromatis for their help and support. Additionally, I owe many thanks to the technical staff, who supported me during my lab work. Special appreciation is directed to Philippe Besson, Frederic Candaudap, Alain Castillo, Carole Causserand, Pascal Gisquet, Manuel Henry, Aurélie Marquet, Stephanie Mounic at the GET, Gwénaëlle Guittier from the Laboratoire de Génie Chimique, Philippe De Parseval, and Teresa Hungria from the Centre de MicroCaractérisation Raimond Castaing Toulouse.

During my PhD I had the opportunity to spend time and learn in other great laboratories. I would like to express my gratitude to Wafa Abouchami, Julien Bouchez, Jérôme Gillardet and Xu Zhang for welcoming and helping me during my stay at the IPG in Paris. Many thanks to Josefine Buhk, Friedhelm von Blanckenburg, Daniel Frick, Jan Schüssler and Maja Tesmer from the GFZ in Potsdam for their support and help during my secondment.

I also want to thank current and former graduate students and post-docs of the GET, Simon Blotevogel, Laetitia Gal, Anna Harrison, Christian Grimm, Chiara Marieni, Helen McFarlane, Melody Premaillon, Giuseppe Saldi, Martin Voigt, Nail Zagretdenov, and many, many others for the time we spent together inside and outside of the lab. Special thanks go to Alisson Akerman, Sylvain Pinet and Leandre Ponthus for all their help and support.

During the past years, I was lucky to find great new friends. I would like to thank Fiorella, Hannah, Sebastian and Valeria for their motivation, and discovering Toulouse with me. I thank Marie and René for the lovely time we spent on IsoNose meetings, in Berlin and Toulouse. I also want to thank FX and Thomas for their constant motivation and help. I was lucky sharing fun coffee breaks, lunches and wonderful evenings together with Marianne and Irina.

I am fortunate to have fantastic friends, who accompanied me for many years. In particular I want to thank Iris, Hanna, Steffi, and Chrissi for their support, motivation, and distracting me by many fun skype conversations, discovering the Pyrenées, and the French cuisine together. Thank you all for always being there.

I owe much gratitude to my parents Gisela and Hermann for their unconditional support and encouragement throughout the years. Thank you, for your advice, and for your confidence. I also thank the rest of my family, my sister Anna-Sophia and her husband Johannes, Eva, and my brothers Sebastian and Johannes. I would like to thank my niece Clara for bringing so much joy into our lives.

Finally, I warmly thank Moritz for his endless support, encouragement, patience and the ability to always make me laugh.

Contents

List of Tables

List of Figures

Nomenclature

Abbreviations

AAS	atomic absorption spectrometry
BET	Brunauer-Emmett-Teller theory
BF	bright field
BSE	backscattered electrons
DF	dark field
EDS	energy-dispersive X-Ray spectrometry
EDTA	ethylenediaminetetraacetic acid
Eqn.	equation
ESA	electrostatic analyser
FEG	field emission gun
HDPE	high-density polyethylene
ICP-MS	inductively coupled plasma mass spectrometry
MC	multi-collector (-ICP-MS)
P-XRD	X-ray powder diffraction
SEM	scanning electron microscopy
SE	standard error
SD	standard deviation
SIS	stable introduction system

Symbols

Å	Angström
a	activity
α	fractionation factor
β	fractionation coefficient
δ	isotopic composition
Δ	fractionation factor
e /eq	equilibrium
F	degree of isotopic exchange
G	Gibbs free energy
i	initial
R	gas constant
K_{eq}	equilibrium constant

r	rate
r_+	forward rate
r_-	backward rate
θ	diffraction angle
T	temperature

Chapter 1

Introduction

1.1a. General introduction (English version)

Silicon (Si) and Magnesium (Mg) are among the most common elements in the Earth's crust, and thus play an important role in many geologic processes. Silicon and magnesium stable isotopes can therefore be used as reliable tracer for many (near-) surface processes, including weathering, mineral growth and precipitation, biological activity, and marine paleo conditions (e.g. Varela et al., 2004; Opfergelt et al., 2008; Wimpenny et al., 2011; Opfergelt et al., 2012a; Pogge von Strandmann et al., 2012; Tipper et al., 2012; Kasemann et al., 2014; Mavromatis et al., 2014; Saenger and Wang, 2014; Fujii et al., 2015; Gao et al., 2016). Since the advent of multi-collector inductively coupled plasma mass spectrometry (MC-ICP-MS), the isotopic composition of Si and Mg could be determined for many terrestrial reservoirs, such as surface waters (Brenot et al., 2008; Georg et al., 2009; De La Rocha et al., 2011; Ding et al., 2011; Grasse et al., 2013; Pokrovsky et al., 2013; Frings et al., 2015), soils (Opfergelt et al., 2014; Riotte et al., 2018a), biosphere, e.g. plants, foraminifera, sponges, diatoms (Savin and Douglas, 1973; Douthitt, 1982; Ding et al., 2008a, 2008b; Bolou-Bi et al., 2010; Pogge von Strandmann et al., 2012; Opfergelt et al., 2012b; Riotte et al., 2018b), and minerals, sedimentary rocks, carbonates, cherts, and banded iron formations (Douthitt, 1982; Ziegler et al., 2005a, 2005b; Georg et al., 2009; Hippler et al., 2009; Steinhoefel et al., 2010; van den Boorn et al., 2010; Savage et al., 2013; Mavromatis et al., 2013; Wimpenny et al., 2014; Schott et al., 2016). Experimental studies have demonstrated that silicon and magnesium isotopic signatures in natural environments can evolve during mineral precipitation (Li et al., 1995; Basile-Doelsch et al., 2005; Mavromatis et al., 2013; Geilert et al., 2014; Roerdink et al., 2015; Oelze et al., 2015), mineral growth, mineral dissolution (Delvigne et al., 2012) or during adsorption of aqueous species onto solid surfaces (Delstanche et al., 2009; Oelze et al., 2014). Isotopic fractionation during these mineral-solution reactions in nature can be influenced by diffusion and kinetic effects (Pearce et al., 2012; Mavromatis et al., 2013; Geilert et al., 2014; Oelze et al., 2015; Roerdink et al., 2015; Poitrasson, 2017). However, the degree of Si and Mg isotope fractionation at isotopic equilibrium between minerals and coexisting fluids is scarcely known, so that the relative impact of kinetic versus equilibrium processes on the fractionation during fluid-mineral interaction cannot be assessed unambiguously.

In natural fluids Si and Mg can occur as different species, in addition to their major aqueous species silicic acid (H_4SiO_4) and $Mg(H_2O)_6^{2+}$ (Mg^{2+}). Additionally, a large number of organic and inorganic aqueous complexes can form with these elements. Aqueous speciation

is known to have an important impact on isotopic fractionation factors, which has been demonstrated for elements such as boron, carbon, magnesium, mercury, transition metals and silicon (Hemming and Hanson, 1992; Zhang et al., 1995; Zeebe, 2005; Klochko et al., 2006, 2009; Asael et al., 2009; Holloway et al., 2011; Jiskra et al., 2012; Ryan et al., 2013; Yin et al., 2013; Fujii et al., 2014, 2015; Dupuis et al., 2015; Noireaux et al., 2015; Schott et al., 2016; Balan et al., 2018; Mavromatis et al., 2019). A critical factor to determining the equilibrium fractionation between a mineral and the coexisting aqueous fluid, is therefore the aqueous speciation of the system.

In the past, several experimental and theoretical *ab initio* studies were performed to determine Si and Mg equilibrium fractionation factors between solid and their coexisting aqueous solutions (Rustad et al., 2010; Li et al., 2011; Schauble, 2011; Pearce et al., 2012; Mavromatis et al., 2013; Li et al., 2014; Oelze et al., 2014; Dupuis et al., 2015; Fujii et al., 2015; Pinilla et al., 2015; Roerdink et al., 2015; Zheng et al., 2016; Schott et al., 2016; Mavromatis et al., 2017; Colla et al., 2018; Gao et al., 2018). These studies give insight into the mechanisms of equilibrium isotopic exchange. This thesis builds upon these efforts through a systematic and carefully controlled experimental study.

This study investigates the effects of aqueous speciation, and the inorganic and organic complexation on the equilibrium isotope fractionation factors of Si and Mg in the amorphous silica (SiO_2) - aqueous solution and brucite ($Mg(OH)_2$) - aqueous solution system respectively. Constraining the equilibrium isotopic fractionation in these systems is crucial to understand the geochemical cycle of silicon and magnesium. Towards this goal, isotopic exchange experiments at bulk chemical equilibrium were performed between solids and fluids of different compositions and at different temperatures using the 'three-isotope method'. The experimentally determined equilibrium isotope fractionation factors are also compared to the results of corresponding *ab inito* calculations and the values obtained from previous experimental and theoretical studies. The results of this study aim to improve our ability to interpret the isotopic composition of Si and Mg in natural systems, and can be used to develop new tools to estimate past environmental conditions

1.1b. Introduction génerale (Version française)

Le silicium (Si) et le magnésium (Mg) sont parmi les éléments les plus abondants de la croute terrestre et ils jouent un rôle important dans de nombreux processus géologiques. Les isotopes stables de Si et de Mg peuvent donc être utilisés comme des traceurs fiables de nombreux processus se déroulant à la surface de la terre comme l'altération, la croissance et la précipitation des minéraux, l'activité biologique ou encore la chimie océanique à travers le temps (e.g. Varela et al., 2004; Opfergelt et al., 2008; Wimpenny et al., 2011; Opfergelt et al., 2012a; Pogge von Strandmann et al., 2012; Tipper et al., 2012; Kasemann et al., 2014; Mavromatis et al., 2014; Saenger and Wang, 2014; Fujii et al., 2015; Gao et al., 2016).

Depuis l'avènement de la spectrométrie de masse à plasma à couplage inductif multi-collection (MC-ICP-MS), les compositions isotopiques de Si et Mg ont été déterminées dans de nombreux réservoirs terrestres tels que les eaux de surface (Brenot et al., 2008; Georg et al., 2009; De La Rocha et al., 2011; Ding et al., 2011; Grasse et al., 2013; Pokrovsky et al., 2013; Frings et al., 2015), sols (Opfergelt et al., 2014 ; Riotte et al., 2018a), la biosphère, y compris plantes, foraminifères, éponges, diatomées (Savin et Douglas, 1973; Douthitt, 1982; Ding et al., 2008a, 2008b; Bolou-Bi et al., 2010; Pogge von Strandmann et al., 2012; Opfergelt et al., 2012b; Riotte et al., 2018b), sans oublier, à l'état minéral, minéraux et roches profonds, roches sédimentaires, carbonates, cherts et formations de fer rubanées (Douthitt, 1982; Ziegler et al., 2005a, 2005b; Georg et al., 2009; Hippler et al., 2009; Steinhoefel et al., 2010; van den Boorn et al., 2010; Savage et al., 2013; Mavromatis et al., 2013; Wimpenny et al., 2014; Schott et al., 2016). Des études expérimentales ont démontré que les signatures isotopiques du silicium et du magnésium dans les milieux naturels peuvent évoluer au cours de la précipitation, de la croissance et de la dissolution des minéraux (Li et al., 1995; Basile-Doelsch et al., 2005; Mavromatis et al., 2013; Geilert et al., 2014; Roerdink et al., 2015; Oelze et al., 2015) ou lors de l'adsorption d'espèces aqueuses sur des surfaces solides (Delstanche et al., 2009; Oelze et al., 2014). Il a été montré que les fractionnements isotopiques naturels de ces éléments au cours des interactions solide-fluide peuvent être influencés par la diffusion et la cinétique des réactions (Pearce et al., 2012; Mavromatis et al., 2013; Geilert et al., 2014; Oelze et al., 2015; Roerdink et al., 2015; Poitrasson, 2017). Cependant, les degrés de fractionnements isotopiques du Si et du Mg à l'équilibre entre les minéraux et les fluides à leur contact sont encore peu documentés, de sorte que l'impact des processus cinétiques sur ces fractionnements pendant les interactions fluide-minéral reste difficile à évaluer sans ambiguïté.

Dans les fluides naturels, Si et Mg peuvent apparaître sous forme de différentes espèces parallèlement à celles qui dominent généralement leur spéciation aqueuse, l'acide silicique (H_4SiO_4) et l'ion Mg^{2+}. En particulier, nombre de ligands organiques et inorganiques peuvent former des complexes aqueux avec ces deux éléments. On sait que des fractionnements isotopiques importants peuvent se produire entre les différentes espèces aqueuses d'un même élément présentes en solution. De tels fractionnements ont été mis en évidence pour des éléments la tels que le bore, le carbone, le magnésium, le mercure, les métaux de transition, le silicium (Hemming et Hanson, 1992; Zhang et al., 1995., 2005; Klochko et al., 2006, 2009; Asael et al., 2009; Holloway et al., 2011; Jiskra et al., 2012; Ryan et al., 2013; Yin et al., 2013; Fujii et al. ., 2014, 2015; Dupuis et al., 2015; Noireaux et al., 2015; Schott et al., 2016; Balan et al., 2018; Mavromatis et al., 2018). Un facteur critique pour déterminer le fractionnement à l'équilibre entre un minéral et le fluide aqueux coexistant est donc la spéciation aqueuse du système.

Dans le passé, plusieurs études ab initio expérimentales et théoriques ont été effectuées pour déterminer les facteurs de fractionnement à l'équilibre du Si et du Mg entre le solide et ses solutions aqueuses coexistantes (Rustad et al., 2010; Li et al., 2011; Schauble, 2011; Pearce et al., 2012; Mavromatis et al., 2013; Li et al., 2014; Oelze et al., 2014; Dupuis et al., 2015; Fujii et al., 2015; Pinilla et al., 2015; Roerdink et al., 2015; Zheng et al., 2016; Schott et al., 2016; Mavromatis et al., 2017; Colla et al., 2018; Gao et al., 2018). Ces études donnent un aperçu des mécanismes à l'origine des échanges isotopiques à l'équilibre. Ce travail de thèse s'appuie sur ces études pour améliorer notre connaissance de ces systèmes grâce à la mise en œuvre d'une méthode expérimentale très rigoureuse pour déterminer les fractionnements isotopiques à l'équilibre.

Afin de mieux comprendre les cycle géochimiques du silicium et du magnésium, cette étude examine l'effet de la spéciation aqueuse et complexation inorganique et organique sur les facteurs de fractionnements isotopiques à l'équilibre de Si et Mg, respectivement dans les systèmes silice amorphe (SiO_2) – solution aqueuse et brucite ($Mg(OH)_2$ – solution aqueuse. A cette fin, des expériences d'échanges isotopiques à l'équilibre chimique ont été effectuées entre des solides et des fluides de différentes compositions et à différentes températures en utilisant la méthode des « trois isotopes ». Les facteurs de fractionnements isotopiques à l'équilibre ainsi déterminés sont comparés aux résultats des calculs *ab inito* effectués sur les mêmes systèmes et aux valeurs obtenues à partir d'études expérimentales et théoriques antérieures. Il est espéré que les résultats acquis dans cette étude permettront d'améliorer notre capacité à interpréter les différentes compositions isotopiques du Si et du Mg dans les

systèmes naturels et pourront être utilisés pour développer de nouveaux outils permettant d'appréhender les conditions environnementales passées.

1.2. Aqueous chemistry

The isotope exchange experiments in this study were performed in aqueous solutions at *bulk chemical equilibrium* with a solid phase and in the presence and absence of *organic ligands*. The fundamental chemical relations used in this study are reviewed briefly in the following sections.

1.2.1. Chemical equilibrium

In nature, aqueous solutions and solids such as minerals and rocks are constantly interacting (e.g. through mineral dissolution or precipitation). These reactions will tend to evolve towards chemical equilibrium over time. In a simplified case, the general chemical reaction can be written (e.g. Garrels and Christ, 1965):

$$bB + cC \leftrightarrow dD + eE \tag{1.1}$$

where *B* and *C* are the reactants, which form the products *D* and *E*, *b, c, d* and *d* are the moles of each reactant in the reaction. When the system reaches equilibrium, the ratio of the activities (*a*) of products and reactant are governed by the law of mass action given by:

$$\frac{a_D^d a_E^e}{a_B^b a_C^c} = K_{eq} \tag{1.2}$$

where K_{eq} designates a thermodynamic equilibrium constant. At equilibrium the interaction between the reactants and products does not cease, however, the net reaction rate (*r*) is zero, as forward rate (r_+) and backward rate (r_-) are equal (e.g. Aagaard and Helgeson, 1982; Garrels and Christ, 1965; Oelkers, 2001; Oelkers et al., 2018; Schott et al., 2009), i.e.

$$r = r_+ - r_- = 0 \tag{1.3}$$

Equilibrium conditions can also be described in terms of the energies of the chemical reaction. At equilibrium conditions at a distinct temperature and pressure the total free energy change ΔG is zero and thus the standard free energy change of the reaction (ΔG_r^o) can be related to the equilibrium constant by (e.g. Garrels and Christ, 1965; White, 2013):

$$\Delta G_r^o = -RT\, lnK_{eq} \tag{1.4}$$

The experimental achievement of equilibrium is challenging as the reactions can slow as equilibrium is approached (Schott et al., 2009) or the system can undergo slight changes during the experiment, which impacts the attainment of equilibrium. Therefore any

experimental system has to be constantly monitored to ensure chemical equilibrium has been attained.

1.2.1. Speciation and complexation in aqueous solution

Metal ions in solution are usually represented as M^{n+}, as though they are bare ions suspended in a structureless medium, whereas they are complexes of water, similar to complexes of other ligands. The number of water molecules bound directly to the metal ion, its coordination number, is generally similar to the number of donor atoms found for the metal in solid state, for example in oxides. In solution there is an inner-sphere of water molecules bound directly to the metal ion, and an outer-sphere of more loosely held water molecules (Martell and Hancock, 1996; White, 2013). Such metal ions in solution are called aquo ions. In aqueous solutions ions can associate with other ions, forming new species or complexes. Complex formation involves replacement of one or several water molecules coordinated to the metal ion by one or several ligands, which may replace either water molecules from the inner-sphere or water molecules from the outer-sphere (Buffle et al., 1988; Stumm, 1995). Outer sphere complexes result from electrostatic attraction between the ligand and the metal ion, but leave at least one water molecule between the metal and ligand, whereas in the inner sphere complex covalent bonds are formed between the metal and the ligand, such that no water molecules are present in between the ions. The rate of formation of a metal ion complex in aqueous solution is comparable to the rate at which water in the inner-sphere of this metal ion exchanges with water in the bulk solution (Martell and Hancock, 1996; Pokrovsky and Schott, 2002). The mean lifetime of water molecules in the first coordination sphere varies considerably with the metal properties ranging from 2×10^{-10}s (Rb^{+}) to 14.4 years (Rh^{3+}; Lincoln and Merbach, 1995).

Aqueous metal ions commonly complex to organic molecules. The principle is similar to the complexation of inorganic anions, however, organic compound often have more than one site, which can bind to the metal (White, 2013). Organic ligands, which have multiple positions to bind the same metal ion, can form multidendate complexes, also known as chelates. These chelates can form rings around the metal ions, and thus can function as metal carriers (Buffle et al., 1988). Due to the multiple positions available to bind the ion, organic ligands are able to change the coordination of the binding metal (Cella et al., 1980; Sjöberg et al., 1985; Kinrade et al., 2001, 2002; Kinrade and Swaddle, 2002; Wang et al., 2016). Additionally, organic compounds are weak acids and have thus an affinity for protons in

solution, therefore the complexation of a metal to an organic ligand is dependent on the pH of the solution (White, 2013).

If a metal ion is complexed in aqueous solution the concentration of its "free ion" in water is reduced compared to the total concentration of the dissolved metal, which leads to an increase of the solubility of the minerals bearing this metal (Bennett et al., 1988; Bennett, 1991; Bennett and Casey, 1994; Ganor et al., 2009; Schott et al., 2009; Appelo and Postma, 2013; White, 2013).

1.3. Principles of stable isotope fractionation

The present study investigates the equilibrium isotopic fractionation of Si and Mg among solids and aqueous solutions. A summary of the basic principles of stable isotopic fractionation are presented in the following sections.

1.3.1. Stable isotopes

Elements consist of atoms with positively charged protons, negatively charged electrons and neutrons, which have no charge. Protons and neutrons are present in the nucleus, which is surrounded by an electron cloud. In a given element the number of protons in the nucleus do not change, however the number of neutrons may vary. Atoms, which contain the same number of protons and electrons but differ in the number of neutrons are called isotopes. Two types of isotopes occur in nature: stable and unstable, i.e. radioactive, isotopes. Most natural elements have one or more stable isotopes. These have a permanent nuclear configuration, and do not undergo any spontaneous transformation in the form of radioactive decay or radiogenic growth.

1.3.2. Stable isotope fractionation

The isotopic composition of different materials, such as rocks, minerals, soils, plants, waters etc. can be compared by normalizing the measured isotopic ratios of these materials to an international reference standard. This standard is systematically analysed along with the samples. The isotopic fractionation between the samples and the standard are expressed using the δ notation:

$$\delta^{y}E = \left[\frac{\left({}^{y}E/{}^{x}E\right)_{sample}}{\left({}^{y}E/{}^{x}E\right)_{standard}} - 1\right] \times 1000\ [‰] \qquad (1.5)$$

where ${}^{x}E$ denotes the lightest isotope of the element *E*, and ${}^{y}E$ any heavier isotope of interest of element *E*.

Theoretically isotopes of a given element exhibit identical chemical properties, as they possess the same electron shell, however isotopes do exhibit different physicochemical properties, due to their mass difference and the resulting quantum mechanical effects. Atoms of the different isotopes of an element will react at different rates, even if they take part in the same reaction. Typically light isotopes or molecules react faster than heavier isotopes or molecules.

The isotopic fractionation factor of an element *E* between two substances *A* and *B* (α_{A-B}) can be expressed by following relation (e.g. Schauble, 2004):

$$\alpha_{A-B} = \frac{\left({}^{y}E/{}^{x}E\right)_{A}}{\left({}^{y}E/{}^{x}E\right)_{B}} \tag{1.6}$$

Note that in terms of physical processes, α_{A-B} could reflect equilibrium or non-equilibrium partitioning of isotopes. For an isotope exchange reaction in which one atom is exchanged, α_{A-B} is equal to the reaction equilibrium constant. Because α_{A-B} is very close to unity (generally on the order of 1.00X), the relation $10^3\ln(1.00X) \approx X$ allows to express the isotopic fractionation factor as the difference of the $\delta^{y}E$ values of substances A and B:

$$10^3 ln\alpha_{A-B} \approx \delta^{y}E_A - \delta^{y}E_B = \Delta_{A-B} \tag{1.7}$$

1.3.3. Stable isotope fractionation processes

Isotopic fractionation can be distinguished into non-equilibrium, i.e. kinetic and equilibrium effects. Kinetic isotope fractionation depends on the different reaction rates of isotopes or isotopic molecules. It commonly occurs with incomplete exchange, unidirectional or fast reactions, such as diffusion, dissociation reactions, evaporation and biological processes (Criss, 1999; Schauble, 2004; Hoefs, 2009; White, 2013). The fractionation associated to kinetic effects can be larger than those associated to equilibrium effects.

Equilibrium isotope fractionation, which is investigated in this study, requires that the system of interest is in chemical equilibrium (Mills and Urey, 1940; Schauble, 2004), and is caused by isotopic substitution, which arises mainly from vibrational motions of the molecules and atoms in the different phases of the system (Urey, 1947). An isotope exchange reaction can be written as follows (e.g. Hoefs, 2009):

$$aA_1 + bB_2 \leftrightarrow aA_2 + bB_1 \quad (1.8)$$

where *A* and *B* denote the two substances in the system of interest, and the subscripts indicate that the phases A and B comprise either the light (*1*) or heavy (*2*) isotope. The fractionation factor α is related to the equilibrium constant *K* of the reaction as:

$$\alpha = K^{1/n} \quad (1.9)$$

where *n* is the number of atoms exchange. Isotopic exchange reactions usually are written for the exchange of one atom. Therefore Eqn. 1.9 reduces to:

$$\alpha = K \quad (1.10)$$

The isotopes in this equilibrium reaction will distribute, depending on their masses, to minimize the vibrational energy of the system. Heavier isotopes will decrease the vibrational energy, and the bond will become more stable.

In general the equilibrium stable isotope fractionation of an element has been known to follow certain rules (Bigeleisen and Mayer, 1947; Schauble, 2004). The three most important are:

1) Increasing temperature will lead to a decrease of the equilibrium isotopic fractionation in proportion of ~$1/T^2$. Exceptions might occur when fractionation is very small or the element of interest is bonded to hydrogen.
2) The equilibrium isotopic fractionation of an element is largest, when the relative mass difference between its isotopes is large.
3) Equilibrium isotopic fractionation is affected by the atomic and molecular bonds of the element. Heavy isotopes will enrich in the compound where it will find the strongest bonds. This is due to the lower binding energy of light isotopes. The equilibrium isotopic fractionation is approximately proportional to the difference in the stiffness of the bonds. Shorter and stronger chemical bonds have the greater bond stiffness. This correlates with element properties, such as high oxidation states, presence of highly covalent bonds, transition elements and low coordination numbers.

For elements with three or more isotopes, the fractionation of the isotopes at equilibrium is typically proportional to their mass difference. This mass dependent process is usually described in a three-isotope plot as a linear curve, called the terrestrial fractionation line (TFL, Matsuhisa et al., 1978). Deviation from the TFL are described as mass-independent fractionation.

1.3.4. Influence of aqueous speciation on isotope fractionation

Aqueous solutions can contain several different species, depending on its composition. The speciation of an element in solution can have an important impact on the fractionation factor of this element. For many elements such as boron, carbon, magnesium, mercury, silicon and various transition metals it has been demonstrated that inorganic and organic speciation influences the isotopic fractionation (Hemming and Hanson, 1992; Zhang et al., 1995; Zeebe, 2005; Klochko et al., 2006, 2009; Asael et al., 2009; Holloway et al., 2011; Jiskra et al., 2012; Ryan et al., 2013; Yin et al., 2013; Fujii et al., 2014, 2015; Dupuis et al., 2015; Noireaux et al., 2015; Schott et al., 2016; Balan et al., 2018; Mavromatis et al., 2019).

In natural fluids, elements often complex to organic ligands, which will also modify the distribution of the aqueous species of this element. Additionally some organic ligands are known to affect the coordination of the metal and thus strongly influence the isotope fractionation of the element. Few theoretical and experimental studies have shown the important influence of organics on the aqueous speciation of elements such as magnesium or iron (Domagal-Goldman and Kubicki, 2008; Klochko et al., 2009; Wiederhold et al., 2006; Li et al., 2014; Mavromatis et al., 2017; Schott et al., 2016).

1.4. Silicon and magnesium isotopic systems

1.4.1. Silicon isotopes

Silicon (Si) is, with 17.1 ± 0.2 % (Allègre et al., 2001), the third most abundant element in the Earth, and has three stable isotopes with following natural abundances (De Biévre and Taylor, 1993):

^{28}Si 92.23 %

^{29}Si 4.68 %

^{30}Si 3.09 %.

Silicon takes part in nearly all geological processes, and therefore the study of its chemical behaviour and isotopic variations is crucial to understand these processes.

In nature, Si is generally bound to oxygen and does not take part in redox reactions. It is found usually in tetravalent oxidation state (4+) and forms numerous silicate minerals (Poitrasson, 2017). As an oxide (SiO_2), silicon mainly occurs as crystalline quartz and amorphous silica. Amorphous silica is found in cherts and plays an important role in biomineralization as it forms widespread biogenic minerals. SiO_2 solids are sparingly soluble

(Iler, 1979; Oelze, 2015). The Si concentrations in natural waters remain mostly below 100 ppm. In natural solutions, Si commonly occurs as monosilicic acid, $H_4SiO_4^o$. The dissolution reaction of SiO_2 in water can be described as (e.g. Iler, 1979):

$$(SiO_2)_{solid} + 2\,H_2O \rightarrow H_4SiO_4^o \tag{1.11}$$

Below pH 8.5, monosilicic acid does not dissociate, resulting in a constant solubility as can be seen in Fig. 1.1. With increasing pH, $H_4SiO_4^o$ starts to dissociate, which increases SiO_2 solubility, due to the following reactions (e.g. (Iler, 1979):

$$H_4SiO_4^o + OH^- \rightarrow H_3SiO_4^- + H_2O \tag{1.12}$$

and with further pH increase, $H_4SiO_4^o$ will further dissociate in accord with:

$$H_4SiO_4^o + 2\,OH^- \rightarrow H_2SiO_4^{2-} + 2\,H_2O \tag{1.13}$$

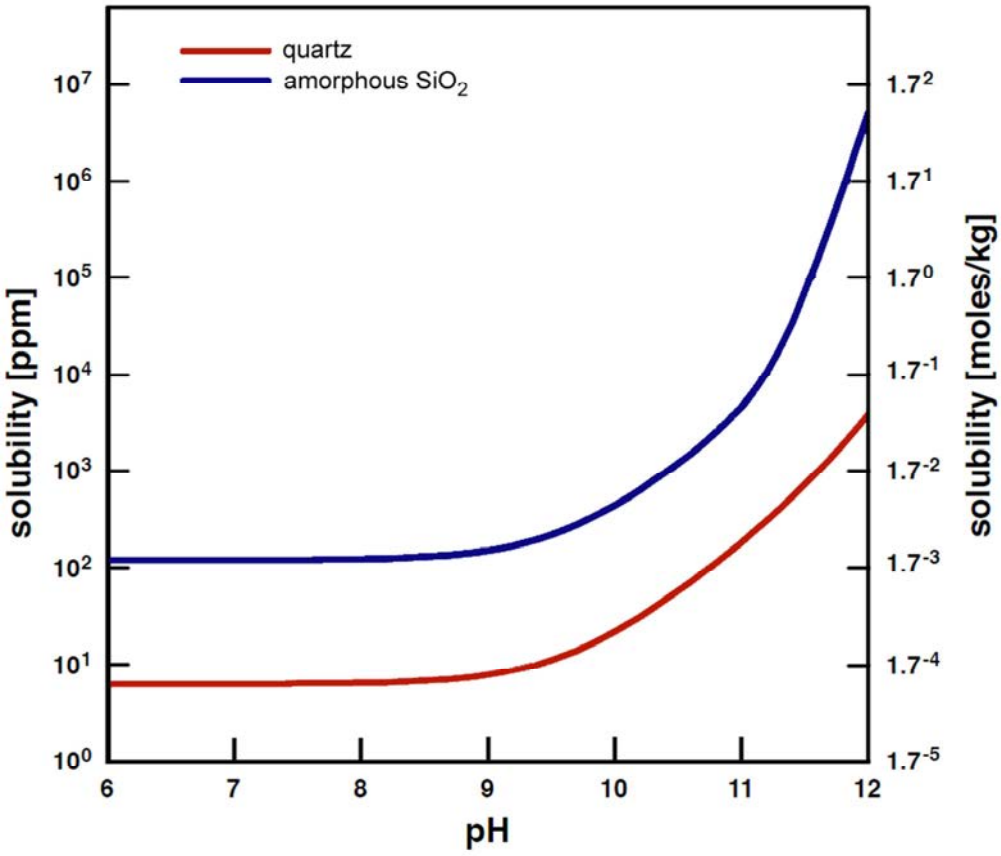

Figure 1.1 - pH dependence of the solubility of SiO2 solids at 25°C. Red curve represents the aqueous Si concentration in equilibrium with quartz and the blue curve with amorphous silica (modified after Oelze, 2015)

Dissolved Si in natural environments not only plays a role in the formation or dissolution of silicate or rock forming minerals, but $H_4SiO_4^o$ also plays an important role in the biological cycle and is used by many organisms (Leng et al., 2009). Biogenic silicon functions as a structural element and is often included as opaline SiO_2 into plants, phytoplankton, zooplankton or sponges (e.g. Leng et al., 2009; Poitrasson, 2017). In these natural environments, Si can complex with organic ligands. Studies have shown that this complexation could have an strong influence on the coordination of Si in solution (Cella et al., 1980; Sjöberg et al., 1985; Kinrade et al., 2001, 2002; Kinrade and Swaddle, 2002; Wang et al., 2016).

Due to its high abundance on Earth, and its importance for the geological and biochemical cycle, Si is a valuable tracer for near surface processes, such as biomineralization and weathering. Therefore the isotopic compositions of many Si reservoirs have been studied. The first measurements of the isotopic compositions of Si in natural samples were performed in the 1950's by Reynolds and Verhoogen (1953), Allenby, 1954 and Tilles (1961). After the moon landing, extensive work has been done on lunar samples an meteorites (e.g. Taylor and Epstein, 1973; Yeh and Epstein, 1978). The two most important studies published on terrestrial samples are from Douthitt (1982) and Ding (1996). As Si is always bound to oxygen in nature and not involved in redox reactions, only small Si isotope fractionations are expected. With the advent of multi-collector inductively coupled mass spectrometry (MC-ICP-MS) small variations in the Si isotope ratio could be determined (Cardinal et al., 2003). Since then, many studies have been performed on various Si reservoirs, demonstrating that the Si fractionation is not as small as might have been expected.

Silicon isotope fractionation varies over a range of 12 ‰, with the lowest value of -6.02 ‰ reported by Wille et al. (2010) for sponges and the highest value of +6.1 ‰ for rice grains reported by Ding et al. (2005). Fig. 1.2 shows the distribution of the Si isotopic compositions of different terrestrial reservoirs. Extra-terrestrial materials (see Poitrasson, 2017, and references herein), igneous, and metamotphic rocks (e.g. Douthitt, 1982; Ding, 1996; Ziegler et al., 2005a, 2005b; Zambardi, 2011 and references herein) are found to exhibit systematic and small ^{30}Si isotopic variations. Sedimentary rocks, such as shales and clastic metasediments exhibit a similar isotopic composition as igneous rocks (e.g. Savage et al., 2013), as they normally derive Si from the physical disintegration of silicate minerals and rocks (Georg, 2006). In contrast, cherts and Banded Iron Formations (BIFs) show a much higher fractionation than the reservoirs described above (e.g. Heck et al., 2011; Marin-Carbonne et al., 2012, 2014; Poitrasson, 2017).

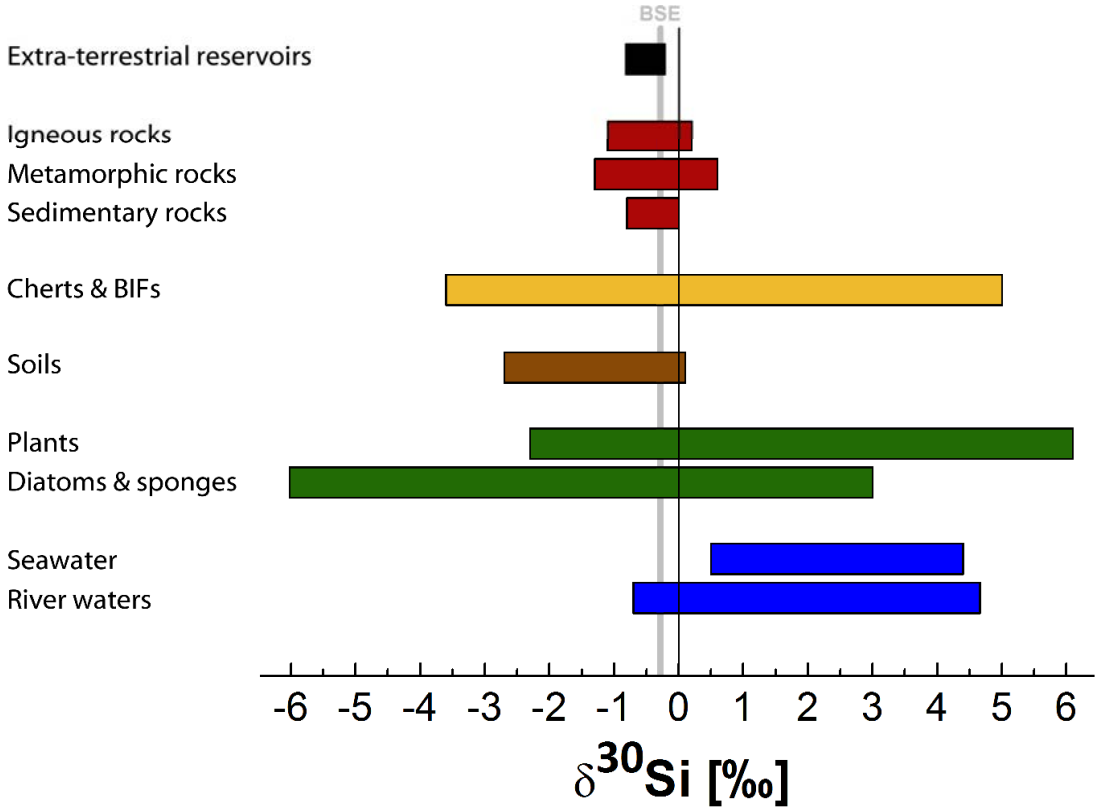

Figure 1.2 - Si isotopic compositions in various major reservoirs relative to bulk silicate Earth (BSE) shown in grey (modified from Zambardi, 2011 and Poitrasson, 2017). Data acquired from Zambardi (2011) and Poitrasson (2017) and references therein, Wille (2010) was added for Si isotope composition in sponges.

Soils depict a distinct negative Si isotope fractionation in comparison to igneous rocks, which is assumed to result from a kinetic fractionation process between clay minerals and natural waters (Opfergelt et al., 2010, 2012b, 2017; Poitrasson, 2017). Silicon is strongly fractionated in biological environments. During the uptake of Si into plants, the light isotopes are preferred (e.g. Ding et al., 2005; Sun et al., 2008; Delvigne et al., 2009; Poitrasson, 2017). However phytoliths can be enriched in heavy isotopes as shown by Ding et al. (2005). This phenomenon was attributed to the evapotranspiration occurring in plants (Ding et al., 2005, 2008b; Opfergelt et al., 2008). A wide range of isotopic fractionation is also exhibited by diatoms and sponges (Douthitt, 1982; De La Rocha et al., 2000; Ding, 1996; De La Rocha, 2003; Wille et al., 2010; Hendry et al., 2010, 2011; Hendry and Robinson, 2012). The process behind the incorporation of preferentially light isotopes is not yet understood.

Dissolved Si in natural waters, such as rivers and seawater, shows an enrichment in heavy isotopes (De La Rocha et al., 2000; Varela et al., 2004; Cardinal et al., 2005; Basile-Doelsch et al., 2005; Basile-Doelsch, 2006; Georg et al., 2006; Reynolds et al., 2006; Ding et al., 2011). During weathering or biomineralization, aqueous $^{28}Si(OH)_4°$ is preferentially

consumed to form secondary minerals, which leads to the observed enrichment of ^{30}Si in the fluid.

The large variation of Si isotopic compositions reviewed above suggests that these compositions could be a useful tool to better understand many geological and biological processes. Knowing the mechanisms behind the Si isotope fractionation in nature might also help to quantify the Si geochemical cycle.

1.4.2. Magnesium isotopes

Magnesium (Mg), an alkaline earth metal, plays an important role in the oceans and in biological and hydrological systems. After oxygen, iron, and silicon, magnesium is the fourth most abundant element in the Earth (Teng, 2017). Mg is a major element in rocks and minerals, such as olivine, pyroxene, amphibole, mica or carbonates. Magnesium has three stable isotopes with following abundances (Berglund and Wieser, 2011):

^{24}Mg 78.99 %

^{25}Mg 10.00 %

^{26}Mg 11.01 %.

Magnesium is always found in a 2+, oxidation state and thus the range of its isotopic compositions in natural materials was believed to be small. However, Mg isotope fractionation varies over a range of ~7 ‰, as can be seen in Fig. 2.3 below. As silicon and other stable isotopes, magnesium fractionates at low temperatures.

Extra-terrestrial Mg reservoirs exhibit a small isotopic fractionation, from -0.61 ‰ in lunar (Sedaghatpour et al., 2013) to 0 ‰ in chondritic samples (Galy and O'Nions, 2000). Also the fractionation within the mantle and the oceanic crust are within 1 ‰ (Teng, 2017) . The continental crust, however, is heterogeneous and Mg isotope compositions of rocks likely reflect their source compositions. The Mg isotopic signature of the upper continental crust is more heterogeneous than that of the deep continental crust and ranges from -1.64 ‰ (Teng, 2017 and citations herein) to 1.8 ‰ in weathered basalts (Liu et al., 2014). The largest Mg isotopic fractionation is seen in carbonates. Due to the weaker bonding strength of Mg in carbonates compared to its aquo ion, these minerals tend to incorporate light Mg isotopes, whereas silicates, with a stronger Mg bonding strength, will tend to incorporate heavy Mg isotopes (e.g. Schauble, 2011; Teng, 2017). Mg also plays an important role during biological processes and exhibits a distinct isotopic fractionation in some bio materials (Fig. 2.3); it has therefore the potential for a reliable tracer of some biologic processes (Teng, 2017).

Magnesium isotopes are also known to fractionate substantially in the presence of organic ligands (e.g. Li et al., 2014; Schott et al., 2016; Mavromatis et al., 2017).

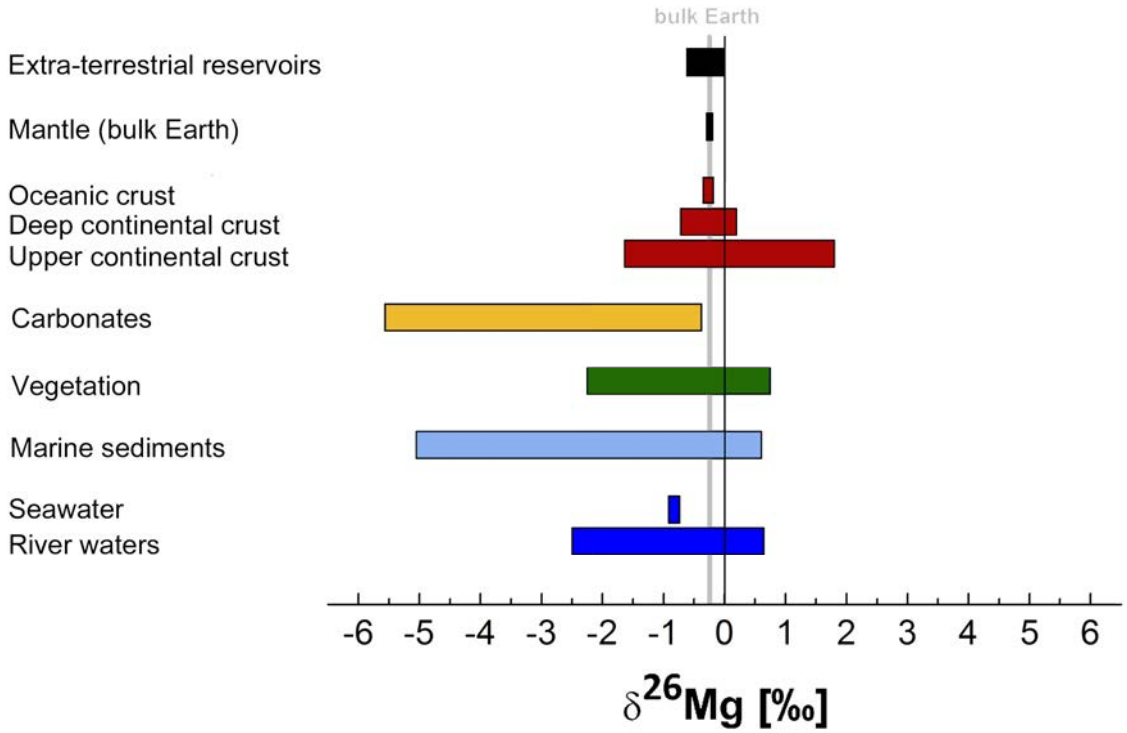

Figure 1.3 - Mg isotopic compositions in major terrestrial reservoirs relative to the average Mg isotopic composition of the mantle, i.e., bulk Earth shown in grey (modified from Teng, 2017). Data acquired from Young and Galy (2004) and Teng (2017) and the references therein.

Magnesium is homogenously distributed in seawater due to its long residence time and has an average isotopic composition of –0.83 ‰ (e.g. Foster et al., 2010; Ling et al., 2011). Corals and foraminifera are significantly lighter than ocean water, with average Mg isotopic compositions of -1 ‰ and -4.5 ‰, respectively (Hoefs, 2009). This suggests that Mg isotopes might provide a tracer of biomineralization. The isotopic composition of rivers was extensively measured by Tipper et al. (2006), and are shown to be highly variable due to isotopic fractionation during water-rock interactions (e.g. Tipper et al., 2006; Wimpenny et al., 2011; Mavromatis et al., 2014; Teng, 2017).

As is the case for silicon understanding the Mg isotopic fractionation should enable the improved quantification of its geological and biogeochemical cycles.

Chapter 2

Materials and Methods

2.1. Theoretical Background

2.1.1. Three-isotope method

The experimental investigation of equilibrium isotope fractionation of Si and Mg in this thesis is based on the 'three-isotope method'. The three-isotope method was originally used to determine the equilibrium isotopic fractionation factors of oxygen between mineral and solution (Matsuhisa et al., 1978; Matthews et al., 1983a, 1983b, 1983c). Over the past 10 years, this method was also successfully applied to non-traditional isotope systems, such as Mg and Fe (Shahar et al., 2008; Beard et al., 2010; Li et al., 2011; Frierdich et al., 2014; Reddy et al., 2015), as well as Si (Zheng et al., 2016). This approach is commonly used to evaluate the kinetics of isotopic exchange reactions between two components (Fig. 2.1; Cole and Chakraborty, 2001; Johnson et al., 2002; Li et al., 2011; Wu et al., 2012; Zheng et al., 2016).

To apply this method to an element it has to have at least three stable isotopes (Shahar et al., 2017) in measurable abundances. The three-isotope method is applied by performing experiments composed of a two-component system, a mineral phase A and an aqueous phase B. Their starting composition begins where both phases plot in a δ vs. δ diagram on the terrestrial fractionation line (TFL) as shown in Fig. 2.1. The TFL is the line where all natural samples plot and in which the isotopic compositions are related by mass-dependent fractionation. To apply the three-isotope method the aqueous phase of the experimental system is altered by the addition of an isotopic spike (^{29}Si or ^{25}Mg in the present study). The isotopic ratio of the spiked fluid is then distinctly offset from the TFL (t_0 of the liquid phase in Fig 2.1). As the system undergoes isotopic exchange towards isotopic equilibrium, the isotopic compositions of the two components will gradually evolve over time (t_0, t_1, t_2,…). When the system reaches isotopic equilibrium, at 100% of isotopic exchange, the two components will plot on a secondary fractionation line (SFL) which has the same slope as the TFL, given the mass dependent behaviour of the isotopic fractionation. The position of the SFL is defined by the isotopic mass balance of the system (see Fig. 2.1).

In many situations, especially at low temperature, the isotopic exchange is slow and equilibrium is rarely reached. The three-isotope method allows determination of the isotopic composition of the two components at 100% exchange.

The degree to which the system attains isotopic equilibrium can be determined using:

$$F = \frac{(\delta_t - \delta_i)}{(\delta_e - \delta_i)} \tag{2.1}$$

where F is the degree of isotopic exchange, and ranges from 0 to 1, δ_t denotes the isotopic composition of either one of the components of the sample at any time, t, during the reaction, and δ_i describes the initial and δ_e the equilibrium isotopic composition of the component.

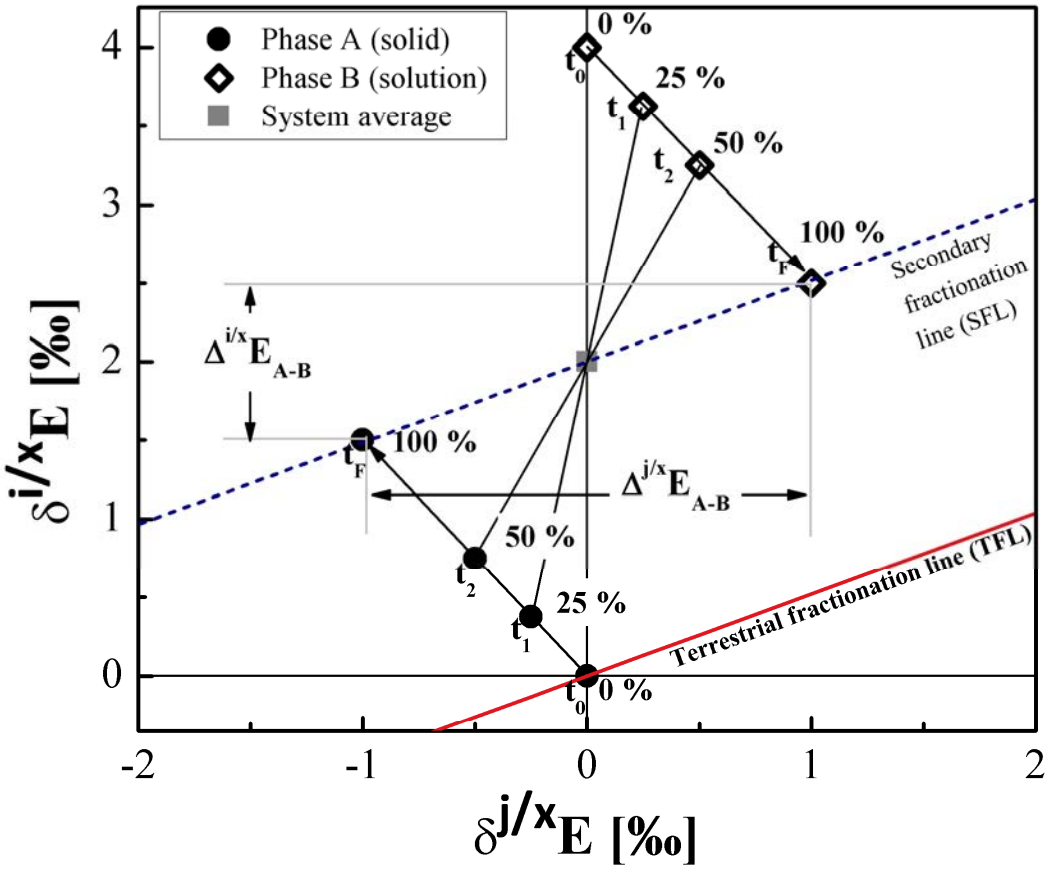

Figure 2.1 - Concept of the three isotope method modified after Li et al. (2011). The solid (Phase A) has a natural isotopic composition and plots on the mass-dependent fractionation line. The solution (Phase B) shows a distinct offset of the TFL, due to spiking of either ^{25}Mg or ^{29}Si. The isotopic composition of the two phases will evolve towards a value of 100% of isotopic exchange. The line connecting the two phases crosses the system average throughout the process, due to isotopic mass balance. At 100% exchange the two phases will plot on a SFL, parallel to the TFL The position of the SFL depends on the isotopic mass balance of the system. For many systems the isotopic exchange will be incomplete, and the isotopic composition at time t_F of total exchange can be calculated by the extrapolation of the time series (t_0 to t_n). The extrapolated value will represent the equilibrium isotopic fractionation factor, if the isotopic exchange is occurring under equilibrium conditions.

In a two-component system δ_e can be derived from the mass balance equation at equilibrium (Zheng et al., 2016), and calculated from:

$$\delta_e = \delta_{mean} - \left(\frac{N_A}{N_A+N_B}\right) \times \Delta_{eq,A-B} \quad (2.2)$$

where δ_{mean} indicates the mean Si isotope composition of the system shown as system average in Fig 2.1, and N_A and N_B denote the moles of Si in the two different Phases A and B. The $\Delta_{eq,A-B}$ of the system is not known, as it is the equilibrium value, which is derived from the three-isotope approach. The solution to Equation 2.2 is done iteratively. A first estimate of $\Delta_{eq,A-B}$ is made. The influence Δ_{A-B} has on the calculation is minimized due to the large isotopic contrast between the starting materials inflicted by the addition of the isotopic tracer, relative to $\Delta_{eq,A-B}$ (Zheng et al., 2016). The isotope fractionation factors can then be obtained by extrapolation of the isotopic compositions of the two components as a function of the degree of isotopic exchange (δ-F diagram) as shown in Fig. 2.2.

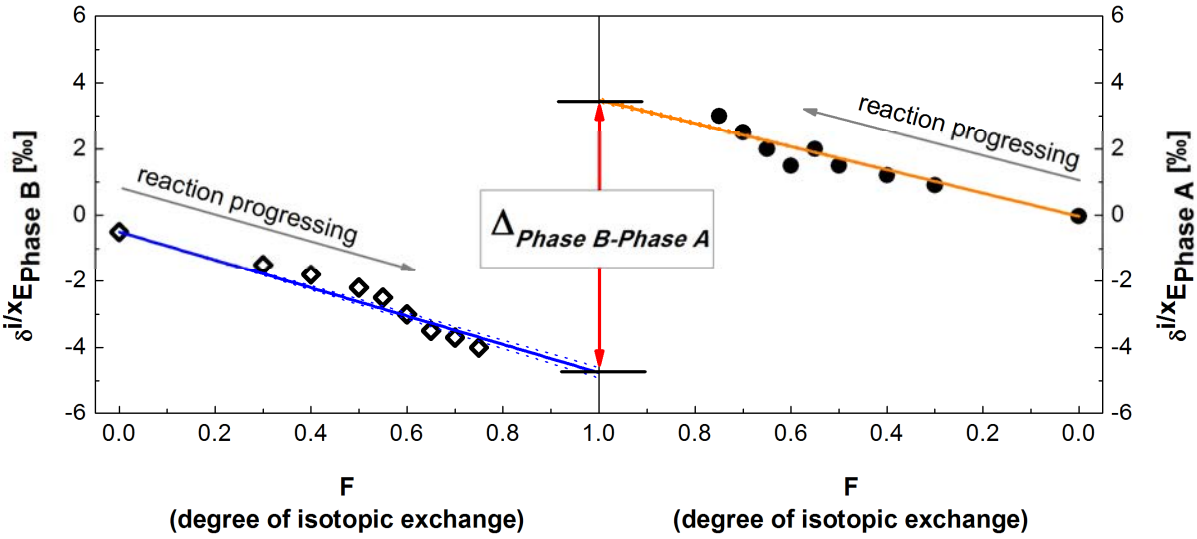

Figure 2.2 - Illustrative example of the extrapolation to obtain the fractionation factor between phase B and phase A. As the reaction is progressing, the two phases approach a degree of isotopic exchange F=1, thus equilibrium. If F=1 is not reached the equilibrium values can be extrapolated, and the Δ_{eq} can be determined.

2.1.2. Kinetics of isotopic exchange reactions

The three-isotope method not only allows the determination of the equilibrium fractionation factors of a solid-solution system, it also allows determination of the kinetics of isotopic exchange. The isotope exchange rates can be quantified using (Cole and Chakrabarty, 2001; Johnson et al., 2002):

$$\frac{-d(1-F)}{dt} = k_n(1-F)^n \quad (2.3)$$

where k_n is a rate constant and n the order of reaction, usually an integer from 0 to 3. Isotope exchange reactions mostly follow either a first-order (n=1) or second-order (n=2) rate law (Criss et al., 1987; Huang and Tsai, 1970; Johnson et al., 2002; Welch et al., 2003; Li et al., 2011; Zheng et al., 2016). The integrated forms of these rates equations with $F_{(t=0)}$= 0 can be written as:

$$ln(1-F) = -k_1 t \quad \text{for } n=1 \quad (2.4)$$

$$\frac{F}{(1-F)} = k_2 t \quad \text{for } n=2 \quad (2.5)$$

The isotopic exchange rates can be determined using the first and second-order rate law by fixing the initial value of F at the intercept of t=0, so that the rate constant can be determined by regression of to obtain the best fit of the data (Cole and Chakraborty, 2001; Johnson et al., 2002; Li et al., 2011).

2.2. Materials

2.2.1. Amorphous Silica (SiO_2,am)

The solid used for all Si experiments was a 100 mesh, Alpha Aeser® silicic acid hydrate powder. To remove fine particles this material was sedimented in deionized (MQ®) water (Pokrovski and Schott, 1998). For this purpose, 40-85 g of amorphous SiO_2 was stirred with MQ®- water in a 1 dm^3 glass beaker until it was suspended. It was then left to settle for 10 minutes, then decanted. This procedure was repeated until the supernatant became clear within the first 5 min. Subsequently, the recovered solid was dried in the oven at 60°C. To avoid hydration of the powder while it cooled to room temperature, it was placed into a desiccator. These powders were then imaged by scanning electron microscopy (SEM; see Chapter 2.4.1.1) and transmission electron microscopy (TEM; see Chapter 2.4.1.2). Subsequently the surface areas of these powders were determined with the BET method (see Chapter 2.4.1.3), and the water content was measured with thermogravimetric analysis (see Chapter 2.4.1.4). The properties of the washed powders used in this study are summarized in Table 2.1.

Table 2.1 - Summary of the properties of the washed amorphous SiO_2 powders used in this study: S_{BET} represents the specific BET surface area of the powders. The water content (m_{H2O}) and the resulting chemical formula of the powder taking account of this water content are provided.

batch n°	batch name	m_{start} [g]	m_{end} [g]	Δm [g]	S_{BET} [m^2/g]	m_{H2O} [wt %]	chemical formula
1	Sib	44.82	23.37	21.45	214.7	8.93	$SiO_2 \cdot 0.33\ H_2O$
2	Sic	62.37	31.05	31.32	195.0	9.15	$SiO_2 \cdot 0.34\ H_2O$
3	Sid	82.17	25.40	56.77	189.8	8.67	$SiO_2 \cdot 0.32\ H_2O$
4	Sig	50.59	32.57	18.02	195.6	7.87	$SiO_2 \cdot 0.28\ H_2O$
5	Sik	73.59	13.73	59.86	179.80	8.86	$SiO_2 \cdot 0.32\ H_2O$

2.2.2. Brucite synthesis

For magnesium experiments, microcrystalline brucite ($Mg(OH)_2$) powder was synthesized by the wet precipitation method previously described by Henrist et al. (2003), Lv et al. (2004), and Estrada et al. (2015). In detail, 100 ml of an aqueous 2M $MgCl_2$ solution was prepared from reagent grade $MgCl_2 \cdot 6H_2O$ powder from VWRChemicals® and deionized Milli-Q® water. This aqueous $MgCl_2 \cdot 6H_2O$ solution was added using a Metrohm® 702 SM Titrino titration device at 2.5 ml/min dropwise into 200 ml suprapur Merck® 25% NH_3 solution, which was constantly stirred and heated to 45°C. This experimental protocol is summarized in Fig. 2.3.

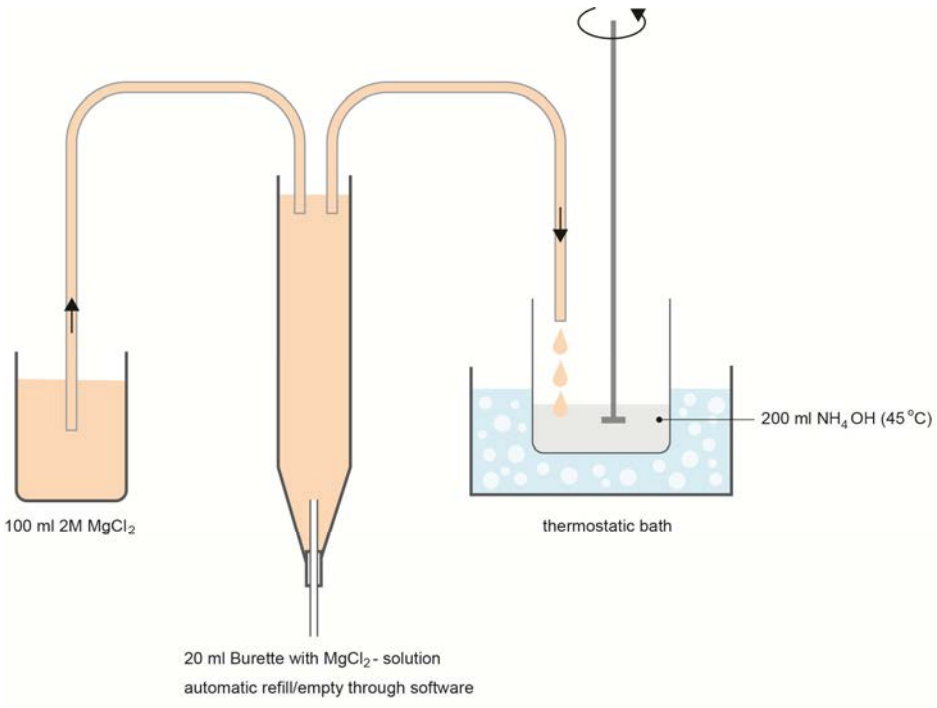

Figure 2.3 - Sketch of the experimental brucite synthesis method.

Brucite immediately precipitates in accord with (Lv et al., 2004):

$$MgCl_2 \cdot 6H_2O + 2\,NH_3 \rightarrow Mg(OH)_2 + 2\,NH_4Cl + 6H_2O \quad (2.6)$$

Nanoparticles, which are formed at the initial stage of the precipitation reaction serve as precipitation nuclei for the growth of larger brucite crystals, which grow by the aging of the reactive fluid. Therefore the reaction vessel was sealed and left at room temperature for three days after the addition of the aqueous $MgCl_2 \cdot 6\ H_2O$ solution. The obtained brucite powder was filtered and washed with Milli-Q® water to remove impurities, such as NH_4Cl. The powder was first dried at 135° C for 1 h, and, to assure it was anhydrous, fully dried at 60°C overnight. A hydrothermal treatment, as proposed by Henrist et al. (2003), Lv et al. (2004), and Estrada et al. (2015) to improve brucite crystallinity, was not performed. Note, however, that the aqueous NH_3 solution used to create powder batch BD was heated briefly to 90°C during the synthesis, in an attempt to generate a higher degree of crystallinity of the grains. To verify that the powder obtained was brucite, it was analysed by X-ray Powder Diffraction (P-XRD, see Chapter 2.4.1.5). The morphology of the samples was analysed using SEM and TEM. The specific surface areas of the powders were determined with the BET method. All synthesized brucite powders are listed in Table 2.2 below.

Table 2.2 - Characteristics of the synthesized brucite powders used in this study.

batch n°	batch name	$T_{precipitation}$ [°C]	$m_{obtained}$ [g]	S_{BET} [m^2/g]
1	BB	48.0	10.58	30.54
2	BC	45.0	7.94	39.4
3	BD	48.1	7.19	29.23
4	BE	53.1	8.27	35.53

2.2.3. Aqueous Solutions

2.2.3.1. Inorganic solutions

Inorganic amorphous silica isotope exchange experiments were performed at pH 6.4 and 9.9 at 25°C, and at pH 5.8 and 9.1 at 75°. The aqueous solutions for these experiments were prepared as follows:

1) Aqueous solutions for experiments at pH ~6 were prepared using high purity de-ionized Milli-Q® water (>18.2 Ω). During the first part of the 25° experiment, the pH

had to be stabilized by the addition of minor quantities of 1 N HCl and 1.4 N NH_4OH, which resulted in an ionic strength of 0.1M.

2) Aqueous solutions for Si experiments performed at pH 9.1 (75°C) and 9.9 (25°C) were prepared as a NH_4Cl - NH_4OH pH-buffer, using suprapure NH_4Cl salt and a 25 % NH_3 solution from Merck®.

The aqueous solutions for the brucite isotope exchange experiments were prepared by:

1) Using high purity de-ionized Milli-Q® water (>18.2 Ω) and bi-distilled HCl and an ionic strength of 0.15 M.
2) Two aqueous sodium sulphate solutions were then prepared at pH 9.5 and 10 by dissolving suprapur Merck® sodium sulphate (Na_2SO_4) powder into de-ionized (MQ®) water with bi-distilled HCl at an ionic strength of 0.14 M and 0.02 M for pH 9.5 and 10 respectively.

2.2.3.2. Aqueous organic solutions

The effect of organic complexation of aqueous Si and Mg on equilibrium mineral-fluid isotopic fractionation was determined for several organic ligands, which were selected because they are known to complex silicon or magnesium cations in solution. Organic silicon experiments were performed with:

1) Catechol: two aqueous solutions with 0.05 M and 0.08 M Catechol were prepared with reagent grade Merck® pyrocatechol ($C_6H_8O_2$) dissolved into a NH_4Cl - NH_4OH pH-buffer solution. These ware prepared using suprapur Merck® NH_4Cl salt and an aqueous Merck® 25 % NH_3 solution.
2) Glucamine: pre-treated amorphous SiO_2 powder was dissolved in a 0.01 M NaOH solution, prepared with Merck® sodium hydroxide pellets dissolved in de-ionized water. When steady state was achieved, a Acros organics® N-Methyl-D-glucamine ($C_7H_{17}NO_5$) powder was dissolved in the fluid at a 1:2 concentration ratio of silicon to glucamine.

For the brucite isotope exchange experiments, two different organic ligands were used:

1) Citrate: a 4×10^{-3} M aqueous citrate solution was prepared using reagent grade Merck® tri-sodium citrate dehydrate ($C_6H_5Na_3O_7 \cdot 2\ H_2O$) powder and deionized MQ® water.

Table 2.3 - Summary of the initial aqueous solutions of each experimental series performed in the present study

Exp. ID	Temperature [°C]	Solution composition	pH	$m_{solution}$ [g]	m_{solid} [g]
		initial aqueous solutions for chemical equilibration of amorphous silica			
SibA	25	pure MQ® water + 0.43 ml 1 N HCl + 0.50 ml 1.4 N NH_4OH	6.2	200.04	3.00
SicB	25	0.1 M NH_4Cl - 0.35 M NH_4OH buffer	10.2	200.00	3.00
Sig75A	75	pure MQ® water	6.0	200.21	3.02
Sik75B	75	0.1 M NH_4Cl - 1.52 M NH_4OH buffer	9.4	200.56	3.01
SigC0.05	25	0.1 M NH_4Cl - 0.35 M NH_4OH buffer + 1.11 g pyrocatechol	9.0	204.99	3.02
SigC0.08	25	0.1 M NH_4Cl - 0.35 M NH_4OH buffer + 1.77 g pyrocatechol	9.1	200.01	3.01
		initial aqueous solutions for chemical equilibration of brucite			
BB	25	pure MQ® water + 7.80 ml 1N HCl + 2.3 ml 10 N HCl	9.6	200.13	3.00
BABE	25	pure MQ® water + 7.80 ml 1N HCl + 2.3 ml 10 N HCl	9.6	200.13	3.00
BB-Citrate	25	pure MQ® water + 1.66 ml 1N HCl + 0.27 g citrate	10.4	200.35	3.01
BCS	25	pure MQ® water + 3.00 ml 9.35 N HCl + 1.11 g Na_2SO_4	9.5	200.48	3.07
BDS	25	pure MQ® water + 0.43 ml 9.6 N HCl + 1.54 g Na_2SO_4	10.0	200.10	3.02
BE-Edta	25	0.1 N EDTA solution (Titriplex III Merck®)	-	201.36	3.01

2) Ethylenediaminetetraacetic acid (EDTA): Titriplex III Merck® 0.1 N EDTA solution for titration with the chemical formula $C_{10}H_{14}N_2Na_2O_8 \cdot 2\ H_2O$ was used to perform Mg-EDTA experiments.

The compositions of all aqueous solutions used in the experiments performed in this study are listed in table 2.3.

2.2.4. Isotopic spike solutions

The aqueous isotopic spike solutions used in this study (see Chapter 2.1.1) were prepared using Eursio-top® SiO_2 and MgO powder isotopically enriched in ^{29}Si and ^{25}Mg, respectively.

The ^{29}Si isotope tracer was prepared by dissolving 40.6 mg of the $^{29}SiO_2$ enriched powder, having an initial composition of 0.21% ^{28}Si, 99.76% ^{29}Si, and 0.03% ^{30}Si into 500 ml of de-ionized water. The pH was then adjusted to 10 using a 2 mol/kg ammonia solution. This solution was then filtered with a 0.22 µm Millipore® Teflon syringe-filter and its concentration was measured with colorimetry (see Chapter 2.3.2.4). Both spike solutions were analysed by High Resolution - ICP-MS (see Chapter 2.3.2.5), to determine the isotope ratios of the spikes. The spike ratios in solution and the properties of spike solutions are listed in Table 2.4.

The ^{25}Mg enriched spike solution was prepared by dissolving 50.7 mg ^{25}MgO enriched powder, with a initial composition of 2.4% ^{24}Mg, 96.4 % ^{25}Mg, and 1.2% ^{26}Mg into a 500 ml 1N HCl solution prepared from MQ® water and bi-distilled HCl. After its complete dissolution, the solution was filtered with 0.22 µm Millipore® Teflon syringe-filter and the pH was adjusted with 4 mol/kg NaOH to 8.8. The concentration of Mg in this fluid was determined by AAS (see Chapter 2.4.2.2).

Table 2.4 - Properties of the spiked ^{25}Mg- and ^{29}Si- aqueous solutions.

solution	pH	Concentration [ppm]	^{24}Mg or ^{28}Si [%]	^{25}Mg or ^{29}Si [%]	^{26}Mg or ^{30}Si [%]
$^{29}SiO_2$	9.8	25.5	0.21	99.76	0.03
^{25}MgO	8.8	40.8	2.43	96.47	1.10

2.3. Experimental design

2.3.1. Chemical equilibration of reactive fluids

All isotope exchange experiments were all performed under bulk chemical equilibrium but isotopic diseqilibrium conditions. To create aqueous solutions in equilibrium with the starting solids, 200 ml of all reactive inorganic and organic solutions were chemically equilibrated with ~3g of either amorphous SiO_2 or synthesized brucite powder in high-density polyethylene (HDPE) Nalgene® bottles. These were placed into either a 25°C or 75°C thermostatic shaking bath. The aqueous solutions were sampled at regular intervals over 70 days. The pH was immediately measured (see Chapter 2.4.2.1), and adjusted with reagent grade HCl, NaOH, or NH_3 if needed. The aqueous Si and Mg concentrations of the sampled solutions were determined by colorimetry (see Chapter 2.4.2.4) and atomic absorption spectrometry (AAS, see Chapter 2.4.2.2), respectively, to assess when chemical equilibrium was reached. The results of these measurements are shown in Fig. 2.4.

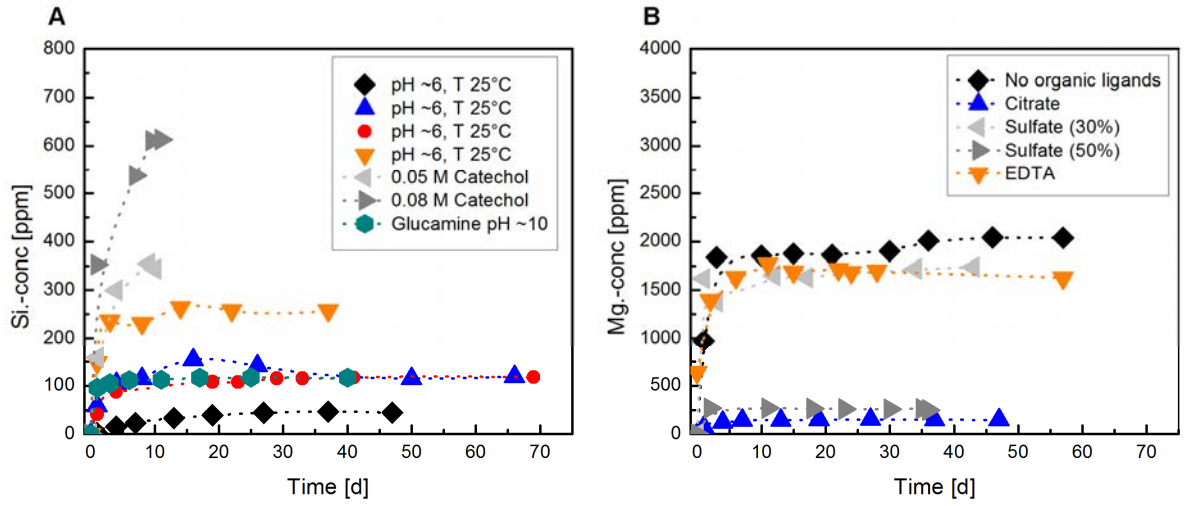

Figure 2.4 - Dissolution curves of amorphous Silica (A) and brucite (B) obtained during the preparation of aqueous solutions for the isotope exchange experiments.

Chemical equilibrium is achieved when the properties of a reacting system do not exhibit any observable change over time or a tendency to change. In a solid-aqueous solution system, this means that the rates of the forward and backward reaction, e.g. dissolution-precipitation, are equal and there is no net exchange in concentration. This condition was assumed to be attained when both pH and concentration of the aqueous solutions remained constant over time at a given fixed temperature. When chemical equilibrium was attained, the aqueous solutions were filtered with 0.2 µm Merck® Teflon syringe filters. The Mg and

Si concentrations and the pH of these fluids were measured and reported in Table 2.5 and hereafter considered as the starting conditions of the isotopic exchange experiments.

Table 2.5 - Measured concentrations and pH of chemical equilibrated, and spiked solutions used in the isotope equilibration experiments performed in this thesis. Note that concentrations and pH did not significantly change due to the addition of the spike, therefore equilibrium conditions are maintained within uncertainty of the analyses.

Experiment ID	Temperature [°C]	*chem. equil. solution*		*spiked solution*	
		pH	Conc. [ppm]	pH	Conc. [ppm]
Solutions for amorphous silica isotope exchange experiments					
SibA	25	6.2	44.40	6.1	47.96
SicB	25	10.1	116.24	9.9	115.42
Sig75A	75	5.8	117.36	5.2	122.27
Sik75B	75	9.3	282.22	9.2	287.16
SigC0.05 M	25	8.9	343.23	8.9	344.64
SigC0.08 M	25	8.9	612.07	8.9	599.30
SidG	25	10.0	115.68	10.0	114.13
Solutions for the brucite isotope exchange experiments					
BB	25	9.4	2018.99	9.0	2084.04
BABE	25	9.4	2019.89	9.4	2002.65
BB-Citrate	25	10.1	147.97	10.2	146.05
BCS	25	9.4	1724.00	9.5	1703.29
BDS	25	9.9	274.16	9.9	271.01
BE-Edta	25	12.5	1626.09	12.4	1715.05

2.3.2. Isotope exchange experiments

The chemical equilibrated solutions were enriched up to ~ 25‰ with either the ^{29}Si and ^{25}Mg isotope tracer for Si and Mg experiments, respectively. After spiking, the concentrations and pH were re-measured and adjusted if necessary by adding small quantities of HCl, NaOH or NH_4OH to maintain these fluids as close as possible to the equilibrium conditions. The compositions of the starting spiked solutions are listed in Table 2.5. The isotopic exchange experiments consisted of a eight series of closed system experiments of different durations. Each experiment of each series was performed in 10 ml polypropylene reactors. Each series consisted of a number of individual experiments of selected durations but identical experimental conditions (e.g starting fluid composition, temperature, mass of solid). At selected times, the reactors were opened and all of the solids and fluids were collected and characterized. This allowed the determination of the fluid and

solid composition at different isotopic exchange states. The amount of powder and aqueous solution used for each experiment series are listed in Table 2.6.

Table 2.6 - Average amount of powder and solution used for each set of isotopic exchange experiment

Experiment ID	Temperature [°C]	m_{powder} [g]	$V_{solution}$ [ml]	powder:solution ratio
amorphous silica isotope exchange experiments				
SibA	25	0.15	5.03	1:33
SicB	25	0.15	5.01	1:34
Sig75A	75	0.15	4.01	1:26
Sik75B	75	0.15	5.04	1:33
SigC0.05 M	25	0.30	9.94	1:33
SigC0.08 M	25	0.30	9.98	1:33
SidG	25	0.31	9.89	1:32
brucite isotope exchange experiments				
BB	25	0.10	5.02	1:50
BABE	25	0.49	5.03	1:10
BB-Citrate	25	0.10	5.02	1:49
BCS	25	0.19	3.04	1:16
BDS	25	0.51	5.04	1:10
BE-Edta	25	0.50	5.00	1:10

To verify that no mass was lost during each closed system experiment, all reactors were weighted at the beginning and the end of each experiment. The sample tubes of experiments at 25°C were placed into an orbital shaker shown in Fig. 2.5 to be constantly mixed. The 75°C experiments were kept in a thermostatic bath and were hand shaken up to twice a day.

Figure 2.5 - Orbital shaker used to constantly mix the isotopic exchange experiments at 25°C

At chosen time intervals, a reactor was removed from the orbital shaker or the thermostatic bath, centrifuged for 20 min at 4500 rpm, and then opened. The supernatant was separated from the powder and filtered with Merck® 0.2 µm Teflon syringe filters. The pH was measured directly after sampling. For the 75°C experiments, the recovered fluids were diluted right after the pH measurement. The concentrations of dissolved metals in these fluids were determined using colorimetry or AAS. The powders recovered from each experiment were washed with de-ionized MQ water, filtered, then oven dried at 40°C. The surface areas of some of these powders were determined using the BET-method, and the morphology of the selected powders were analysed by TEM and SEM. All reactive fluids and the powders were prepared for ion chromatography (see Chapter 2.3.3.1 and 2.3.3.2), and subsequently analysed with Multi-collector ICP mass spectrometry (see Chapter 2.3.3.3). The speciation of the collected fluids were then calculated with PhreeqC (see Chapter 2.5), so that the fractionation factor between the different solution species, and the solid phase could be calculated.

2.4. Analytical methods

2.4.1. Characterization of solid phases

2.4.1.1. Scanning electron microscopy (SEM)

Representative experimental powders were imaged using the MEB JEOL JSM-7800F Prime electron microscope (Fig.2.6 A) located at the Raimond Castaing Microcharacterization Centre (Toulouse, France). This technique enables surface structure imaging of the powder samples with up to a ~10^5 magnification (Putnis, 1992). The sample was fixated on a carbon film, coated with platinum, and placed into the electron microscope under vacuum. The electron source is a Field Emission Gun (FEG) that produces a narrow electron beam of high and stable energy, enabling high resolution imaging. The amorphous silica and brucite samples were scanned with a 5 kV and 10 kV electron beam respectively. Two types of electrons are emitted back from the sample surface:

1) The secondary electrons, which result from the collision of the incident electrons beam with the atoms of the sample. During this collision, they interact with the atomic structure of the sample, which impacts their energy. They are emitted at its surface in every direction. The collected electrons thus display different contrasts, which are used to image topography.

2) The backscattered electrons (BSE), which result from the initial electron beam hitting the sample surface and collected at a single high angle from this surface. Their high energy is modulated by the level of absorption of the surface, which itself is dependent on its chemical composition.

The emitted electrons are collected and subsequently amplified. The collected electron signal changes the brightness of a cathode ray tube that scans the sample simultaneously with the electron probe. This enables a high magnification of the sample topography. Specific detectors distinguish between the different emitted electrons. As a result, the sample can be shown either as a secondary electron (Fig. 2.6 B and C) or Back Scatter Electron (BSE) image. As the powders in this study consist of a only single phase, no BSE images were collected. When the sample is scanned with an electron beam it also emits X-ray photons. These have characteristic wavelengths and energies, according to the elemental composition of the sample. The obtained photons yield the energy-dispersive X-ray spectra (EDS), which is used for the non quantitative chemical identification, to confirm the purity of the powders.

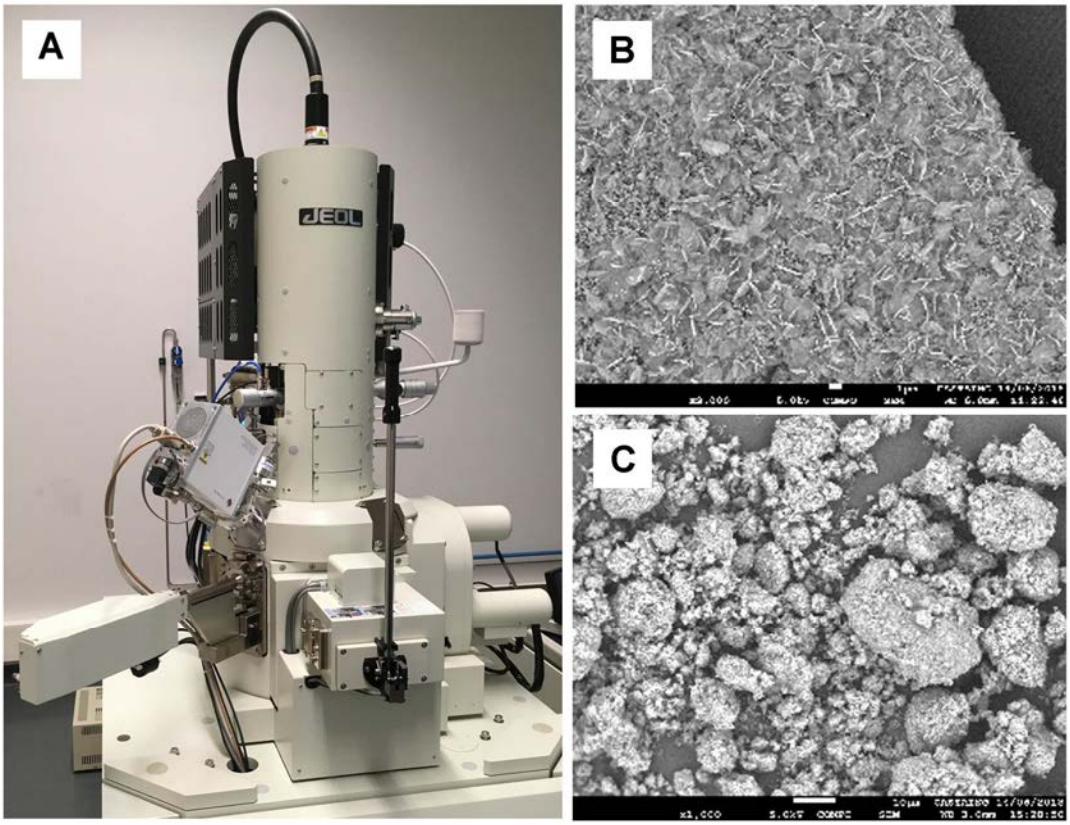

Figure 2.6 - A. The MEB JEOL JSM-7800F Prime scanning electron microscope used in this thesis. B. The secondary electron image of Brucite. C. The secondary electron image of amorphous silica.

2.4.1.2. Transmission electron microscopy (TEM)

Transmission electron microscopy (TEM) enables very high spatial resolution (several Ångströms, Å) imaging and direct identification of the crystalline lattice of solid samples. It is therefore ideally suited to identify any changes in powder morphology at the sub grain scale before and after experiments. Representative amorphous silica and synthesised brucite powders before and after experiments were analysed using the JEOL JEM-ARM200F Cold FEG transmission electron microscope (Fig.2.7 A) located at the Raimond Castaing Microcharacterization Centre (Toulouse, France). The samples were prepared by suspending a small amount of powder in ethanol, which are subsequently captured on a Cu grill lined with a carbon film (Fig. 2.7 B). The electron beam generated by a FEG electron source, was accelerated between 60 and 200 kV, and was focused on the sample by condenser lenses. The electrons transmitted through the thin sample are transmitted or diffracted through the crystalline or amorphous lattice and focussed by an objective lens. This beam is subsequently projected onto a fluorescent screen with magnification up to 10^6. The samples were imaged in several modes (Putnis, 1992):

1) Diffraction contrast imaging: Enables the magnification of very specific sample areas (Fig. 2.7 C)
2) Bright field (BF) image: Only the transmitted (undiffracted) beam is used to form the image
3) Dark field (DF) image: Diffracted beams are used to form the image. It is considered as a negative of the bright field image.

These three modes were used to characterize and image the structure, mainly of the amorphous silica powders, as SEM imaging could not provided sufficient resolution for these samples. The TEM permits, as well as the SEM described above, chemical analysis in form of X-ray spectroscopy.

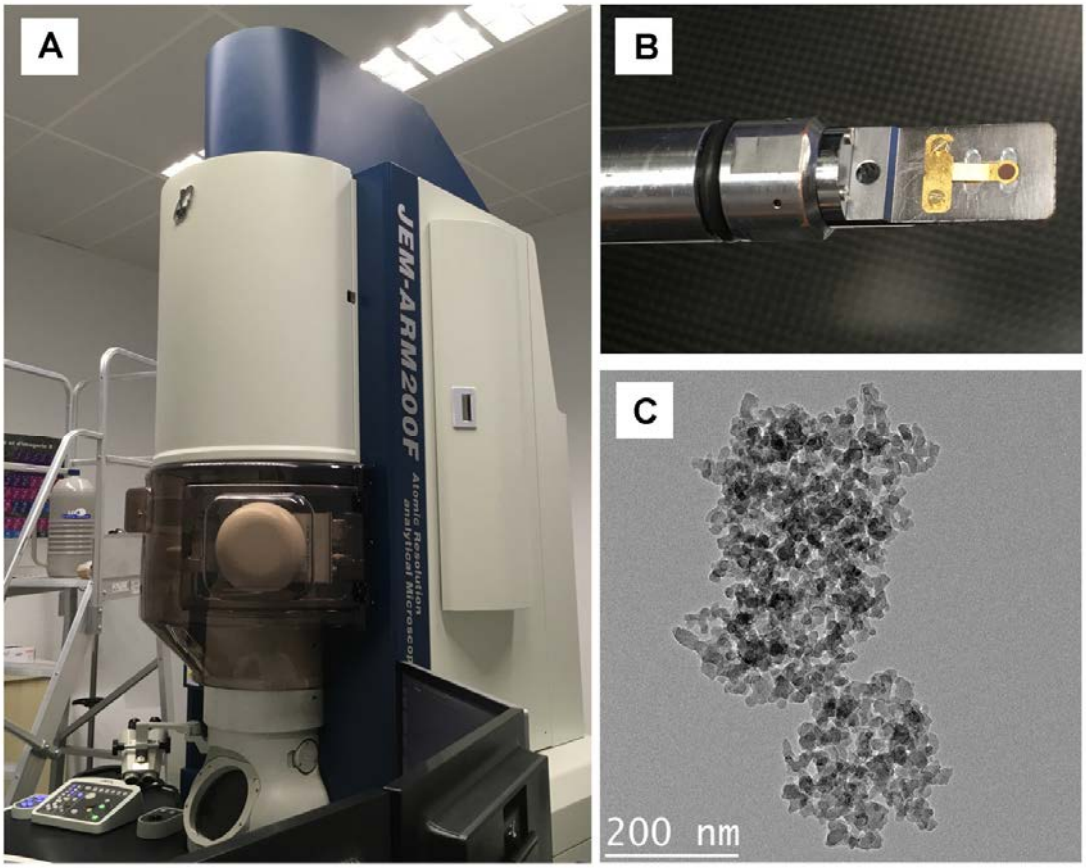

Figure 2.7 - A. The JEOL JEM-ARM200F Cold FEG Transmission electron microscope used in this thesis. B. A sample holder with small Cu grill C. A diffraction contrast image of SiO_2 powder.

2.4.1.3. Surface area

The specific surface areas of initial and final powders were determined with a Quantachrome Autosorb-1 MP using the multipoint BET method (Brunauer et al., 1938), and nitrogen (N) as the adsorbing gas. The sample surface was first cleaned from possible contaminants such as water and oils by heating the sample up to 100°C under vacuum; this treatment is also known as degassing. After this pre-treatment, the sample is brought to a constant temperature of 77.3°C in a thermostatic bath. Then, liquid nitrogen (-196 °C, at atmospheric pressure) is gradually introduced into the evacuated sample chamber. The nitrogen is adsorbed onto the sample surface and forms a monomolecular layer, covering the entire surface. Taking account of the density of nitrogen, the adsorbed mass of N, and the sample weight, one can calculate the surface area, based on the Brunauer, Emmett and Teller (BET) theory (Brunauer et al., 1938). Subsequently, the system is degassed, and the desorption of gas from the powder can be determined. The uncertainty of the measurements collected in this thesis is estimated to be ± 10% with a reproducibility of ~2%.

2.4.1.4. Thermogravimetric analysis

Thermogravimetric analyses were performed with the Mettler Toledo® ATG/DSC1 located at the National Polytechnic Institute in Toulouse, France to quantify the water content of the amorphous silica powder. These analyses were performed by placing a known mass of the powder samples into platinum crucibles and heating these at 10°C/min up to 1000°C. The mass difference of the sample before and after heating indicates the loss of water from the crystal lattice, and thus the total water content of the powder. It is expressed as weight loss in percent.

2.4.1.5. X-ray Powder Diffraction (P-XRD)

Synthesized brucite powders were analysed with a 2nd Generation Bruker® D2 Phaser, to determine the quality of the synthesized mineral. The brucite samples were irradiated with monochromatic X-rays. These were produced by accelerated electrons, generated in a cathode ray tube by a heated filament, with 30 kV onto a Copper (Cu) single-crystal. These X-rays have a characteristic $CuK\alpha_1$ radiation of 1.54056Å, which are then filtered by a nickel (Ni) foil to produce monochromatic X-rays. These X-rays are then bundled onto the sample. Both the sample and detector are rotated so that the measurements covers a 2θ diffraction angle ranging from 2 - 80°. According to Bragg's law, the interaction of the X-rays with the sample generates a material specific constructive interference and a diffracted ray pattern. As the samples have a random position in the diffractometer, all diffraction directions of the lattice are detected. These diffraction peaks can be converted into mineral specific lattice spacings (d-spacings), which allows mineral identification by their comparison with standard reference patterns (see representative brucite pattern in Annex I).

2.4.2. Characterization of aqueous solutions

2.4.2.1. pH measurements

Solution pH was measured with a Metrohm® 913 pH Meter connected to a glass microelectrode (pH= 0-14 / T= 0-80°C) containing a 3M KCl electrolyte solution. Electrode calibration was performed using Orion Thermo Scientific® buffers with certified values of 4.01, 7.00, and 10.01 at 25°C. The pH 4.01 buffer was repeatedly measured (n=39) over 5 months to assure measurement quality. The average deviation between the value indicated

by the pH meter, and that calculated from the electrode voltage was 0.006. This lies within the error of the measurement, therefore it is considered as negligible.

Experimental solutions from the T ≈ 75°C experiments cooled during sampling and thus had to be measured at lower temperatures. The sample temperature was thus determined simultaneously with the pH. Values of pH were automatically corrected for the measured temperature by the pH meter. These pH values could later be recalculated with PHREEQC (see Chapter 2.4) for T=75°C.

2.4.2.2. Atomic absorption spectroscopy (AAS)

Aqueous magnesium concentrations were measured by Flame Atomic Absorption Spectroscopy (*F*-AAS). The principle of these analyses were first described by Walsh (1955) and further developed by Russell et al. (1957) and Box and Walsh (1960). The solution sample is introduced as an aerosol into an air-acetylene-flame. The radiation from a hollow-cathode lamp, which emits the specific wavelength of Mg (285.21 nm) crosses through the flame. Some of the photons crossing the aerosol are absorbed by the Mg atoms of the sample present in the flame. The absorption is detected, measured and directly relates to the concentration. An intensity to concentration calibration curve is established by measuring standards solutions prepared in the same matrix as the samples.

Aqueous Mg concentration measurements in this study were carried out for concentrations from 0.1 and 0.6 ppm using a Perkin Elemer AAnalyst 400. Calibration solutions were prepared using the sample matrix (2% HNO_3, 0.05 M HCl, EDTA, sulphate, citrate) and to avoid interference was used a 1000 ppm $Mg(NO_3)_2$ Merck-Certipur® standard solution diluted into aqueous 0.05mol/kg HNO_3. Prior to measurements all samples were diluted. Therefore concentrations were close to the middle of the measurement concentration range (± 0.3 ppm). To minimize the effect of possible interference, a small quantity lanthanum oxide (30µL in 10 ml sample) was added to each sample and the standards prior to analysis. The limit of detection (LOD) and the limit of quantification (LOQ) were determined for each matrix to be 5 ppb and 1 ppb respectively. Measurements had an uncertainty of ±1%.

2.4.2.3. Atomic emission spectroscopy (AES)

The sodium content of samples containing Na were determined by flame atomic emission spectrophotometry (F-AES). The aqueous sample is introduced as a solution into a flame. The electrons of the outer valence layer are excited towards a higher electronic state. When

the electrons fall back to their fundamental state, photons are emitted at a characteristic wavelength (e.g. Na= 589.00 nm). The emission spectrum was measured by the atomic absorption spectrometer (Perkin Elemer AAnalyst 400) in the flame emission mode. As previously described (see AAS Chapter 2.4.2.2) a calibration curve is established allowing the determination of the Na concentration.

Sodium measurements were carried out at concentrations ranging from 0.5 to 6 ppm. Sodium concentrations in purified samples were expected to be below the limit of quantification. Due to a high sample consumption (4 mL), samples needed to be diluted by a factor of 2.7 prior to analysis. The LOQ and LOD were determined at 0.06 ppm and 0.02 ppm respectively.

2.4.2.4. Colorimetry

Aqueous silicon concentrations in this thesis were determined by the application of the molybdate blue method (Strickland, 1952) following the procedure of Tréguer and Le Corre (1975). The principle of this method is the formation of a yellow β-molybdosilic acid (silicomolybdate), when ammonium molybdate is added to an acidic Si-rich solution. This reaction can be written as:

$$7\,Si(OH)_4 + 12\,H_6Mo_7O_{24}\cdot 4\,H_2O + 126\,H_2O \leftrightarrow 7\,H_8Si(Mo_8O_7)_6\cdot 28\,H_2O \qquad (2.7)$$

Sulfuric acid is added to the molybdate solution as an acidifying agent, and oxalic acid is added to the sample solution to reduce possible phosphate interferences. Finally ascorbic acid is added to the sample solution to reduce the ammonium molybdate complex. This leads to a blue coloration of the solution. The absorbance of this color relative to a blank solution can be measured at 660 nm and is proportional to the dissolved Si concentration. Standards of known concentrations were measured to establish a calibration curve.

Aqueous Si concentrations measurements were carried out at concentrations of 0.05 to 1 ppm, and from 0.1 to 10 ppm using a Bran & Luebbe technicon analyser III coupled to a Seal XY-2 autosampler and an auto analyser II mixing unit. The solution samples were introduced into the mixing unit at a flow rate of 0.32 ml/min.. The ammonium molybdate solution is mixed with this sample solution at a flow rate of ~0.8 ml/min. Subsequently oxalic acid and finally ascorbic acid are added at a flow rate of ~0.23 ml/min to the measuring solution. Calibration solutions were prepared by diluting a 1000 ppm Merck-Certipur® Si standard solution with deionized MQ® water. The sample solutions were likewise diluted with deionized MQ® water so that their concentrations fell in the middle of

the measurement range. At the beginning and end of each set of measurements a standard, was measured to monitor for potential instrument drift. For measurements of Si concentrations between 0.05 and 1 ppm, a Mississippi 03 standard was used; for measurements of Si concentrations between 0.1 and 10 ppm a Miramichi 02 and later a Sangamon 03 standard were used. For the range of 0.05 to 1 ppm LOD was determined to be 0.004 ppm and the LOQ to be 0.013 ppm. The LOD and LOQ for measurements between 0.1 and 10 ppm were determined to be 0.01 ppm, and 0.04 ppm respectively. The long-term reproducibility of these measurements was within 3%.

2.4.2.5. Organic carbon measurements

Organic carbon was determined in aqueous solution samples containing organic ligands. The measurements were performed using a Shimadzu® TOC-VCSN analyser, equipped with an ASI-V auto sampler and TOC-Control V software. The principle is based on a combustion catalytic oxidation method developed by Shimadzu®. The sample is acidified to convert the carbonate and bicarbonate ions into dissolved carbon dioxide. The sample is then automatically injected with a syringe into a quartz tube filled with air and a platinum catalyst, which is then heated to 680°C. This transforms the dissolved organic carbon into CO_2, which is transported to the infrared detector. The total organic carbon concentration (TOC) is obtained by comparison of infrared measurements to a calibration curve, which is established from a set of reference solutions under the same conditions as the sample measurements.

TOC measurements were carried out at carbon concentrations ranging from 2 to 30 ppm. The aqueous samples were to concentrated, they were diluted with MQ® water in glass tubes prior to their analysis. Subsequently they were slightly acidified with bi-distilled HCl.

2.4.2.6. Quadrupole - ICP-MS

The element concentrations of the IAPSO and JDol-1 standard solutions after their cleaning by ion exchange chromatography (see Chapter 2.4.3.2) were measured on the Agilent® 7500 quadrupole ICP-MS. The solution to be analysed is converted into a fine aerosol by a micro nebuliser and introduced under a constant argon gas flow into an argon plasma torch at temperatures between 5000 and 10000°K. The sample is then ionized. The ions are extracted via a high voltage anode through a set of two cones, which filter all the contaminants and create an ion beam. On their way to the detector, the ions and molecular species go through two filtering systems:

1) The collision/reaction cell: a closed space where ions of low kinetic energy and large molecules are stopped, deviated or broken by large ions (e.g. O, H or He) or react with these to form other species of higher mass, to be further measured. The latter function was not used during this thesis.
2) The quadrupole: this consists of four parallel rods (Fig 2.8). Opposite rods are charged with an adjustable high voltage, which is inverted for the normal pair of rods. The charged ions entering the system follow a spiral pathway, which depends on their mass to charge ratio and on the applied voltage. Hence, only the chosen mass/charge ratios are not deviated and can be measured afterwards.

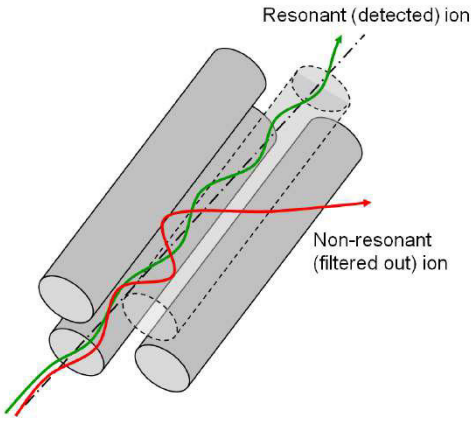

Figure 2.8 - The four parallel rods of the quadrupole

The signal of the ions is measured by an electron multiplier detector, which enables quantification of the abundances of the different ionic species, in counts per second. These abundances are directly proportional to the concentration of this species in the injected sample. Abundance to concentration calibration curves are established by measuring the abundances of known standards.

Prior to the measurements, the samples were diluted in 2% bi-distilled HNO_3 to obtain a concentration <500 ppm in the target element. A known volume of an indium and rhenium enriched solution of known concentration was added as an internal standard. The measured uncertainties of measured concentrations vary between 2 and 15%, depending of the concentration of the sample solution. If the uncertainty of the measurements exceeded 15%, the concentrations determined for this element was discarded. The detection limit of the measurements was found to vary from 0.1 to 10 ppt, depending on the element analysed.

2.3.2.7. High Resolution - ICP-MS (HR-ICP-MS)

The isotope abundance in the spike solutions were determined by high resolution inductively coupled plasma mass spectrometry (HR-ICP-MS). The measurements were performed on a Thermo Sicentific ELEMENT-XR® with a reversed Nier-Johnson geometry. The detailed functioning of an ICP-MS is described in detail in section 2.4.3.3.

The ^{29}Si and ^{25}Mg-spike solutions were diluted to concentrations between 0.05 and 2 ppm in 2% HNO_3 prior to the measurements. The magnesium and silicon samples were introduced with a free aspirating stable introduction system (SIS) and measured in medium resolution mode, with a mass resolution of ~4300. Silicon was additionally measured in high mass resolution mode (R ~9300). A 1 ppb Li tuning solution was used. The diluted spike solutions were introduced with Ar gas into the plasma. Blanks of 2% HNO_3 were measured for each measurement sequence. The intensities of the 3 stable isotopes with the masses 27.9764, 28.9760, 29.9732, and 23.9845, 24.9853, 25.9821 for silicon and magnesium. respectively, were measured. These were detected in either triple mode (Faraday and electron multiplier in analogue and pulse modes) for the magnesium spike solutions, or in analogue mode for the silicon spike solutions, with a secondary electron multiplier. The samples signals were corrected for a blank using the blank signals. The signal detected for the different isotopes directly depends on the concentration of the Si and Mg isotopes in the solution. The isotopic ratios could therefore be determined from the ratio of the blank corrected signal of the individual isotopes.

2.4.3. Isotopic Analysis

All samples for isotopic ratio determination needed to be purified to remove any potentially interfering elements prior to their analysis. These purification procedures are described in this section, along with the principles of the Multi Collector ICP-MS (MC-ICP-MS).

2.4.3.1. Silicon sample preparation and ion-exchange chromatography

Silicon bearing powders and aqueous solutions had to be purified prior to their analysis by MC-ICP-MS (see Chapter 2.4.3.3). For the amorphous SiO_2 powders, the sample purification is based on the alkaline fusion preparation protocol described in Zambardi & Poitrasson (2011). This protocol calls for:

1) 1 to 5 mg of the powders were weighted into silver crucibles (XRF scientific, Montreal, Canada), together with ~200 mg Merck® suprapure NaOH pellets. If the

powders were in contact with organic solutions, a calcination was performed prior to the addition of the NaOH pellets. Therefore SiO_2 sample powder in the crucibles in a furnace at 500°C for 4h, similar to the approach for soils of Cornu et al. (1999).

2) The crucibles were placed into a 720°C pre-heated furnace for 10 min.
3) After cooling to room temperature, the crucibles were placed into 30 cc Savillex® Teflon beakers filled with 20 ml Milli-Q® water to dissolve the fusion cake..
4) After 24 hours, the resulting solutions were transferred to 60 cc polypropylene bottles and diluted with 20 ml Milli-Q® water to obtain a 40 ml solution.
5) These solutions were then acidified to a pH of 1.5 using ~10 N HCl and placed on a heating plate at 50°C for 24 to 48 h to ensure that possible suspended material is completely and efficiently dissolved.

Aqueous samples of experiments run without the presence of organic ligands were prepared for Si isotope analysis by diluting the solutions - if needed - and subsequently acidifying them to pH ~2 using bi-distilled 3N HCl. Organic bearing fluid samples had to be carefully treated, as the presence of organic matter likely causes interferences during Si isotope measurements using the MC-ICP-MS. Therefore solutions containing organic ligands had to be processed to ensure complete removal of these organic compounds. For this standard methods such as the use of H_2O_2 and UV-light were tested in a first attempt. These methods proved to be ineffective as confirmed by the organic carbon measurements. The following sample preparation protocol was therefore adopted to purify aqueous solutions containing organic ligands:

1) 5 ml of the organic bearing aqueous sample was evaporated to dryness in silver crucibles in a laminar flow box.
2) Calcination was performed by heating the SiO_2 and organic residue in the crucibles in a furnace at 500°C for 4h, similar to the approach of Cornu et al. (1999) for soils.
3) Approximately ~200 mg of Merck® NaOH pellets were added into the silver crucibles.
4) The fusion of the remaining SiO_2 powder was performed by placing the crucibles into a furnace at 720°C for 10 min.
5) The crucibles were cooled to room temperature, and subsequently placed in 30 cc Savillex® Teflon beakers filled with 15 ml Milli-Q® water to dissolve the amorphous SiO_2 powder.
6) The resulting solutions were transferred after 24 hours into 30 cc polypropylene bottles and diluted with Milli-Q® water to 20 ml.

7) Samples were acidified to a pH of 1.5 using ~10 N aqueous HCl.

After sample preparation, the resulting solutions were purified by the cation-exchange chromatography protocol described by Zambardi and Poitrasson (2011). In this method, 10 ml BioRad® polypropylene columns were filled with 2 ml BioRad® AG50W-12X (200–400 mesh) cationic resin. Before the samples were treated, the resin was cleaned and conditioned with 3 ml HCl and HNO_3 in following order: 3 N HCl, 6 N HCl, 7 N HNO_3, 10 N HCl, 6 N HCl, and 3 N HCl (Georg et al., 2006). The resin was then flushed with Milli-Q®, so that the pH before the sample was loaded was close to neutral. The sample solutions were loaded (0.5-2 ml, depending on the Si concentration). Si is not retained by the resin, as non ionic $H_4SiO_4^o$ largely dominates Si species in solution below pH 9, and was therefore directly collected. The columns were subsequently eluted twice with Milli-Q® water to obtain a 6 ml sample solution. These sample solutions were then diluted to obtain 3 ppm of Si and acidified with 10 N bi-distilled HCl to obtain a 0.05 M HCl matrix. Silicon recovery after processing was determined by colorimetry to be between 90 to 100 %.

2.4.3.2. Magnesium sample preparation and ion chromatography

The magnesium bearing powders and aqueous solutions collected from the isotopic exchange experiments had also to be prepared and subsequently purified by ion exchange chromatography prior to their isotopic measurement with the Neptune® MC-ICP-MS. The processing of the brucite powder consisted of:

1) ~1 mg of brucite powder and the JDo-1 standard were weighted and placed in Savillex® beakers.
2) These powders were dissolved overnight in 2 ml of 15 N bi-distilled HNO_3.
3) The resulting solutions were evaporated to dryness at 120°C, and the residues were re-dissolved in 5 ml 1N HNO_3.
4) Mg concentrations of these latter solutions were determined using AAS.
5) Aliquots of the solutions containing 15 µg Mg were evaporated and re-dissolved in 2 ml 1M HNO_3 to be ready for column chemistry.

The Mg bearing aqueous solutions were prepared as follows:

1) Aliquots of the fluid samples (10-500 µl) and the IAPSO seawater standard containing 15 µg Mg were placed into Savillex® beakers. In case of the presence of organic ligands ~0.5 ml H_2O_2 was added and left to react for 3-6 hours.

2) Sample solutions were evaporated to dryness at 120°C.
3) The solid residues were re-dissolved in 2 ml of 1M HNO_3 to be ready for column chemistry.

The sample preparation follows the Teng et al. (2007) method. All the samples were processed in 10 ml Bio-Rad® polypropylene (PP) columns filled with 1 ml Bio-Rad® AG50W-X8 200–400 mesh cationic exchange resin. The resin was pre-cleaned with 1 N HCl before filled into the columns. Once in the column, the resin was further cleaned with 10 ml of Milli-Q® water, 20 ml of 4M HCl and finally once more with 10 ml of Milli-Q® water. The resin was then conditioned with 10 times the resin volume of aqueous 1N HNO_3. 2 ml of the prepared sample solutions were loaded onto the resin and the elements of interest (in this case only Mg) were eluted by the subsequent washing of the resin with 1 M HNO_3. Sodium is removed, and eluted within the first 10 ml after loading the sample. The Mg fraction was then collected in the following 20 ml of elution, and Ca was removed lastly from the resin, and then eluted within the next 30 ml (Teng et al., 2007).

As ion exchange chromatography can significantly fractionate Mg isotopes (Chang et al., 2003; Teng et al., 2007), it is essential to obtain a Mg yield close to 100 %. A resin calibration was performed to ensure all the Mg was collected during column chromatography. Seven fractions of the two standards JDol-1 and IAPSO were collected starting from the last 2 ml of the sodium elution until the first 2 ml of the calcium elution. These were subsequently analysed with the Agilent 7500 quadrupole ICP-MS (see Chapter 2.4.2.6) to determine the concentrations of all elements in solution. The elution curve for Mg in Fig. 2.9 shows no shift compared to the protocol of Teng et al. (2007), which indicates that Mg was eluted completely through the columns, validating the method used in this thesis.

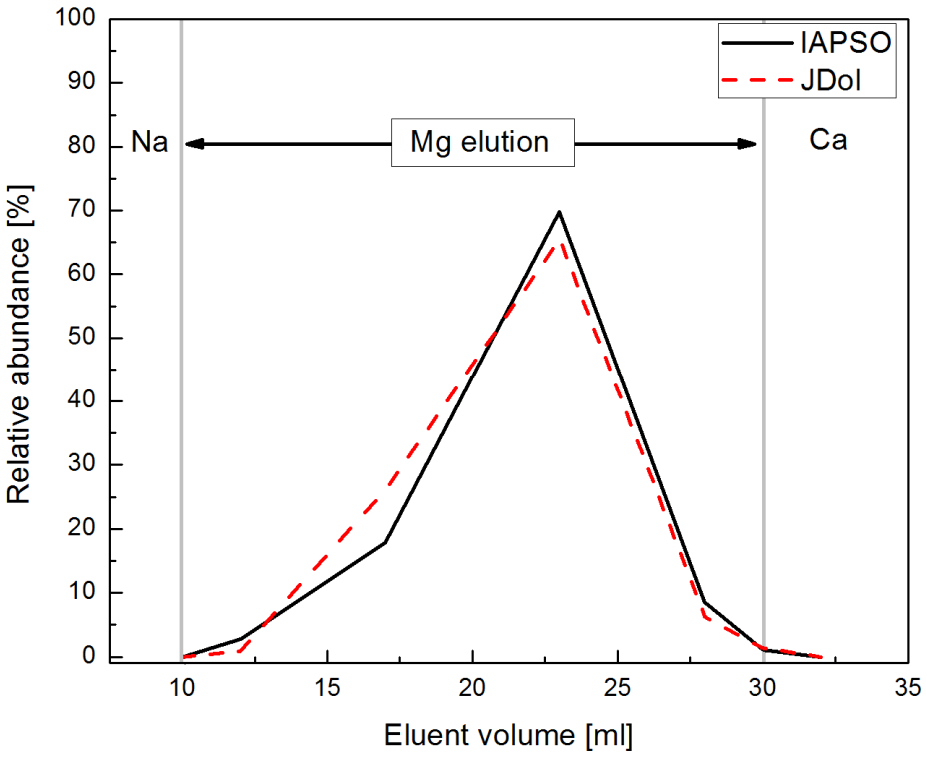

Figure 2.9 - Elution profile of the Mg, demonstrating that all Mg is collected during column chromatography.

For samples collected from the sulphate bearing experiments was additionally recovered fluid analyses were made using AES measurements (see Chapter 2.4.2.3) to assure that the recovered solutions were free of sodium, as element this could affect the Mg isotopic measurements.

2.4.3.3. Principles of the Neptune® Multi Collector ICP-MS (MC-ICP-MS)

The isotopic compositions of the aqueous solutions and solid powders recovered from the isotopic exchange experiments were obtained using a Thermo Fisher Scientific Neptune® **M**ulti-**C**ollector **I**nductively **C**oupled **P**lasma **M**ass **S**pectrometer (MC-ICP-MS). The Neptune® MC-ICP-MS is a double focussing mass spectrometer, which is capable of preforming measurements with a highly accurate mass resolution using its multi collector mode (Weyer and Schwieters, 2003). Its principle is based on the physical separation of isotopes in an ion beam by both an electrostatic analyser (ESA), which correspond to an energy filter, and a magnet that works as a mass filter. The ESA is placed before the magnet, as shown in Fig. 2.10 based on the Nier and Johnson geometry.

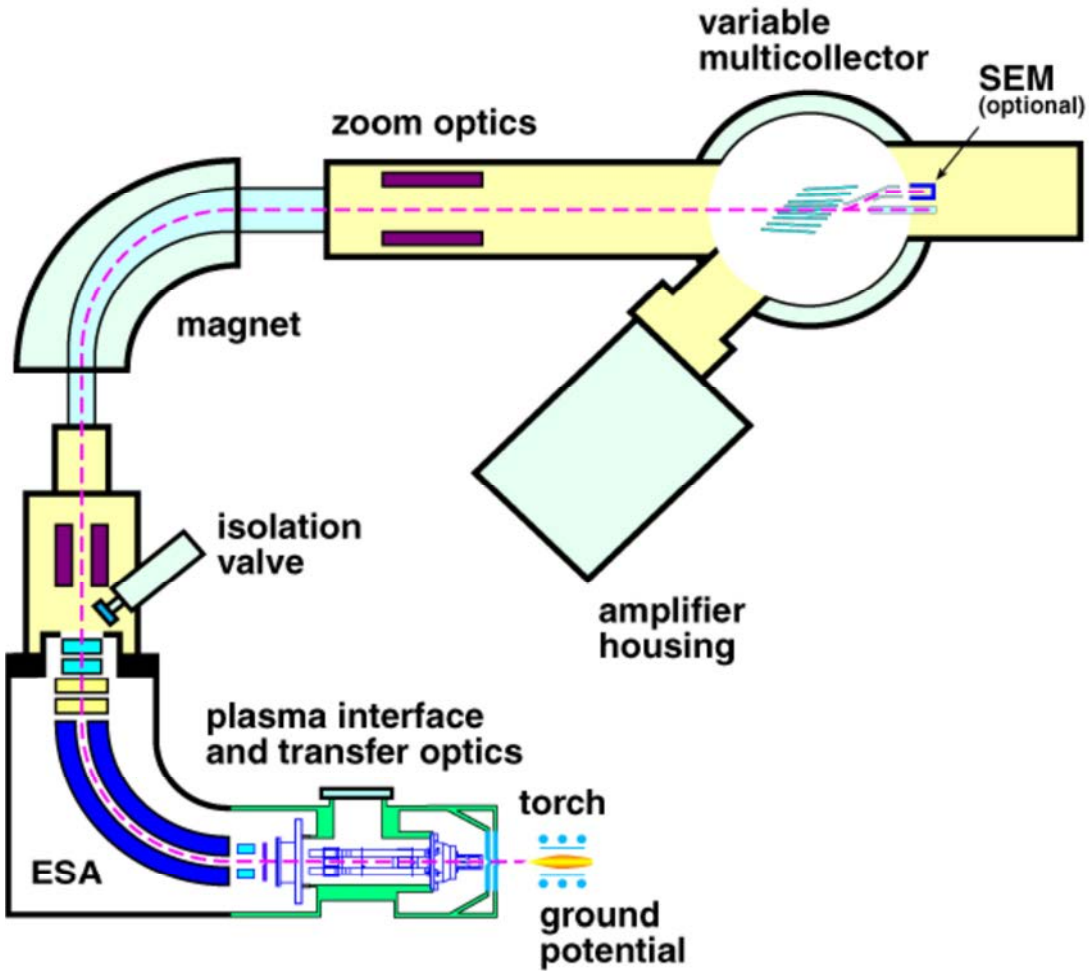

Figure 2.10 - Schematic design of the Neptune MC-ICP-MS (after ThermoScientific and Weyer and Schwieters, 2003)

All samples were prepared for analysis in weakly acidic aqueous solutions and converted into a fine aerosol in the nebulizer. The sample is subsequently introduced under a constant argon gas flow through the spray chamber into the torch. In the torch, an inductively coupled Argon plasma is generated at high temperatures (> 8000 K; Georg et al., 2006) in which the mixture of sample and gas is ionized. When the ions leave the torch, their energy will vary between 0.5 and 5 eV (Georg et al., 2006). The magnet alone could not be able to achieve a good isotope separation due to this energy variation. Therefore the ESA is placed before the magnet to deflect the ions as a function of their kinetic energy. This means that if the ion beam containing ions with different velocities reaches the ESA entrance only ions with the same kinetic energy will pass. Three entrance slits are located in front of the ESA enabling measurements in low, medium and high mass resolution. The ions leaving the ESA unit will be deflected by the magnet according to their mass to charge ratio. The isotopes thus will have an individual path according to their mass. The beam leaving the magnet, therefore contains various sub-beams, where each beam can be associated with a given isotope. The

sub-beams are collected in 9 available Faraday cups. These generate an electrical signal, which can be detected by either a Faraday or SEM detector, allowing the determination of the relative isotopic abundances.

2.4.3.4. Silicon isotope measurements

Silicon isotope measurements were performed using the Thermo Scientific Neptune® MC-ICP-MS located at the Observatoire Midi-Pyrénées / Laboratoire Géosciences Environnement Toulouse (GET), France, or that located at the GeoForschungsZentrum (GFZ) in Potsdam, Germany. Measurements were preformed in medium mass resolution mode with a total of 1.5 to 2 ppm Si in solution, under wet plasma (GET) and dry plasma (GFZ) conditions. For the wet plasma, the samples were introduced into the spectrometer via a ThermoFinnigan stable introduction system (SIS) with a double-pass cyclonic spray chamber. For dry plasma conditions at the GFZ, an Aridus desolvating unit was used.

Prior to any analysis, the signal sensitivity and intensity had to be verified and adjusted. Silicon isotope measurements can be influenced by polyatomic interferences from combinations of elements such as $^{12}C^{16}O^{+}$, $^{14}N_2$, $^{14}N^{15}N^{+}$, $14N_2{}^{1}H^{+}$ and $^{14}N^{16}O^{+}$, as shown in Fig 2.11. It is crucial, therefore, to tune the spectrometer so that that it samples the plateau where only the three Si isotopes are present (Fig 2.10).

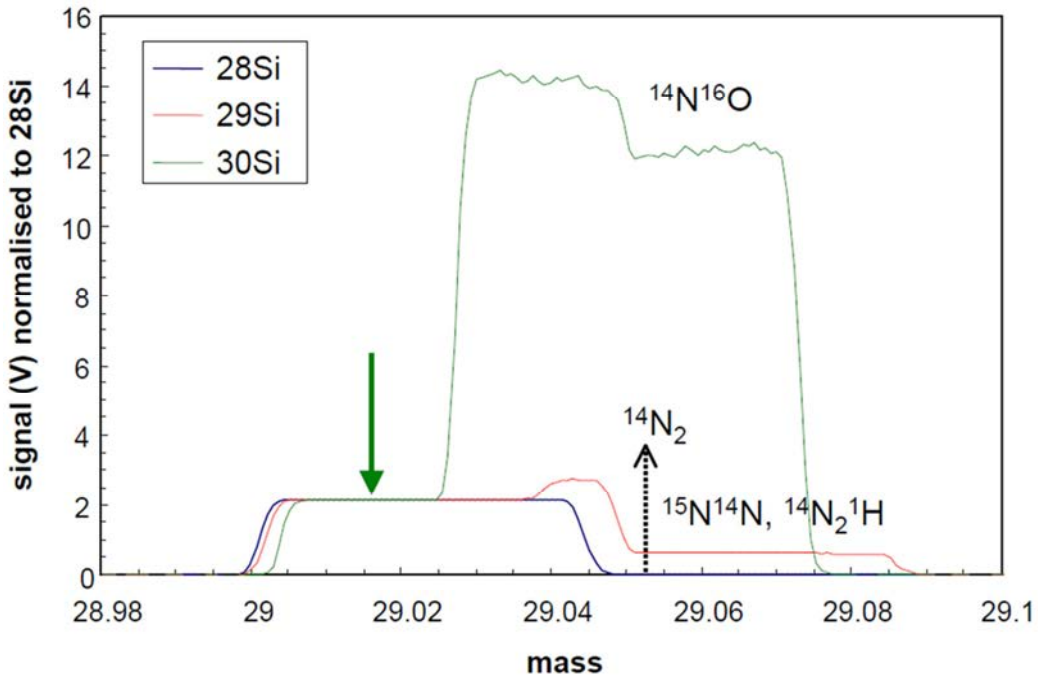

Figure 2.11 - Peak scan for Si isotopes in medium mass resolution with representative interferences. The green arrow indicates the Si plateau, where Si isotopes can be measured without interferences (modified after Bouman, 2005)

The 'mass resolution' corresponds to the resolving power of the mass spectrometer. The mass resolution ($R_{resolution}$) is expressed by:

$$R_{resolution} = \frac{m}{\Delta m} \tag{2.8}$$

where m is the mass of the isotope considered, measured in the middle of the plateau where no interferences occur, Δm denotes the difference between the mass at 5% and 95% of the height of the peak. The mass resolution has to be at least 2000 to separate all three Si^+ ion beams from its interfering beams.

During measurements, an instrumental mass bias drift occurs, which can be attributed to isotopic fractionation generated by the instrument. It is generated by the vibrational excitation of the ions in the plasma and the ion beam due to interatomic collisions. This generally leads to a preferential expulsion of light isotopes, which results in an overestimation of the concentration of heavy isotopes during measurements (e.g., Zambardi, 2011). Most of the time, the instrumental mass bias is not constant, and its variations may depend on various parameters, such as matrix effects or the stability of the gas and sample flow. This can cause a mass bias drift. A first and effective approach to correct for the instrumental mass bias drift is the standard bracketing. This is based on the measurement of an isotopic standard solution, in the case of silicon, NBS-28, before and after each sample or a triple-sample set. This enables quantification of the isotopic fractionation of the sample from the average isotopic ratios of the standard over a period of time. The sample standard bracketing is, however, ineffective if the mass bias drift changes too fast and/or is non-linear. Such situations can occur, especially during the first 24h of a measurement session, a solution consists of combining sample standard bracketing with the addition of an internal standard. Therefore the samples and the external NBS-28 standard were doped with a multi-isotopic element with a mass close to that of the element of interest. In the present study, the samples and standards for Si isotope analysis were doped with Magnesium. The ^{25}Mg-^{24}Mg ratios of these doped solutions were measured in a dynamic measurement mode. It is assumed that the mass bias drift will be the same for both magnesium and silicon isotopes. The application of this correction is widely used for silicon isotopes (De La Rocha, 2002; Cardinal et al., 2003; Engström et al., 2006; Zambardi and Poitrasson, 2011; Zheng et al., 2016). Its principle is based on Russels's exponential law (Russell et al., 1978), which can be applied to correct the mass bias drift during one run, given by:

$$R_i = r_i \times \left(\frac{M_i}{M_k}\right)^{\beta} \tag{2.9}$$

where R_i denotes the corrected isotopic ratio, and r_i the measured isotopic ratio. M_i is the mass of the isotope of interest, thus ^{29}Si or ^{30}Si, and M_k is the mass of ^{28}Si . β indicates the fractionation coefficient calculated from the measurements fort magnesium, and considered to be identical to that of silicon (Zambardi, 2011). The fractionation coefficient β can be derived from Eqn. 2.9, and can be written as:

$$\beta = \frac{ln(R_i/r_i)}{ln(M_i/M_k)} \tag{2.10}$$

The fractionation coefficient for magnesium β^{Mg} can thus be calculated with:

$$\beta^{Mg} = \frac{ln(R_i^{Mg}/r_i^{Mg})}{ln(M_i^{Mg}/M_k^{Mg})} \tag{2.11}$$

Where R_i^{Mg} denotes the theoretical isotopic ratio of ^{25}Mg/^{24}Mg, which could be fixed at 0.126598 as the magnesium added to the samples and standards has a natural isotopic composition, and isotope distribution. r_i^{Mg}denotes the measured ^{25}Mg/^{24}Mg ratio $M_{\mathrm{i}}^{\mathrm{Mg}}$ in this case refers to the mass of ^{25}Mg, and $\mathrm{M_k^{Mg}}$ to the mass of ^{24}Mg. As the mass bias drift of Mg is assumed to be identical to that of Si, the fractionation coefficient of Mg can be applied to Eqn. 2.9 as mass bias correction for Si:

$$R_i^{Si} = r_i^{Si} \times \left(\frac{M_i^{Si}}{M_k^{Si}}\right)^{\beta^{Mg}} \tag{2.12}$$

To ensure the accuracy and precision of isotopic analyses, the Si isotopic composition of the BHVO-2 reference material was measured during each measurement session. For the wet plasma conditions, this resulted in a long-term reproducibility of δ^{30}Si= -0.26 ± 0.14 ‰, and δ^{29}Si= -0.13 ± 0.09 ‰ (2 S.D, n=105). Dry plasma conditions at GFZ led to a long-term reproducibility δ^{30}Si= -0.28 ± 0.09 ‰, and δ^{30}Si= -0.14 ± 0.06 ‰ (n=18). The measured values of the Si isotope compositions of this standard obtained from both wet and dry plasma analysing conditions are plotted in Fig. 2.12. This figure also shows showing that the measured results obey the mass-dependent fractionation law within the average error. The measured BHVO-2 values in this study are in close agreement with values reported in previous studies (e.g. Abraham et al., 2008; Zambardi and Poitrasson, 2011; Savage et al., 2013, 2014).

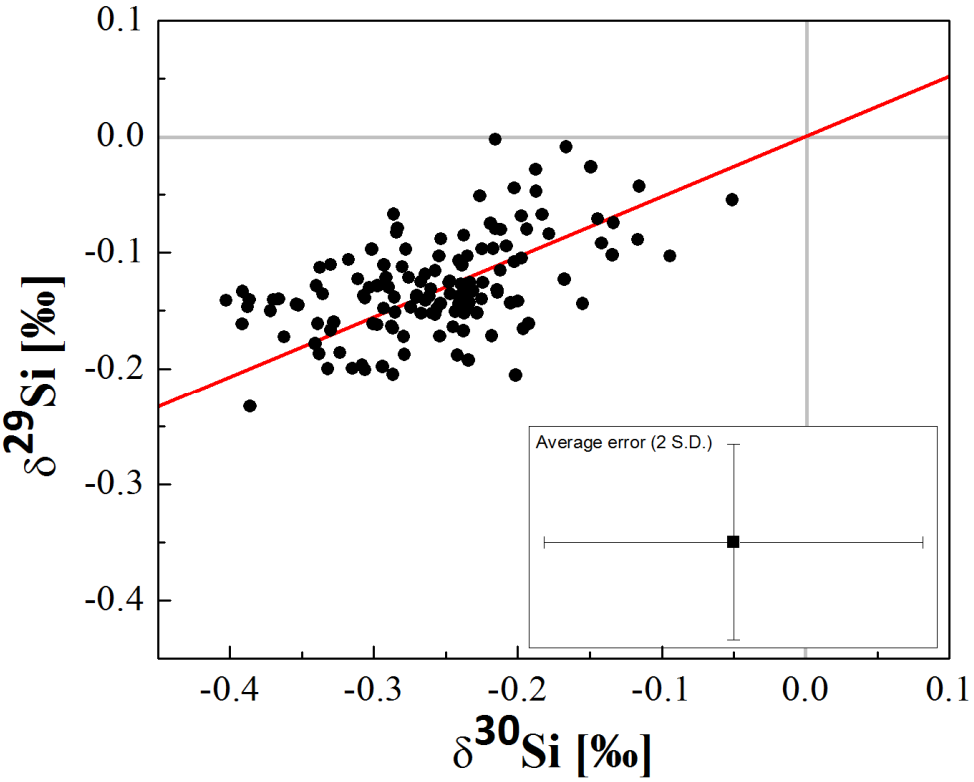

Figure 2.12 - All BHVO-2 Si isotope compositions measured in this study, values are related to the mass-dependent fractionation law within uncertainty. The red line marks the Si mass-dependent isotopic fractionation line. Average uncertainty on the measurements is shown in bottom right corner.

The quality and purity of the sample preparation, and ion chromatography was verified by measuring the ^{28}Si signal of the procedural blank. This was found to be on average < 2% of the total signal and therefore considered negligible.

2.4.3.5. Magnesium isotope measurements

Magnesium isotope measurements were performed using the Thermo Scientific Neptune® MC-ICP-MS located at the Observatoire Midi-Pyrénées / Laboratoire Géosciences Environnement Toulouse (GET), France. The samples were introduced into the plasma dissolved in 0.37N aqueous HNO_3 with the SIS coupled to a double-pass cyclonic spray chamber. The measurements were performed in low mass resolution mode at aqueous Mg concentrations of 600 ppb. Before starting the measurements, the signal sensitivity and intensity was verified and adjusted. As the Mg isotopic measurements are not affected by major interferences, the measurement position is chosen at the peak centre, as shown in Fig. 2.13.

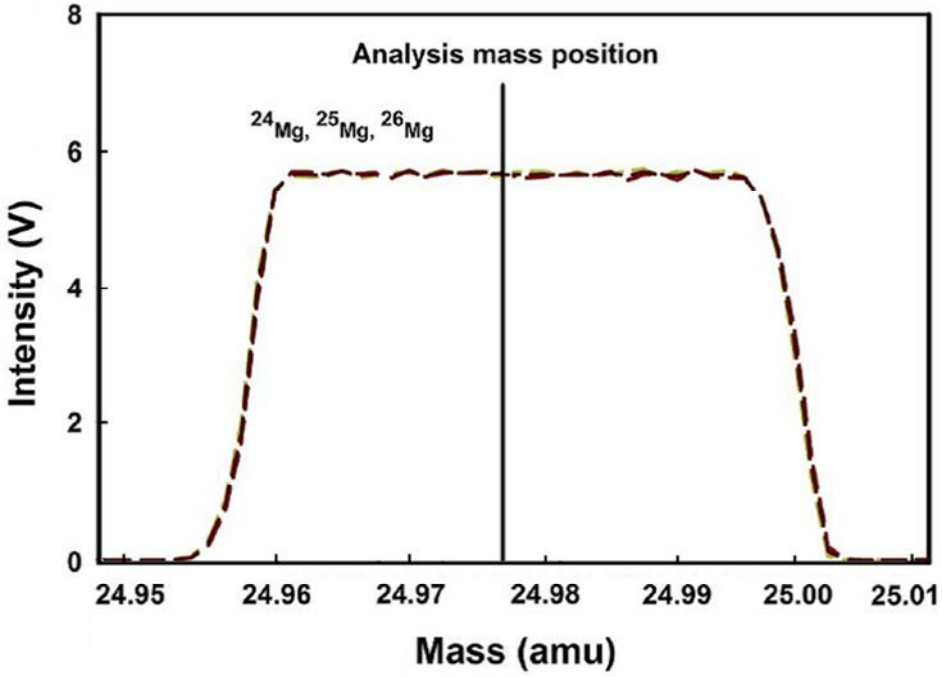

Figure 2.13 - Mass scan for Mg isotopes in medium mass resolution. The vertical line represents the peak centre and thus the mass position where measurements were carried out (modified after Sikdar and Rai, 2017).

Magnesium isotopic compositions in this study are given with respect to the DSM-3 standard (Galy et al., 2003). Due to the limited access of the DSM-3 standard, the measurements were performed using the sample standard bracketing method described above, with respect to an in house $MgNO_3$ standard. The composition of the in house $MgNO_3$ standard was determined by repeated measurements (n=61) relative to DSM-3, with an isotopic composition of $\delta^{25}Mg = 0.16 \pm 0.08$ ‰ and $\delta^{26}Mg = 0.32 \pm 0.14$ ‰. The measured Mg samples were then corrected with these values to generate isotopic compositions of sampled fluids relative to the DSM-3 standard established by Galy et al. (2003).

The long-term reproducibility of the isotopic analyses was assessed by repeated analysis of the JDol-1 dolomitic carbonate standard, and the IAPSO seawater standard during each analytical session. The values obtained (Fig. 2.14) were $\delta^{25}Mg$ of -1.21 ± 0.08 ‰, and $\delta^{26}Mg$ of -2.32 ± 0.15 ‰, and $\delta^{25}Mg$ -0.45 ± 0.11 ‰, and $\delta^{26}Mg$ -0.86 ± 0.20 ‰, respectively. These are in close agreement with corresponding measurements reported by previous studies (e.g. Pogge von Strandmann et al., 2008; Wombacher et al., 2009; Immenhauser et al., 2010; Wimpenny et al., 2011; Mavromatis et al., 2013, 2014a, 2014b, 2016). Repeated measurements of the $MgNO_3$ in house standard, gave a 2 S.D. of 0.07 ‰, and 0.12 ‰ for $\delta^{25}Mg$, and $\delta^{26}Mg$ respectively.

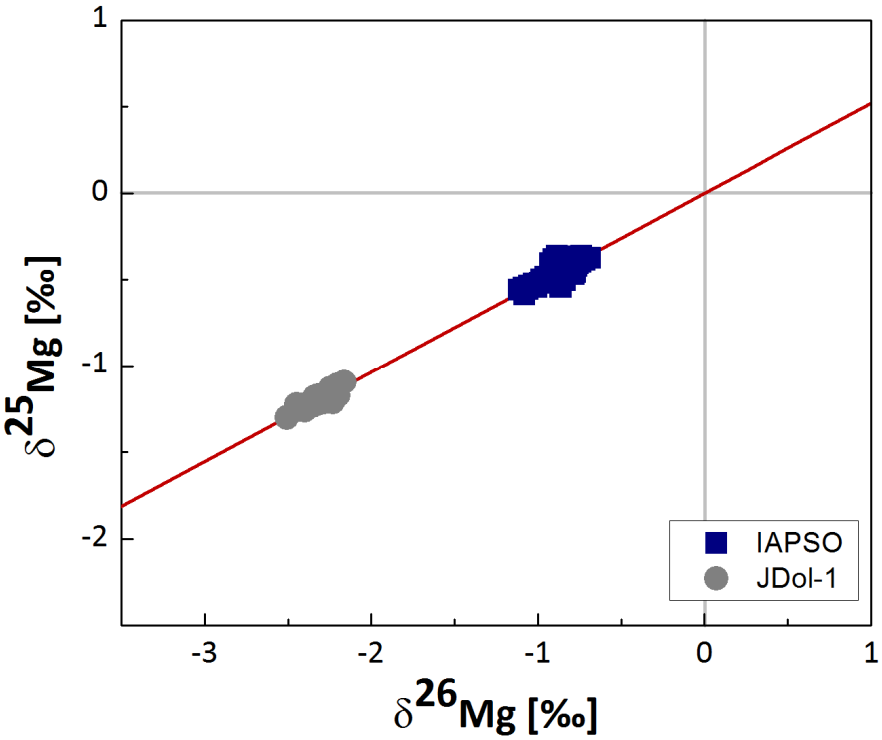

Figure 2.14 - All Mg isotope standard measurements of IAPSO (blue) and JDol (grey) performed in this thesis. Values obey the mass-dependent fractionation law within uncertainties (shown within the symbols). Red line marks the Mg mass-dependent isotopic fractionation line.

In contrast to the studies of Li et al. (2011, 2014) the Mg bearing aqueous solutions containing EDTA and sulphate were only treated with H_2O_2. As a result the sample matrices of the measured solutions contained some remaining EDTA and sulphate. To assess the impact of these different sample matrices on the measurements, the bracketing standard was doped with Citrate, EDTA and sulphate in the concentrations used in the experiments. This led to a maximum deviation of 0.02 ‰, and 0.03 ‰ for δ^{25}Mg, and δ^{26}Mg, respectively, for the in-house standard compared to the corresponding isotope compositions of ligand-free solutions. Therefore the impact of the presence of dissolved citrate, EDTA, and sulphate on the measured Mg isotope compositions are considered to be negligible.

The ^{24}Mg signal of the procedural blank was measured to verify the quality and purity of the sample preparations, and ion chromatography methods. The blanks showed an average ^{24}Mg signal < 0.5% of the total signal and are therefore negligible.

2.4.3.6. Analytical reproducibility

The accuracy of the isotopic measurement is not only validated by the measurement of blanks and standards, but also by the repeated measurements of the sampled aqueous

solutions and solids. During the analysis, the Si samples were measured in blocks of 25 single measurements and the Mg samples in blocks of 30 single measurements. The average of these 25 or 30 measurements is then taken to be sample composition. Each sample was measured from 2 an 6 times to estimate the reproducibility of the measured isotopic ratio. Starting materials were measured up to 9 times to further assess the uncertainties, as these starting materials need to be accurate to generate accurate extrapolations using the three-isotope method. In this thesis the standard error (*SE*) is used as the uncertainties of the isotopic measurements. The *SE* is given by:

$$SE = \frac{t \times SD}{\sqrt{n-1}} \tag{2.13}$$

where *SD* is the standard deviation of the *n* measurements, and *t* is the student t-correcting factor (Platzner et al., 1997), which is an essential correction for measurements with less than 15 replicates.

2.5. Geochemical calculations with PHREEQC

2.5.1. Thermodynamic modelling

All geochemical calculations in this study were performed using the PHREEQC code (Parkhurst and Appelo, 2013). The standard state adopted is that of unit activity for pure minerals, solids and H_2O. For aqueous species the standard state is unit activity of a hypothetical one molal solution extrapolated to infinite dilution at any given temperature and pressure. The activity coefficients of charged aqueous species were calculated using the Davies equation, whereas the activity coefficients of neutral species were assumed to be equal to one. In situ aqueous solution speciation and pH for experiments performed at 75°C were computed from the measured Si and Mg concentration, the pH measured at room temperature, and the organic ligand concentration. Equilibrium constants for the dissolution reactions of amorphous SiO_2 and brucite were determined from the dissolution experiments performed during the chemical equilibration of initial reactive fluids (see Chapter 2.3.1). This was done considering the following dissolution reactions:

For amorphous silica:

$$SiO_2 + 2\,H_2O \leftrightarrow H_4SiO_4^o \tag{2.14}$$

and for brucite:

$$Mg(OH)_2 + 2\,H^+ \leftrightarrow Mg^{2+} + 2\,H_2O \tag{2.15}$$

The law of mass action for the reactions (2.14) and (2.15) are given by:

$$K_{eq} = \frac{a_{H_4SiO_4^0}}{a_{SiO_{2,am}} a_{H2O}^2} \tag{2.16}$$

and:

$$K_{eq} = \frac{a_{Mg^{2+}} (a_{H_2O})^2}{a_{Mg(OH)_2} (a_{H^+})^2} \tag{2.17}$$

where K_{eq} stands for an equilibrium constant and a_i refers to the activity of the subscripted species or phase. Taking account of the standard state, in pure water Eqn. (2.16) reduces to:

$$K_{eq} = a_{H_4SiO_4^0} \tag{2.18}$$

and Eqn. (2.17) reduces to:

$$K_{eq} = \frac{a_{Mg^{2+}}}{(a_{H^+})^2} \tag{2.19}$$

The activities of the different species were first determined using by entering the results of the dissolution experiments at steady state into PHREEQC, and subsequently using these to calculate the equilibrium constants of theses reactions.

2.4.2. Si speciation calculations

Silicon speciation and pH at 75°C were calculated using the Livermore National Laboratory (llnl) database (Johnson et al., 2000). The equilibrium constant for the dissolution of the amorphous SiO_2 powder in pure water was determined to be -2.80 and -2.38 at 25°C and 75°C respectively. The equilibrium constants for the Si aqueous species $H_3SiO_4^-$ and $H_2SiO_4^{2-}$, and the polymeric species were used as included in the database, whereas the equilibrium constants of the catechol organic ligand complex were added, following Sillen and Martell (1971), Sverjensky et al. (1997), and Pokrovski and Schott (1998) as listed in Table 2.7. No thermodynamic data is available for the Si-glucamine complex.

Table 2.7 - Equilibrium constant added to the PHREEQC llnl database

Reaction	log K	Source
$SiO_2 + 2\ H_2O \leftrightarrow H_4SiO_4^o$	-2.80	this study
$SiO_2 + 2\ H_2O \leftrightarrow HSiO_3^-$	-9.95	Sverjensky (1997)
$SiO_2 + 2\ H_2O \leftrightarrow H_2SiO_4^{2-} + 2\ H^+$	-22.96	Sverjensky (1997)
$H_2Cat^o \leftrightarrow HCat^- + H^+$	-9.45	Sillen & Martell (1971)
$H_2Cat^o \leftrightarrow HCat^{2-} + 2\ H^+$	-22.45	Sillen & Martell (1971)
$SiO_2 + 3\ H_2Cat \leftrightarrow SiCat_3^{--} + 2\ H^+ + 2\ H_2O$	-12.00	Pokrovski & Schott (1998)

2.4.3. Mg speciation calculations

Speciation calculations for the fluids collected from all the brucite isotope exchange experiments were performed using the core10 database (Neveu et al., 2017). The equilibrium constant for the brucite dissolution reaction (2.15) was calculated from the measured fluid compositions of experiments run to pre-equilibrate the fluids used in the brucite isotope exchange experiment without organic ligands and then corrected in the database. Additionally, the equilibrium constants of aqueous citrate and EDTA complexes were added to the database to perform speciation calculations for solutions containing these organic ligands. The equilibrium constants added are listed in Table 2.8.

Table 2.8 - Equilibrium constants added for speciation calculation to the core10 database.

Reaction	log K	Source
$Mg(OH)_2 + 2H^+ = 2\ H_2O + Mg^{2+}$	17.209	this study
Sulphate		
$SO_4^{2-} + Mg^{2+} \leftrightarrow MgSO_4$	2.41	McCollom & Shock (1997)
Citrate		
$Citrate^{3-} + H^+ \leftrightarrow HCitrate^{2-}$	6.40	Bénézeth et al. (1997)
$HCitrate^{2-} + H^+ \leftrightarrow H_2Citrate^-$	4.76	Bénézeth et al. (1997)
$H_2Citrate^- + H^+ \leftrightarrow H_3Citrate^{2-}$	3.13	Bénézeth et al. (1997)
$Mg^{2+} + Citrate^{3-} \leftrightarrow Mg(Citrate)^-$	5.00	Covingron & Danish (2009)
$Mg^{2+} + HCitrate^{2-} \leftrightarrow MgHCitrate$	2.59	Covingron & Danish (2009)
$Mg^{2+} + H_2Citrate^- \leftrightarrow MgH_2Citrate^+$	1.00	Covingron & Danish (2009)
$Mg^{2+} + 2Citrate^{3-} \leftrightarrow Mg(Citrate)_2^{4-}$	5.49	Covingron & Danish (2009)
EDTA		
$EDTA^{4-} + H^+ \leftrightarrow HEDTA^{3-}$	10.95	Carini & Martell (1953)
$EDTA^{4-} + 2\ H^+ \leftrightarrow H_2EDTA^{2-}$	17.22	Carini & Martell (1953)
$EDTA^{4-} + 3\ H^+ \leftrightarrow H_3EDTA^-$	20.37	Hummel (2005)
$EDTA^{4-} + 4\ H^+ \leftrightarrow H_4EDTA$	22.60	Hummel (2005)
$EDTA^{4-} + 5\ H^+ \leftrightarrow H_5EDTA^+$	23.90	Hummel (2005)
$Mg^{2+}\ EDTA^{4-} \leftrightarrow MgEDTA^{2-}$	10.45	Gautier (2013)
$Mg^{2+}\ EDTA^{4-} + H^+ \leftrightarrow MgHEDTA^-$	20.87	Hummel (2005)
$Na^+ + EDTA^{4-} \leftrightarrow NaEDTA^{3-}$	2.70	Felmy & Mason (2003)

Chapter 3

The experimental determination of equilibrium Si isotope fractionation factors among $H_4SiO_4^o$, $H_3SiO_4^-$ and amorphous silica ($SiO_2 \cdot 0.32\ H_2O$) AT 25 and 75 °C using the three isotope method

A version of this chapter is published as: "Franziska M. Stamm, Thomas Zambardi, Jérôme Chmeleff, Jacques Schott, Friedhelm von Blanckenburg, Eric H. Oelkers: The experimental determination of equilibrium Si isotope fractionation factors among $H_4SiO_4^o$, $H_3SiO_4^-$ and amorphous silica ($SiO_2 \cdot 0.32\ H_2O$) AT 25 and 75 °C using the three isotope method. Geochimica et Cosmochimica Acta 255, 49-6. DOI: 10.1016/j.gca.2019.03.035"

Abstract

The accurate interpretation of Si isotope signatures in natural systems requires knowledge of the equilibrium isotope fractionation between Si bearing solids and the dominant Si-bearing aqueous species. Aqueous silicon speciation is dominated by silicic acid ($H_4SiO_4^o$) in most natural aqueous fluids at pH <8.5, but forms $H_3SiO_4^-$, $H_2SiO_4^{2-}$, and polymeric Si species in more alkaline fluids. In this study isotope exchange experiments were performed at *bulk chemical* equilibrium between amorphous silica ($SiO_2 \cdot 0.32\ H_2O$) and inorganic aqueous fluids at pH ranging from 5.8 to 9.9 at 25° and 75°C with experiments running as long as 375 days. The 'three isotope method' was used to quantify the equilibrium Si isotope fractionation, $\Delta_{eq}^{30}Si$, between amorphous silica and aqueous Si; this equilibrium fractionation factor was found to be 0.45 ± 0.20 ‰ at pH=6.4 and 25°C, and 0.07 ± 0.06 ‰ at pH=5.8 and 75°C. At more basic pH, equilibrium fractionation factors between solid and aqueous solution are higher, 1.63 ± 0.23 ‰ at pH=9.9 and 25°C, and 1.06 ± 0.13 ‰ at pH=9.1 and 75°C. Taking account of the distribution of the aqueous Si species, an equilibrium fractionation factor between $H_3SiO_4^-$ and $H_4SiO_4^o$ of -2.34 ± 0.13 ‰ and -2.21± 0.05 ‰ for 25 and 75°C was determined, respectively. The distinct equilibrium isotope fractionation factors of $H_3SiO_4^-$ and $H_4SiO_4^o$, and the variation of the equilibrium isotope fractionation factors with temperature can be used to establish paleo-pH and temperature proxies. The application of the three-isotope method also provides insight into the rates of isotopic exchange. For the solid grain size used (~20 nm), these rates match closely the measured bulk dissolution rates for amorphous silica for most of the isotope exchange process, suggesting the dominant isotope exchange mechanism in the experiments is detachment and reattachment of material at the amorphous silica surface.

3.1. Introduction

Silicon stable isotopes have been used as a tracer of a number of Earth (near-) surface processes, including weathering, biological activity, and marine paleo-temperature (e.g. De La Rocha et al., 1998; Ding et al., 2005; Ziegler et al., 2005a; Opfergelt et al., 2006, 2010, 2012, 2017; Georg et al., 2007; De La Rocha et al., 2011; Demarest et al., 2009; Hendry et al., 2011; Hendry and Robinson, 2012; Pogge von Strandmann et al., 2012; Pokrovsky et al., 2013; Marin-Carbonne et al., 2014; Oelze et al., 2014; Frings et al., 2015; He et al., 2016). The Si isotopic composition of many terrestrial reservoirs have been measured, including that of oceans, lakes, rivers and groundwaters (e.g. De La Rocha et al., 2000, 2011; Wischmeyer et al., 2003; Reynolds et al., 2006; Georg et al., 2009; Ding et al., 2011; Grasse et al., 2013; Pokrovsky et al., 2013; Frings et al., 2015), soils (Riotte et al., 2018a), and plants (Douthitt, 1982; Ding et al., 2008a, 2008b; Pogge von Strandmann et al., 2012; Opfergelt et al., 2012; Riotte et al., 2018b), and minerals, sedimentary rocks, cherts, and banded iron formations (e.g. Douthitt, 1982; Ziegler et al., 2005a, 2005b; Georg et al., 2009; Steinhoefel et al., 2010; van den Boorn et al., 2010; Savage et al., 2013). Constraining isotopic fractionation among these reservoirs is crucial to understanding the Si geochemical cycle.

Experimental studies have demonstrated that the Si isotopic signatures in natural environments can evolve during mineral precipitation (Li et al., 1995; Basile-Doelsch et al., 2005; Geilert et al., 2014, 2015; Roerdink et al., 2015; Oelze et al., 2015), mineral dissolution (Delvigne et al., 2012) or during adsorption of aqueous species (Delstanche et al., 2009; Oelze et al., 2014). Silicon isotopic fractionation during such mineral-aqueous fluid reactions in nature have been considered to be influenced by kinetic isotope fractionation (Geilert et al., 2014; Oelze et al., 2015; Roerdink et al., 2015; Poitrasson, 2017). However the degree of Si isotope fractionation at equilibrium is scarcely known, so that the relative impact of kinetic versus equilibrium processes on Si isotope fractionation during fluid-mineral interactions cannot be assessed unambiguously.

A critical factor to determine the equilibrium fractionation between a mineral and its coexisting aqueous fluid is the aqueous speciation of the system. The impact of aqueous speciation on the mineral/fluid fractionation factor has been demonstrated for elements such as boron, carbon, magnesium, mercury, transition metals and silicon (Hemming and Hanson, 1992; Zhang et al., 1995; Zeebe, 2005; Klochko et al., 2006, 2009; Asael et al., 2009; Holloway et al., 2011; Jiskra et al., 2012; Ryan et al., 2013; Yin et al., 2013; Fujii et al.,

2014, 2015; Dupuis et al., 2015; Noireaux et al., 2015; Schott et al., 2016; Balan et al., 2018; Mavromatis et al., 2019). Dissolved silicon in aqueous environments can occur in various distinct species. Aqueous Si speciation depends on the solution pH and total dissolved Si concentration. In inorganic systems at ambient temperature, pH < 8.5 and $m_{Si} \leq 10^{-2.7}$ M (~ amorphous silica solubility), silicic acid ($H_4SiO_4^o$) dominates Si aqueous speciation. As pH increases, the species, $H_3SiO_4^-$ and $H_2SiO_4^{2-}$, form at the expense of silicic acid, whereas polymeric Si species become increasingly important in aqueous solutions supersaturated with respect to amorphous silica (Dietzel, 2000). Figure 3.1 shows the aqueous speciation of Si in a solution containing 1.6×10^{-3} M Si (corresponding to the equilibrium with amorphous silica at pH<9) as a function of pH for 25°C and 75°C, respectively. As the speciation of aqueous silicon changes with pH, equilibrium isotope fraction between this fluid and any Si bearing mineral will change accordingly (Dupuis et al., 2015; Fujii et al., 2015).

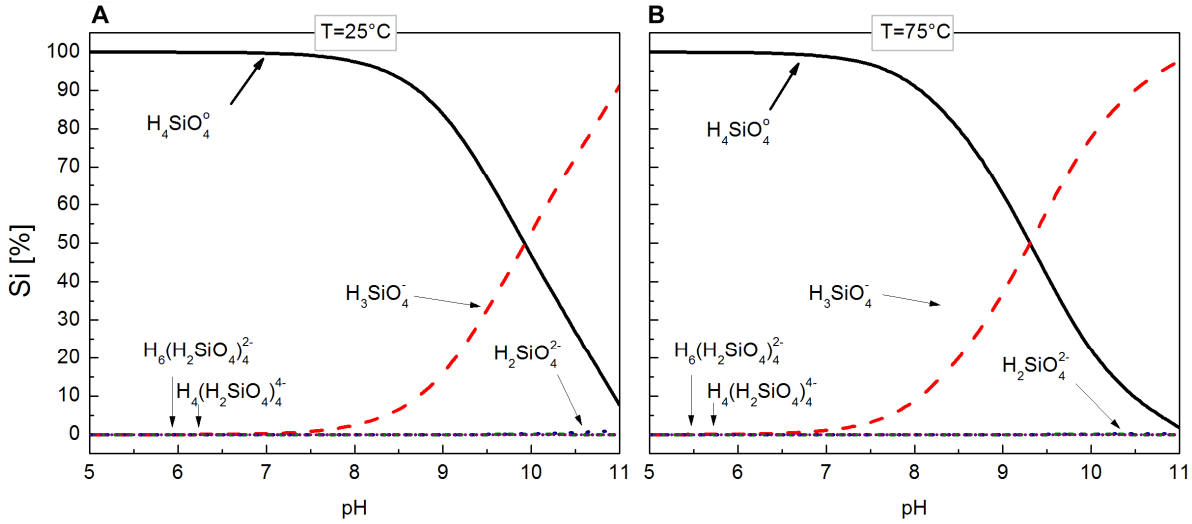

Figure 3.1 - Distribution of aqueous Si species in equilibrium with amorphous silica as a function of pH, for A. 25°C and B. 75°C.

Several past studies have aimed to determine Si equilibrium fractionation factors between amorphous silica and its coexisting aqueous solutions (Geilert et al., 2014; Oelze et al., 2014; Roerdink et al., 2015). Most reported an enrichment of the solid in light (^{28}Si) isotopes, which could be explained by non-equilibrium fractionation during precipitation of amorphous silica from a supersaturated solution (Dupuis et al., 2015). Zheng et al. (2016) measured Si isotopic fractionation at chemical equilibrium between a Fe(III)-bearing silica gel and artificial Archean seawater; they reported a 25°C equilibrium fractionation factor, $\Delta^{30}Si_{gel\text{-}fluid}$ of ~ -3.5 ‰. Dupuis et al. (2015) used first-principle methods to calculate the 25 °C equilibrium fractionation factors between quartz and its co-existing aqueous solution,

and kaolinite and its co-existing aqueous solution. These calculations predict a $\Delta^{30}Si_{mineral-solution}$ at neutral pH of 2.1 ± 0.2‰ and 0.4 ± 0.2‰, for the quartz-aqueous solution and kaolinite-aqueous solution system, respectively. Additionally these authors reported the 25°C equilibrium fractionation factor of -1.6 ± 0.3‰, between the $H_3SiO_4^-$ and $H_4SiO_4^0$ aqueous silicon species. Similarly, Fujii et al. (2015) experimentally and theoretically determined the equilibrium fractionation factor between the two aqueous species $H_3SiO_4^-$ and $H_4SiO_4^0$. Their determined values of -3.5 ‰ (experimental) and -3 ‰ (ab initio calculations) are somewhat inconsistent with those calculated by Dupuis et al. (2015).

The aim of this study is to expand on these past efforts, by determining experimentally the equilibrium fractionation factors between amorphous SiO_2 and the aqueous Si species as a function of pH over a range of $5.8 < pH < 10$ at temperatures of 25°C and 75°C. To assure the attainment of isotopic equilibrium, the 'three-isotope method' was applied. The purpose of this paper is to report the results of this experimental study and provide new insights into how aqueous solution speciation and temperature can affect the Si equilibrium isotopic fractionation between amorphous silica and an aqueous solution.

3.2. Theoretical background

3.2.1. Geochemical calculations of amorphous silica dissolution rates

All geochemical calculations in this study were performed using the PHREEQC code (Parkhurst and Appelo, 2013) together with its llnl thermodynamic database. The standard state adopted in this study calls for unit activity of pure minerals, solids, and H_2O. For aqueous species, the standard state is unit activity of a 1 molal solution extrapolated to infinite dilution. The activity coefficients of charged aqueous species were calculated using the Davies equation, whereas the activity coefficients of neutral species were assumed to be equal to one.

The experiments in the present study were begun by first equilibrating an initially Si free aqueous solution of known pH with amorphous silica. The dissolution reaction for amorphous silica is described by:

$$SiO_{2,am} + 2\,H_2O \rightarrow H_4SiO_4^0 \qquad (3.1)$$

The law of mass action for reaction (3.1) is given by:

$$K_{eq} = \frac{a_{H_4SiO_4^0}}{a_{SiO_{2,am}} a_{H2O}^2} \tag{3.2}$$

where K_{eq} stands for an equilibrium constant and a_i refers to the activity of the subscripted species or phase. Taking account of this standard state, in pure water ($a_{\mathrm{H_4SiO_4^0}} = C_{\mathrm{H_4SiO_4^0}}$, where C_i stands for the concentration of the subscripted species), Eqn. (3.2) reduces to:

$$K_{eq} = C_{\mathrm{H_4SiO_4^0},eq} \tag{3.3}$$

where $C_{\mathrm{H_4SiO_4^0},eq}$ stands for the concentration of $\mathrm{H_4SiO_4^0}$ in equilibrium with amorphous silica. The rates of amorphous silica dissolution (r) in a closed system and in the absence of specific inhibitors or catalysts can be described using (Rimstidt and Barnes, 1980):

$$r = \frac{dC_{\mathrm{H_4SiO_4^0}}}{dt} = S/M\left(k_+ - k_- C_{\mathrm{H_4SiO_4^0}}\right) \tag{3.4}$$

S and M refer to the interfacial surface area and mass of solution normalized and k_+ and k_- designates amorphous silica dissolution and precipitation rate constants, respectively. Note $C_{\mathrm{H_4SiO_4^0}}$ in Eqn (4) has units of mol/kg H_2O. Rearranging Eqn. (3.4) and integrating it between times t= 0 and t gives

$$t = (1/k'_-) ln\left(\frac{k'_+ - k'_- C_{\mathrm{H_4SiO_4^0}}}{k'_+ - k'_-.C_{(\mathrm{H_4SiO_4^0})_0}}\right) \tag{3.5}$$

where $k'_+ = (\frac{S}{M})k_+$ and $k'_- = (\frac{S}{M})k_-$, and $C_{(\mathrm{H_4SiO_4^0})_0}$ denotes $C_{\mathrm{H_4SiO_4^0}}$ at time zero. When starting from a zero concentration of $\mathrm{H_4SiO_4^0}$ in solution, Eqn. (3.5) reduces to

$$t = (1/k'_-) ln\left(\frac{k'_+ - k'_- C_{\mathrm{H_4SiO_4^0}}}{k'_+}\right). \tag{3.6}$$

Noting that $\frac{k'_+}{k'_-} = C_{(\mathrm{H_4SiO_4^0})_{eq}}$, where $C_{(\mathrm{H_4SiO_4^0})_{eq}}$ again denotes the concentration of dissolved silica in equilibrium with amorphous silica, the temporal evolution of dissolved silica concentration in the closed system is described by:

$$C_{\mathrm{H_4SiO_4^0}} = C_{(\mathrm{H_4SiO_4^0})_{eq}}\left(1 - e^{-t.k'_-}\right) \tag{3.7}$$

3.2.2. Si isotope systematics

Silicon isotope compositions in this study are reported using the standard δ-notation in per mil (‰) relative to the international NBS-28 standard (NIST RM-8546), computed using:

$$\delta^{x}\mathrm{Si} = \left[\frac{(\,^{x}\mathrm{Si}/^{28}\mathrm{Si})_{Sample}}{(\,^{x}\mathrm{Si}/^{28}\mathrm{Si})_{NBS-28}} - 1\right] \tag{3.8}$$

where $(\,^{x}\mathrm{Si}/^{28}\mathrm{Si})_{Sample}$ refers to the atomic ratio of the Si with mass *x,* which denotes either ^{29}Si or ^{30}Si, to that of ^{28}Si in the sample of interest. The Si isotopic fractionation factor between a solid and an aqueous fluid $(\alpha^{x/28}_{solid-fluid})$ is defined as:

$$\alpha^{x/28}_{solid-fluid} = \frac{(\,^{x}\mathrm{Si}/^{28}\mathrm{Si})_{solid}}{(\,^{x}\mathrm{Si}/^{28}\mathrm{Si})_{fluid}} \tag{3.9}$$

The silicon isotopic fractionation between a solid and a coexisting aqueous phase can be also described using $\Delta^{x}\mathrm{Si}_{solid-fluid}$, which is defined by:

$$\Delta^{x}\mathrm{Si}_{solid-fluid} = \delta^{x}\mathrm{Si}_{solid} - \delta^{x}\mathrm{Si}_{fluid} \tag{3.10}$$

Note that $\Delta^{x}\mathrm{Si}_{solid-fluid}$ is approximately related to $\alpha^{x/28}_{solid-fluid}$ by:

$$\Delta^{x}\mathrm{Si}_{solid-fluid} \approx 10^{3} ln\alpha^{x/28}_{solid-fluid} \tag{3.11}$$

The fractionation factor between the solid and the aqueous fluid depends on the proportion of the different species present in this fluid and their individual fractionation factors with the solid $\alpha^{x/28}_{solid-i}$ consistent with (Zhang et al., 1995):

$$10^{3} ln\alpha^{x/28}_{solid-fluid} = \sum_{i}(x_i \times 10^{3} ln\alpha^{x/28}_{solid-i}) \tag{3.12}$$

where x_i refers to the mole fraction of the dissolved Si present in the subscripted aqueous species.

3.2.3. Three-isotope method

Equilibrium fractionation factors in the present study were generated using the 'three-isotope method'. The three-isotope method was originally used to determine the equilibrium isotopic fractionation factors of oxygen between mineral and co-existing aqueous solutions (Matsuhisa et al., 1978; Matthews et al., 1983a, 1983b, 1983c). Over the past 10 years, this

method was also successfully applied to non-traditional isotopic systems, such as Mg and Fe (Shahar et al., 2008; Beard et al., 2010; Li et al., 2011; Frierdich et al., 2014; Reddy et al., 2015), as well as Si (Zheng et al., 2016). This approach is commonly used to evaluate the kinetics of isotopic exchange reactions between two components (Cole and Chakraborty, 2001; Johnson et al., 2002; Li et al., 2011; Wu et al., 2012; Zheng et al., 2016).

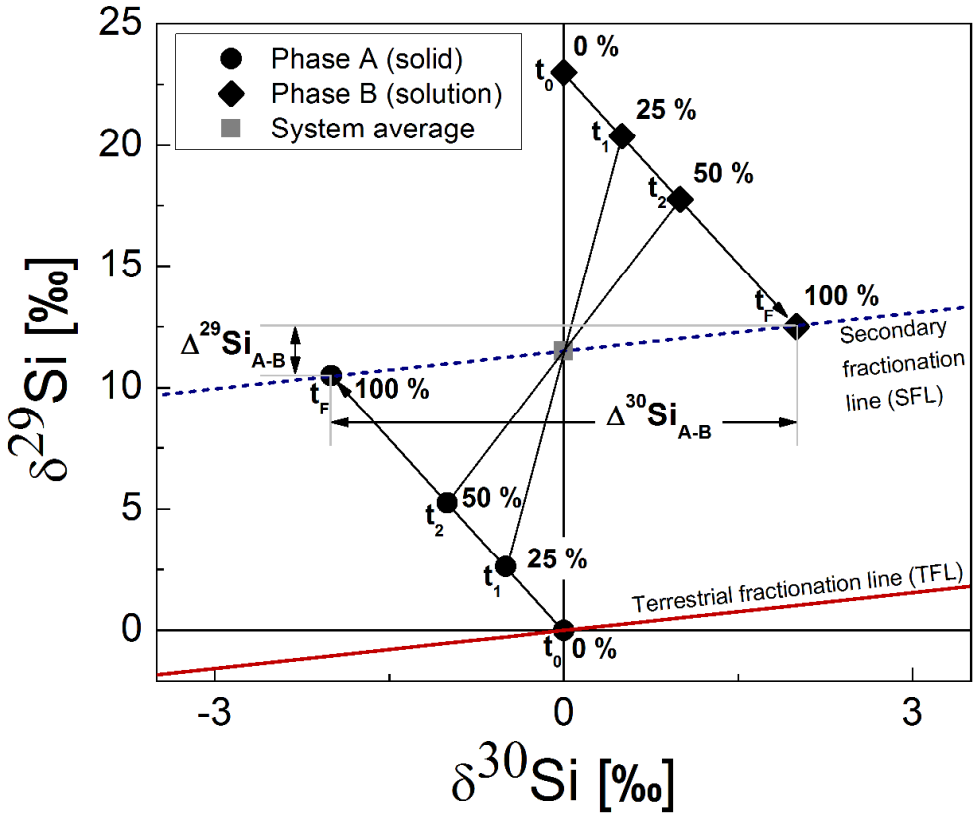

Figure 3.2 - Schematic diagram of the three-isotope method applied to Si, after Li et al. (2011) and Zheng et al. (2016). At time (t) zero, and in the absence of isotopic exchange (shown in %) Phase A plots as the isotopically "normal" component on the terrestrial fractionation line (TFL). At t0 Phase B shows a distinct offset from the TFL as it is enriched in 29Si. The isotopic composition of phases A and B gradually evolve towards 100% isotopic exchange. The lines connecting the two phases at a given time always cross the system average as required by isotope mass balance. When isotopic exchange is complete, the two phases plot on a secondary fractionation line, whose position is dictated by the isotopic mass balance of the system.

Before exchange, one component (Phase A, typically the solid) exhibits a "natural" isotopic composition and plots on a δ vs. δ diagram, such as Fig. 3.2, on a primary fractionation line, also known as the terrestrial fractionation line (TFL). This line follows a mass-dependent relation where $\delta^{30}Si \approx 1.93 \times \delta^{29}Si$ (Young et al., 2002; Zheng et al., 2016). The second component (Phase B, typically the fluid) is enriched in one isotope (for example, ^{29}Si in the present study) and thus has a distinct and known offset from the TFL. As the system undergoes isotopic exchange, the isotopic compositions of the two components will

gradually evolve over time (t) towards isotopic equilibrium. Once the isotopic exchange is complete and isotopic equilibrium has been attained, the isotopic compositions of the two phases will fall on a secondary fractionation line (SFL) parallel to the TFL. The position of the SFL is defined by the isotopic mass balance of the system (see Fig. 3.2).

For many systems, isotopic exchange is slow and therefore often incomplete. The three-isotope method, nevertheless, allows validation of the attainment of isotopic equilibrium. The degree to which the system has attained isotopic equilibrium can be quantified using the degree of isotope exchange (F), defined by:

$$F = \frac{(\delta_t - \delta_i)}{(\delta_e - \delta_i)} \tag{3.13}$$

where δ_t denotes the isotopic composition of either one of the phases at any time, t, during the isotope exchange reaction, and δ_i and δ_e describe the initial and equilibrium isotopic composition of this phase. The parameter F ranges from 0 to 1 as isotopic equilibrium is attained. In a two-component system δ_e can be derived from the mass balance constraints (Zheng et al., 2016), and calculated from

$$\delta_e = \delta_{mean} - \left(\frac{N_{solid}}{N_{solid} + N_{fluid}}\right) \times \Delta_{solid-fluid,eq} \tag{3.14}$$

where δ_{mean} in this study stands for the mass averaged Si isotope composition of the system, $\Delta_{solid-fluid,eq}$designates the equilibrium isotope fractionation between the solid and fluid phases, and N_{solid} and N_{fluid} denote the number of moles of Si in the solid and fluid phase, respectively. If the $\Delta_{solid-fluid,eq}$ of the system is not known, it can be obtained from an iterative fit of experimental data (Zheng et al., 2016).

3.2.4. Kinetics of isotopic exchange

The three-isotope method not only allows determination of the equilibrium fractionation factors of a solid-fluid system, but also allows determination of the kinetics of isotopic exchange. Following the approach of Cole and Chakraborty (2001) and Johnson et al. (2002) isotope exchange rates can be quantified using

$$\frac{-d(1-F)}{dt} = k_n(1-F)^n \tag{3.15}$$

where k_n stands for the rate constant of reaction order n, where this reaction order is usually an integer from 0 to 3. Isotope exchange reactions typically follow either a first-order (n=1)

or second-order (n=2) rate law (Criss et al., 1987; Huang and Tsai, 1970; Johnson et al., 2002; Welch et al., 2003; Li et al., 2011; Zheng et al., 2016). The integrated form of this rate equation can be written as either

$$\ln(1 - F) = -k_1 t \qquad \text{for } n=1 \qquad (2.16)$$

$$\frac{F}{(1-F)} = k_2 t \qquad \text{for } n=2 \qquad (2.17)$$

Isotope exchange rate constants can be quantified by fitting the experimental value of F to Eqn. (3.16) for the first order rate constant or Eqn. (3.17) for the second order rate constant (Cole and Chakraborty, 2001; Johnson et al., 2002; Li et al., 2011).

3.3. Methods

3.3.1. Experimental approach

3.3.1.1. Starting powder - amorphous silica

All experiments in the present study were performed in series using Alpha Aeser® 100 mesh hydrated silicic acid powder. This powder was cleaned prior to each experimental series by sedimentation in >18.2 Ω de-ionized water (Milli-Q®) to remove ultrafine particles (Pokrovski and Schott, 1998). In each case, from 40 to 75 g of the powder was suspended by stirring in a 1dm^3 glass beaker. The powder was sedimented for 10 minutes and then decanted. This operation was repeated until the supernatant became clear within the first 5 min. Subsequently the powder was oven dried at 60°C. To avoid hydration of the powder while it cooled to room temperature, it was placed into a desiccator. Representative scanning electron microscope (SEM) and transmission electron microscope (TEM) images of the resulting powders are shown in Fig. 3.3 A and B. These images were acquired using a MEB JEOL JSM-7800F Prime electron microscope and a JEOL JEM-ARM200F Cold FEG transmission electron microscope at the Raimond Castaing Microcharacterization Centre (Toulouse, France), respectively. The TEM images were used to measure average grain size with the ImageJ software package (Schindelin et al., 2012); the average measured grain size was ~21 ± 5 nm (2SD, n=100). Energy dispersive spectroscopy (EDS) analyses indicate the powder contained pure Si without other metals present. Thermogravimetric analyses, performed with a Mettler Toledo® ATG/DSC1, showed that the powders also contained

~8.7 % H_2O, which is consistent with the chemical formula $SiO_2 \bullet 0.32\ H_2O$. The specific surface areas of the cleaned amorphous silica were determined with a Quantachrome Autosorb-1MP using the nitrogen multipoint BET method (Brunauer et al., 1938). The average surface area of the initial amorphous silica powders is 196.3 m^2/g, and ranged from 175 m^2/g to 215 m^2/g with an estimated uncertainty of ± 10%.

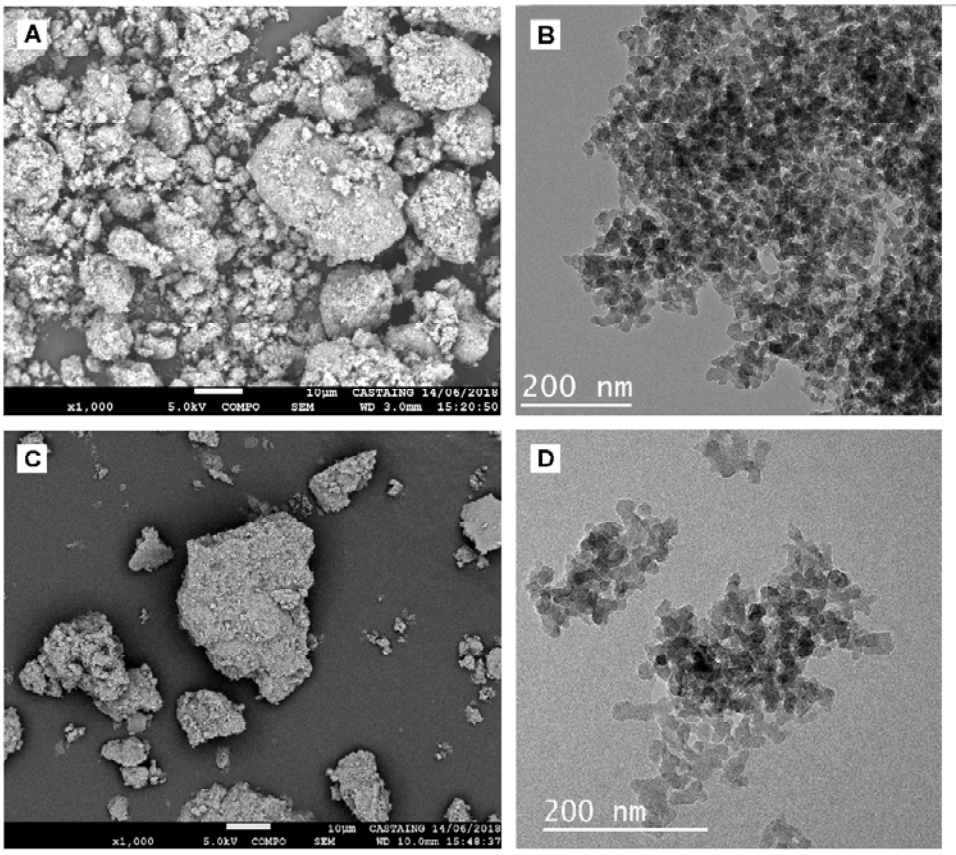

Figure 3.3 - Representative images of amorphous SiO2 powders. A) SEM image of the initial powder showing agglomerates of amorphous SiO2 grains. B) TEM image of the initial powder showing rounded ~ 21 nm SiO2 grains. C) Representative SEM image of reacted amorphous silica powder. D) TEM image of reacted amorphous silica recovered from the longest duration experiment performed at T ~25°C, pH ~6.

3.3.1.2. Initial aqueous solutions

The initial aqueous solutions used in the experiments were prepared at pH ~6 and ~10 for the 25°C experiments and at pH ~6 and ~9 for the 75°C experiments; experiments run with these fluids are labelled SibA, SicB, SigA, and SikB, respectively. The pH of the fluids were selected so that it would be possible to quantify the effect of the aqueous $H_3SiO_4^-$ species on equilibrium fractionation factors at these two temperatures. These solutions were prepared using high purity de-ionized Milli-Q® water (>18.2 Ω), and reagent grade HCl, NH_4OH and NH_4Cl. The compositions of these initial solutions are provided in Table 3.1.

3.3.1.3. Characterization of the aqueous solutions

The aqueous solution pH was regularly monitored during the experiments with a Metrohm® 913 pH Meter connected to a standard glass microelectrode. This electrode was calibrated using certified Orion Thermo Scientific® buffers. The uncertainty in the measurements was determined to be 0.05, equal to 2 standard deviations of ~40 repeated measurements of the pH=4.01 calibration standard. For experiments at 75°C, the pH was measured at 25°C and later calculated to this higher temperature with PHREEQC.

Aqueous silicon concentrations were determined by the molybdate blue method (Truesdale and LeCorre, 1975) using a Bran & Luebbe® analyser-III colorimeter coupled to a Seal XY-2 autosampler and a Technicon analyser II mixing unit. The measurements were conducted over the 0.1 to 10 ppm concentration range. The long-term reproducibility of these measurements was determined to be within 3% and the quantification limit was 0.04 ppm.

3.3.1.4. Experiment design: Step 1 Equilibration of reactive fluids

Experiments in this study were conducted in four distinct series. Each series began by equilibrating 200 ml of an initial aqueous fluid of selected composition with 3 g of pre-washed amorphous SiO_2 powder in closed polypropylene bottles (see Table 3.1). Once closed, these bottles were placed in shaking thermostatic baths at either ~25°C or ~75°C. The aqueous fluids in the bottles were sampled 8 times at regular intervals during the 19 to 65 days of this equilibration stage. The pH was measured immediately after each sampling at room temperature. The samples collected from the 75°C experiments were then diluted to prevent precipitation. Aqueous Si concentrations were determined by colorimetry on all samples. Chemical equilibrium was assumed to be attained when both pH and the Si concentration of the aqueous solutions attained constant values within uncertainty.

This initial stage was stopped once these constant values were reached. The fluids were then filtered with Teflon syringe filters (Merck® 0.2 µm). Fluids recovered from the 75°C experiments were kept in the thermostatic bath until subsequently used in the isotopic exchange experiments described below.

Table 3.1 - Summary of the initial conditions of the first stage of each experimental series performed in the present study. Quantity in grams of fluids and solids used are denoted as $m_{initial\ sol}$ and $m_{SiO_2,am}$.

Experiment ID	Temperature [°C]	Initial aqueous solution composition	pH	$m_{initial\ sol}$ [g]	$m_{SiO2:am}$ [g]
SibA	25	pure MQ® water + 0.43 ml 1 N HCl + 0.50 ml 1.4 N NH_4OH	6.2	200.04	3.00
SicB	25	0.1 M NH_4Cl - 0.35 M NH_4OH buffer	10.2	200.00	3.00
Sig75A	75	pure MQ® water	6.0	200.21	3.02
Sik75B	75	0.1 M NH_4Cl - 1.52 M NH_4OH buffer	9.4	200.56	3.01

3.3.1.5. Experiment design: Step 2 Isotopic exchange experiments

The four chemical equilibrated fluids were enriched with a ^{29}Si isotope tracer to obtain $\delta^{29}Si = \sim 23‰$ (see Table 3.2). The added ^{29}Si isotope tracer was prepared by dissolving Eursio-top® $^{29}SiO_2$ powder, having an initial composition of 0.21% ^{28}Si, 99.76% ^{29}Si, and 0.03% ^{30}Si in de-ionized water. After the addition of this spike to the equilibrated fluids, the Si concentration and pH were measured. For experiments at pH ~ 6 the fluid pH was adjusted, if necessary, by adding a small quantity of HCl or NH_4OH to assure these initial fluids were as close to equilibrium with amorphous silica as possible. Each series of exchange experiments consisted of a suite of 8 closed system experiments of selected durations. This approach was selected so that both the solids and fluids could be collected and analysed after distinct experiment durations. The overall duration of each experimental series were selected so that degree of isotopic exchange would approach 1 at the end of each series; these overall durations are provided in Table 3.2. Each individual experiment was performed in 10 ml polypropylene reactors. Into each reactor was added ~ 0.15 g of amorphous SiO_2 powder with a known Si isotope composition and 5 ml of the prepared ^{29}Si enriched fluid. The 25°C experiments were placed into an orbital shaker to be constantly mixed. The 75°C experiments were placed into a thermostatic bath and hand shaken once or twice a day. To verify that no leakage occurred during any experiment, all reactors were weighted both at the beginning and the end of each experiment. At pre-chosen time intervals, the reactors were centrifuged for 20 min at 4500 rpm and then opened. The supernatant was separated from the powder and filtered using Merck® 0.2 µm Teflon syringe filters. The pH was measured immediately after sampling, and fluids recovered from the 75°C experiments were diluted just after measuring pH. The recovered powder was washed and filtered with de-ionized water, oven-dried at 40°C, and stored for further analysis.

Table 3.2 - Overview of the results of the isotopic exchange experiments performed in this study. Uncertainties of the isotopic measurements are expressed as 2 SD (Standard Deviation) and 2 SE (Standard Error). The 2 SE is computed following the relation: $\boldsymbol{SE = \frac{SD}{\sqrt{(n-1)}} \times t}$, where n denotes the number of measurements performed and t denotes the Student t-factor (Platzner et al., 1997). δ_{eq} represents the equilibrium isotopic composition of ^{29}Si and F denotes the degree of isotopic exchange. [a] denotes the spiked initial solution.

Exp.	elapsed time	Temp.	pH	Si-conc.	S_{BET}	*solution*						*amorphous SiO_2*						δ_{eq}	$F_{sol.}$	ln(1-F)
	[d]	[°C]		[ppm]	[m^2/g]	δ^{30}Si	2SD	2SE	δ^{29}Si	2SD	2SE	δ^{30}Si	2SD	2SE	δ^{29}Si	2SD	2SE	δ^{29}Si		
						[‰]	[‰]	[‰]	[‰]	[‰]	[‰]	[‰]	[‰]	[‰]	[‰]	[‰]	[‰]			
SibA:																		-0.22		
SibA 0	0	25	6.2	44.4	214.7	***-0.69***	*0.20*	*0.10*	***-0.33***	*0.10*	*0.05*	***-0.07***	*0.18*	*0.11*	***-0.06***	*0.03*	*0.02*			
SibA0-S[a]	0	25	6.1	48.0		***-0.63***	*0.13*	*0.07*	***22.85***	*0.16*	*0.08*	***-0.07***	*0.18*	*0.11*	***-0.06***	*0.03*	*0.02*		0.000	0.00
SibA 1	0.25	25	6.4	47.4		***-0.55***	*0.15*	*0.12*	***14.23***	*0.16*	*0.13*	***0.00***	*0.15*	*0.12*	***0.03***	*0.09*	*0.07*		0.374	-0.47
SibA 2	1	25	6.5	48.2		***-0.47***	*0.20*	*0.16*	***10.14***	*0.05*	*0.04*	***-0.07***	*0.10*	*0.08*	***0.01***	*0.03*	*0.03*		0.551	-0.80
SibA 3	3	25	6.3	48.5		***-0.55***	*0.09*	*0.11*	***6.16***	*0.06*	*0.07*	***-0.01***	*0.20*	*0.16*	***0.05***	*0.03*	*0.02*		0.723	-1.29
SibA 4	10	25	6.4	49.1		***-0.54***	*0.08*	*0.10*	***3.74***	*0.17*	*0.21*	***-0.01***	*0.12*	*0.10*	***0.05***	*0.12*	*0.10*		0.828	-1.76
SibA 5	30	25	6.5	49.8		***-0.82***	*0.12*	*0.14*	***2.42***	*0.08*	*0.10*	***-0.09***	*0.10*	*0.13*	***0.03***	*0.07*	*0.09*		0.886	-2.17
SibA 6	66	25	6.4	50.1		***-0.77***	*0.11*	*0.13*	***1.88***	*0.02*	*0.02*	***-0.13***	*0.04*	*0.05*	***0.04***	*0.10*	*0.12*		0.909	-2.39
SibA 7	171	25	6.4	57.0		***-0.61***	*0.05*	*0.06*	***1.33***	*0.08*	*0.10*	***-0.08***	*0.09*	*0.12*	***0.02***	*0.03*	*0.03*		0.933	-2.70
SibA 8	351	25	6.4	53.8	137.1	***-0.29***	*0.17*	*0.09*	***0.14***	*0.17*	*0.09*	***-0.08***	*0.10*	*0.13*	***0.04***	*0.03*	*0.04*		0.984	-4.17
SicB:																		-0.54		
SicB 0	0	25	10.1	116.2	195.0	***-1.62***	*0.09*	*0.06*	***-0.84***	*0.05*	*0.03*	***-0.09***	*0.12*	*0.15*	***-0.03***	*0.03*	*0.04*			
SicB 0-S[a]	0	25	9.9	115.4		***-1.57***	*0.07*	*0.04*	***23.30***	*0.19*	*0.10*	***-0.09***	*0.12*	*0.15*	***-0.03***	*0.03*	*0.04*		0.000	0.00
SicB 1	0.25	25	9.8	114.7		***-1.24***	*0.04*	*0.03*	***3.04***	*0.02*	*0.01*	***-0.06***	*0.05*	*0.06*	***0.16***	*0.02*	*0.03*		0.850	-1.90
SicB 2	1	25	9.9	115.6		***-1.34***	*0.17*	*0.14*	***2.00***	*0.09*	*0.07*	***-0.09***	*0.02*	*0.02*	***0.14***	*0.00*	*0.01*		0.893	-2.24
SicB 3	3	25	9.9	120.7		***-1.43***	*0.17*	*0.22*	***1.81***	*0.08*	*0.09*	***-0.12***	*0.09*	*0.11*	***0.18***	*0.05*	*0.06*		0.901	-2.31
SicB 4	10	25	9.9	119.9		***-1.56***	*0.14*	*0.18*	***1.15***	*0.05*	*0.06*	***-0.09***	*0.10*	*0.13*	***0.21***	*0.03*	*0.03*		0.929	-2.64
SicB 5	30	25	9.9	115.3		***-1.65***	*0.16*	*0.20*	***0.42***	*0.21*	*0.27*	***-0.09***	*0.06*	*0.07*	***0.17***	*0.06*	*0.08*		0.960	-3.21
SicB 6	66	25	9.8	111.0		***-1.77***	*0.03*	*0.04*	***0.27***	*0.07*	*0.08*	***-0.10***	*0.07*	*0.09*	***0.21***	*0.02*	*0.02*		0.966	-3.38
SicB 7	179	25	9.9	106.0		***-1.62***	*0.20*	*0.16*	***0.02***	*0.11*	*0.09*	***-0.09***	*0.05*	*0.07*	***0.18***	*0.02*	*0.03*		0.976	-3.75
SicB 8	385	25	9.6	104.3	164.1	***-1.69***	*0.20*	*0.16*	***0.00***	*0.08*	*0.06*	***-0.05***	*0.04*	*0.04*	***0.24***	*0.12*	*0.15*		0.977	-3.79

Table 3.2 - continued

Exp.	elapsed time [d]	Temp. [°C]	pH	Siconc. [ppm]	S_{BET} [m^2/g]	*solution* $\delta^{30}Si$ [‰]	2SD [‰]	2SE [‰]	$\delta^{29}Si$ [‰]	2SD [‰]	2SE [‰]	*amorphous SiO_2* $\delta^{30}Si$ [‰]	2SD [‰]	2SE [‰]	$\delta^{29}Si$ [‰]	2SD [‰]	2SE [‰]	δ_{eq} $\delta^{29}Si$	$F_{sol.}$	ln(1-F)
Sig75A																		0.11		
Sig75A 0	0	75	5.8	117.4	195.6	***-0.02***	*0.15*	*0.12*	***0.00***	*0.09*	*0.07*	***-0.04***	*0.14*	*0.17*	***-0.03***	*0.13*	*0.17*			
Sig75A 0-S	0	75	5.2	122.3		***-0.10***	*0.25*	*0.16*	***22.87***	*0.09*	*0.06*	***-0.04***	*0.14*	*0.17*	***-0.03***	*0.13*	*0.17*		0.000	0.00
Sig75A 1	0.25	75	5.8	119.0		***-0.12***	*0.10*	*0.06*	***14.13***	*0.10*	*0.06*	***-0.08***	*0.17*	*0.10*	***0.09***	*0.11*	*0.07*		0.384	-0.48
Sig75A 2	1	75	5.8	115.5		***-0.23***	*0.09*	*0.07*	***8.54***	*0.01*	*0.01*	***-0.12***	*0.03*	*0.04*	***0.12***	*0.05*	*0.06*		0.629	-0.99
Sig75A 3	3	75	5.9	114.9		***-0.22***	*0.12*	*0.15*	***5.12***	*0.06*	*0.07*	***-0.08***	*0.05*	*0.06*	***0.18***	*0.01*	*0.02*		0.780	-1.51
Sig75A 4	10	75	6.2	113.9		***-0.18***	*0.16*	*0.10*	***3.72***	*0.09*	*0.06*	***-0.18***	*0.04*	*0.05*	***0.20***	*0.05*	*0.06*		0.841	-1.84
Sig75A 5	21	75	5.8	114.3		***-0.22***	*0.26*	*0.16*	***3.07***	*0.09*	*0.05*	***-0.14***	*0.02*	*0.02*	***0.18***	*0.07*	*0.09*		0.870	-2.04
Sig75A 6	33	75	5.8	118.6		***-0.22***	*0.28*	*0.17*	***2.65***	*0.05*	*0.03*	***-0.16***	*0.08*	*0.10*	***0.20***	*0.07*	*0.09*		0.888	-2.19
Sig75A 7	43	75	5.9	114.6		***-0.20***	*0.18*	*0.11*	***2.40***	*0.07*	*0.04*	***-0.09***	*0.11*	*0.07*	***0.22***	*0.06*	*0.04*		0.899	-2.30
Sig75A 8	55	75	6.0	109.5	171.7	***-0.13***	*0.14*	*0.11*	***2.09***	*0.07*	*0.06*	***-0.14***	*0.06*	*0.08*	***0.20***	*0.04*	*0.05*		0.913	-2.44
Sik75B																		0.01		
Sik75B 0	0	75	9.3	282.2	179.8	***-1.50***	*0.11*	*0.14*	***-0.76***	*0.08*	*0.10*	***-0.04***	*0.15*	*0.09*	***0.02***	*0.06*	*0.04*			
Sik75B 0-S	0	75	9.2	287.2		***-1.57***	*0.14*	*0.09*	***23.14***	*0.26*	*0.16*	***-0.04***	*0.15*	*0.09*	***0.02***	*0.06*	*0.04*		0.000	0.00
Sik75B 1	0.25	75	9.1	233.0		***-1.00***	*0.06*	*0.25*	***3.02***	*0.02*	*0.09*	***-0.12***	*0.07*	*0.06*	***0.45***	*0.07*	*0.05*		0.870	-2.04
Sik75B 2	1	75	9.1	237.2		***-1.10***	*0.13*	*0.10*	***1.60***	*0.11*	*0.09*	***0.01***	*0.22*	*0.14*	***0.50***	*0.16*	*0.10*		0.931	-2.67
Sik75B 3	3	75	9.1	227.3		***-1.18***	*0.11*	*0.08*	***1.17***	*0.08*	*0.06*	***-0.02***	*0.21*	*0.13*	***0.54***	*0.13*	*0.08*		0.950	-2.99
Sik75B 4	10	75	9.0	205.9		***-1.30***	*0.18*	*0.14*	***0.76***	*0.07*	*0.06*	***-0.06***	*0.17*	*0.10*	***0.53***	*0.06*	*0.04*		0.968	-3.43
Sik75B 5	21	75	8.9	178.0		***-1.27***	*0.14*	*0.18*	***0.71***	*0.07*	*0.08*	***0.05***	*0.20*	*0.25*	***0.57***	*0.04*	*0.06*		0.970	-3.50
Sik75B 6	33	75	8.7	163.5	119.0	***-1.18***	*0.15*	*0.18*	***0.64***	*0.12*	*0.15*	***-0.08***	*0.17*	*0.21*	***0.55***	*0.09*	*0.11*		0.973	-3.60
Sik75B 7	43	75	8.6	137.3		***-1.15***	*0.14*	*0.17*	***0.60***	*0.10*	*0.13*	***0.05***	*0.08*	*0.10*	***0.57***	*0.09*	*0.11*		0.974	-3.66
Sik75B 8	55	75	8.5	118.2		***-1.09***	*0.08*	*0.10*	***0.61***	*0.05*	*0.06*	***0.03***	*0.15*	*0.19*	***0.54***	*0.02*	*0.02*		0.974	-3.64

3.3.2. Si isotope analysis

Silicon isotope compositions were measured in the fluid and solid samples collected from all isotope exchange experiments, as well as the initial washed SiO_2 powders, the spiked initial fluid and the non-spiked chemical equilibrated fluids. Aqueous samples were prepared by first acidifying the solutions using bi-distilled 3N HCl to pH ~2. Amorphous silica powders were processed using the alkali fusion method described by Zambardi and Poitrasson (2011). From 2 to 5 mg of the solids were weighted into silver crucibles (XRF scientific, Montreal, Canada) together with a ~200 mg Merck® NaOH pellet. The crucibles were capped and placed into a furnace heated at 720°C for 10 min. They were subsequently cooled to room temperature and placed into 30 cm^3 Savillex® Teflon beakers filled with 20 ml Milli-Q® water for 24 hours to dissolve the fusion cake. The resulting fluids were then transferred to 60 cm^3 polypropylene bottles and diluted to 40 ml by adding Milli-Q® water. These 40 ml samples were then acidified using ~10 N bi-distilled HCl to obtain a pH of 1.5.

All prepared Si-bearing fluids generated from either the solid or fluid samples were purified by cation-exchange chromatography using the Bio-Rad® AG50W-12X cationic resin (Georg et al., 2006; Zambardi and Poitrasson, 2011). The detailed cleaning procedure of the resin is described in Zambardi and Poitrasson (2011). From 0.5 to 2 ml of prepared fluids containing up to 70 µg Si were loaded, directly collected, and eluted twice with de-ionized MQ® water to obtain 6 ml samples. These were then diluted and acidified to obtain a 3 ppm solution with a total 0.05 M HCl concentration. Silicon recovery after processing was determined to be between 90 to 100 %. The ^{28}Si signal of the procedural blank, processed in the same way, was found to be less than < 2% and was thus considered as negligible.

Silicon isotope ratios were determined using a Thermo Scientific Neptune® MC-ICP-MS either at the Observatoire Midi Pyrenées / Laboratorie Géosciences Environnement Toulouse (GET), France, or the GeoForschungsZentrum (GFZ) in Potsdam, Germany. Measurements were performed in medium resolution under either wet plasma (GET) or dry plasma (GFZ) conditions. The wet plasma samples were introduced with a Thermo SIS system with a double-pass cyclonic spray chamber. An ESI ApexHF desolvator (having sample path made of Perfluoroalkoxy alkane, PFA) and fitted with a PFA nebulizer was used for dry plasma conditions at the GFZ (Schuessler and von Blanckenburg, 2014). The instrumental mass bias drift was corrected using the sample standard bracketing technique relative to NBS-28 (NIST SRM 8546), combined with Mg doping as an internal standard in all measured samples and standards. Measurements of $^{25}Mg/^{24}Mg$ ratios were performed in the dynamic mode, alternating between Si and Mg isotopes. Russell's exponential law

(Russell et al., 1978) was then used to correct for the mass bias drift. The accuracy and precision of the isotopic analysis were validated by repeated measurement of the BHVO-2 reference material. They yielded a long-term reproducibility of $\delta^{30}Si$= -0.26 ± 0.13 ‰ for the GET analyses (2 S.D, n=59) and $\delta^{30}Si$= -0.28 ± 0.09 ‰ for the GFZ analyses (2 S.D, n=18), which are in close agreement with data from previous studies (e.g. Abraham et al., 2008; Zambardi and Poitrasson, 2011; Savage et al., 2013, 2014).

3.4. Results

3.4.1. Attainment of fluid-amorphous SiO_2 equilibrium during the fluid equilibration

Each experimental series began by equilibrating the initial Si-free fluids with the pre-treated amorphous SiO_2. The temporal evolution of dissolved Si concentration and pH in these fluids are provided in Table A of the electronic supplement (Annex I); the Si concentrations are also shown in Fig. 4.

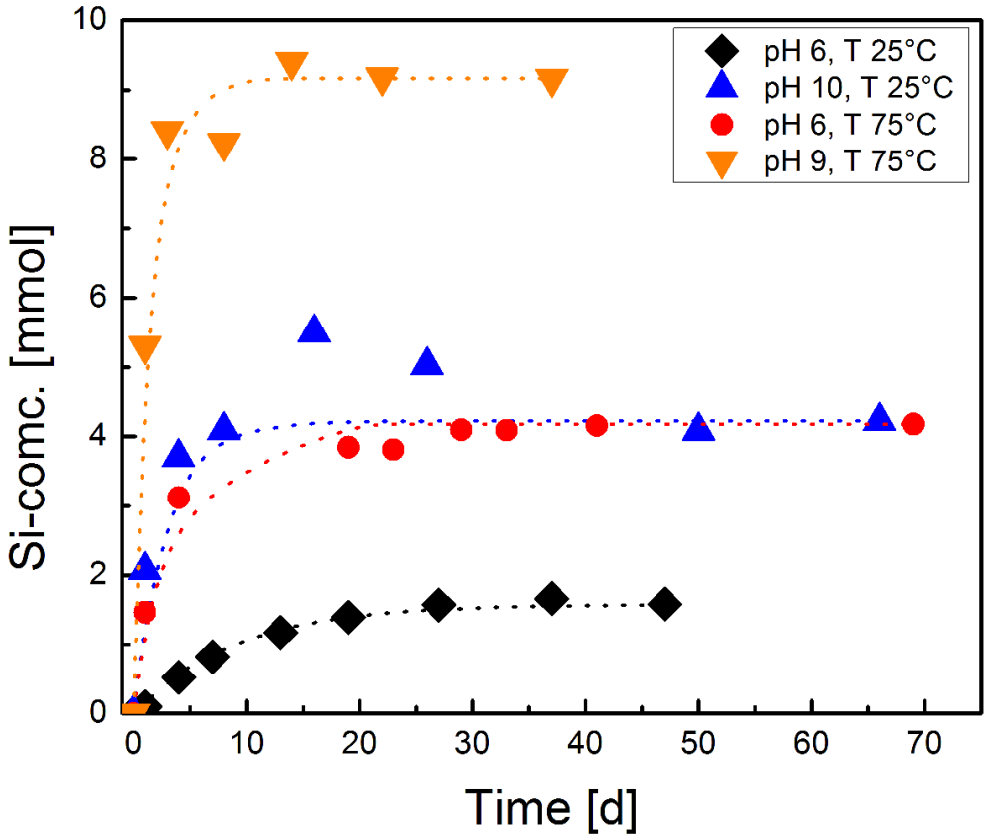

Figure 3.4 - Temporal evolution of dissolved Si concentration during the equilibration of the initial reactive fluids with amorphous silica during the first stage of each experimental series. The dashed lines represent a fit of the data using Eqn. 7 with values of rate constant k'- listed in Table 3.

The Si concentration of the pH 6 initial fluids at both 25° and 75°, and the pH 9.1 fluid at 75°C systematically increase to a constant maximum value. In contrast, the dissolved Si concentrations of the pH 10 and 25°C experiment first maximizes then decreases to a final constant value. The constant final Si concentrations were within 10 % of those calculated to be in equilibrium of amorphous SiO_2 using PHREEQC. The curve drawn through these measured Si concentrations correspond to a fit of these data to Eqn. (3.7); the rate constants obtained by this regression are provided in Table 3.3.

Table 3.3 - Concentration of aqueous Si in equilibrium with amorphous silica and dissolution rate constants obtained from the first stage of the four experimental series run in this study.

Exp.	Si-conc.$_{equilibrium}$ [mmol]	k'- [1/s]	k_+ [mol/(m²*s)]
SibA	1.6	1.36×10^{-6}	3.13×10^{-12}
SicB	4.2	4.63×10^{-6}	2.85×10^{-11}
Sig75A	4.2	4.05×10^{-6}	2.47×10^{-11}
Sik75B	9.2	9.26×10^{-6}	1.24×10^{-10}

3.4.2. Results of Isotope exchange experiments

3.4.2.1. Observations on the solid phases

SEM and TEM images of amorphous SiO_2 collected from the longest duration experiment run of each experimental series were obtained; representative images are provided in Fig. 3.3 C and D. These images show that these final solids contain only amorphous SiO_2, and are identical in appearance to the pre-experiment, pre-treated solids.

A summary of the various measured characteristics of the solids collected after the longest duration experiment of each series is provided in Table B of the electronic supplement (Annex I). The measured grain sizes of the collected final solids were 20 ± 1 nm (n=85, 2 S.D.), which are identical, within uncertainty, to the corresponding pre-treated solids. The water content of these final solids was measured at 8.4% by TGA, which is identical within uncertainty to that of the original pre-treated solids. Measured BET surface areas of the final reacted powders are somewhat lower than those of the original pre-treated solids; the largest decreases were those of the final pH 6.4, 25°C experiment and the final pH 9.1, 75°C experiment, which exhibited a decrease of ~35%. This could result from Ostwald ripening affecting the silica grains during the runs. Overall the post-experiment

solids, however, appear to have been essentially unchanged by these isotope exchange experiments.

3.4.2.2 Chemical and isotopic evolution of the isotope exchange experiments

The temporal evolution of the pH, the bulk Si composition of the fluids, and the isotopic Si compositions fluids and solids during the second stage of all experimental series are provided in Fig. 3.5. The pH of the fluids remained close to constant during the experimental series other than during series run at pH 9.1 and 75°C, where the pH decreased. This decrease could be due to a loss of NH_4OH through evaporation over time from the reactors. Note that pH variations at alkaline conditions will alter the relative importance of the $H_3SiO_4^-$ versus $H_4SiO_4^0$ species in solution. As such the isotopic compositions of the final fluids of the high pH series were not considered in the determination of equilibrium fractionation factors given below. The dissolved Si concentrations remained close to constant during the pH ~6 experiments, but tended to decrease with time during the higher temperature experiments; this decrease is consistent with the observed decrease in pH, which tends to decrease amorphous silica solubility. The $\delta^{29}Si$ values of the fluids and solids mirror one another; in each case, the $\delta^{29}Si$ value of the ^{29}Si enriched fluid phase decreases rapidly at the beginning of each experimental series, while the $\delta^{29}Si$ value in the corresponding solid increases. Note that $\delta^{29}Si$ of the solids increase far less than the $\delta^{29}Si$ decreases in the fluid phase due to the relative masses of Si in these phases.

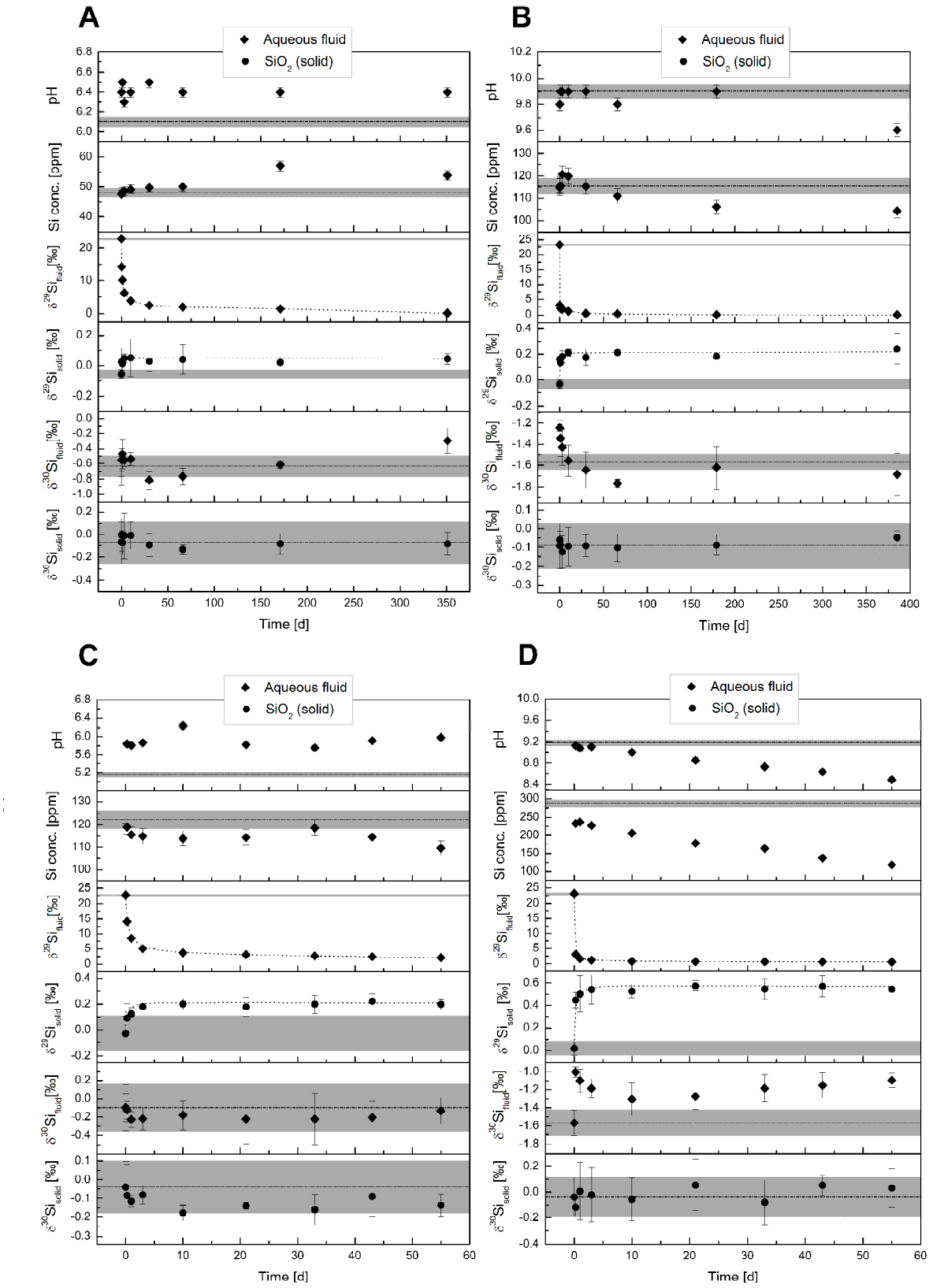

Figure 3.5 - Plots of pH, Si concentrations and isotopic compositions of solid and fluid phases as a function of time during the second stage of each experimental series. The 2 S.D. uncertainties of data points are denoted by the error bars. Initial values are represented by dashed lines with their 2 S.D. error envelope shaded in grey. A) pH= 6.4 at 25 °C, B) pH= 9.9 at 25 °C, C) 5.8 at 75 °C, and D) 9.1 at 75 °C.

3.4.3. Silicon isotope fractionation factors

The equilibrium Si fractionation factors, $\Delta_{eq}{}^{30}Si_{SiO_2,am\text{-}fluid}$, at the conditions of the four experimental series considered in this study were generated with the aid of Fig. 3.6 as described in section 3.2.3. The value of $\Delta_{eq}{}^{30}Si_{SiO_2,am\text{-}fluid}$ was estimated from the extrapolation to F = 1 of the solid lines drawn though the isotopic data shown in these figures. This fit was aided by the fact that these isotopic exchange reactions approached close to isotopic equilibrium in each experimental series. A close correspondence can be seen between the isotopic data and these fits. The values of $\Delta_{eq}{}^{30}Si_{SiO_2,am\text{-}fluid}$ obtained from these fits are provided in Table 3.4 and vary with temperature and pH. Note that as mentioned above, the final few measurements of the experimental series performed at pH 9.9 and 25°C, and pH 9.1 and 75°C were excluded from the fit due to pH drift; their exclusion affected negligibly the retrieved values of $\Delta_{eq}{}^{30}Si_{SiO_2,am\text{-}fluid}$. The $\Delta_{eq}{}^{30}Si_{SiO_2,am\text{-}fluid}$ decreases by ~0.4‰ with increasing temperature from 25 to 75°C at pH 6. With increasing pH to ~9, however, the $\Delta_{eq}{}^{30}Si_{SiO_2,am\text{-}fluid}$ increases by 1.0 to 1.2 ‰.

The observed $\Delta_{eq}{}^{30}Si_{SiO_2,am\text{-}fluid}$ variation with pH can be attributed to the dependence of aqueous Si speciation on pH. The speciation of Si in the reactive fluids of each series is provided in Table 3.4. Aqueous Si was present almost exclusively as $H_4SiO_4{}^0$ in the pH ~6 experiments, but as much as 48% of dissolved Si in the pH ~9 experiments was present as the $H_3SiO_4{}^-$ species – see Fig. 3.1. Addition to the major Si species, $H_4SiO_4{}^0$ and $H_3SiO_4{}^-$ in solution, polymeric Si species represent <5 % of total Si speciation and are therefore considered negligible.

Therefore $H_4SiO_4°$ and $H_3SiO_4{}^-$ are assumed to be 100 % of total Si-speciation in solution. Taking account of Eqns. (3.10) – (3.12) and the calculated speciation of Si in the aqueous phase in the experiments, the equilibrium fractionation factors between the species $H_3SiO_4{}^-$ and $H_4SiO_4°$ ($\Delta_{eq}{}^{30}Si_{H_3SiO_4^- - H_4SiO_4^o}$) were determined at both 25° and 75°C. The resulting values are provided in Table 4.

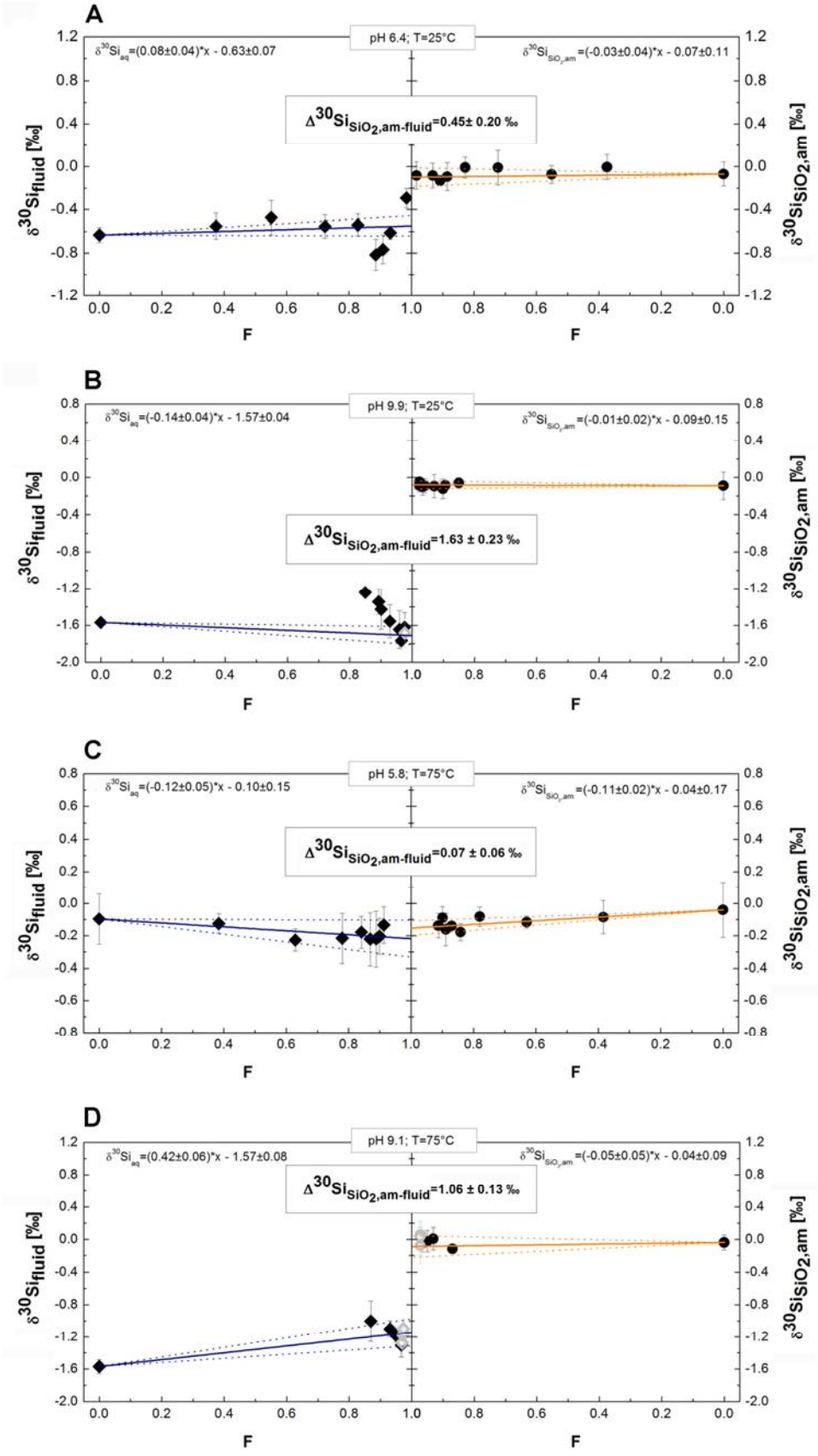

Figure 3.6 - Plots of the isotopic composition of the solid and fluid phases as a function of the degree of isotope exchange during the second stage of each experimental series. A) pH= 6.4 at 25 °C , B) pH= 9.9 at 25 °C, C) 5.8 at 75 °C, and D) 9.1 at 75 °C. Excluded data from the fit are shown by grey symbols – see text.

Table 3.4 - Average aqueous Si-speciation during the second stage of each experimental series run in this study together with the resulting isotopic fractionation factors between solid and solution, solid and the $H_3SiO_4^-$ species, and between $H_3SiO_4^-$.

									Speciation							
Exp	pH	T	Si conc.	$\Delta^{30}Si_{SiO_2,am\text{-}fluid}$	2SD	$\Delta^{30}Si_{SiO_2,am\text{-}H_4SiO_4^0}$	2SD	$\Delta^{30}Si_{SiO_2,am\text{-}H_3SiO_4^-}$	2SD	$H_4SiO_4^0$	$H_3SiO_4^-$	$H_6(H_2SiO_4)_4^{2-}$	$H_2SiO_4^{2-}$	$H_4(H_2SiO_4)_4^{4-}$	$\Delta^{30}Si_{H_3SiO_4^-\text{-}H_4SiO_4^0}$	2SD
		[°C]	[mmol]	[‰]	[‰]	[‰]	[‰]	[‰]	[‰]	[%]	[%]	[%]	[%]	[%]	[‰]	[‰]
SibA	6.37	25	1.8	0.45	0.20	0.45	0.20			99.97	0.03	0.00	0.00	0.00		
SicB	9.84	25	4.0	1.63	0.23			2.79	0.15	47.49	48.20	3.99	0.07	0.25	-2.34	0.13
Sig75A	5.82	75	4.1	0.07	0.06	0.07	0.03			99.97	0.03	0.00	0.00	0.00		
Sik75B	9.11	75	8.5	1.06	0.13			2.28	0.07	54.16	43.78	2.05	0.00	0.01	-2.21	0.05

3.4.4. Isotope exchange kinetics

The rate of attainment of isotopic equilibrium provides insight into the mechanism of isotope exchange. The temporal evolutions of the degree of isotope exchange, *F*, for the four experimental series in this study are shown in Fig 3.7. It can be seen that isotope exchange is relatively rapid during the first 10 days of each experimental series. After 10 days, the exchange reaction slows as the system begins to attain isotopic equilibrium. The curves in this figure were generated using the first order rate law, Eqn. (3.16), to be consistent with the amorphous SiO_2 rate expression provided by Eqn. (3.3) to (3.7).

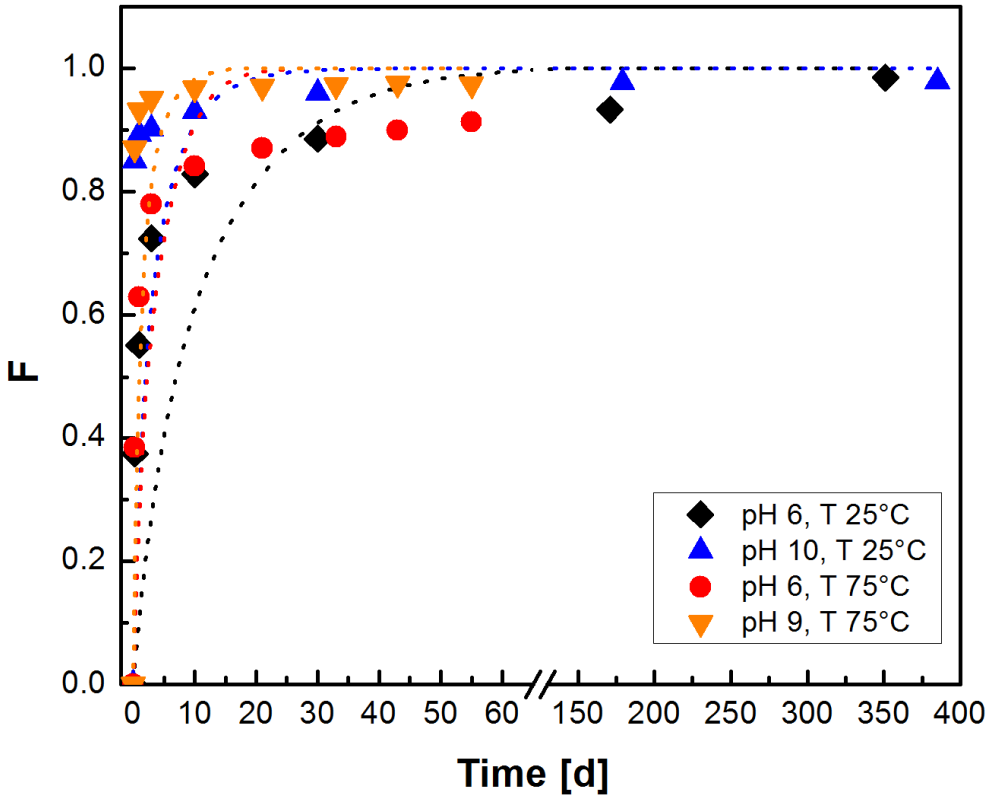

Figure 3.7 - The temporal evolution of the degree of isotopic exchange *F* during the four experimental series run this study. Dashed lines are generated assuming a first order rate law (Eqn. 16), using the dissolution rate constants from the amorphous silica dissolution rate experiments performed as the first stage of each experimental series.

The rate constants used to generate these curves were those retrieved from the amorphous silica dissolution rate experiments run at the beginning of each series – see above and Table 3.3. It can be seen that the initial isotopic exchange rates shown in Table 3.5 are similar to- if not faster than- those of the bulk amorphous silica dissolution rates obtained from the first stage of each experimental series. As isotopic equilibrium is approached, these isotope exchange rates become slow relative to that calculated from the bulk amorphous silica dissolution rates.

Table 3.5 Initial isotopic exchange rates, calculated from the first 10 days of isotope exchange based on a first order rate law. Included in this table are values of k_{exch}, where $k_{exch}=k_1 C_{Si,eq}/(S/M)$, where $C_{Si,eq}$ refers to the total aqueous Si concentration in the fluid, k_{exch} are directly comparable to k_+ in Table 3.3.

		initial exchange	
Exp.	Si-conc. [mmol]	k_{exch} [1/s]	k_{exch} [mol/(m²*s)]
SibA	9.0	2.36 x 10^{-6}	6.64 x10^{-13}
SicB	20.3	3.08 x 10^{-6}	2.71 x10^{-12}
Sig75A	16.5	6.50 x 10^{-6}	3.63 x10^{-12}
Sik75B	42.7	1.40 x 10^{-5}	2.20 x10^{-11}

3.5. Discussion

3.5.1. Silicon isotope fractionation between amorphous silica and aqueous solution

The equilibrium isotopic fractionation factors between amorphous silica (SiO_2•0.32 H_2O) and aqueous solutions determined in this study at 25°C and pH 6.4 is $\Delta_{eq}{}^{30}Si_{SiO_2 am\text{-}fluid}$= 0.45 ± 0.20 ‰. This value is identical, within uncertainty with those of Roerdink et al. (2015), who reported a $\Delta_{eq}{}^{30}Si_{SiO_2 am\text{-}fluid}$ of 0.0 ± 1.1 ‰ at 20 °C and 0.5 ± 0.6‰ at 35 °C for this system. Note that these former values were obtained at a pH of 8.5 from amorphous silica precipitation experiments using a surface kinetic model to correct for the effect of precipitation kinetics. Oelze et al. (2014) proposed a $\Delta_{eq}{}^{30}Si_{SiO_2 am\text{-}fluid}$ of -0.3 ‰ from experiments measuring the adsorption of silica onto gibbsite, and Oelze et al. (2015) proposed a $\Delta_{eq}{}^{30}Si_{SiO_2 am\text{-}fluid}$ of around 0 ‰ based on amorphous silica precipitation experiments in the presence and absence of Al. The results of the present study, performed using the three-isotope method, which thereby verifies the attainment of isotopic equilibrium in the amorphous silica - aqueous solution system validates the results of these former studies. The three-isotope method was also adopted by Zheng et al. (2016) to assess the Si equilibrium fractionation factor between a Fe(III)-Si gel and an aqueous solution at pH 8. These authors report an equilibrium fractionation factor, $\Delta_{eq}{}^{30}Si_{SiO_2 am\text{-}fluid}$ of -2.3 ± 0.23 ‰. The differences between this result and those reported in the present study are likely attributable to the substantial presence of Fe(III) in the solid phase ($X_{Fe(III)}/X_{Si}$ = 0.5).

Many studies have shown that the absolute values of isotopic fractionation decreases as temperature increases (e.g. Urey, 1947; Bigeleisen, 1965; Schauble, 2004; Shahar et al.,

2011; Huang et al., 2014). Such is also the case in the present study. At pH ~6 the $\Delta_{eq}{}^{30}Si_{SiO_2,am\text{-}fluid}$ decreases from 0.45 ± 0.20 ‰ to 0.07 ± 0.06 ‰ as temperature increases from 25 to 75 °C. Similarly, the $\Delta_{eq}{}^{30}Si_{SiO_2,am\text{-}fluid}$ decreases from 1.63 ± 0.23 ‰ to 1.06 ± 0.13 ‰ at pH between 9.1 and 9.9.

3.5.2. Isotope fractionation among Si aqueous species

The combination of fluid speciation and measured equilibrium fractionation factors at two different pH allowed the determination of the equilibrium fractionation among amorphous silica, and the $H_4SiO_4^0$ and $H_3SiO_4^-$ aqueous species. These distinct equilibrium fractionation factors among these species can be represented as $\Delta_{eq}{}^{30}Si_{SiO_2,am\text{-}H_4SiO_4^o}$, $\Delta_{eq}{}^{30}Si_{SiO_2,am\text{-}H_3SiO_4^-}$, and $\Delta_{eq}{}^{30}Si_{H_3SiO_4^- \text{-} H_4SiO_4^0}$, and are listed in Table 3.4. Dupuis et al. (2015) estimated $\Delta_{eq}{}^{30}Si_{quartz\text{-}\ H_4SiO_4^o}$ from *ab initio* calculations, obtaining 2.1± 0.20 ‰ for 25°C, which is somewhat higher than that obtained between amorphous silica and this aqueous species in the present study. These differences can be explained by the different structures of the solids. Quartz, with its continuous framework of SiO_4 tetrahedra, has an ordered structure, which is not the case of the partially hydrated amorphous silica used in this study. Therefore, the structural gap between quartz and aqueous $H_4SiO_4^0$ is more important than between amorphous silica and aqueous $H_4SiO_4^0$. As such, quartz is expected to be enriched in ^{30}Si compared to amorphous silica.

The equilibrium Si isotope fractionation factor among the two major Si bearing aqueous Si species, $\Delta_{eq}{}^{30}Si_{\ H_3SiO_4^- \text{-}\ H_4SiO_4^o}$ were found in the present study to be -2.34 ± 0.13 ‰ and -2.21 ± 0.05 ‰ at 25° and 75°C, respectively. These values can be directly compared to the corresponding values determined using *ab initio* calculations. Dupuis et al. (2015) reported that at 25°C, $\Delta_{eq}{}^{30}Si_{\ H_3SiO_4^- \text{-}\ H_4SiO_4^o}$ is -1.6 ± 0.30 ‰. In contrast, Fujii et al. (2015) reported that at 25°C, $\Delta_{eq}{}^{30}Si_{\ H_3SiO_4^- \text{-}\ H_4SiO_4^o}$ is -3 ‰. The value generated in the present study falls between these calculated values.

The equilibrium Si isotope fractionation factor among the two major Si bearing aqueous species determined in the present study can also be compared to that measured by Fujii et al. (2015); this previous experimental study measured a 25°C $\Delta_{eq}{}^{30}Si_{\ H_3SiO_4^- \text{-}\ H_4SiO_4^o}$ equal to -3.5 ‰. The Fujii et al. (2015) study, however, took a different approach to determine this equilibrium fractionation factor than that of the present study. Their method

relied on the purification of a Na_2SiO_4 solution at pH 9.4 by column chromatography using an anionic resin. The two dominant Si aqueous species were collected in different elutions. These elutions were then measured for their Si isotopic compositions. This approach allows running experiments at much lower Si concentrations than those of the present study since there is no need for the solutions to be in equilibrium with a solid Si-bearing phase. Note that at amorphous silica-aqueous fluid equilibrium at pH >9 there is a possibility of the formation of minor amounts of polynuclear Si bearing aqueous species (Dietzel, 2000) that could affect the measured equilibrium isotopic fractionation between amorphous silica and its coexisting aqueous fluid. The method used by Fuji et al. (2015) however, does not verify that isotopic equilibrium is attained. Additionally, undefined fractionation may have occurred during the column separation by sorption of Si on the anionic resin (Fuji et al., 2015).

3.5.3. Kinetics of Si isotope exchange

The first part of each experimental series began by dissolving amorphous SiO_2 to equilibrium with an aqueous solution. The dissolution rates of these experiments were retrieved by fitting these data to the transition state rate equations (3.4) to (3.7). The rates, reported in Table 3.3, range from 3.13 x 10^{-12} to 1.24 x 10^{-10} mol/m^2/s; these rates increase with increasing temperature and increasing pH. The rates are similar to the dissolution rates of quartz obtained at corresponding temperature and pH conditions by Brady and Walther (1989), Berger et al. (1994), and Icenhower and Dove, (2000); these past reported values ranged from 10^{-12} to 10^{-13} mol/m²/s. Our values are also similar to the amorphous silica and the phytoliths dissolution rates at 25°C and pH 5 of 10^{-12} and 3×10^{-12} mol/m²/s reported by Plettnick et al. (1994) and Fraysse et al. (2006), respectively. In contrast, our rates are substantially slower than that of amorphous silica nanoparticles at 25°C and pH 7 reported by Diedrich et al. (2012).

The rates of isotopic equilibration provide some insight into the process controlling isotopic equilibration. The variation of the degree of isotopic exchange (F) is plotted at a function of time in Fig 3.7. The curves through the data points in this figure were generated using the first order rate equation (Eqn. 3.16), to be consistent with the bulk dissolution rate equation. The rate constants used for these calculations were obtained from the dissolution of the amorphous silica during the first stage of each experimental series. It can be seen in this figure that the curves are close to, but somewhat lower than the F values during the first 10 days of reaction, when isotope exchange has progressed to 80-95%. The isotope

exchange rates tend to slow down relative to that estimated using the corresponding bulk amorphous silica dissolution rates as the systems approach isotopic equilibrium. This behaviour suggests that the dominant rate-controlling mechanism of isotope equilibration in the present study over the first 10 to 20 days is the detachment and reattachment of material to the amorphous silica surface. If this is the case, it would imply that Si transport within the amorphous silica grains in this study is relatively fast compared to the rate of detachment and attachment of SiO_2 at the surface for the bulk of the isotopic exchange process. This faster rate is likely due to the relatively small grain size of the amorphous SiO_2 used in the experiments; the average grain size of these particles was 21 ± 5 nm. Based on the unit cell dimension of quartz, which is ~ 5Å (Danielsson et al., 1976), it is likely that these grains are no more than ~40 unit cells across. In addition, the presence of water in the amorphous silica structure may facilitate the diffusive transport of Si into and out of these grains. Only after isotopic exchange has attained 80 to 90% of their equilibrium values do these exchange rates slow compared to bulk amorphous silica dissolution rates. This may indicate that the final equilibration of the isotope exchange reaction is becoming transport-limited near the end of each experimental series. Nevertheless, all experimental series performed in this study approached isotopic equilibrium within the 55 to 360 days of each experimental series. If the rapid rate of the total Si isotopic equilibration as observed here is also the case in natural ambient temperature systems, the preservation of original Si isotopic signatures in natural fine grained amorphous SiO_2 materials may be rare.

3.5.4. Can Si fractionation be used as a paleo pH and temperature proxy?

Fujii et al. (2015) proposed the use of Si isotope fractionation as a proxy of seawater paleo-pH due to the pH-dependent concentration of the $H_3SiO_4^-$ and $H_4SiO_4°$ species and the consequent variation of solid-aqueous fluid fractionation factors with pH. Seawater however has a pH of ~8 and thus mainly $H_4SiO_4°$ will be present. As such, Si isotopes may be more useful for determining pH in more alkaline environments. Numerous such environments can be found in nature, for example alkaline lakes (e.g. Mono lake, California USA) or in mafic/ultramafic rocks. The results of this study confirm the possibility of using Si isotopic signatures in precipitated minerals as pH proxies of natural waters and provides the equilibrium Si isotope fractionation factors between amorphous SiO_2, the dominant SiO_2 phase precipitating at ambient conditions with its coexisting aqueous solution at different pH. The variation of amorphous SiO_2 – aqueous fluid fractionation factors determined as a function of pH at 25° and 75°C using the equilibrium fractionation factors from this study

are provided in Fig 3.8. Although the variation of this fractionation factor with pH is substantially smaller than that of boron (Zeebe, 2005; Klochko et al., 2006; Noireaux et al., 2015), as the Si does not change its coordination in inorganic systems, it has the advantage of a simpler and better-defined aqueous and solid speciation, potentially making it a more precise tool for constraining paleo-pH values. Note, however, that the experiments presented in this study suggest that small (~20 nm) amorphous silica grains can rapidly equilibrate with its co-existing aqueous fluid in the laboratory. As such further work should be made on the kinetics of isotopic exchange as a function solid grain size, to assess the degree to which the Si isotope signatures of precipitated amorphous SiO_2 are preserved over geologic timeframes.

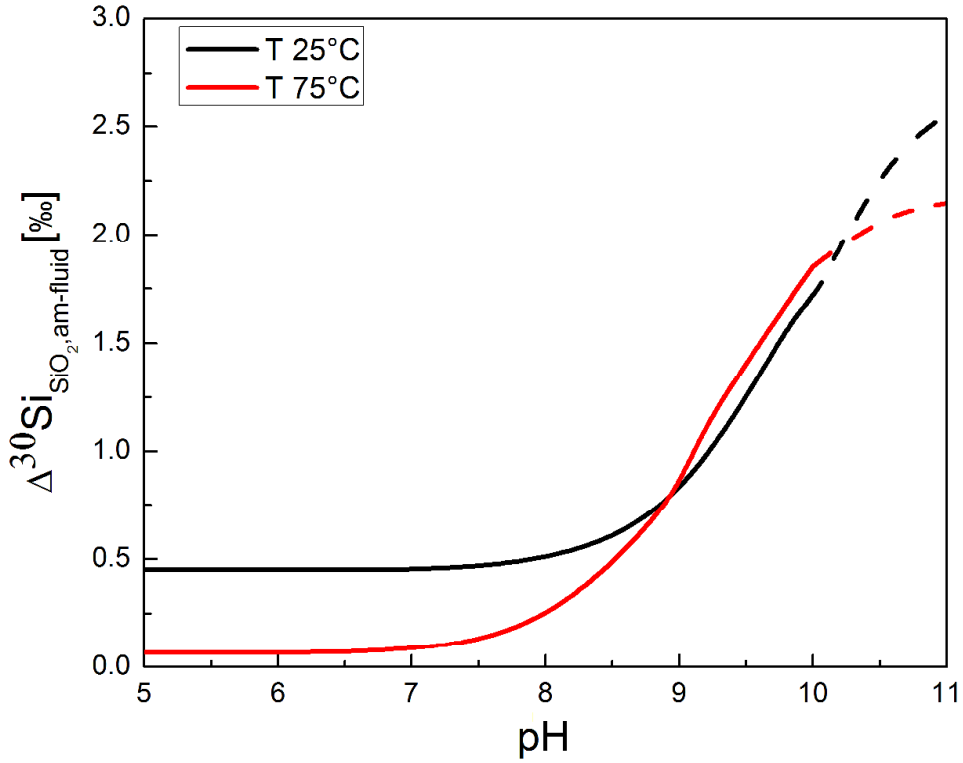

Figure 3.8 - Si equilibrium fractionation factors between amorphous silica and the fluid at 25°C and 75°C as a function of pH calculated using the Si equilibrium fractionation factors derived in the present study together with the aqueous speciation of Si shown in Fig 3.1. The curves in this figure are dashed at elevated pH as this calculation does not take into account polyatomic Si aqueous complexes, which may become important at these conditions.

The data obtained in this study not only show a distinct Si isotopic fractionation depending on solution pH, but also on solution temperature. The equilibrium Si isotope fractionation factor between amorphous SiO_2 and $H_4SiO_4°$ at 75°C is significantly lower than that at ambient temperature. Si isotopic fraction becomes more important at lower temperatures. In Fig. 3.9, the equilibrium isotope fractionation factors of the present study at neutral pH are

extrapolated to 0 °C, showing that a fractionation of ~0.9 ‰ can be expected at this temperature. This conclusion is supported by the *ab initio* calculations of Dupuis et al. (2015) shown in Fig. 3.9, exhibiting a much stronger fractionation factor between quartz and $H_4SiO_4°$ as temperature decreases. This relatively large low temperature fractionation factor might explain the low $\delta^{30}Si$ signatures found in Banded Iron Formations (BIFS, Chakrabarti et al., 2012) or the $\delta^{30}Si$ variation of Archean cherts (Marin-Carbonne et al., 2012).

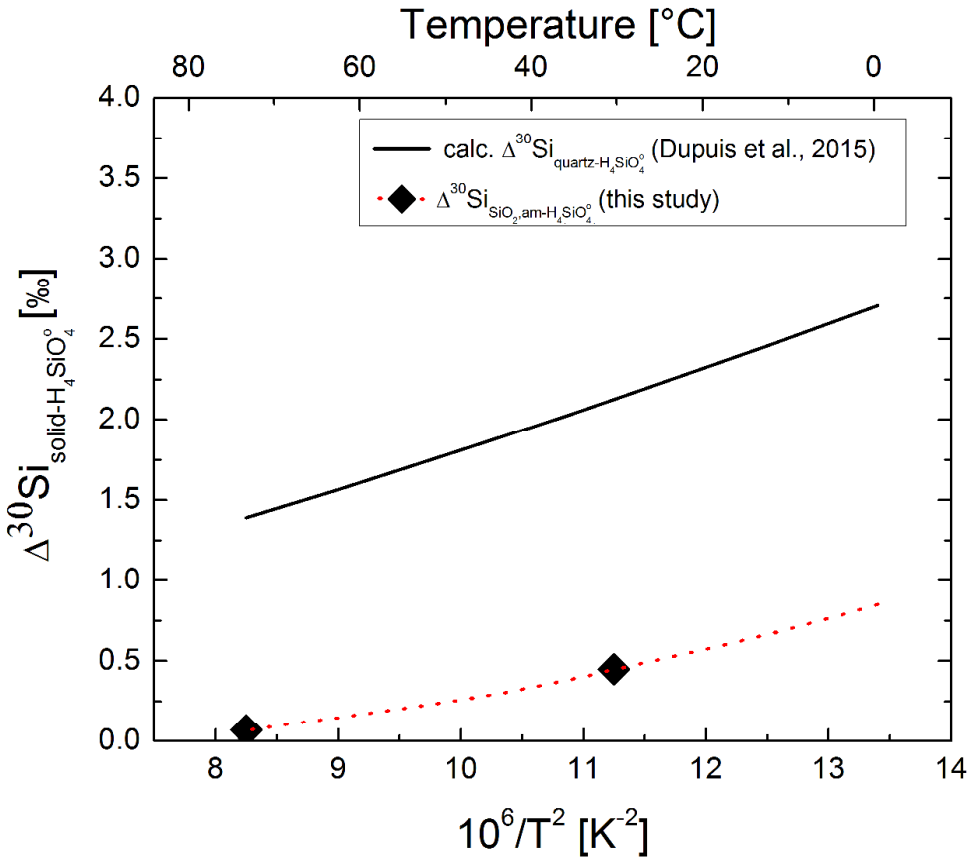

Figure 3.9 - Si equilibrium fractionation factors between quartz (Dupuis et al., 2015) and amorphous silica and H4SiO4o (this study) as a function of temperature. Red dotted describes extrapolated values.

3.6. Conclusion

The results presented in this study confirm the significance of aqueous silica speciation on equilibrium isotope fractionation between fluids and Si-bearing solids. The equilibrium fractionation factor between amorphous SiO_2 and its co-existing aqueous solution $\Delta_{eq}{}^{30}Si_{SiO_2,am\text{-}fluid}$ at 25°C is 0.45 ± 0.20 ‰ at pH 6 and 1.63 ± 0.23 ‰ at pH 9.9. Using these values and the distribution of the species in the aqueous solution, an equilibrium isotope fractionation value between $H_3SiO_4^-$ and $H_4SiO_4°$, $\Delta_{eq}{}^{30}Si_{H_3SiO_4^- - H_4SiO_4^o}$ = -2.34 ± 0.13 ‰ at 25°C was obtained. Such results suggest the possible use of the Si isotope signatures of precipitated Si bearing minerals as a paleo pH proxy. Furthermore the Si isotopic fractionation between amorphous silica and coexisting fluid decreases with increasing temperature, for example from 0.45 ± 0.20 ‰ at 25°C to 0.07 ± 0.06 ‰ at 75°C and pH 6. It follows that the Si isotopic compositions of precipitated minerals may provide insight into the temperature of their formation.

This study also further validates the use of the three-isotope method as an effective means to determine both the rates of isotope exchange and equilibrium isotope fractionation factors. Such equilibrium fractionation factors facilitate greatly the interpretation of natural isotope signatures. Moreover the rates of isotope exchange rates determined by this approach may provide new insight into both the mechanism of isotope exchange and the conditions at which mineral isotopic signatures are best preserved in natural systems.

Chapter 4

Extreme silicon isotope fractionation between silicic acid and aqueous organosilicon complexes: Implication for silica biomineralization

A version of this chapter will be submitted for publication as: “Franziska M. Stamm, Merlin Méheut, Thomas Zambardi, Jérôme Chmeleff, Jacques Schott, Eric H. Oelkers: Extreme silicon isotope fractionation between silicic acid and aqueous organiosilicon somplexes: Implication for silica biomineralization”

Abstract

Silicon plays a key role in the geological and biological cycles at the Earth surface. In aqueous fluids, silicon occurs mainly as 4-coordinated silicic acid ($H_4SiO_4^o$). However, it takes a 5 or 6 fold coordination when it reacts with organic ligands like diphenol and polyalcohols to form aqueous organosilicon complexes. Investigating the impact of such organic complexes and thus the impact of the change in Si coordination on its Si isotopic fractionation is crucial to understand the biochemical cycle of Si. Towards the improved understanding of the effect of aqueous organic complexing on the Si isotopic signatures recorded in natural (bio)minerals, isotope exchange experiments were performed at bulk chemical equilibrium between amorphous silica and aqueous fluids containing 0.05 mol/kg and 0.08 mol/kg of catechol ($C_6H_4(OH)_2$) at pH ~8.8 and 25°C. At these catechol concentrations, 85-90% of aqueous silicon is present as 6-fold Si-catecholate complexes involving 5-membered rings configurations. The equilibrium Si isotope fractionation, $\Delta_{eq}^{30}Si$, between Si-catecholate complexes and amorphous silica and silicic acid were quantified using the three-isotope method and found to be $\Delta^{30}Si_{Si\text{-}Cate\text{-}SiO_2,am}$ = -19.50 ± 0.97 ‰ and $\Delta^{30}{}_{SiSicatechol\text{-}H_4SiO_4^\circ}$ = -19.05 ± 0.49 ‰, respectively. These experimental values are in close agreement with *ab initio* calculations performed using density functional theory (DFT) method, which predicts an equilibrium fractionation factor of -21.03 ‰ and -18.91 ‰ between aqueous Si catecholate complexes and quartz and aqueous $H_4SiO_4°$, respectively. The results of this study indicate that the complexation of Si by those organic ligands, which change the coordination of aqueous Si, can lead to extreme equilibrium Si isotope fractionation between aqueous fluids and solid phases. Such results can therefore be used to improve our ability to interpret the Si isotope compositions of natural solids, and in particular those associated with marine silica biomineralization processes (e.g. sponge spicules).

4.1. Introduction

Silicon (Si) is a major element in the Earth's crust and thus in biological systems. There are various biogenic uses of Si. In marine environments, Si is used by phytoplankton, zooplankton and sponges in the form of opal to form frustules, tests or spicules (e.g. De La Rocha et al., 1998; Kubicki and Heaney, 2003; Hendry et al., 2011; Poitrasson, 2017), in plants Si occurs mostly as phytoliths, which are responsible for structural stability and defensive mechanisms (e.g. Kubicki and Heaney, 2003; Ding et al., 2005; Sun et al., 2008; Delvigne et al., 2009; Poitrasson, 2017). In higher organisms, such as animals or humans Si is used for bone or tissue formation (e.g. Birchall, 1995; Jugdaohsingh et al., 2015). The fractionation of Si during such biomineralization processes can be significant with δ^{30}Si reported values ranging between +3 and -6.5 ‰ (Poitrasson, 2017). In general, biogenic solid phases prefer the uptake of light Si isotopes (De La Rocha et al., 1998; De La Rocha, 2003; Ding et al., 2005; Basile-Doelsch et al., 2005; Basile-Doelsch, 2006; Opfergelt et al., 2006; Sun et al., 2008; Wille et al., 2010; Hendry et al., 2011; Hendry and Robinson, 2012; Poitrasson, 2017). In marine environments, the strongest Si isotopic fractionation of -6.02 ‰ has been observed in sponges (Wille et al., 2010). The processes and mechanisms controlling these observed fractionations are not yet fully understood (Kinrade et al., 2002; Kubicki and Heaney, 2003; Poitrasson, 2017).

Dissolved Si can form strong aqueous complexes with a number of organic ligands including polyols, saccharides, phenols, pyridine and tropolones (Rosenheim et al., 1931; Weiss and Harvey, 1964; Cella et al., 1980; Sjöberg et al., 1985; Sedeh et al., 1992, 1993; Pokrovski and Schott, 1998; Kinrade, 1999; Kinrade et al., 2001a, 2001b, 2002; Kinrade and Swaddle, 2002; Benner et al., 2003; Kinrade et al., 2003; Kubicki and Heaney, 2003; Peloquin and Schmedake, 2016; Wang et al., 2016). Such complex formation alters the coordination environment of aqueous Si and thus has an impact on its aqueous-mineral fractionation factor, as has been demonstrated for a large number of stable isotopes (Wiederhold et al., 2006; Domagal-Goldman and Kubicki, 2008; Klochko et al., 2009; Li et al., 2014; Pokrovsky et al., 2014; Noireaux et al., 2015; Schott et al., 2016; Saldi et al., 2018).

Past studies based on Nuclear Magnetic Resonance (NMR) have shown that Si, which usually occurs as the four-coordinated silicic acid ($H_4SiO_4^o$) complex in aqueous solution can form five- and six-coordinated complexes in the presence of organic ligands such as phenols and polyols (Cella et al., 1980; Sjöberg et al., 1985; Kinrade et al., 2001b,

2002; Kinrade and Swaddle, 2002; Wang et al., 2016). Furthermore, the direct evidence of a six-coordinated organosilicon compound formed *in-vivo* has been provided by the ^{29}Si nuclear resonance study of the fresh water diatom *Navicula pelliculosa* (Kinrade et al., 2002). Such coordination changes can significantly alter Si isotope fractionation during fluid-(bio)mineral interaction as suggested by Kubicki and Heaney (2003).

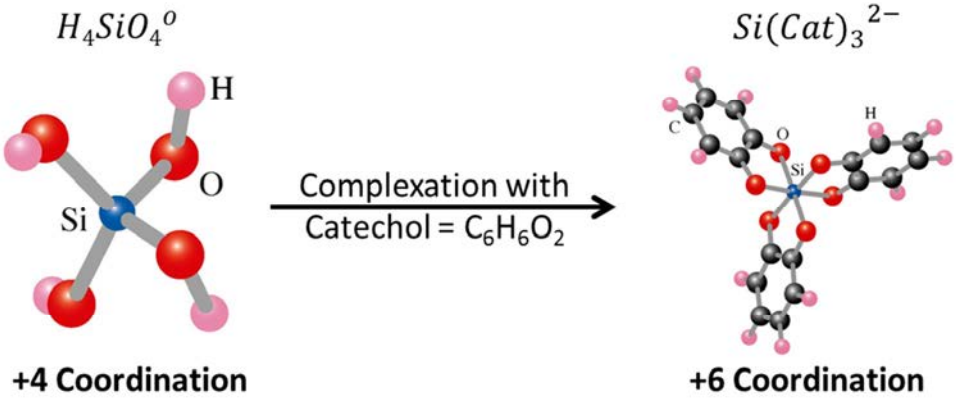

Figure 4.1 - Si coordination of $H_4SiO_4^o$ aqueous species and when it complexes to catechol

The objective of this study is to investigate the effect of aqueous organic Si complexation on equilibrium Si isotope fractionation in water-rock systems. This study used catechol ($C_6H_4(OH)_2$) as a representative aqueous organic ligand because it readily binds to Si (Rosenheim et al., 1931; Barnum, 1970; Pokrovski and Schott, 1998; Gulley-Stahl et al., 2010) and changes the usual 4 coordinated aqueous Si to a hexacoordinated complex with a 6-membered ring structure (Fig. 4.1; Rosenheim et al., 1931; Sjöberg et al., 1985; Sedeh et al., 1992, 1993; Kinrade, 1999). To determine the equilibrium fractionation factor, this study used the 'three-isotope method'. Experiments were performed at pH ~8.8 and 25°C, with aqueous catechol concentrations of 0.05 M and 0.08 M. The results of these experimental efforts are compared with further *ab initio* calculations performed in this study. The purpose of this paper is to report the results of this combined experimental and theoretical study and to provide a new insights into the effects of aqueous organic complexations on Si isotope equilibrium fractionation in the biosphere and hydrosphere.

4.2. Experimental methods

4.2.1. Starting materials

All experiments were performed using Alpha Aeser® 100 mesh hydrated silicic acid powder. Ultrafine particles were removed from this powder by sedimentation following the procedure of Pokrovski and Schott (1998). Fifty grams of the powder was suspended in >18.2 Ω de-ionized Milli-Q®, water by stirring in a 1dm^3 glass beaker. The solid was sedimented and then decanted. This was repeated until the supernatant became clear within the first 5 min. The powder was subsequently oven dried, and placed into a desiccator while cooling. Scanning electron microscope (SEM) and transmission electron microscope (TEM) images, shown in Fig. 4.2 A and B, were acquired using a MEB JEOL JSM-7800F Prime electron microscope and a JEOL JEM-ARM200F Cold FEG transmission electron microscope, respectively.

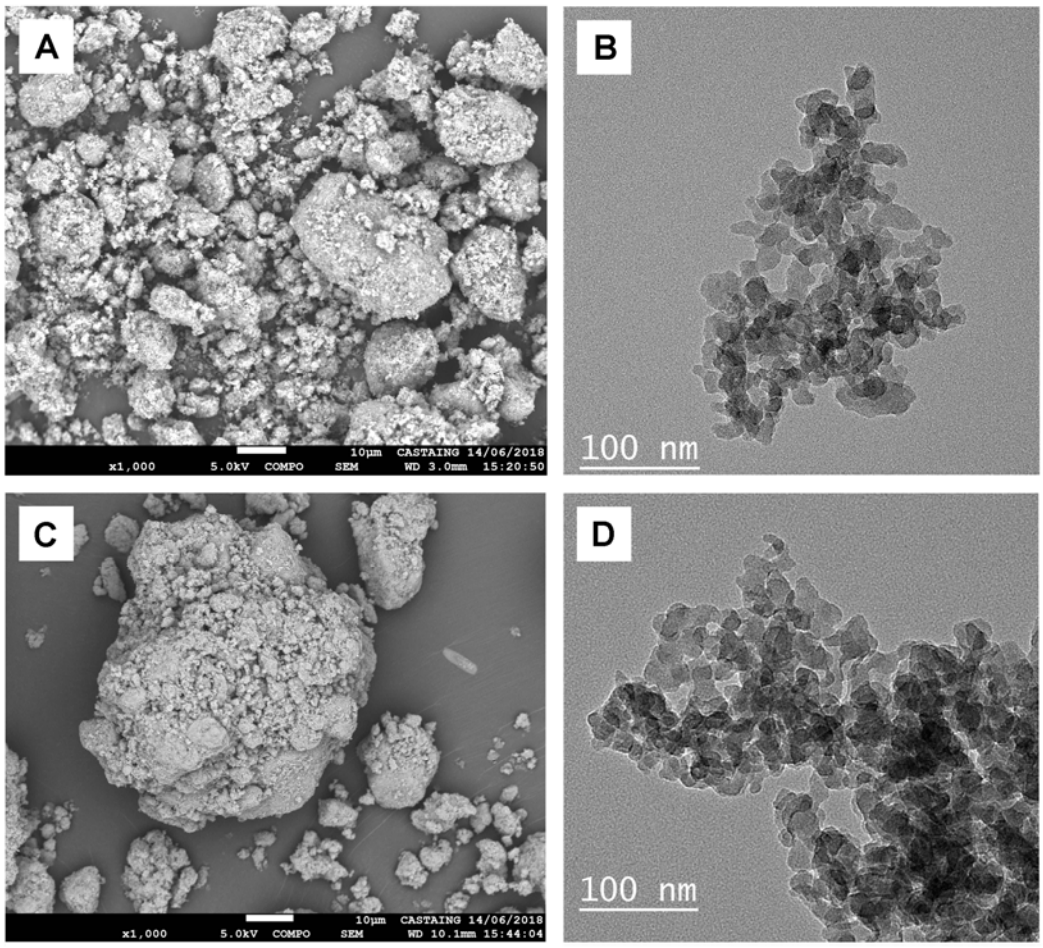

Figure 4.2 - Representative images of amorphous SiO2 powders. A. SEM image of starting powder showing agglomerates of SiO2 grains. B. TEM image of starting powder showing rounded ~ 21 nm SiO2 grains. C. Representative SEM image of reacted silicon powder. D. TEM image with 40 000x magnification of powder reacted at T ~25°C, pH ~6.

The average grain size of the recovered silicic acid powder was 23 ± 10 nm as determined using TEM images and the ImageJ software package (Schindelin et al., 2012). This uncertainty is 2 standard deviation from a mean of 78 measurements. The water content of the powder was determined to be 7.86 % by thermogravimetric analysis using a Mettler Toledo® ATG/DSC1. This is consistent with the chemical formula $SiO_2 \bullet 0.28\ H_2O$. The surface area of the cleaned amorphous SiO_2 powder was determined to be 195.6 m^2/g with an estimated uncertainty of ± 10% using a Quantachrome Autosorb-1MP, together with the nitrogen multipoint BET method (Brunauer et al., 1938).

Two aqueous solutions, one containing 0.05 mol/kg and the other 0.08 mol/kg catechol were prepared by dissolving Merck® pyrocatechol ($C_6H_4(OH)_2$) in a $NH_4Cl - NH_3$ pH-buffer solution. The buffer solution was prepared from de-ionized Milli-Q® water, suprapur Merck® NH_4Cl salt and Merck® 25 % NH_3 solution. In total concentrations of 0.1 mol/kg NH_4Cl and 0.36 mol/kg NH_3 were used to prepare these buffer solutions.

4.2.2. Experimental design

The three-isotope method was used in the present study to determine the equilibrium isotopic fractionation factor between amorphous SiO_2 and the selected aqueous catechol solutions. This method permits evaluation of the degree of isotopic exchange between the solid and its coexisting aqueous solution after adding a ^{29}Si tracer to the aqueous phase. A detailed description of this method is given by previous studies (Matsuhisa et al., 1978; Matthews et al., 1983a, 1983b, 1983c; Shahar et al., 2008; Beard et al., 2010; Li et al., 2011, 2014; Frierdich et al., 2014; Reddy et al., 2015; Zheng et al., 2016; Stamm et al., 2019).

All experiments performed in this study were conducted at bulk chemical equilibrium but isotopic disequilibrium conditions to minimize the potential effect of kinetics on the isotopic fractionation. The experiments were performed within experimental series consisting of two steps.

4.2.2.1. Step 1: Equilibration of the reactive aqueous solutions with amorphous SiO_2

Two experimental series were conducted in this study. One with an aqueous 0.05 mol/kg catechol solution and the other with a 0.08 mol/kg catechol solution as described above. Each solution (200 mL) was first equilibrated with 3 g of washed amorphous SiO_2 powder in a closed polypropylene bottle. The closed bottles were placed in a constantly shaking thermostatic bath at 25°C. The aqueous solutions were regularly sampled over 10 days. The short equilibration period was chosen as catechol decomposes or reacts with ammonia over

time in solution (Rosenheim et al., 1931; Barnum, 1972; Pillar et al., 2015, 2014). The pH and concentration of the solutions were measured immediately after each sampling. Aqueous Si concentration of each sample was determined by colorimetry. When both the measured pH and Si concentrations of the sampled solutions attained a constant value, chemical equilibrium was assumed to be attained. These equilibrated solutions were then filtered with Teflon syringe filters (Merck® 0.2 µm).

4.2.2.2. Step 2: Isotopic exchange experiments

To employ the three-isotope method, the chemical equilibrated solutions were enriched with a ^{29}Si isotope tracer solution having an initial composition of 0.21% ^{28}Si, 99.76% ^{29}Si, and 0.03% ^{30}Si, to obtain starting reactive fluids having a $\delta^{29}Si$ ~23‰ (see Table 4.1). To ensure that these solutions were still at equilibrium with amorphous SiO_2 after adding the spike, the pH and Si concentrations of this spiked solution were measured. The isotope exchange experiments in this study were conducted in series. Each series consisted of 8 individual closed system experiments and lasted 7 days. The short duration of the experiments avoids the decomposition of the aqueous catechol. Moreover by performing individual closed system experiments solids and fluids could be collected and analysed after a selected experiment duration. For the individual experiments, ~0.30 g of pre-washed amorphous SiO_2 powder with a known Si isotope composition was placed in 10 ml polypropylene reactors together with 10 ml of the prepared ^{29}Si enriched aqueous catechol solution. The reactors were wrapped in aluminium foil, to avoid light, and placed in an orbital shaker to be constantly mixed at 25 °C. To verify that the reactors were indeed closed, they were weighted at the beginning and end of each experiment. The experiments were terminated at pre-chosen times. Once an experiment was complete, the reactor was centrifuged for 20 min at 4500 rpm. The supernatant was then separated from the powder and filtered with Merck® 0.2 µm Teflon syringe filters. The pH and Si concentrations of the recovered aqueous solutions were measured immediately after sampling. These solutions were then immediately prepared for column chromatography to avoid any isotopic fractionation during decomposition of the organic ligand. The powders were washed and filtered with de-ionized Milli-Q® water, oven dried at 40°C, then stored prior to Si isotopic analysis.

Table 4.1 - Overview of the results of the isotopic exchange experiments performed in this study. Uncertainties of the isotopic measurements are expressed as 2 SD (Standard Deviation) and 2 SE (Standard Error). The 2 SE is computed following the relation: $\boldsymbol{SE = \frac{SD}{\sqrt{(n-1)}} \times t}$, where *n* denotes the number of measurements performed and *t* denotes the Student t-factor (Platzner et al., 1997). δ_{eq} represents the equilibrium isotopic composition of ^{29}Si and F denotes the degree of isotopic

Exp.	Time	pH	Si-conc.	S_{BET}	*solution*						*amorphous SiO_2*						δ^{29}_{eq}	$F_{sol.}$	ln(1-F)
	[d]		[ppm]	[m^2/g]	δ^{30}Si [‰]	2SD [‰]	2SE [‰]	δ^{29}Si [‰]	2SD [‰]	2SE [‰]	δ^{30}Si [‰]	2SD [‰]	2SE [‰]	δ^{29}Si [‰]	2SD [‰]	2SE [‰]	[‰]		
0.05 M Catechol																	-7.70		
SigC0.05-0	0	8.9	343.2	195.6	***-8.60***	*0.27*	*0.22*	***-4.42***	*0.06*	*0.05*	***-0.04***	*0.20*	*0.09*	***-0.01***	*0.15*	*0.07*			
SigC0.05-0 S	0	8.9	344.6		***-8.40***	*0.32*	*0.26*	***21.31***	*0.14*	*0.11*	***-0.04***	*0.20*	*0.09*	***-0.01***	*0.15*	*0.07*		0.000	0.00
SigC0.05-1	0.13	8.9	299.1		***-10.83***	*0.12*	*0.10*	***7.87***	*0.02*	*0.02*	***-0.02***	*0.04*	*0.05*	***0.56***	*0.05*	*0.06*		0.463	-0.62
SigC0.05-2	0.25	8.9	295.0		***-11.37***	*0.08*	*0.07*	***7.81***	*0.03*	*0.02*	***0.06***	*0.16*	*0.10*	***0.60***	*0.08*	*0.05*		0.466	-0.63
SigC0.05-3	0.5	8.9	321.3		***-11.93***	*0.40*	*0.50*	***9.97***	*0.19*	*0.23*	***0.06***	*0.08*	*0.05*	***0.53***	*0.03*	*0.02*		0.391	-0.50
SigC0.05-4	1	8.8	331.1		***-13.04***	*0.34*	*0.42*	***5.82***	*0.09*	*0.11*	***0.17***	*0.16*	*0.10*	***0.72***	*0.07*	*0.05*		0.534	-0.76
SigC0.05-5	1.5	8.9	314.0		***-13.55***	*0.20*	*0.24*	***5.51***	*0.06*	*0.07*	***0.21***	*0.13*	*0.16*	***0.70***	*0.03*	*0.03*		0.545	-0.79
SigC0.05-6	3	8.8	314.8		***-14.17***	*0.29*	*0.36*	***3.00***	*0.13*	*0.17*	***0.13***	*0.06*	*0.07*	***0.86***	*0.03*	*0.04*		0.631	-1.00
SigC0.05-7	5	8.9	318.3		***-14.20***	*0.05*	*0.06*	***2.04***	*0.03*	*0.04*	***0.12***	*0.02*	*0.03*	***0.89***	*0.10*	*0.12*		0.664	-1.09
SigC0.05-8	7	8.8	293.0	174.7	***-14.20***	*0.31*	*0.39*	***1.37***	*0.08*	*0.09*	***0.15***	*0.16*	*0.10*	***0.90***	*0.03*	*0.02*		0.688	-1.16
0.08 M Catechol																	-7.53		
SiC 0.08 0	0	8.9	612.1	195.6	***-5.73***	*0.24*	*0.19*	***-2.90***	*0.06*	*0.05*	***-0.04***	*0.20*	*0.09*	***-0.01***	*0.15*	*0.07*			
SiC 0.08 0 S	0	8.9	599.3		***-5.70***	*0.15*	*0.12*	***22.92***	*0.02*	*0.02*	***-0.04***	*0.20*	*0.09*	***-0.01***	*0.15*	*0.07*		0.000	0.00
SiC 0.08 1	0.13	8.8	565.0		***-7.86***	*0.17*	*0.13*	***11.28***	*0.09*	*0.07*	***0.06***	*0.16*	*0.07*	***0.97***	*0.11*	*0.05*		0.382	-0.48
SiC 0.08 2	0.25	8.8	557.6		***-8.88***	*0.27*	*0.22*	***11.33***	*0.09*	*0.07*	***0.17***	*0.23*	*0.11*	***0.94***	*0.10*	*0.05*		0.381	-0.48
SiC 0.08 3	0.5	8.7	547.3		***-10.21***	*0.23*	*0.19*	***12.80***	*0.15*	*0.12*	***0.21***	*0.22*	*0.10*	***0.78***	*0.11*	*0.05*		0.332	-0.40
SiC 0.08 4	1	8.7	547.6		***-10.97***	*0.14*	*0.11*	***9.57***	*0.06*	*0.05*	***0.28***	*0.09*	*0.04*	***1.04***	*0.07*	*0.03*		0.438	-0.58
SiC 0.08 5	1.5	8.7	535.0		***-11.59***	*0.16*	*0.13*	***9.27***	*0.04*	*0.03*	***0.41***	*0.08*	*0.04*	***1.11***	*0.09*	*0.04*		0.448	-0.59
SiC 0.08 6	3	8.7	540.4		***-12.28***	*0.09*	*0.07*	***7.16***	*0.07*	*0.06*	***0.36***	*0.20*	*0.09*	***1.21***	*0.17*	*0.08*		0.518	-0.73
SiC 0.08 7	5	8.7	533.0		***-12.63***	*0.14*	*0.11*	***6.26***	*0.06*	*0.04*	***0.42***	*0.16*	*0.07*	***1.40***	*0.11*	*0.05*		0.547	-0.79
SiC 0.08 8	7	8.7	496.3	165.6	***-13.04***	*0.03*	*0.02*	***5.41***	*0.08*	*0.06*	***0.45***	*0.09*	*0.05*	***1.39***	*0.06*	*0.03*		0.575	-0.86

4.2.3. Analytical methods

4.2.3.1. Characterization of aqueous solutions

The pH of all aqueous solutions was determined using a Metrohm® 913 pH Meter connected to a standard glass microelectrode. Electrode calibration was performed using certified Orion Thermo Scientific® buffers. The uncertainty of the measurements was determined to be 0.05, and set equal to 2 standard deviations by repeated measurements (n=40) of the pH=4.01 calibration standard.

Aqueous silicon concentrations were determined by the molybdate blue method (Truesdale and LeCorre, 1975) using a Bran & Luebbe® analyser-III colorimeter coupled to a Seal XY-2 autosampler and a Technicon analyser II mixing unit. The measurements ranged from 0.1 to 10 ppm, with a long-term reproducibility within 3% and a quantification limit of 0.04 ppm.

4.2.3.2. Data reporting and Si isotope analysis

Silicon isotope compositions were measured on all aqueous solutions and powders sampled from the isotope exchange experiments, as well as the initial powder, the non-spiked chemical equilibrated solutions, and the spiked initial solutions. The silicon isotope compositions in this study are expressed as the standard δ-notation in per mil (‰) relative to the international NBS-28 standard (NIST RM-8546) in accord with:

$$\delta^{x}\mathrm{Si} = \left[\frac{(\,^{x}\mathrm{Si}/^{28}\mathrm{Si})_{Sample}}{(\,^{x}\mathrm{Si}/^{28}\mathrm{Si})_{NBS-28}} - 1\right] \times 1000 \qquad (4.1)$$

where x denotes the mass of Si, either ^{29}Si or ^{30}Si, and $(\,^{x}\mathrm{Si}/^{28}\mathrm{Si})_{Sample}$ refers to the molar ratio of the Si with mass x to that of mass 28 in the sample.

The fractionation factor between an aqueous solution and a solid ($\alpha^{x/28}_{solution-solid}$) is defined either as

$$\alpha^{x/28}_{solution-solid} = \frac{(\,^{x}\mathrm{Si}/^{28}\mathrm{Si})_{solution}}{(\,^{x}\mathrm{Si}/^{28}\mathrm{Si})_{solid}} \qquad (4.2)$$

or as $\Delta^{x}\mathrm{Si}_{solution-solid}$, which is defined by

$$\Delta^{x}\mathrm{Si}_{solution-solid} = \delta^{x}\mathrm{Si}_{solution} - \delta^{x}\mathrm{Si}_{solid} \qquad (4.3)$$

Note that $\Delta^{x}\mathrm{Si}_{solid-fluid}$ is approximately related to $\alpha^{x/28}_{solution-solid}$ by:

$$\Delta^{x}\mathrm{Si}_{solution-solid} \approx 10^{3} ln\alpha^{x/28}_{solution-solid} \quad (4.4)$$

To determine their isotopic compositions, amorphous SiO_2 powders were prepared by an initial calcination of 1-5 mg of the reacted powder at 500°C (Cornu et al., 1999) and then using the alkali fusion method of Zambardi and Poitrasson (2011), as described in detail by Stamm et al. (2019). The sampled aqueous solutions were prepared by a combination of calcination at 500°C, similar to the approach of Cornu et al. (1999) for soils, and the modified alkali fusion method of Zambardi and Poitrasson (2011). Five ml of aqueous solution was evaporated in silver crucibles (XRF scientific, Montreal, Canada). The remaining Si and organic residue was then calcined by heating the crucibles in a furnace at 500°C for 4h, destroying all remaining organic residue thus leaving only the Si of the solution behind. After cooling, ~200 mg of Merck® NaOH pellets were weighted into these crucibles. The crucibles were capped and placed into a furnace heated at 720°C for 10 min. After cooling to room temperature the crucibles were placed into 30 ml Savillex® Teflon beakers filled with 15 ml Milli-Q® water to dissolve the amorphous SiO_2 powder. The resulting aqueous solutions were transferred after 24 hours into 30 mL polypropylene bottles and diluted with Milli-Q® water to 20 ml and subsequently acidified with ~10 N bi-distilled HCl to a pH of 1.5.

All samples were purified prior to Si isotope analysis by cation exchange chromatography using 2 ml of Bio-Rad® AG50W-12X cationic resin filled into 10 ml Bio-Rad® polypropylene columns. The resin was initially cleaned as described in Georg et al. (2006). After cleaning, 2 ml of the samples were loaded on to the column, directly collected, and eluted twice with 2 ml Milli-Q® water. The collected fluids were then diluted and acidified to obtain a 3 ppm solution and a total HCl concentration of 0.05 mol/kg. The overall Si recovery was determined to be between 90 and 100 %. The ^{28}Si signal of the procedural blank was found to be less than < 3% of the total signal and thus considered negligible.

Silicon isotope ratios were determined using the Thermo Scientific Neptune® MC-ICP-MS located at the Laboratore Géosciences Environnement Toulouse (GET), France. Measurements were performed under wet plasma conditions in medium resolution. A Thermo SIS system was used together with a double-pass cyclonic spray chamber to inject the samples into the spectrometer. Instrumental mass bias drift was corrected using sample-standard bracketing combined with Mg addition as an internal standard. Measurements of

$^{25}Mg/^{24}Mg$ ratios were performed in the dynamic mode. The Russell's exponential law (Russell et al., 1978) was used to further correct for the mass bias drift.

To ensure the accuracy and precision of the isotopic analysis, the BHVO-2 reference material was repeatedly measured during each run. The reproducibility of $\delta^{30}Si$= -0.25 ± 0.16 ‰, and $\delta^{29}Si$= -0.13 ± 0.08 ‰ (2 S.D, n=48) was determined, which is in close agreement with measured BHVO-2 values of previous studies (e.g. Abraham et al., 2008; Zambardi and Poitrasson, 2011; Savage et al., 2013, 2014).

4.3.3. Speciation calculations

All aqueous speciation calculations in this study were performed using the PHREEQC code (Parkhurst and Appelo, 2013) together with its llnl thermodynamic database, with some minor modifications. First the equilibrium constant for the amorphous SiO_2 dissolution reaction reported by Stamm et al. (2019) was included in the llnl database; those values were obtained on the same amorphous SiO_2 powder as used in the present study. Second, the dissociation constants of aqueous catechol from Sillen and Martell (1971) and the formation constant of the Si-catechol complex from Pokrovski and Schott (1998) summarized in Table 4.2 were added to the used llnl database.

Table 4.2 - Summary of dissociation constants added to the PHREEQC llnl database and their reference

Reaction	log K	Source
$SiO_2 + 2\ H_2O \leftrightarrow H_4SiO_4^o$	-2.80	Stamm et al. (2019)
$H_2Cat^o \leftrightarrow HCat^- + H^+$	-9.45	Sillen & Martell (1971)
$H_2Cat^o \leftrightarrow HCat^{2-} + 2\ H^+$	-22.45	Sillen & Martell (1971)
$SiO_2 + 3\ H_2Cat \leftrightarrow SiCat_3^{--} + 2\ H^+ + 2\ H_2O$	-12.00	Pokrovski & Schott (1998)

The equilibrium fractionation factor between the solution and amorphous silica depends on the Si speciation of the solution, and the individual fractionation factors, $\alpha^{x/28}_{i-SiO_2,am}$, of each *i* Si aqueous species with respect to amorphous silica. Therefore, the Si isotopic fractionation factor between the solution and amorphous silica can be expressed as (Zhang et al., 1995):

$$10^3 ln\alpha^{x/28}_{solution-SiO_2,am} = \sum_i (x_i \times 10^3 ln\alpha^{x/28}_{i-SiO_2,am}) \quad (4.5)$$

where x_i refers to the mole fraction of the subscripted Si aqueous species present in solution.

4.4. Ab initio calculations

In this work, we are interested in the equilibrium fractionation of Si isotopes between Si-catechol complexes and amorphous silica or H_4SiO_4. To model the Si-catechol complex, we considered the crystalline structure of $Li_2[Si(cat)_3]$ 3.5 dme (cat = catecholate dianion, dme = dimethoxy ethane CH_3-O-CH_2-CH_2-O-CH_3) synthesized and characterized by Hahn et al. (1995). The modeling of amorphous silica is a difficult task because its structure is not defined. Instead, we considered the cases of SiO_2-quartz and of dissolved H_4SiO_4, which can be seen as two compositional end-members of amorphous silica.

The equilibrium fractionation of silicon isotopes between two phases is obtained by combining the β-factors of both phases. The β-factor corresponds to the isotopic fractionation factor between the phase *A* and a perfect gas of *Si* atoms. This quantity can be computed, within the harmonic approximation, from the vibrational frequencies of the phase of interest (Bigeleisen and Mayer, 1947). All the details regarding the calculation of the β-factor of quartz and of dissolved H_4SiO_4 in the harmonic approximation are given in Méheut et al., (2007) and Dupuis et al. (2015), respectively. The β-factor of the Si catecholate model is computed from its phonon frequencies at the Γ-point, center of the Brillouin zone (according to equation (5) of Dupuis et al., 2015). The phonon frequencies are computed from first-principles using density functional theory (DFT) (Hohenberg and Kohn, 1964; Kohn and Sham, 1965). The calculation was based on the exchange-correlation functional of Perdew, Burke and Ernzerhof (PBE) (Perdew et al., 1996), a plane-wave basis set, and atomic pseudopotentials as implemented in the Quantum Espresso package. The pseudopotentials used for Si, O and H are described in the electronic annexes of Méheut et al. (2007). The pseudopotential used for Li is taken from the PSlibrary (Dal Corso, 2014). The pseudopotental used for C is described in Füger et al. (2018). Electronic wave-functions are expanded in plane-waves up to an energy cutoff ε_{cut} = 80 Ry and the charge density cut-off is set to 4 ε_{cut}. The electronic structure calculation is performed at the Γ-point of the first Brillouin zone. Phonon frequencies are computed using linear response theory (Baroni et al., 2001) with the Quantum Espresso package (Giannozzi et al., 2009).

4.5. Results

4.5.1. Attainment of equilibrium between the fluid and amorphous SiO_2

The initial aqueous Si-free solutions with 0.05, and 0.08 mol/kg catechol were first equilibrated with pre-washed amorphous SiO_2 prior to running the isotope exchange experiments. The evolution of the aqueous solution Si concentration and pH over the 10 days of this equilibration stage and the calculated equilibrium Si concentrations with PHREEQC are provided in Table A of the electronic supplement (Annex II). The temporal evolution of these aqueous Si concentrations are also shown in Fig. 4.3.

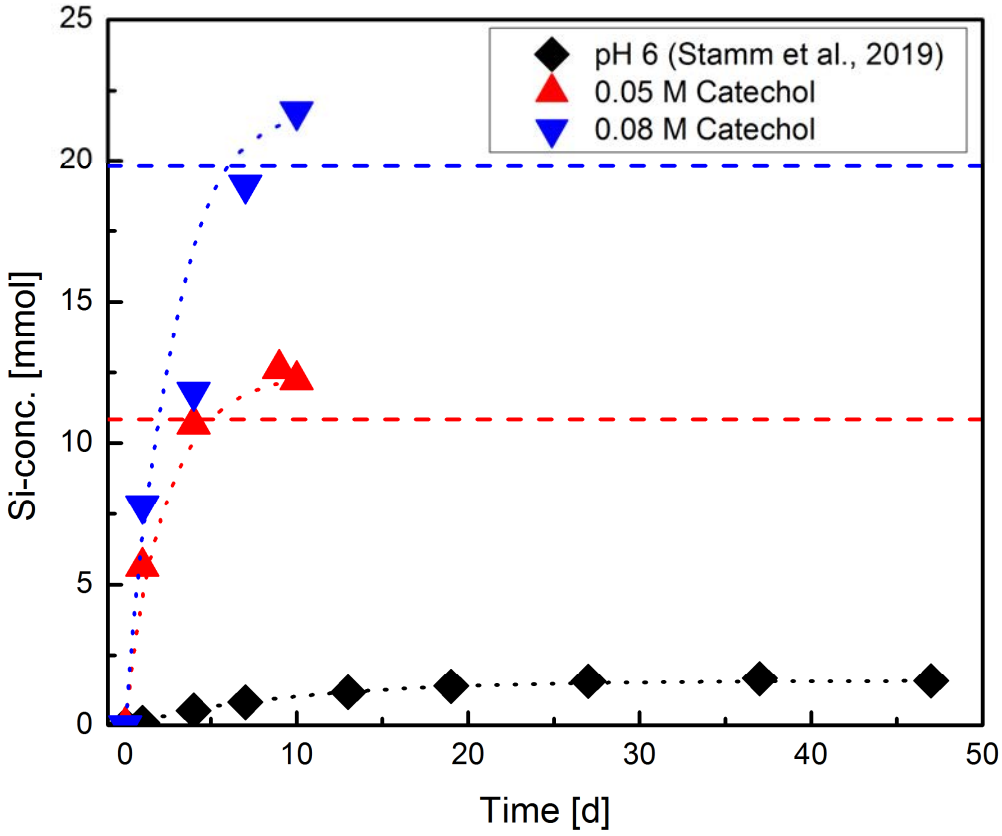

Figure 4.3 - Dissolved Si concentration during the 7 day equilibration of the experimental solutions containing 0.05 mol/kg and 0.08 mol/kg catechol, compared to a solution without organic ligands at pH 6 (data from Stamm et al., 2019). Dashed lines represent the equilibrium concentration calculated for 0.05 mol/kg and 0.08 mol/kg catechol experiments with PHREEQC.

The aqueous solutions show a steady increase and their concentrations begin to stabilize at a constant value after 10 days of equilibration. The aqueous Si concentration of the 0.05 mol/kg catechol solution reaches equilibrium as confirmed with PHREEQC calculations. The final equilibrium concentration of the 0.08 mol/kg catechol solution is ~8 % higher than the corresponding value calculated using PHREEQC, which lies within the

error of the calculation; this measured value was thus adopted as the equilibrium Si concentration of this fluid. Note that the presence of aqueous catechol increases substantially the concentration of aqueous Si in equilibrium with amorphous SiO_2 (Fig. 4.3). Assuming that the activity of dissolved silica is equal to the aqueous silica concentration C_{SiO_2}, the rates of the amorphous silica dissolution (r) in a closed system can be calculated using (Rimstidt and Barnes, 1980):

$$r = \frac{dm_{\mathrm{SiO_{2,am}}}}{dt} = S/M\left(k_+ - k_- C_{SiO_2}\right) \tag{4.6}$$

where S and M refer to the interfacial surface area and mass of solution normalized to 1 kg of water and k_+ and k_- designates amorphous silica dissolution and precipitation constants, respectively. The temporal evolution of dissolved silica concentration in the closed system can be described by (Rimstidt and Barnes, 1980; Stamm et al., 2019):

$$\mathrm{C_{SiO_2}} = \mathrm{C_{(SiO_2)_{eq}}}\left(1 - \mathrm{e}^{-\mathrm{t.k'_-}}\right) \tag{4.7}$$

Noting that $\frac{k'_+}{k'_-} = C_{(\mathrm{SiO_2})_{\mathrm{eq}}}$, where $\mathrm{C_{(SiO_2)_{eq}}}$ represents the concentration of dissolved silica in equilibrium with amorphous silica and $k'_- = \left(\frac{S}{M}\right) k_-$ and $k'_+ = (\frac{S}{M})k_+$.

The curves drawn through these measured Si concentrations were calculated by fitting the measured Si concentration to Eqn. (4.7). The rate constants for the amorphous silica dissolution reactions are provided in Table 4.3.

Table 4.3 - Equilibrium silicon concentrations in solutions and dissolution rate constants obtained from chemical equilibration of amorphous SiO_2 with solutions containing catechol.

Exp.	Si-conc.$_{\text{equilibrium}}$ [mmol]	k'$_-$ [1/s]	k_+ [mol/(m²*s)]	Source
SibA	1.58	1.36×10^{-6}	3.13×10^{-12}	Stamm et al. (2019)
SigC0.05	12.22	6.94×10^{-6}	9.72×10^{-11}	this study
SigC0.08	21.75	5.21×10^{-6}	1.65×10^{-10}	this study

4.5.2. Results of isotope exchange experiments

Representative SEM and TEM images of the amorphous SiO_2 collected from the longest duration experiment in the presence of 0.08 ml/kg catechol were obtained, and are provided in Fig. 2C and D. These solids appear close to identical to the pre-treated amorphous SiO_2 prior to the experiments. The grain sizes of the reacted powders were determined to be 21 ± 9 nm (n=100, 2 S.D.), which is identical to that of the initial cleaned powder. The water content, however, was lower; it was reduced from an initial value of 7.86 % to 6.54 % consistent with the chemical formula $SiO_2 \bullet 0.18\ H_2O$. The measured BET surface areas of the final reacted powders (e.g. the powders recovered from the longest reacted individual closed reactors in each series) are 10-15 % lower than that of the pre-experiment powders and were equal to 174.7 m^2/g and 165.6 m^2/g for the 0.05 and 0.08 mol/kg catechol solution respectively. These changes could result from some minor Ostwald ripening of the amorphous silica grains during the experiments, however the experimental solids appear to be unchanged during the isotope exchange experiments under SEM.

The temporal evolution of the pH, Si concentration, and the Si isotopic compositions of the aqueous solutions and solids during 7 days of isotopic exchange are shown in Fig. 4.4. The pH of the aqueous 0.05 mol/kg catechol solution remained constant during the experiments. The pH of the aqueous 0.08 mol/kg catechol experiments decreased at the beginning of the experimental series, but remained constant thereafter. The aqueous Si concentration in 0.05 mol/kg catechol series remained constant, whereas in the 0.08 mol/kg catechol series it first decreased, but then stabilised after 1 day. Due to a decrease in dissolved Si concentration of more than 10%, the composition of the aqueous solution collected from the longest duration experiment of the 0.08 mol/kg catechol experiment series was not considered in the retrieval of equilibrium isotope fractionation factors described below.

In both experimental series the $\delta^{29}Si$ values of the fluids and solids (Tab. 4.1) mirror one another. The $\delta^{29}Si$ value of the ^{29}Si enriched solutions decreases rapidly in the first 3 h of the experiment experimental series and the corresponding $\delta^{29}Si$ value of the solids increased. The same trend is exhibited by the $\delta^{30}Si$ values.

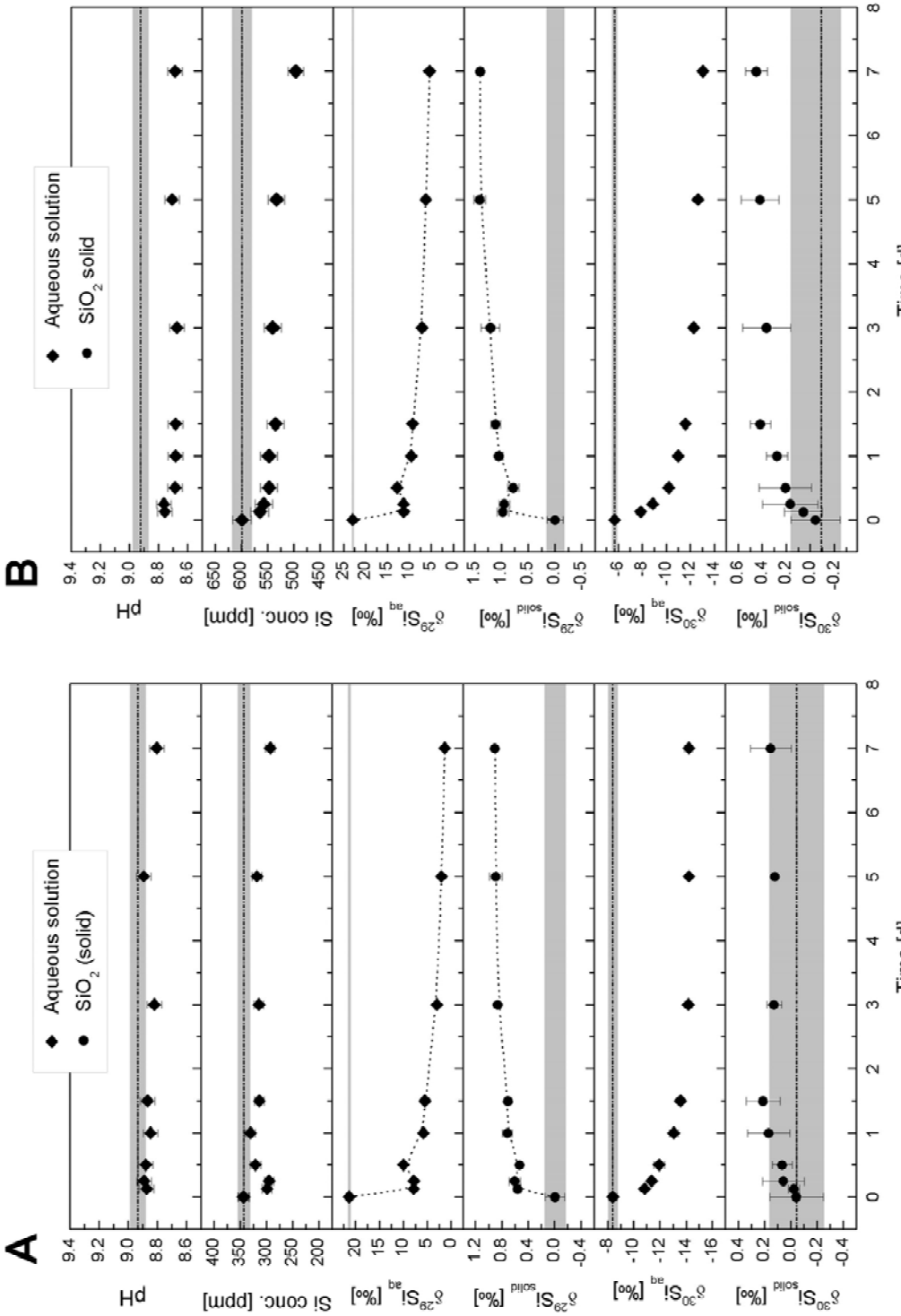

Figure 4.4 - Plots of pH, Si concentrations and isotopic compositions of solids and solutions over time during the isotopic exchange experiments. The 2 S.D. uncertainties of data points are denoted by the error bars. Initial values are represented by dashed lines with their 2 S.D. error envelope. A: 0.05 M catechol experiment, B. 0.08 M catechol experiment

4.5.3. Experimental and theoretical silicon isotope fractionation factors

Equilibrium Si fractionation factors, $\Delta_{eq}{}^{30}Si_{Si_{aq}\text{-}SiO_2,am}$, were calculated iteratively as described in detail in Stamm et al. (2019). In brief the equilibrium isotopic composition of amorphous silica ($\delta^{30}Si_{SiO_2,am}$) and the solution ($\delta^{30}Si_{aq}$) were obtained from a plot of measured $\delta^{30}Si_{Si_{aq}}$ and $\delta^{30}Si_{SiO_2,am}$ as a function of the degree of isotopic exchange F and linear extrapolation of $\delta^{30}Si$ values to 100% isotope exchange (F=1). F was calculated using

$$F = \frac{(\delta_t - \delta_i)}{(\delta_e - \delta_i)} \tag{4.8}$$

where δ_t denotes $\delta^{29}Si$ of the fluid at any time t during the reaction, and δ_i and δ_e describe the initial and equilibrium $\delta^{29}Si$ value of the fluid, respectively; δ_e was deduced iteratively from mass balance considerations. The δ-F plots for $\delta^{30}Si$ are shown in Fig. 4.5. A close correspondence can be observed between the experimental $\delta^{30}Si$ values and the extrapolation straight-lines forced to the points of the starting materials. It can be seen that at the end of the longest runs about 70 an 60 % of equilibrium fractionation was reached in 0.05 mol/kg and 0.08 mol/kg catechol solutions (Fig.4.5 B and C), respectively. The values of $\Delta_{eq}{}^{30}Si_{Si_{aq}\text{-}SiO_2,am}$ retrieved by this analysis are provided in Table 4.4. As mentioned above, the isotopic measurements of the fluid and solid recovered from the longest duration experiment of the 0.08 mol/kg catechol series was excluded due to a significant decrease in its aqueous Si concentration. This exclusion, however, did not significantly affect the retrieved values of $\Delta_{eq}{}^{30}Si_{Si_{aq}\text{-}SiO_2,am}$.

Values of $\Delta_{eq}{}^{30}Si_{Si_{aq}\text{-}SiO_2,am}$ generated from the experiments performed in this study from the experimental series run in the 0.05 mol/kg catechol solutions was -16.45 ± 1.75 ‰ and that obtained from the experiments run on the presence of 0.08 mol/kg catechol was -18.60 ± 3.44 ‰. This isotope fractionation is dramatically higher than that determined with the same amorphous SiO_2 powder in the absence of catechol at pH 6.4 reported by Stamm et al. (2019). That study reported an equilibrium fractionation factor between an organic-ligand free aqueous solution and amorphous SiO_2 of -0.45 ± 0.22 ‰ (see Table 4.4).

The extreme variation of $\Delta_{eq}{}^{30}Si_{Si_{aq}\text{-}SiO_2,am}$ can be attributed to the complexation of Si to aqueous catechol in solution taking account of the distribution of the aqueous species, calculated with PHREEQC and listed in Table 4.4.

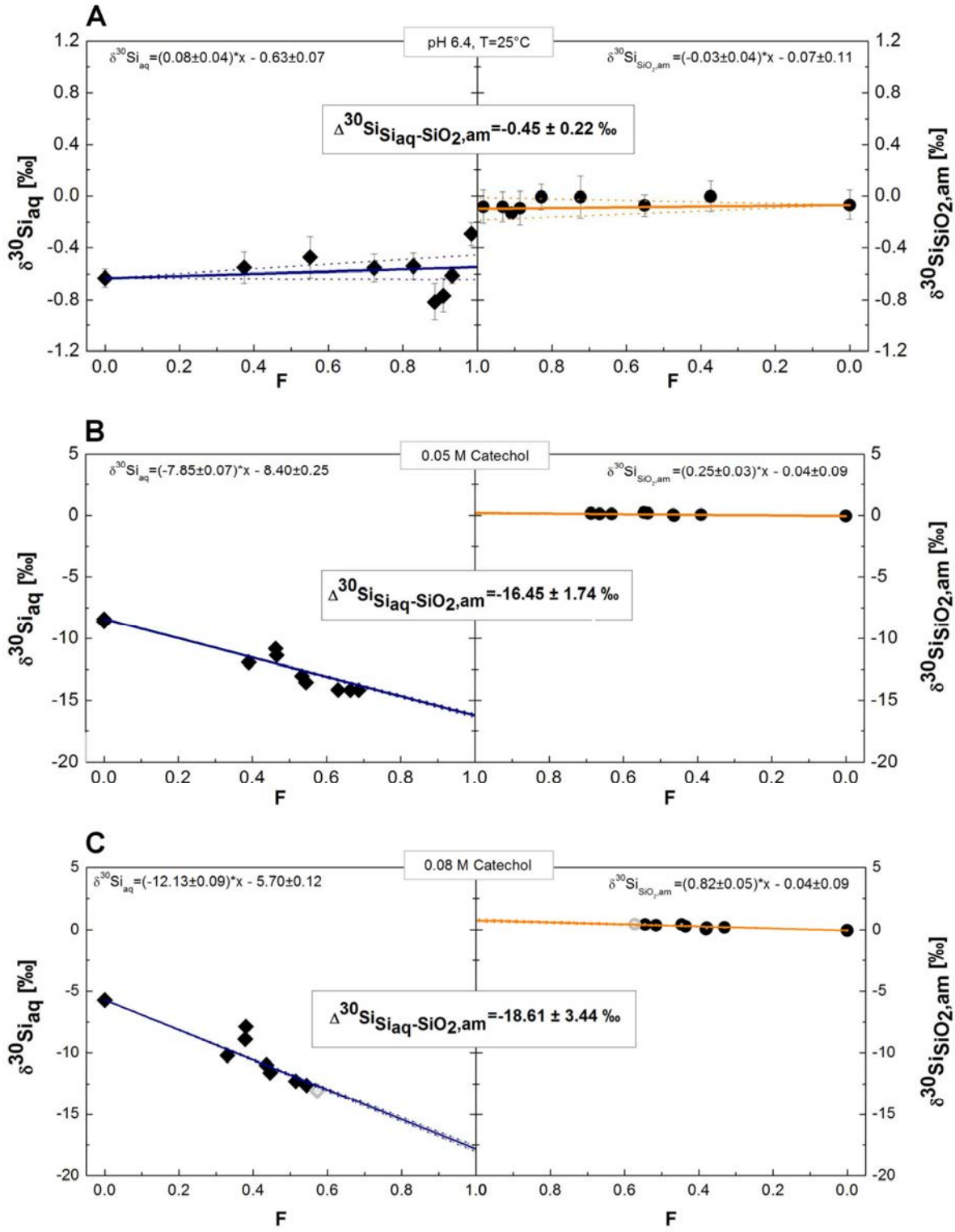

Figure 4.5 - Plots the isotopic composition of the solids and solutions as a function of the degree of isotope exchange (*F*) during the isotope exchange experiments. A. pH= 6.4 at 25 °C (modified after Stamm et al., 2019), B: 0.05 M catechol experiment, C. 0.08 M catechol experiment.

Table 4.4 - Average aqueous Si-speciation of the isotope exchange experiments together with the resulting isotopic fractionation factors between catechol bearing solution and the solid, Si catecholate and amorphous SiO_2, and between Si catecholate and $H_4SiO_4^\circ$ (H4).

					Speciation			Equilibrium fractionation factors							
Exp.	pH	Si conc.	$\Delta_{eq}{}^{30}Si_{Siaq\text{-}SiO_2,am}$	err	Si-Cat	$H_4SiO_4^\circ$	$H_3SiO_4^-$	$\Delta_{eq}{}^{30}Si_{H4\text{-}SiO_2,am}$	err	$\Delta_{eq}{}^{30}Si_{SiCat\text{-}SiO_2,am}$	err	$\Delta_{eq}{}^{30}Si_{SiCat\text{-}H4}$	err
		[mmol]	[‰]	[‰]	[%]	[%]	[%]	[‰]	[‰]	[‰]	[‰]	[‰]	[‰]
SibA[a]	6.37	1.8	-0.45	0.20		100.00		-0.45	0.20				
Cat-0.05	8.87	4.0	-16.45	1.71	87.26	12.74				-18.78	0.88	-18.33	0.44
Cat-0.08	8.74	8.5	-18.60	3.43	91.83	8.17				-20.22	1.73	-19.77	0.86

[a] data from Stamm et al. (2019)

The major aqueous species is represented by the Si catecholate complex (Si-Cat) with 86 % and 91 % for the 0.05 mol/kg and the 0.08 mol/kg catechol experiment, respectively. Note that the $H_3SiO_4^-$ species in solution represents less than 5 % of total Si speciation, which lies within the error of the calculation and is therefore considered as negligible. Therefore the Si catecholate and $H_4SiO_4^o$ species will be assumed to be 100 % of total Si-speciation in solution. Using Eqn. (4.5) the equilibrium isotopic fractionation factor between the Si catecholate complex and amorphous SiO_2 ($\Delta_{eq}{}^{30}Si_{SiCat-SiO_2,am}$) can be calculated for both experimental solutions and are shown in Tab. 4. Moreover, knowing the fractionation between $H_4SiO_4^0$ and amorphous silica (Stamm et al., 2019), it is possible to determine the equilibrium fractionation factor between Si catecholate and $H_4SiO_4^o$ ($\Delta_{eq}{}^{30}Si_{SiCat-H_4SiO_4^0}$). The experimentally derived equilibrium fractionation factors result in two distinct isotopic fractionation factors: $\Delta_{eq}{}^{30}Si_{SiCat-SiO_2,am}$ of -19.50 ± 0.97 ‰ and a $\Delta_{eq}{}^{30}Si_{SiCat-H_4SiO_4^0}$ of -19.05 ± 0.49 ‰.

Ab initio calculations performed in this study predict that isotopic fractionation between Si catecholate and quartz $\Delta_{eq}{}^{30}Si_{SiCat-quartz}$ can expected to be -21.03 ‰ at 25 °C. Based on the theoretical value of the fractionation factor between quartz and $H_4SiO_4^0$ generated at 25°C by Dupuis et al. (2015), $\Delta_{eq}{}^{30}Si_{H_4SiO_4^0-quartz}$ -2.10 ‰ the fractionation factor between Si catecholate and $H_4SiO_4^o$ $\Delta_{eq}{}^{30}Si_{SiCat-H_4SiO_4^0}$ at 25 °C is calculated to be -18.91 ‰ at 25°C, and thus slightly heavier than $\Delta_{eq}{}^{30}Si_{SiCat-quartz}$. This value is in excellent agreement with that determined experimentally in the present study. Fig. 4.6 shows the calculated Si isotopic fractionation factors between Si catecholate and quartz, and Si catecholate and $H_4SiO_4^o$ as a function of temperature, which are fitted with the polynomial functions of 1/T shown in Table 4.5.

Table 4.5 - Fits of 1000 ln $\alpha^{30}Si_{Si\ catecholate-silica}$ based on $ax^2 + bx^3$, with $x=10^3/T$

Silica	T [°C]	a	b
quartz	0-1100	-3.01	0.34
H_4SiO_4	0-1100	-2.96	0.38

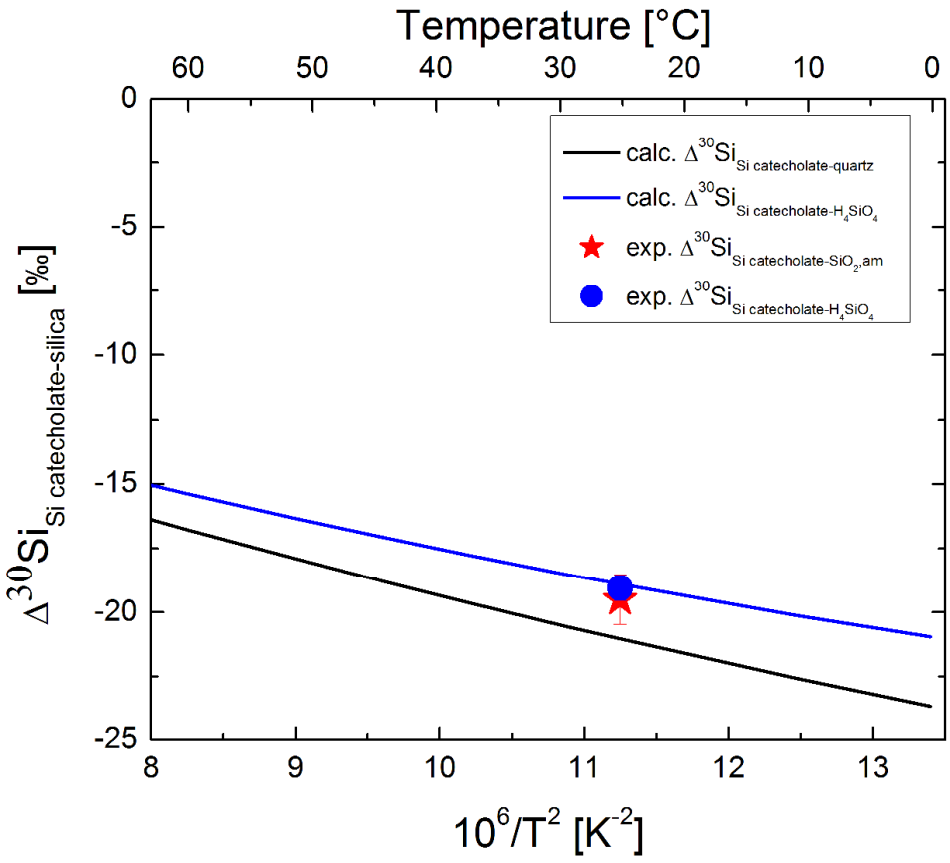

Figure 4.6 - Results of ab initio calculations, showing the evolution of the fractionation factor between Si catecholate and quartz, and Si catecholate and silicic acid as a function of temperature. Experimental data of this study are shown by the star and circle symbols.

4.5.4. Isotope exchange kinetics

The rate with which isotopic equilibrium is attained helps constraining the mechanism of the isotope exchange process. Fig. 4.7 shows the temporal evolution of the degree of isotopic exchange (*F*) in the absence of organic ligand (Stamm et al., 2019), and of in the presence of aqueous catechol. The curves in this figure are generated assuming a first order rate law (Cole and Chakraborty, 2001; Johnson et al., 2002; Stamm et al., 2019) and using the rate constants retrieved form the silica equilibration experiments and provided in Table 4.3. It can be seen that the isotope exchange of the catechol experiments is rapid during the first 1.5 days. After this time the exchange reaction rate slows noticeable. The solutions reached only ~60 to 70 % of isotopic equilibrium over the 7 days of the isotopic exchange experimental series which is significantly less than the degree of isotopic exchange attained in the absence of organic ligand over the same period of time (~82%).

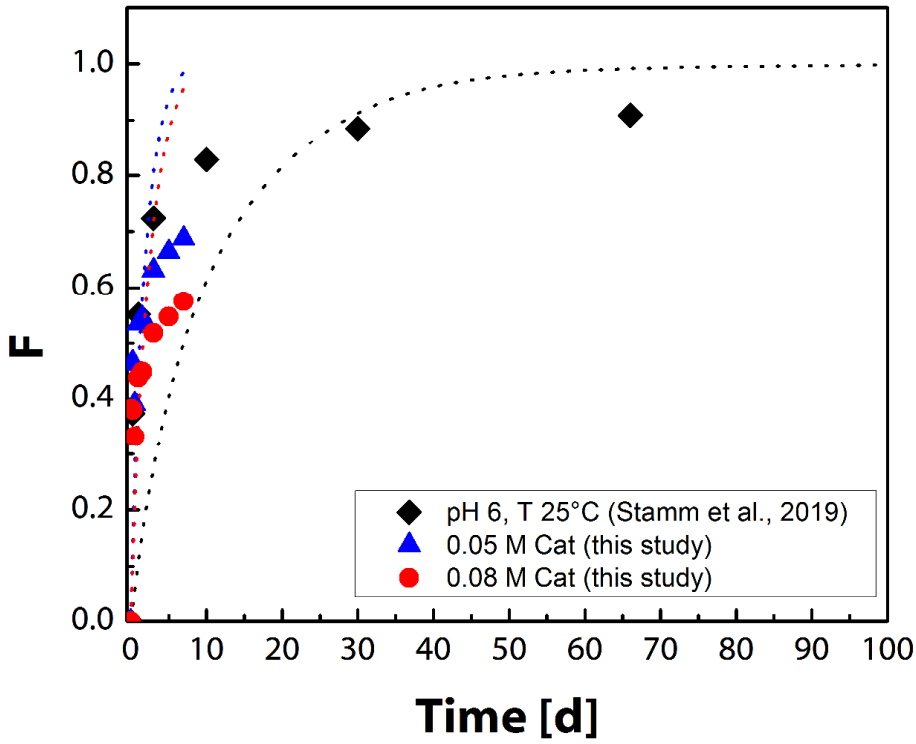

Figure 4.7 - The temporal evolution of the degree of isotopic exchange of the organic experiments of this study and experiments without organic ligands of Stamm et al. (2019). Dashed lines are generated assuming a first order rate law (Eqn. 4.10), using the dissolution rate constants from the amorphous silica dissolution experiments.

4.6. Discussion

4.6.1. Silicon isotope fractionation in the presence of catechol

The equilibrium fractionation factor $\Delta_{eq}{}^{30}Si_{Si_{aq}\text{-}SiO_{2,am}}$ determined in this study in the presence of 0.05 mol/kg and 0.08 mol/kg catechol exhibits a much stronger fractionation of -16.45 ± 1.74 ‰ and -18.60 ± 3.44 ‰, respectively, than that determined in catechol-free solution by Stamm et al. 2019 ($\Delta_{eq}{}^{30}Si_{Si_{aq}\text{-}SiO_{2,am}}$= -0.45 ‰). The solid is enriched in the heavier isotopes in both studies but to a much greater extent in the presence of catechol. The strong isotopic fractionation observed in our experiments can be attributed to the formation of organosilicon complexes. Aqueous catechol complexes strongly with Si (Barnum, 1970, 1972; Cella et al., 1980; Pokrovski and Schott, 1998; Gulley-Stahl et al., 2010) and this complexation leads to a Si coordination change (Cella et al., 1980; Boudin et al., 1988; Kinrade, 1999; Kinrade et al., 2001a, 2001b; Benner et al., 2003; Kubicki and Heaney, 2003). In the present case, the complexation of silicon with catechol leads to a six-fold

coordination of the Si atom bonded to thee catechol molecules. This coordination change is responsible for the strong equilibrium Si fractionation observed in this study.

Our experimental results and ab initio calculations are in close agreement. The equilibrium fractionation factor between the Si-catecholate complex and quartz at 25°C was calculated to be ~ -21 ‰. The experimental $\Delta_{eq}{}^{30}Si_{SiCat\text{-}SiO_2,am}$ determined in this study is equal to -19.50 ± 0.97 ‰. This result matches that generated from our *ab initio* calculations within uncertainty. A similar close agreement between experimental results and *ab initio* calculations were found for the equilibrium fractionation factor between Si-catecholate and silicic acid, with experimental and theoretical $\Delta_{eq}{}^{30}Si_{SiCat\text{-}H_4SiO_4°}$ values of -19.05 ± 0.49 ‰ and -18.9 ‰, respectively These close agreements validate our interpretation that the presence of aqueous catechol is responsible for the large equilibrium isotopic fractionation observed in this study. Note that the amount of catechol used in our experimental study is far higher than that typically found in nature. Yet even a small concentration of catechol or any organic ligand forming with Si organosilicon complexes containing hexaoxo- or pentaoxo-silicon sites can have a significant effect on the equilibrium fractionation factors between aqueous Si and co-existing solid phases.

4.6.2. Si isotope exchange kinetics in the presence of catechol

Our isotope exchange experiments began by first equilibrating amorphous SiO_2 with aqueous solutions containing either 0.05 or 0.08 mol/kg catechol. The temporal variation of Si concentration in the aqueous fluids during this equilibration step yields amorphous silica dissolution rates in these systems. The rates obtained from these equilibration steps are 9.72×10^{-11} to 1.65×10^{-10} mol/m^2/s, and increase with increasing catechol concentration (see Table 3). These rates are slightly faster than those obtained for amorphous SiO_2 dissolution in aqueous organic-ligand free solutions at pH 6.4 in Stamm et al. (2019) using the identical amorphous silica powder. The rates obtained in this study in the presence of aqueous catechol are also faster than those reported for different amorphous silica powders obtained in organic-ligand free solutions by Brady and Walther (1989), Plettnick et al. (1994), and Fraysse et al. (2006). The presence of aqueous organic ligands, such as catechol, have been reported to enhance silicate mineral dissolution rates in a number of studies (Bennett et al., 1988; Bennett, 1991; Bennett and Casey, 1994; Ganor et al., 2009; Schott et al., 2009).

The application of the three-isotope method allows evaluation of the kinetics of isotopic exchange and hence can provide insight into the mechanism driving isotopic equilibration. The rates of isotopic equilibration in this study were generated following the approach of Cole and Chakraborty (2001) and Johnson et al. (2002) using:

$$\frac{-d(1-F)}{dt} = k_n(1-F)^n \tag{4.9}$$

where k is the rate constant and n the order of reaction. Typically isotope exchange rates follow either a first-order (n=1) or a second-order (n=2) rate law (Criss et al., 1987; Huang and Tsai, 1970; Johnson et al., 2002; Welch et al., 2003; Li et al., 2011; Zheng et al., 2016). The integrated form of Eqn. (4.7) can thus be written as

$$\ln(1-\mathrm{F}) = -\mathrm{k}_1\mathrm{t} \qquad \text{for } n\text{=1} \tag{4.10}$$

$$\frac{\mathrm{F}}{(1-\mathrm{F})} = \mathrm{k}_2\mathrm{t} \qquad \text{for } n\text{=2} \tag{4.11}$$

In the present study the first order rate equation (Eqn. 4.10) was applied to calculate F values as this rate law is consistent with the dissolution rate of the amorphous SiO_2 determined above. Values of F generated as a function of time from Eqn. (4.10) using amorphous silica rate constants derived from Eqn. (4.7) are compared with experimental F values of this study in Fig. 4.7. It can be seen in this figure that during the first 1.5 days of reaction F values derived from amorphous silica dissolution rate are close to the measured F values. Over this period of time isotope exchange experiments attained up to 55 % of their final equilibrium value. After 1.5 days the isotopic exchange rate slows significantly (Table 4.6). This suggests that within the first 1.5 days the rate controlling mechanism is the detachment and reattachment of material to the amorphous silica surface, whereas, for longer times, the rate controlling mechanism is the Si transport within the amorphous silica grain.

Table 4.6 - Isotopic exchange rate constants, calculated after 1.5 days of isotopic exchange.

Exp.	Si-conc. [mmol]	k_{exch} [1/s]	k_{exch} [mol/(s*m²)]
SibA	9.0	2.36×10^{-6}	6.64×10^{-13}
SigC0.05	11.1	7.02×10^{-7}	1.32×10^{-12}
SigC0.08	19.4	4.77×10^{-7}	1.56×10^{-12}

4.6.3. Implications for biomineralization

Silicon is an essential element in biological processes. It is an important structural component for plants, phytoplankton, zooplankton and sponges (Poitrasson, 2017). Various sea sponges and microorganisms, such as diatoms and radiolarian, secrete skeletal structures in silica via dissolved Si uptake (Hendry et al., 2011). Species-dependent silicon isotope fractionation ranging from -0.5 to -2 ‰ has been reported for marine diatoms (Sutton et al., 2013) whereas fractionation up to -6.5 ‰ between sponges spicules and co-existing fluids have been measured (Douthitt, 1982; De La Rocha, 2003; Wille et al., 2010; Hendry et al., 2010, 2011; Hendry and Robinson, 2012). $H_4SiO_4^o$ is taken up by the sponge through a sodium transporter, and is subsequently precipitated via a central organic filament (Hendry et al., 2011). The biomineralization occurs with the help of the enzyme silicatein (Perry, 2003; Uriz et al., 2003; Müller et al., 2007). This enzyme is considered by some studies to form five coordinated intermediates (Kinrade et al., 2002, Zhou et al., 1999). The important fractionation reported in sponge spicules therefore could be explained by the change in coordination of Si due to the enzyme silicatein, which then would lead to the preferential incorporation of light Si isotopes into the spicules.

Like sponges and diatoms, plants preferentially incorporate light Si isotopes into their structure during the incorporation of Si from the soil solutions (Ding et al., 2005; Sun et al., 2008; Delvigne et al., 2009; Opfergelt and Delmelle, 2012; Sun et al., 2014). However, the biochemistry of Si in plants is not well known, and only a few Si transporters in plants have been yet identified (Poitrasson, 2017). Kubicki and Heaney (2003) advocated that the Si transport may not occur as $H_4SiO_4^o$ through plant, but as hypercoordinated organosilicon complexes formed by silicon with phenols or carbohydrates molecules containing at least four adjacent hydroxyl groups. The results presented in this study suggest that such hypercoordinated organosilicon complexes would lead to a strong negative fractionation between the fluid phase and Si incorporated in the plant structure.

As aqueous Si complexion can readily alter the fractionation of this metal into solids, and as aqueous ligands are abundant in various organisms, it seems reasonable to conclude that much insight could be gained into the biomineralizaion process if it were possible to interpret quantitatively the Si isotopic signals in biomaterials. Such will only be the case if we are able to quantify in detail the degree to which some aqueous Si-organic compounds alter equilibrium fractionation factors. The results in this study show that both rigorous experiments and detailed *ab initio* calculations can aid in this effort.

4.7. Conclusion

The results of this study demonstrate that the formation of organosilicon complexes containing hexaoxo-silicon sites rather than the four-coordinated Si centres typical of aqueous silica species can have an important influence on the equilibrium isotope fractionation between fluids and Si-bearing solids. Indeed it was shown in the present study that the equilibrium fractionation factor between quartz (amorphous silica) and the Si-catechol complex is about 20 ‰ lighter than the equilibrium factor between quartz (amorphous silica) and silicic acid. These values are in close agreement with the results of *ab initio* calculation performed in this study demonstrating the robustness of both type of Si isotopes quantifications. Note that the Si isotope composition of organosilicon complexes containing pentaoxo-silicon is likely to be also much lighter, by about 10 ‰ than that of $H_4SiO_4°$. Such results demonstrate that the presence of aqueous organic ligands in natural systems can play an important role on the Si isotopes fractionation and thus might explain the strong negative fractionation found in biological systems.

Chapter 5

Determination of the equilibrium magnesium isotope fractionation factors between brucite and aqueous Mg inorganic and organic species

A version of this chapter will be submitted for publication as: “Franziska M. Stamm, Thomas Zambardi, Jérôme Chmeleff, Jacques Schott, Eric H. Oelkers: Determination of the equilibrium magnesium isotope fractionation factors between brucite and aqueous inorganic and organic species”

Abstract

Magnesium (Mg) is a major element in seawater, rock-forming minerals, and biological systems. Stable Mg isotopes exhibit fractionation during silicate weathering and carbonate mineralization, and hence are a promising tool to trace these processes. Notably Mg can be present in natural aqueous solutions as a number of distinct inorganic and organic complexes including $MgHCO_3^+$, $MgCO_3^0$, $Mg(OH)^+$, $Mg(citrate)^-$ and $Mg(EDTA)^{2-}$ in addition to Mg^{2+}. The formation of these species can significantly alter the fractionation of Mg isotopes between minerals and natural fluids. To quantify these effects, isotope exchange experiments were performed at *bulk chemical equilibrium* between brucite and aqueous solutions containing different organic (citrate, EDTA) and inorganic (SO_4^-) ligands at 25 °C. Isotope exchange experiments ran as long as 511 days. The three-isotope method was used to quantify the equilibrium Mg isotope fractionation factors $\Delta_{eq}{}^{26}Mg$, between brucite and aqueous Mg. Retrieved equilibrium Mg isotope fractionation factors were found to be $\Delta_{eq}{}^{26}Mg_{brucite\text{-}Mg^{2+}} = -0.36 \pm 0.38$ ‰ between brucite and aqueous Mg^{2+}, and an average $\Delta_{eq}{}^{26}Mg_{brucite\text{-}MgSO4^\circ} = 0.79 \pm 0.17$ ‰ between brucite and aqueous $MgSO_4°$. Mg isotope equilibrium fractionation factors between brucite and aqueous $Mg(citrate)^-$ and between brucite and aqueous $Mg(EDTA)^{2-}$ retrieved from experiments performed in the presence of these organic ligands are $\Delta_{eq}{}^{26}Mg_{brucite\text{-}Mg(citrate)^-} = 0.06 \pm 0.19$ and 0.21 ± 0.21 ‰, and $\Delta_{eq}{}^{26}Mg_{brucite\text{-}Mg(EDA)^{2-}} = 2.43 \pm 0.20$ ‰. The values determined in this study for $\Delta_{eq}{}^{26}Mg_{brucite\text{-}Mg^{2+}}$ and $\Delta_{eq}{}^{26}Mg_{brucite\text{-}Mg(EDA)^{2-}}$ are in close agreement with the experimental values reported by Li et al. (2014) and the density functional theory (DFT) estimates of $\Delta_{eq}{}^{26}Mg_{Mg^{2+}\text{-}Mg(EDA)^{2-}}$ from Schott et al. (2016). However *ab initio* calculations of Mg isotope fractionation between brucite and aqueous Mg^{2+}, and between aqueous Mg^{2+} and inorganic and organic ligands such as sulphate or citrate predict higher fractionation factors of $\Delta_{eq}{}^{26}Mg_{brucite\text{-}Mg^{2+}}$ (≈ + 3 ‰, Colla et al., 2018; Gao et al., 2018), $\Delta_{eq}{}^{26}Mg_{Mg^{2+}\text{-}Mg(citrate)^-}$, and $\Delta_{eq}{}^{26}Mg_{Mg^{2+}\text{-}MgSO_4^\circ}$ (≈ -3 and -2.6 ‰, respectively, Schott et al., 2016) than measured in this study. These discrepancies between experimental and theoretical values need to be resolved to accurately predict the behaviour of Mg isotopes in natural systems. Furthermore, this study shows that the fractionation of Mg isotopes is strongly dependent on the nature of the ligands present in the Mg aquo ion coordination sphere. Therefore Mg speciation in natural fluids has to be accurately known to interpret Mg isotopic signatures in natural environments.

5.1. Introduction

Magnesium is a key element in continental weathering, in hydrological systems, such as the carbonate precipitation in oceans, in diagenetic reactions, as well as in biochemical processes (Brenot et al., 2008; Pogge von Strandmann et al., 2008; Hippler et al., 2009; Foster et al., 2010; Immenhauser et al., 2010; Li et al., 2011; Wimpenny et al., 2011; Opfergelt et al., 2012; Pogge von Strandmann et al., 2012; Mavromatis et al., 2013; Li et al., 2014; Liu et al., 2014; Kasemann et al., 2014; Mavromatis et al., 2014a; Opfergelt et al., 2014; Wimpenny et al., 2014; Gao et al., 2016; Schott et al., 2016; Oelkers et al., 2018). The behaviour of Mg isotopes during these processes could be applied to understand the Mg geochemical cycle and to precisely reconstruct paleoclimate conditions.

Numerous studies have been aimed at quantifying Mg fractionation during the formation of various minerals including calcite, dolomite, magnesite or brucite (Immenhauser et al., 2010; Pearce et al., 2012; Li et al., 2014; Mavromatis et al., 2013, 2014a). These studies showed that these carbonate minerals and brucite preferentially incorporate light Mg isotopes, whereas epsomite and clay minerals are likely to incorporate heavy Mg isotopes (Tipper et al., 2006a; Li et al., 2011; Tipper et al., 2012a, 2012b; Opfergelt et al., 2012). In biological environments, plant roots can be enriched in heavy Mg isotopes, whereas the upper parts of the plants are isotopically lighter (Bolou-Bi et al., 2012). These differences can stem from the different bonding environments of Mg, in most cases the bond lengths between magnesium and oxygen ions (Schott et al., 2016). Mg isotopic signatures can also be significantly affected by reaction kinetics during solid-solution interactions (i.e. transport to and from the reacting interface, dissolution or precipitation), such as shown by Schott et al. (2009), Pearce et al. (2012), and Mavromatis et al. (2013). Another reason for the differences in Mg fractionation in mineral-aqueous solutions systems is the Mg aqueous speciation in the aqueous fluid (Schott et al., 2016; Mavromatis et al., 2017). The influence of aqueous speciation on isotopic fractionation has already been demonstrated not only for magnesium but also for boron, carbon, mercury, silicon and several transition metals (Hemming and Hanson, 1992; Zhang et al., 1995; Zeebe, 2005; Klochko et al., 2006, 2009; Asael et al., 2009; Holloway et al., 2011; Jiskra et al., 2012; Ryan et al., 2013; Yin et al., 2013; Fujii et al., 2014, 2015; Dupuis et al., 2015; Noireaux et al., 2015; Schott et al., 2016; Balan et al., 2018; Mavromatis et al., 2019). The influence of the bonding environment of the metal and the reaction kinetics on the equilibrium fractionation factor in mineral-solution reaction is yet not fully understood.

Several past studies have aimed to experimentally and theoretically determine the Mg equilibrium fractionation factor between minerals and the coexisting aqueous solutions (Li et al., 2011, 2014; Schott et al., 2016; Mavromatis et al., 2017; Colla et al., 2018; Gao et al., 2018). The studies of Li et al. (2014), Colla et al. (2018) and Gao et al. (2018) focussed on the fractionation between brucite and its co-existing aqueous solution. Brucite, also used in this study, is an important secondary mineral, which occurs in a wide range of geological settings (e.g. Hostetler et al., 1966; Alabaster, 1977; Brown et al., 1985; Bach et al., 2006; Li et al., 2014). It has a structure similar to phyllosilicates and is therefore believed to be a suitable proxy for studying Mg isotopic fractionation during the weathering and alteration of Mg silicate rocks (Li et al., 2014). Brucite also occurs in the skeletons of corals, diatoms and algae (Weber and Kaufman, 1965; Nothdurft et al., 2005; Buster and Holmes, 2006; Tesson et al., 2008) where it is involved in biomineralization processes.

The experimental values obtained by Li et al. (2014) show that brucite in the presence of ligand-free solution preferentially incorporates light Mg isotopes resulting in a $\Delta_{eq}{}^{26}Mg_{brucite\text{-}solution}$ of -0.17 ± 0.07 ‰. This result, however, is inconsistent with the *ab inito* calculations reported by Colla et al. (2018) and Gao et al. (2018), who proposed a fractionation factor $\Delta_{eq}{}^{26}Mg_{brucite\text{-}solution}$ of 2.7 and 3.3 ‰, respectively. Additionally, Li et al (2014) reported a fractionation factor between brucite and EDTA, $\Delta_{eq}{}^{26}Mg_{brucite\text{-}MgEDTA^{2-}} \geq 2.0$ ‰. This value is in good agreement with the *ab initio* calculations reported by Schott et al. (2016). This study also reported the Mg isotope fractionation factors among aqueous Mg^{2+} species and numerous aqueous inorganic and organic complexes including $Mg(citrate)^-$, $MgSO_4^o$, $MgHCO_3^+$, $MgCO_3^\circ$.

The aim of this study is to experimentally determine the equilibrium Mg isotope fractionation factors between brucite and aqueous Mg in the presence and absence of inorganic and organic ligands at 25°C. The 'three isotope method' was adopted in this study to determine unambiguously these fractionation factors at equilibrium. This paper reports the results of the experimental study, which are compared with corresponding results generated from existing computational models. Taken together, these results will provide new insight into how aqueous solution speciation can affect the Mg equilibrium isotopic fractionation among minerals and aqueous solutions.

5.2. Methods

5.2.1. Starting materials

5.2.1.1. Brucite synthesis

The experiments in this study were performed using microcrystalline brucite ($Mg(OH)_2$). This brucite was synthesized by the wet precipitation method of Henrist et al., (2003), Lv et al. (2004), and Estrada et al. (2015). Consistent with this method, 100 ml of an aqueous 2M $MgCl_2 \cdot 6\ H_2O$ solution was prepared and added dropwise at a rate of 2.5 ml/min using a Metrohm® 702 SM Titrino titrator, into 200 ml of a constantly stirred 45°C suprapur Merck® 25% NH_3 solution. Brucite nanoparticles form immediately and serve as precipitation nuclei for the growth of larger brucite crystals. The larger crystals form by the aging of the solid-solution suspension. The reaction vessel was thereby sealed and left at room temperature. After three days the precipitated brucite powder was filtered, washed with Milli-Q® water and subsequently dried at 135° C for 1 h. The resulting solids were then allowed to further dry overnight at 60°C. A hydrothermal treatment, as proposed by Henrist et al. (2003), Lv et al., (2004), and Estrada et al. (2015) to improve brucite crystallinity, was not performed. The dried powder was analysed by X-ray diffraction using a 2nd Generation Bruker® D2 Phaser, to determine the purity of the precipitated phase. The morphology of these solids were analysed using a MEB JEOL JSM-7800F Prime electron microscope (SEM) at the Raimond Castaing Microcharacterization Centre (Toulouse, France). Images of two representative synthesized brucite powders are shown in Fig. 5.1 A and B. The specific surface areas of these powders were determined using a Quantachrome Autosorb-1MP together with the nitrogen multipoint BET method (Brunauer et al., 1938) within an estimated uncertainty of ± 10%. Details of the synthesized brucite powders used in this study are listed in Table 5.1.

Table 5.1 - Synthesized brucite powders used in this study. Note that the aqueous NH_3 solution used to create powder batch BD was heated briefly to 90°C during the synthesis, in an attempt to generate a higher degree of crystallinity of the grains.

batch n°	batch name	$T_{precipitation}$ [°C]	m [g]	S_{BET} [m^2/g]
1	BB	48.0	10.58	30.54
2	BC	45.0	7.94	39.4
3	BD	48.1	7.19	29.23
4	BE	53.1	8.27	35.53

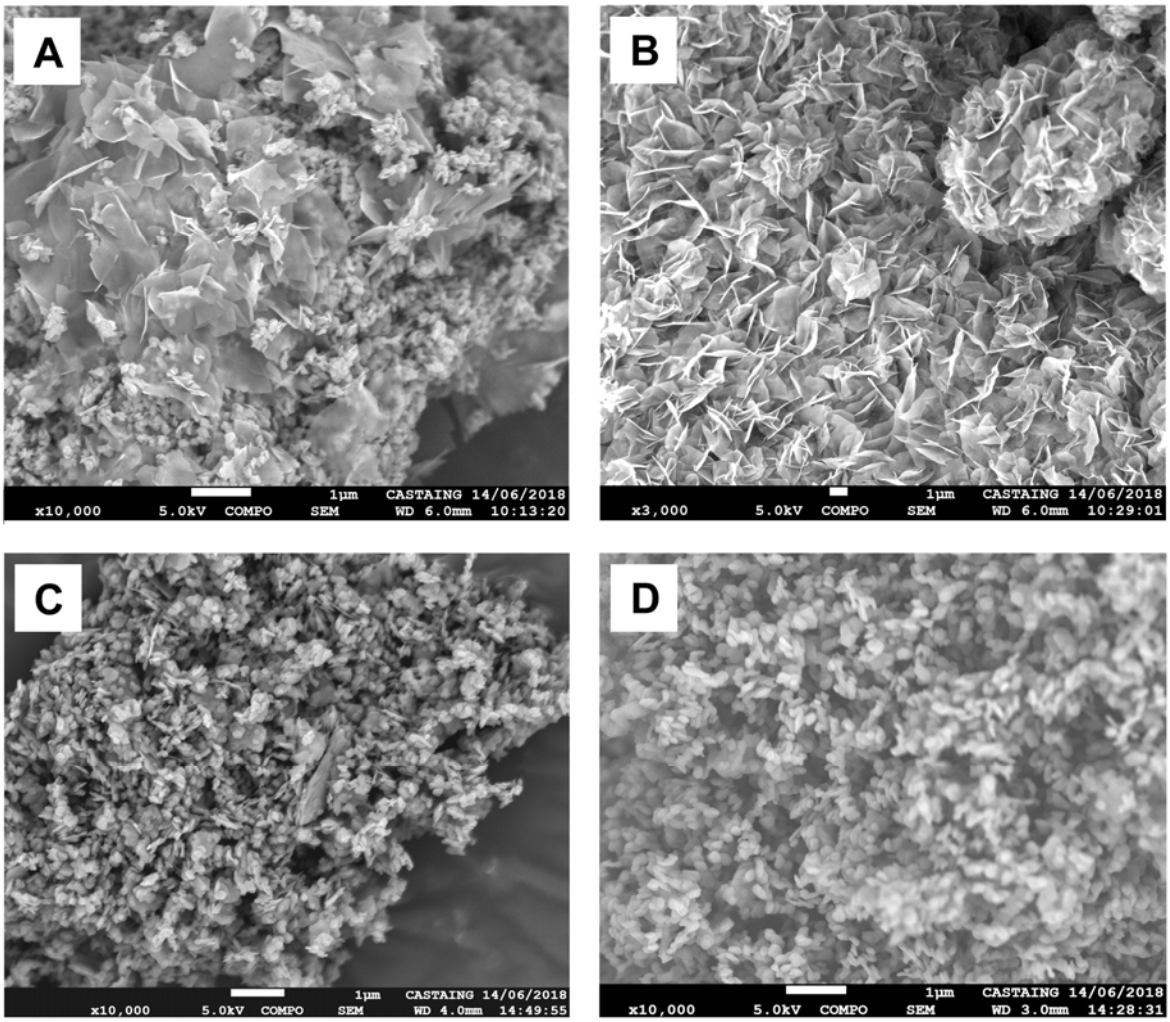

Figure 5.1 - Representative images of synthesized brucite powders. A. SEM image of the initial powder BB showing agglomerates brucite grains and fine brucite platelets . B. SEM image of the initial powder BE showing fine brucite platelets C. Representative SEM image of reacted brucite powder of the sulphate experiment. D. Representative SEM image of reacted brucite powder of the EDTA experiment.

5.2.1.2. Initial reactive aqueous solutions

The experiments of this study were performed in six distinct series; each series was conducted using a distinct initial aqueous solution. The compositions of these initial aqueous solutions are listed in Table. 5.2. All initial aqueous solutions were prepared at pH between 9.5 and 10.5 at 25°C from de-ionized Milli-Q® water (>18.2 Ω), bi-distilled HCl, suprapur Merck® Na_2SO_4, reagent grade Merck® tri-sodium citrate dehydrate and Titriplex III Merck® 0.1 N Na_2EDTA solution. According to their composition and the initial brucite powder used, the experimental series were named BB and BABE for the inorganic experiments, BBC for the aqueous citrate bearing experiments, BCS and BDS for the aqueous sulphate bearing experiments with ~35 and 65 % $MgSO_4$ complexation in solution, and BE-EDTA for the aqueous EDTA bearing experiments.

Table 5.2 - Initial aqueous solutions prepared for chemical equilibration of brucite.

Exp.	T [°C]	Solution composition	pH	$V_{solution}$ [ml]	m_{solid} [g]
BB	25	pure MQ® water + 7.80 ml 1N HCl + 2.3 ml 10 N HCl	9.3	200.13	3.00
BABE	25	pure MQ® water + 7.80 ml 1N HCl + 2.3 ml 10 N HCl	9.3	200.13	3.00
BBC	25	pure MQ® water + 1.66 ml 1N HCl + 0.27 g citrate	10.4	200.35	3.01
BCS	25	pure MQ® water + 3.00 ml 9.35 N HCl + 1.11 g Na_2SO_4	9.5	200.48	3.07
BDS	25	pure MQ® water + 0.43 ml 9.6 N HCl + 1.54 g Na_2SO_4	10.0	200.10	3.02
BE-EDTA	25	0.1 N Na_2EDTA solution (Titriplex III Merck®)	-	201.36	3.01

5.2.1.3. Characterization of sampled experimental solutionss

Aqueous solution samples were collected from all experiments. The pH of these samples was measured using a Metrohm® 913 pH Meter connected to a standard glass microelectrode with a 2 SD uncertainty of 0.05. The magnesium concentrations of these samples were determined by Flame Atomic Absorption Spectroscopy (F-AAS). These analyses were performed for concentrations from 0.1 to 0.6 ppm Mg using a Perkin Elemer AAnalyst 400. Analytic standards were prepared using an identical matrix to that of the experimental series analysed to avoid interference during measurements. The limit of detection (LOD) and the limit of quantification (LOQ) of these measurements were determined for each matrix to be 5 ppb and 1 ppb, respectively. These measurements had an uncertainty of ±1%.

5.2.2. Experimental design

The three-isotope method (Matsuhisa et al., 1978) was used in this study to determine the equilibrium isotopic fractionation factor between brucite and aqueous solutions. This method allows determination of the degree of isotopic exchange between brucite and the aqueous solution as it evolves over time. Isotopic disequilibria in the mineral-solution system is provoked by enriching the solution with ^{25}Mg. The system will strive to isotopic equilibrium over time. As isotopic exchange is slow and equilibrium is not reached during the experiments, the three-isotope method allows the extrapolation of the degree of isotopic change so that the isotopic composition of the two components at 100% exchange (e.g. isotopic equilibrium) can be determined. A detailed description of this method is given by previous studies (Matsuhisa et al., 1978; Matthews et al., 1983a, 1983b, 1983c; Shahar et al., 2008; Beard et al., 2010; Li et al., 2011, 2014; Frierdich et al., 2014; Reddy et al., 2015; Zheng et al., 2016; Stamm et al., 2019). The application of the three-isotope method in this study was performed at conditions of bulk chemical equilibrium but isotopic disequilibrium. As such each experimental series consisted of two parts. The first part was the chemical equilibration of the water-brucite system. The equilibrated solution collected at the end of this first step was then enriched in heavy Mg and used in the second step, a isotope equilibration step performed with fresh brucite powder. These two steps are described in detail below.

5.2.2.1. Step 1: Equilibration of initial aqueous solutions with $Mg(OH)_2$

Six experimental series were performed in this study. Each series began by equilibrating 200 mL of an initial aqueous solution with 3 g of synthesized brucite powder in closed-system polypropylene reactors. The composition of these initial aqueous solutions are provided in Table 5.2. To ensure constant temperature, the reactors were placed in a continuously shaking thermostatic bath at 25°C. The reactor solutions were regularly sampled over the 35 to 57 days duration of this first equilibration step. The solution pH was immediately measured after sampling. Part of each solution sample was acidified with 10 µl 10 N bi-distilled HCl to avoid any Mg precipitation during storage prior to their further analysis. The aqueous Mg concentrations of these solutions were determined with F-AAS. Once the pH and Mg concentration of the experimental aqueous solutions were constant over time chemical equilibrium was assumed to have been attained. The solutions were then filtered with Merck® 0.2 µm Teflon syringe filters. The pH and Mg concentrations of the

solutions were re-measured, and the collected solutions used in the second step of each experimental series for the isotopic exchange experiments (see Table 5.3).

Table 5.3 - Mg concentrations and pH of solutions after chemical equilibration, and after adding the isotopic spike, and the average amount of powder and solution used in the isotope exchange experiments.

	chem. equil. solution		*spiked solution*		*isotope exchange experiments*		
Exp.	pH	Mg-conc. [ppm]	pH	Mg-conc. [ppm]	m_{powder} [g]	$m_{solution}$ [g]	powder:solution
BB	9.4	2018.99	9.0	2084.04	0.10	5.02	1:50
BABE	9.4	2019.89	9.4	2002.65	0.49	5.03	1:10
BBC	10.1	147.97	10.2	146.05	0.10	5.02	1:49
BCS	9.4	1724.00	9.5	1703.29	0.19	3.04	1:16
BDS	9.9	274.16	9.9	271.01	0.51	5.04	1:10
BE-EDTA	12.5	1626.09	12.4	1715.05	0.50	5.00	1:10

5.2.2.2. Step 2: Isotopic exchange experiments

Prior to beginning the isotopic exchange experiments, the chemical equilibrated solutions collected from step 1 were enriched with a ^{25}Mg isotope tracer with a initial composition of 2.4% ^{24}Mg, 96.4% ^{25}Mg, and 1.2 % ^{26}Mg, to obtain a total $\delta^{25}Mg$ of ~ 20 ‰ (see Eqn. 5.2 and Table 5.4). Due to the addition of this spike solution, the Mg concentrations of the experimental solutions were lowered. Consequently a small amount of $MgCl_2 \cdot 6\ H_2O$ was added to these solutions to re-attain equilibrium Mg concentrations (see Table 5.3). In addition the pH of these solutions were adjusted with bi-distilled HCl or suprapur NaOH solution if necessary.

Step 2 of each experimental series were performed as 8 individual batch reactor experiments, which ran for as long as 263 to 522 days depending on the series. For each individual experiment, a known quantity of synthesized brucite powder was placed in 10 ml polypropylene reactors together with the prepared ^{25}Mg enriched solutions. The masses of solution and solid in each reactor are provided in Table 5.3. The reactors were sealed and placed into a constantly mixing orbital shaker. Closed system conditions were verified by weighing the reactors at the beginning and end of each experiment. At pre-chosen time intervals, an individual experiment was stopped. The reactors were centrifuged for 20 min at 4500 rpm and the supernatant was separated from the powder and filtered with Merck® 0.2 µm Teflon syringe filters. The pH of the solutions were measured immediately after sampling. The remaining sample was acidified with 10 µl 15 N HNO_3 and subsequently analysed for Mg concentration and isotopic composition. The recovered brucite powders

were washed with de-ionized Milli-Q® water and oven dried at 40°C, and later analysed for Mg isotope composition.

5.2.3. Data reporting and Mg isotope analysis

The isotopic compositions of the magnesium bearing powders and the experimental solutions collected from the isotope exchange experiments, the initial chemical equilibrated solutions, and the spiked initial solutions were measured using a Thermo Scientific Neptune® MC-ICP-MS at the Obersvatoire Midi-Pyrénées / Laboratoie Géosciences Environnement Toulouse (GET), France.

The obtained Mg isotopic compositions of ^{26}Mg and ^{25}Mg in the samples are expressed with the standard δ-notation in per mil (‰) relative to the international DSM-3 standard following the relation:

$$\delta^{26}\mathrm{Mg} = \left[\frac{(^{26}Mg/^{24}\mathrm{Mg})_{Sample}}{(^{26}Mg/^{24}\mathrm{Mg})_{DSM-3}} - 1\right] \times 1000 \quad (5.1)$$

and

$$\delta^{25}\mathrm{Mg} = \left[\frac{(^{25}Mg/^{24}\mathrm{Mg})_{Sample}}{(^{25}Mg/^{24}\mathrm{Mg})_{DSM-3}} - 1\right] \times 1000 \quad (5.2)$$

The Mg fractionation factor between an aqueous solution and a solid ($\alpha^{26/24}_{solid-fluid}$) is defined as:

$$\alpha^{26/24}_{solid-solution} = \frac{(^{26}Mg/^{24}\mathrm{Mg})_{solid}}{(^{26}Mg/^{24}\mathrm{Mg})_{solution}} \quad (5.3)$$

or as $\Delta^{26}\mathrm{Mg}_{solid-fluid}$, which is expressed by:

$$\Delta^{26}\mathrm{Mg}_{solid-solution} = \delta^{26}\mathrm{Mg}_{solid} - \delta^{26}\mathrm{Mg}_{solution} \quad (5.4)$$

Note that as $\alpha^{26/24}_{solid-solution} \approx 1$, $\Delta^{26}\mathrm{Mg}_{solid-solution}$ is approximately related to $\alpha^{26/24}_{solid-solution}$ by:

$$\Delta^{26}\mathrm{Mg}_{solid-solution} \approx 10^3 ln\alpha^{26/24}_{solid-solution}. \quad (5.5)$$

The samples were prepared for MC-ICP-MS measurements using an approach similar to that of Teng et al. (2007), Pearce et al. (2012), and Mavromatis et al. (2013, 2014a, 2014b). One mg of sampled brucite or JDo-1 dolomitic carbonate standard powder were dissolved into 2 ml 15 N bi-distilled HNO_3, and subsequently evaporated to dryness at 120°C. This residual was then re-dissolved into 5 ml 1 N HNO_3. The Mg concentration of these solution were determined using F-AAS. Aliquots containing 15 µg Mg were once again evaporated

and re-dissolved into 2 ml 1 N HNO_3. For the experimental solutions and the IAPSO seawater standard, aliquots containing 15µg Mg were evaporated to dryness, then re-dissolved into 2 ml 1 N HNO_3. For solutions containing organic ligands (i.e. citrate or EDTA) ~0.5 ml of 30 % H_2O_2 was added to the solutions and left to react between 3-6 hours prior to evaporation to remove these species.

All samples were purified by cation exchange chromatography using 1 ml Bio-Rad® AG50W-12X 200-400 mesh cationic resin. The resin was originally cleaned and the samples were eluted as described by Teng et al. (2007). As Mg isotopes could be significantly fractionated during ion exchange (Chang et al., 2003; Teng et al., 2007), it was necessary to obtain close to 100% Mg yields from the column chemistry; Mg yields were determined by F-AAS to be ~97 %. The average ^{24}Mg signal of the procedural blank was found to be less than < 0.5% of the total ^{24}Mg signal and were therefore considered negligible.

Magnesium isotope ratio measurements were performed in low resolution at aqueous Mg concentrations of 600 ppb. A Thermo SIS system was used together with a double-pass cyclonic spray chamber to introduce the samples, after their dissolution into 0.37N aqueous HNO_3 into the plasma. The instrumental mass bias drift was corrected using the sample-standard bracketing technique. An in house $MgNO_3$ standard was used for the sample-standard bracketing due to limited access to the DSM-3 standard. The isotopic composition of this in house standard was determined to be $\delta^{25}Mg = 0.16 \pm 0.08$ ‰ and $\delta^{26}Mg = 0.32 \pm 0.14$ ‰ by repeated measurements (n=61) relative to DSM-3. The Mg isotope composition of the measured samples were then corrected with these values to generate isotopic compositions of the samples relative to the DSM-3 standard (Galy et al., 2003).

The experimental solution samples containing EDTA and sulphate were treated as described above, in contrast to the studies of Li et al. (2011, 2014). The impact of these dissolved species on the measurements was evaluated by doping the bracketing standard with aqueous citrate, EDTA and sulphate in the concentrations used in the experiments. The maximum deviation measured from the in-house standard was of 0.02 ‰, and 0.03 ‰ for $\delta^{25}Mg$, and $\delta^{26}Mg$ respectively. The impact of aqueous citrate, EDTA, and sulphate on the measured Mg isotope compositions are thus considered to be negligible.

During each analytical session, the JDol-1 standard and the IAPSO seawater standard were repeatedly measured to monitor the accuracy and precision of the measurements. The measured composition of these standards over the long-term was $\delta^{25}Mg = -1.21 \pm 0.08$ ‰ and $\delta^{26}Mg = -2.32 \pm 0.15$ ‰ for the JDo-1 standard, and $\delta^{25}Mg = -0.45 \pm 0.11$ ‰, and $\delta^{26}Mg = -0.86 \pm 0.20$ ‰ for the IAPSO seawater standard. These are in close agreement

with previously reported values (e.g. Pogge von Strandmann et al., 2008; Wombacher et al., 2009; Immenhauser et al., 2010; Wimpenny et al., 2011; Mavromatis et al., 2013, 2014a, 2014b, 2016).

5.2.4. Geochemical and speciation calculations with PHREEQC

Geochemical and speciation calculations in the present study were performed using the PHREEQC code (Parkhurst and Appelo, 2013) together with its core10 thermodynamic database after adding the equilibrium constants for aqueous sulphate, citrate and EDTA bearing species to this database listed in Table A of the electronic supplement (Annex III). The adopted standard state is that of unit activity for pure minerals, solids and H_2O. The standard state for the aqueous species is unit activity of a 1 molal solution extrapolated to infinite dilution at any given temperature and pressure. The activity coefficients of neutral species were assumed to be equal to one, whereas the activity coefficients of charged aqueous species were calculated using the Davies equation. The dissolution of brucite can be described by:

$$Mg(OH)_2 + 2\,H^+ \leftrightarrow Mg^{2+} + 2\,H_2O \tag{5.6}$$

for which law of mass action is given by:

$$K_{eq} = \frac{a_{Mg^{2+}}\,(a_{H_2O})^2}{a_{Mg(OH)_2}(a_{H^+})^2} \tag{5.7}$$

where K_{eq} stands for an equilibrium constant and a_i refers to the activity of the subscripted species or phase. Taking account of the standard state in pure water and for pure brucite, Eqn. (5.7) reduces to:

$$K_{eq} = \frac{a_{Mg^{2+}}}{(a_{H^+})^2} \tag{5.8}$$

To be consistent with the solids used in this study, the equilibrium constant (Table A of the electronic supplement; Annex III) used for brucite solubility in geochemical calculations was determined from Eqn. (5.8) and PHREEQC using the measured equilibrium Mg concentration and pH of aqueous samples collected in the first-step equilibration of the ligand-free experimental series after the solutions attained steady-state conditions (Table B of the electronic supplement Annex III).

The proportion and identity of Mg-bearing aqueous species present in the solution phase has a significant effect on the mineral-solution equilibrium Mg isotope fractionation

factor. The mineral-solution Mg fractionation factor corresponds to the weighted average of the individual isotope fractionation factors of all the Mg bearing species in the solution in accord with (Zhang et al., 1995):

$$10^3 ln\alpha^{x/24}_{solid-solution} = \sum_i (x_i \times 10^3 ln\alpha^{x/24}_{solid-i}) \quad (5.9)$$

where x_i refers to the mole fraction of the total Mg in the solution that is present in the subscripted aqueous species and , $\alpha^{x/24}_{solid-i}$ corresponds to the fractionation factor between the solid and the it Mg bearing aqueous species.

5.3. Results

5.3.1. Equilibrium between solution and brucite

Prior to performing isotope exchange experiments, the initial Mg-free solutions were equilibrated with synthesized brucite powder. The evolution of the aqueous Mg concentration over the 35-60 days of equilibration of each experimental series is shown in Fig. 5.2 and listed in Table B of the electronic supplement (Annex III).

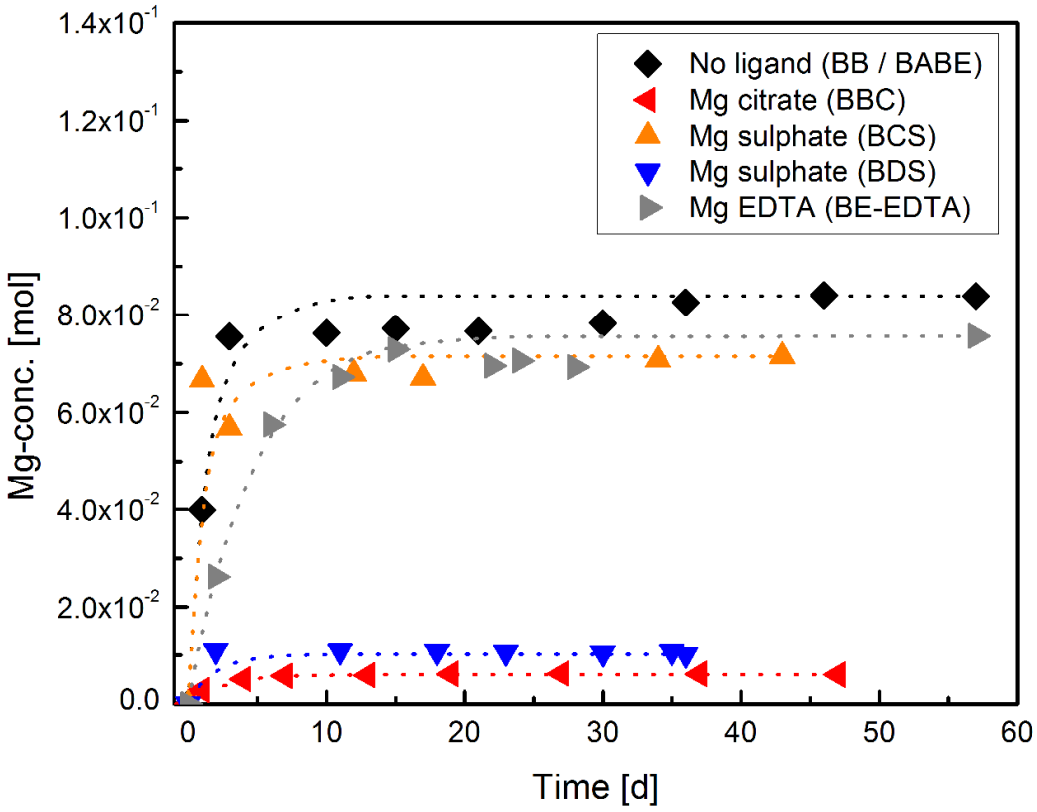

Figure 5.2 - Temporal evolution of dissolved Mg concentration during the equilibration of the initial reactive solutions during the first step of each experimental series. The dashed lines represent a fit of the data using Eqn. 11 with values of rate constant k'. listed in Table 5.4.

The experimental solutions during this first equilibration step exhibit a steady Mg concentration increase before stabilising within 20 days. Supposing that reaction (5.6) is an elementary reaction, the rate of the brucite dissolution (r) at a given constant pH is given by:

$$r = \frac{dC_{\mathrm{Mg}}}{dt} = S/M\left(k_{+} - k_{-}C_{\mathrm{Mg}}\right) \tag{5.10}$$

where S and M refer to the brucite-aqueous solution interfacial surface area and mass of solution, and k_+ and k_- designates brucite dissolution and precipitation rate constants, respectively. Assuming that the activity of aqueous magnesium is equal to the dissolved aqueous Mg concentration, the temporal evolution of dissolved Mg concentration in a closed system can be described using:

$$C_{\mathrm{Mg}} = C_{(\mathrm{Mg})_{eq}}\left(1 - e^{-t.k'_{-}}\right) \tag{5.11}$$

where $k'_{-} = \left(\frac{S}{M}\right)k_{-}$, $C_{(\mathrm{Mg})_{eq}}$ stands for the concentration of aqueous Mg in equilibrium with brucite, and t denotes the elapsed time since the beginning of the experiment. The curves drawn through the measured Mg concentrations shown in Fig. 5.2 were calculated using Eqn. (5.11). The rate constants for the brucite dissolution reactions generated from these curves are provided in Table 5.4. Brucite far from equilibrium dissolution rates determined in this study in the absence of organic and inorganic ligands are similar to those determined by Pokrovsky and Schott (2004) who reported values ranging from 6×10^{-9} mol/m^2/s at pH 9.5 to 10^{-10} mol/m^2/s at pH 12.

Table 5.4 - Equilibrium Mg concentrations in solutions and dissolution rate constants obtained from chemical equilibration of synthesized brucite with solutions with and without inorganic and organic ligands.

Exp.	pH	$C_{(Mg)eq}$ [mmol]	k'_{-} [1/s]	k_{+} [mol/(m²s)]
BB/BABE	9.3	83.9	9.26 x 10^{-6}	3.87 x 10^{-9}
BBC	10.2	6.0	5.79 x 10^{-6}	1.87 x 10^{-10}
BCS	9.5	71.5	1.16 x 10^{-5}	4.70 x 10^{-9}
BDS	10.0	10.3	1.74 x 10^{-5}	1.08 x 10^{-9}
BE EDTA	12.5	75.7	2.89 x 10^{-6}	2.32 x 10^{-9}

5.3.2. Results of isotope exchange experiments

Representative SEM images of the brucite powders collected from the longest duration Mg isotope exchange experiments are provided in Fig. 5.1 C and D. The appearance of these solids is significantly different than that of the initial synthesized brucite. The initial synthesized brucite consists mainly of thin platelet structures (Fig. 5.1 A and B) with small rounded grains, whereas the reacted brucite powder (Fig. 5.1 C and D) exhibits mainly small rounded grains. The measured BET surface areas of the reacted powder, provided in Table 5.5, are within 10 % of their initial values, with the exception of the brucite recovered from the longest experiment of series BB, run without organic ligands, which exhibited a surface area increase of 24%, and the brucite recovered from the longest exchange experiment of series BE EDTA, run in the presence of aqueous EDTA, which exhibited a surface area decrease of 53 %. The evolution of the pH, aqueous Mg concentrations, and the Mg isotopic compositions of the solutions and solids during all isotopic exchange experiments are shown in Fig. 5.3.

The pH of the isotope exchange experiments exhibits some variation, notably for the experiments run in the presence of aqueous citrate, sulphate, and EDTA. These pH variations have a measurable impact on the dissolved Mg concentration in the experimental aqueous solutions. If the aqueous Mg concentration of a reactive solution during an isotope exchange experiment differed by more than 10 % from its original value, the experiment was not considered in the determination of the equilibrium fractionation factors retrieved below. The experimental runs in the presence of citrate show an increase in the aqueous Mg concentration, which stabilizes in the longest duration experiments (Fig. 5.3 C). Therefore the equilibrium fractionation factor was determined using: i) all measured isotopic data and, ii) only the data from long duration runs exhibiting constant aqueous Mg concentration. Note that after an initial increase in the pH and aqueous Mg concentration, the conditions of the experiments run in the presence of aqueous EDTA remained constant and were considered as equilibrium conditions (Fig. 5.3 F).

Table 5.5 - Overview of the results of the isotopic exchange experiments performed in this study. a denotes the spiked initial solution. Uncertainties of the isotopic measurements are expressed as 2 SD (Standard Deviation) and 2 SE (Standard Error). The 2 SE is computed following the relation: SE=SD/√((n-1))×t, where n denotes the number of measurements performed and t denotes the Student t-factor (Platzner et al., 1997). δ_{eq} represents the equilibrium isotopic composition of ^{25}Mg and F denotes the degree of isotopic exchange.

Exp.	Time	pH	Mg-conc.	S_{BET}	*solution*						*brucite*						δ^{25}_{eq}	$F_{sol.}$	ln(1-F)
	[d]		[ppm]	[m^2/g]	δ^{25}Mg [‰]	2SD [‰]	2SE [‰]	δ^{26}Mg [‰]	2SD [‰]	2SE [‰]	δ^{25}Mg [‰]	2SD [‰]	2SE [‰]	δ^{26}Mg [‰]	2SD [‰]	2SE [‰]	[‰]		
BB:																	5.15		
BB 0	0	9.4	2019.0	30.5	***0.02***	*0.08*	*0.10*	***0.04***	*0.07*	*0.08*	***-0.01***	*0.10*	*0.04*	***-0.02***	*0.20*	*0.08*			
BB 0 - S[a]	0	9.0	2084.0		***20.05***	*0.04*	*0.05*	***0.16***	*0.04*	*0.05*	***-0.01***	*0.10*	*0.04*	***-0.02***	*0.20*	*0.08*		0.000	0.00
BB 1	0.06	9.3	2129.6		***18.95***	*0.03*	*0.04*	***0.19***	*0.03*	*0.03*	***0.16***	*0.04*	*0.06*	***0.11***	*0.06*	*0.07*		0.073	-0.08
BB 2	1	9.3	2157.4		***18.60***	*0.01*	*0.01*	***0.15***	*0.04*	*0.05*	***0.20***	*0.04*	*0.05*	***0.06***	*0.02*	*0.03*		0.097	-0.10
BB 3	3	9.3	2146.2		***18.62***	*0.13*	*0.07*	***0.17***	*0.22*	*0.11*	***0.26***	*0.03*	*0.04*	***0.07***	*0.05*	*0.06*		0.096	-0.10
BB 4	10	9.3	2149.8		***18.43***	*0.18*	*0.09*	***0.15***	*0.22*	*0.12*	***0.29***	*0.05*	*0.06*	***0.09***	*0.10*	*0.12*		0.109	-0.12
BB 5	15	9.4	2098.7		***18.34***	*0.17*	*0.09*	***0.13***	*0.22*	*0.11*	***0.23***	*0.05*	*0.06*	***0.02***	*0.12*	*0.15*		0.115	-0.12
BB 6	42	9.5	2089.1		***18.12***	*0.10*	*0.04*	***0.18***	*0.24*	*0.10*	***0.29***	*0.04*	*0.05*	***0.01***	*0.00*	*0.00*		0.129	-0.14
BB 7	330	9.3	1743.0		***16.31***	*0.12*	*0.05*	***0.28***	*0.13*	*0.05*	***0.79***	*0.00*	*0.00*	***0.03***	*0.03*	*0.03*		0.251	-0.29
BB 8	522	9.4	2031.1	40.1	***15.59***	*0.10*	*0.04*	***0.33***	*0.12*	*0.05*	***1.04***	*0.05*	*0.06*	***0.02***	*0.08*	*0.10*		0.299	-0.36
BABE:																	0.95		
BABE 0	0	9.4	2019.9	33.0	***0.06***	*0.07*	*0.04*	***0.13***	*0.14*	*0.08*	***0.02***	*0.13*	*0.05*	***0.02***	*0.19*	*0.08*			
BABE 0 - S[a]	0	9.4	2002.7		***18.25***	*1.85*	*0.97*	***0.30***	*0.58*	*0.30*	***0.02***	*0.13*	*0.05*	***0.02***	*0.19*	*0.08*		0.000	0.00
BABE 1	5	9.4	2084.3		***11.99***	*0.05*	*0.06*	***0.21***	*0.07*	*0.08*	***0.21***	*0.12*	*0.06*	***-0.04***	*0.18*	*0.09*		0.362	-0.45
BABE 2	10	9.2	2105.7		***10.95***	*0.05*	*0.06*	***0.29***	*0.07*	*0.09*	***0.24***	*0.05*	*0.06*	***-0.09***	*0.07*	*0.09*		0.422	-0.55
BABE 3	29	9.3	1966.9		***10.73***	*0.04*	*0.05*	***0.22***	*0.06*	*0.07*	***0.37***	*0.02*	*0.02*	***-0.04***	*0.05*	*0.06*		0.435	-0.57
BABE 4	62	9.3	1939.0		***9.57***	*0.17*	*0.10*	***0.17***	*0.31*	*0.19*	***0.49***	*0.12*	*0.07*	***-0.03***	*0.16*	*0.10*		0.502	-0.70
BABE 5	95	9.2	2002.4		***9.55***	*0.14*	*0.09*	***0.17***	*0.14*	*0.09*	***0.52***	*0.06*	*0.03*	***0.07***	*0.14*	*0.09*		0.503	-0.70
BABE 6	130	9.4	2107.3		***8.77***	*0.04*	*0.02*	***0.20***	*0.06*	*0.04*	***0.48***	*0.08*	*0.07*	***-0.05***	*0.15*	*0.12*		0.548	-0.79
BABE 7	161	9.1	2119.3		***8.64***	*0.09*	*0.05*	***0.08***	*0.18*	*0.09*	***0.51***	*0.05*	*0.04*	***0.01***	*0.15*	*0.12*		0.556	-0.81
BABE 8	304	9.3	2166.7	30.5	***7.46***	*0.06*	*0.07*	***0.13***	*0.04*	*0.05*	***0.44***	*0.04*	*0.05*	***-0.03***	*0.05*	*0.06*		0.624	-0.98

Table 5.5 - continued

Exp.	Time	pH	Mg-conc.	S_{BET}	*solution*						*brucite*						δ^{25}_{eq}	$F_{sol.}$	ln(1-F)
	[d]		[ppm]	[m^2/g]	δ^{25}Mg	2SD	2SE	δ^{26}Mg	2SD	2SE	δ^{25}Mg	2SD	2SE	δ^{26}Mg	2SD	2SE	[‰]		
					[‰]	[‰]	[‰]	[‰]	[‰]	[‰]	[‰]	[‰]	[‰]	[‰]	[‰]	[‰]			
BBC																	0.45		
BBC 0	0	10.1	148.0	30.5	***0.02***	*0.03*	*0.01*	***0.05***	*0.06*	*0.03*	***-0.01***	*0.10*	*0.04*	***-0.02***	*0.20*	*0.08*			
BBC 0 - S[a]	0	10.2	146.0		***26.33***	*0.08*	*0.04*	***0.26***	*0.11*	*0.06*	***-0.01***	*0.10*	*0.04*	***-0.02***	*0.20*	*0.08*		0.000	0.00
BBC 1	0.06	10.3	200.8		***15.83***	*0.02*	*0.02*	***0.20***	*0.03*	*0.04*	***0.05***	*0.01*	*0.01*	***-0.04***	*0.03*	*0.04*		0.406	-0.52
BBC 2	1	10.3	200.4		***14.17***	*0.02*	*0.03*	***0.19***	*0.05*	*0.06*	***0.09***	*0.03*	*0.04*	***-0.02***	*0.03*	*0.04*		0.470	-0.64
BBC 3	3	10.1	194.2		***14.38***	*0.03*	*0.03*	***0.12***	*0.04*	*0.05*	***0.10***	*0.05*	*0.07*	***-0.03***	*0.05*	*0.07*		0.462	-0.62
BBC 4	10	10.4	197.3		***12.99***	*0.02*	*0.03*	***0.12***	*0.04*	*0.05*	***0.12***	*0.02*	*0.03*	***-0.01***	*0.03*	*0.04*		0.516	-0.72
BBC 5	15	10.1	196.1		***13.16***	*0.01*	*0.02*	***0.11***	*0.01*	*0.02*	***0.12***	*0.04*	*0.05*	***-0.03***	*0.05*	*0.06*		0.509	-0.71
BBC 6	42	10.1	200.3		***12.36***	*0.01*	*0.02*	***0.06***	*0.03*	*0.04*	***0.14***	*0.03*	*0.03*	***0.01***	*0.04*	*0.06*		0.540	-0.78
BBC 7	284	9.8	291.9		***9.04***	*0.08*	*0.04*	***0.31***	*0.13*	*0.07*	***0.15***	*0.06*	*0.07*	***0.02***	*0.04*	*0.05*		0.668	-1.10
BBC 8	476	9.9	293.2	37.3	***8.00***	*0.10*	*0.12*	***0.18***	*0.16*	*0.19*	***0.20***	*0.04*	*0.05*	***0.06***	*0.03*	*0.04*		0.709	-1.23
BCS																	1.21		
BCS 0	0	9.4	1724.0	39.4	***0.13***	*0.05*	*0.06*	***0.24***	*0.15*	*0.18*	***0.07***	*0.19*	*0.08*	***0.13***	*0.31*	*0.13*			
BCS 0 - S[a]	0	9.5	1703.3		***19.08***	*0.14*	*0.08*	***0.29***	*0.15*	*0.09*	***0.07***	*0.19*	*0.08*	***0.13***	*0.31*	*0.13*		0.000	0.00
BCS 1	5	9.5	1620.2		***13.03***	*0.04*	*0.05*	***0.45***	*0.07*	*0.09*	***0.44***	*0.10*	*0.05*	***0.15***	*0.11*	*0.06*		0.339	-0.41
BCS 2	10	9.4	1552.2		***12.08***	*0.15*	*0.09*	***0.43***	*0.27*	*0.17*	***0.51***	*0.06*	*0.04*	***0.13***	*0.13*	*0.08*		0.392	-0.50
BCS 3	29	9.3	1568.8		***13.21***	*0.15*	*0.09*	***0.41***	*0.14*	*0.09*	***0.40***	*0.01*	*0.01*	***0.14***	*0.01*	*0.01*		0.329	-0.40
BCS 4	62	9.4	1510.6		***13.33***	*0.16*	*0.10*	***0.32***	*0.31*	*0.19*	***0.50***	*0.06*	*0.08*	***0.16***	*0.12*	*0.14*		0.322	-0.39
BCS 5	95	9.3	1574.4		***11.86***	*0.11*	*0.07*	***0.27***	*0.17*	*0.11*	***0.55***	*0.15*	*0.09*	***0.21***	*0.26*	*0.16*		0.404	-0.52
BCS 6	130	9.5	1724.1		***11.72***	*0.06*	*0.07*	***0.18***	*0.08*	*0.10*	***0.60***	*0.10*	*0.04*	***0.17***	*0.15*	*0.06*		0.412	-0.53
BCS 7	161	9.4	1692.3		***11.08***	*0.05*	*0.06*	***0.16***	*0.07*	*0.09*	***0.56***	*0.03*	*0.04*	***0.12***	*0.08*	*0.09*		0.447	-0.59
BCS 8	304	9.2	1724.1	35.2	***10.10***	*0.03*	*0.04*	***0.14***	*0.06*	*0.08*	***0.60***	*0.05*	*0.07*	***0.11***	*0.06*	*0.08*		0.502	-0.70

Table 5.5 - continued

Exp.	Time	pH	Mg-conc.	S_{BET}	*solution*						*brucite*						δ^{25}_{eq}	$F_{sol.}$	ln(1-F)
	[d]		[ppm]	[m^2/g]	δ^{25}Mg	2SD	2SE	δ^{26}Mg	2SD	2SE	δ^{25}Mg	2SD	2SE	δ^{26}Mg	2SD	2SE	[‰]		
					[‰]	[‰]	[‰]	[‰]	[‰]	[‰]	[‰]	[‰]	[‰]	[‰]	[‰]	[‰]			
BDS																	0.07		
BDS 0	0	9.9	274.2	29.2	***-0.06***	*0.10*	*0.05*	***-0.13***	*0.18*	*0.10*	***0.06***	*0.11*	*0.05*	***0.14***	*0.21*	*0.09*			
BDS 0 - S[a]	0	9.9	271.0		***18.98***	*0.21*	*0.13*	***0.04***	*0.17*	*0.11*	***0.06***	*0.11*	*0.05*	***0.14***	*0.21*	*0.09*		0.000	0
BDS 1	5	9.9	471.2		***4.84***	*0.07*	*0.04*	***0.47***	*0.06*	*0.04*	***0.16***	*0.04*	*0.05*	***0.19***	*0.05*	*0.06*		0.748	-1.38
BDS 2	10	9.8	384.8		***3.49***	*0.10*	*0.06*	***0.61***	*0.06*	*0.04*	***0.18***	*0.02*	*0.02*	***0.21***	*0.03*	*0.03*		0.819	-1.71
BDS 3	29	9.8	354.4		***4.09***	*0.48*	*0.30*	***-0.05***	*0.36*	*0.22*	***0.20***	*0.10*	*0.08*	***0.17***	*0.01*	*0.01*		0.787	-1.55
BDS 4	62	9.8	369.2		***3.43***	*0.01*	*0.02*	***0.03***	*0.04*	*0.06*	***0.17***	*0.04*	*0.03*	***0.20***	*0.12*	*0.10*		0.822	-1.73
BDS 5	95	9.9	386.9		***3.23***	*0.01*	*0.01*	***0.01***	*0.04*	*0.05*	***0.20***	*0.03*	*0.03*	***0.21***	*0.05*	*0.06*		0.833	-1.79
BDS 6	130	9.8	362.9		***2.90***	*0.02*	*0.03*	***-0.01***	*0.07*	*0.09*	***0.18***	*0.03*	*0.03*	***0.20***	*0.06*	*0.08*		0.851	-1.90
BDS 7	161	9.9	362.8		***2.82***	*0.00*	*0.00*	***-0.02***	*0.03*	*0.04*	***0.18***	*0.04*	*0.05*	***0.20***	*0.06*	*0.07*		0.854	-1.93
BDS 8	263	9.9	317.9	32.9	***1.79***	*0.11*	*0.06*	***-0.09***	*0.23*	*0.12*	***0.18***	*0.03*	*0.04*	***0.15***	*0.04*	*0.05*		0.909	-2.40
BE EDTA																	-0.53		
BE EDTA - 0	0		1626.1	35.53	***-0.34***	*0.01*	*0.01*	***-0.61***	*0.05*	*0.06*	***0.09***	*0.06*	*0.03*	***0.19***	*0.05*	*0.02*			
BE EDTA - S[a]	0	12.4	1715.0		***18.07***	*0.06*	*0.02*	***-0.43***	*0.06*	*0.02*	***0.09***	*0.06*	*0.03*	***0.19***	*0.05*	*0.02*		0.000	0.00
BE EDTA - 0.5	2.5	11.9	2051.4		***7.80***	*0.07*	*0.04*	***-0.98***	*0.12*	*0.07*	***0.43***	*0.04*	*0.05*	***0.26***	*0.09*	*0.11*		0.552	-0.80
BE EDTA - 1	5	11.9	2102.2		***5.79***	*0.02*	*0.03*	***-1.31***	*0.03*	*0.04*	***0.58***	*0.05*	*0.06*	***0.26***	*0.07*	*0.09*		0.660	-1.08
BE EDTA - 2	10	11.9	2071.0		***2.80***	*0.12*	*0.15*	***-1.63***	*0.15*	*0.19*	***0.74***	*0.07*	*0.09*	***0.27***	*0.03*	*0.04*		0.821	-1.72
BE EDTA - 3	29	11.9	2012.9		***0.22***	*0.05*	*0.06*	***-2.09***	*0.09*	*0.11*	***0.84***	*0.04*	*0.05*	***0.29***	*0.06*	*0.07*		0.960	-3.22
BE EDTA - 4	62	11.9	1999.9		***-0.46***	*0.06*	*0.03*	***-2.20***	*0.03*	*0.02*	***0.84***	*0.04*	*0.03*	***0.30***	*0.09*	*0.05*		0.996	-5.64
BE EDTA - 5	104	12.0	2083.6		***-0.51***	*0.01*	*0.01*	***-2.24***	*0.09*	*0.11*	***0.70***	*0.32*	*0.14*	***0.23***	*0.14*	*0.06*		0.999	-6.64
BE EDTA - 6	131	12.1	2113.4		***-0.53***	*0.09*	*0.11*	***-2.30***	*0.04*	*0.05*	***0.77***	*0.05*	*0.06*	***0.19***	*0.08*	*0.09*		1.000	
BE EDTA - 7	131	12.2	2146.1	18.88	***-0.48***	*0.02*	*0.03*	***-2.29***	*0.05*	*0.07*	***0.76***	*0.04*	*0.06*	***0.18***	*0.05*	*0.07*		0.998	-6.01

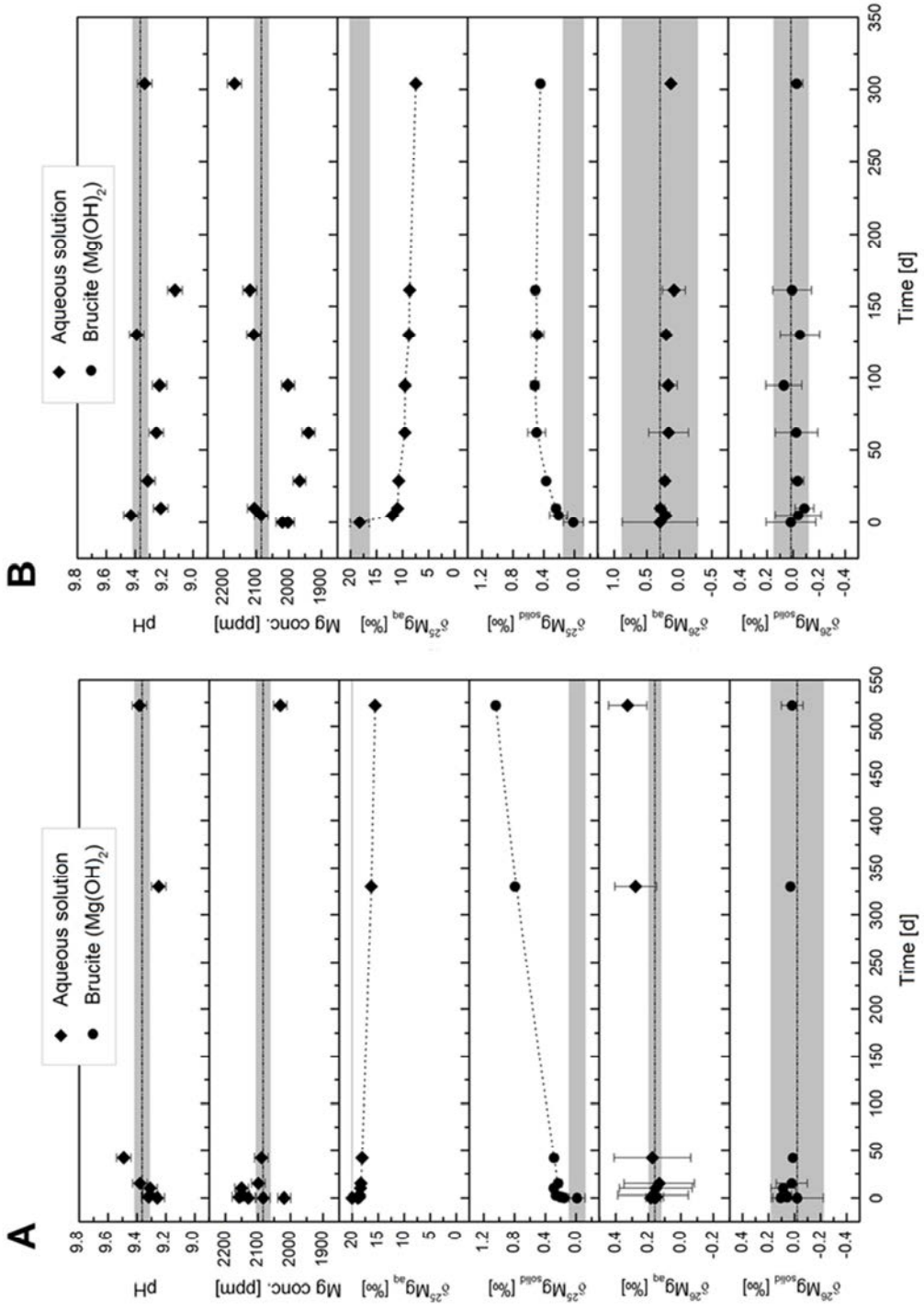
A
B
Aqueous solution
Brucite (Mg(OH)2)
pH
Mg conc. [ppm]
δ25Mgaq [‰]
δ25Mgsolid [‰]
δ26Mgaq [‰]
δ26Mgsolid [‰]
Time [d]

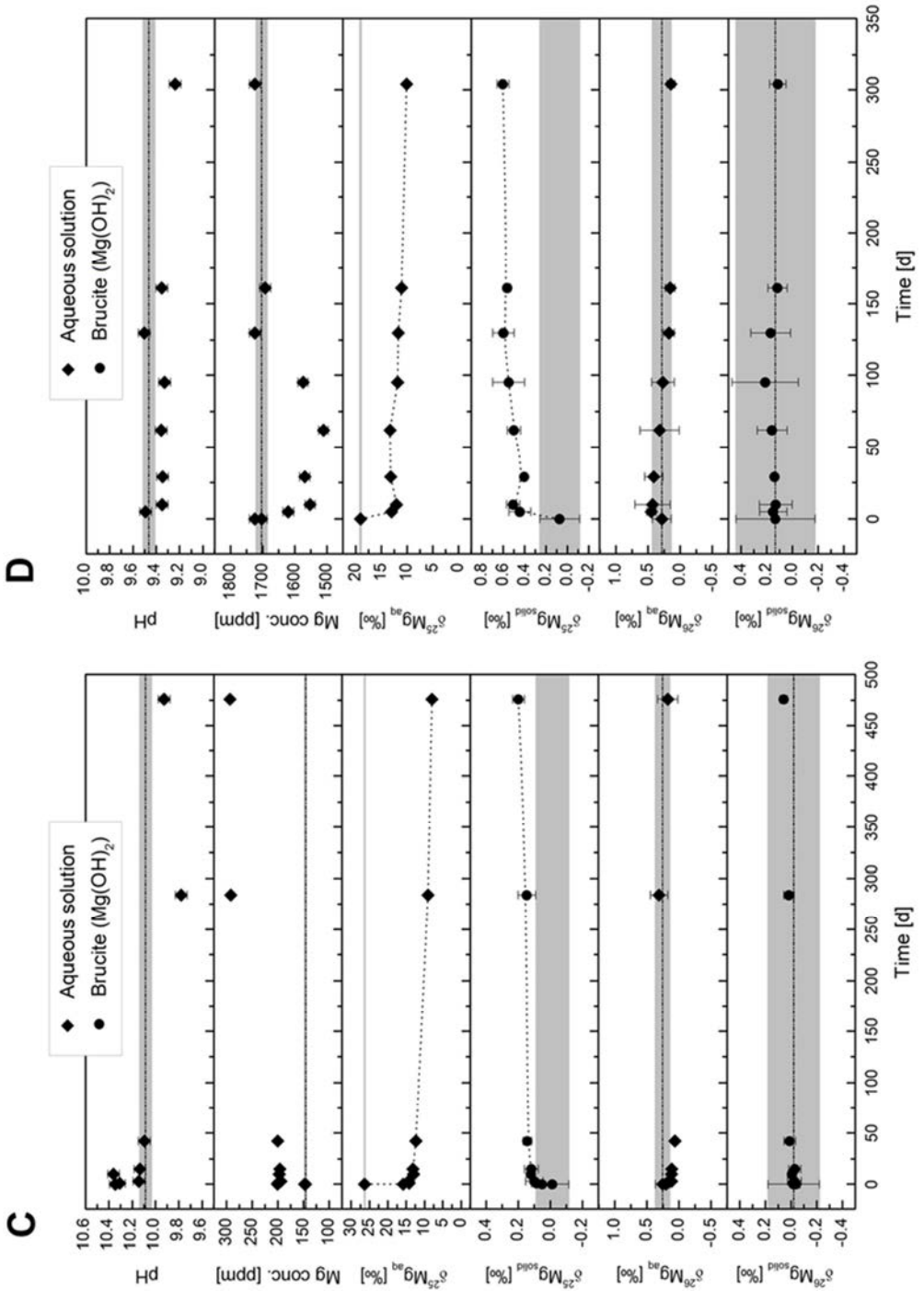
C
D
Aqueous solution
Brucite (Mg(OH)2)
pH
Mg conc. [ppm]
δ25Mgaq [‰]
δ25Mgsolid [‰]
δ26Mgaq [‰]
δ26Mgsolid [‰]
Time [d]

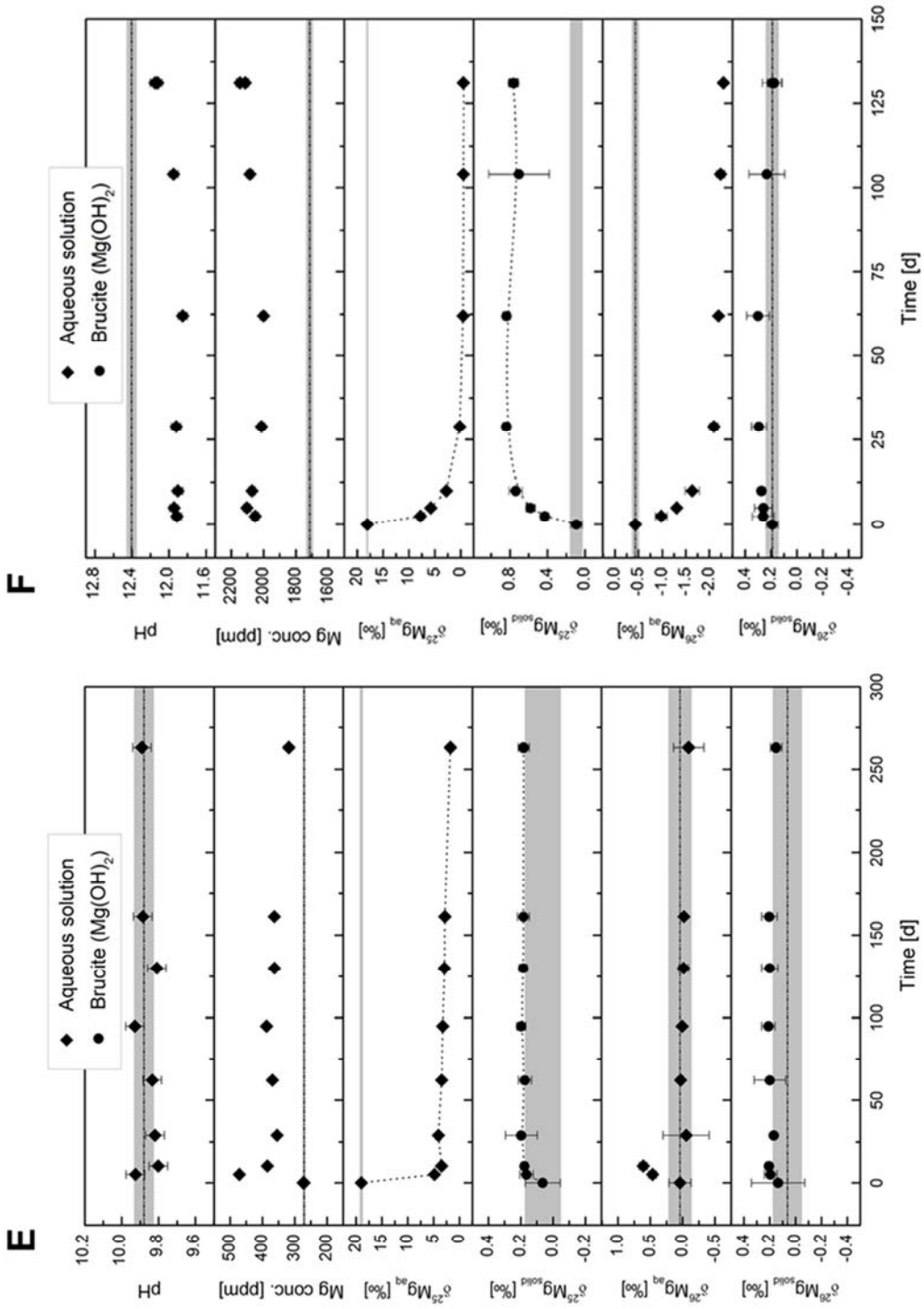

Figure 5.3 - Plots of pH, Mg concentrations and isotopic compositions of solid phase and solutions as a function of time during the second stage of each experimental series. The 2 S.D. uncertainties of data points are denoted by the error bars. Initial values are represented by dashed lines with their 2 S.D. error envelope (grey shades). A. No inorganic or organic ligand (BB) , B: No inorganic or organic ligand (BABE) C. Mg citrate experiment (BBC), and D. Mg sulphate experiment (BCS), E. Mg sulphate experiment (BDS), F. Mg EDTA experiment (BE-EDTA).

In all experimental series, the δ^{25}Mg values of the solutions and solids, shown in Fig. 5.3 and given in Table 5.5, mirror one another. The δ^{25}Mg value of the ^{25}Mg enriched solutions decreases significantly over the first 5 days of the experiments and the corresponding δ^{25}Mg brucite powder value increases. The δ^{26}Mg values of the aqueous solutions and the powders only show small variations within uncertainty of the initial value. The only exception was the experiments run in the presence of aqueous EDTA. These experiments show significant decreasing of aqueous δ^{26}Mg with time, while the δ^{26}Mg of the corresponding brucite powder increases slightly.

5.3.3. Determination of magnesium equilibrium isotope fractionation factors

Equilibrium fractionation factors, $\Delta_{eq}{}^{26}Mg_{brucite\text{-}\ solution,}$ were determined using the three-isotope method as described in previous studies (e.g. Li et al., 2011, 2014; Zheng et al., 2016; Stamm et al., 2019). In accord with this method, the measured $\delta^{26}Mg_{aq}$ and $\delta^{26}Mg_{brucite}$ values are plotted as a function of the degree of isotopic exchange (*F*). The degree of isotopic exchange was calculated using:

$$F = \frac{(\delta_t - \delta_i)}{(\delta_e - \delta_i)} \tag{5.12}$$

where δ_t denotes the isotopic composition of either one of the phases at any time *t* during the reaction, and δ_i and δ_e describe the initial and equilibrium isotopic composition of this phase. *F* increases from 0 to 1 as isotopic equilibrium is attained. A more detailed description of the determination of *F* can be found in previous studies (Li et al., 2011; Zheng et al., 2016; Stamm et al., 2019). As isotopic exchange of this two-phase system is incomplete in the experimental series performed in this study, these compositions can be extrapolated to 100 % isotopic exchange (*F*=1). The δ-*F* plots for all experiments performed in this study are shown in Fig. 5.4 and the resulting $\Delta_{eq}{}^{26}Mg_{brucite\text{-}solution}$ generated from the extrapolation are listed in Table 5.6.

The equilibrium Mg isotope fractionation factors between brucite and aqueous solution at 25°C in the absence of either aqueous organic ligands or aqueous sulphate, $\Delta_{eq}{}^{26}Mg_{brucite\text{-}\ solution}$ was determined to be -0.62 ± 0.72 ‰ and -0.09 ± 0.21 ‰ for powder to solution ratio of 0.02 (series BB, Fig. 5.4A) and 0.1 (series BABE, Fig 4B), respectively. Two equilibrium Mg isotope fractionation factors for experiments containing aqueous citrate were determined, $\Delta_{eq}{}^{26}Mg_{brucite\text{-}\ solution}$= -0.07± 0.21 ‰ and -0.17± 0.10 ‰ for a fraction of $Mg(citrate)^-$ in solution of 0.51 and 0.44, respectively (Fig. 5.4 C and D).

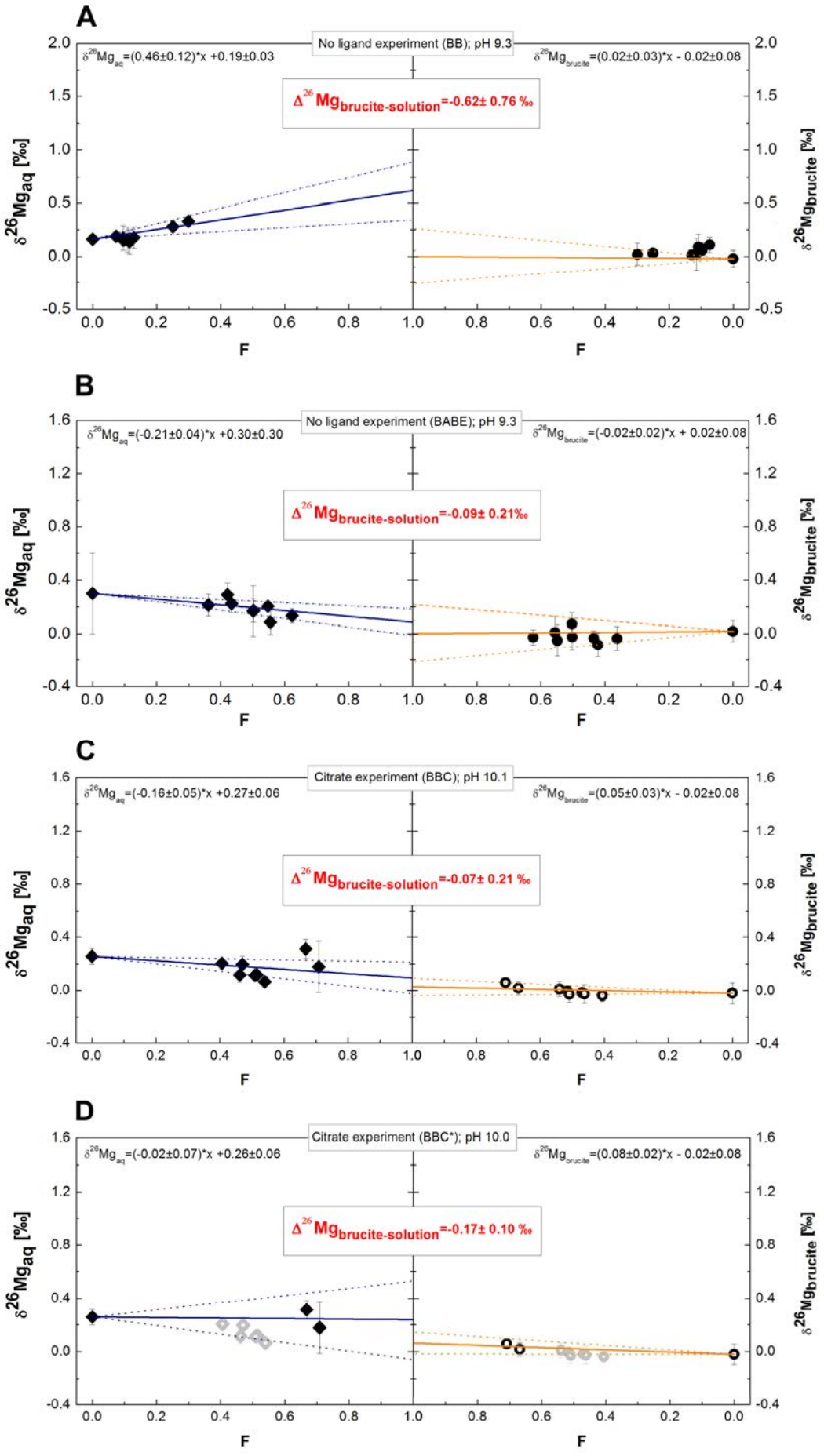
A
No ligand experiment (BB); pH 9.3
δ26Mgaq=(0.46±0.12)*x +0.19±0.03
δ26Mgbrucite=(0.02±0.03)*x - 0.02±0.08
Δ26Mgbrucite-solution=-0.62± 0.76 ‰
δ26Mgaq [‰]
δ26Mgbrucite [‰]
F
B
No ligand experiment (BABE); pH 9.3
δ26Mgaq=(-0.21±0.04)*x +0.30±0.30
δ26Mgbrucite=(-0.02±0.02)*x + 0.02±0.08
Δ26Mgbrucite-solution=-0.09± 0.21‰
C
Citrate experiment (BBC); pH 10.1
δ26Mgaq=(-0.16±0.05)*x +0.27±0.06
δ26Mgbrucite=(0.05±0.03)*x - 0.02±0.08
Δ26Mgbrucite-solution=-0.07± 0.21 ‰
D
Citrate experiment (BBC*); pH 10.0
δ26Mgaq=(-0.02±0.07)*x +0.26±0.06
δ26Mgbrucite=(0.08±0.02)*x - 0.02±0.08
Δ26Mgbrucite-solution=-0.17± 0.10 ‰

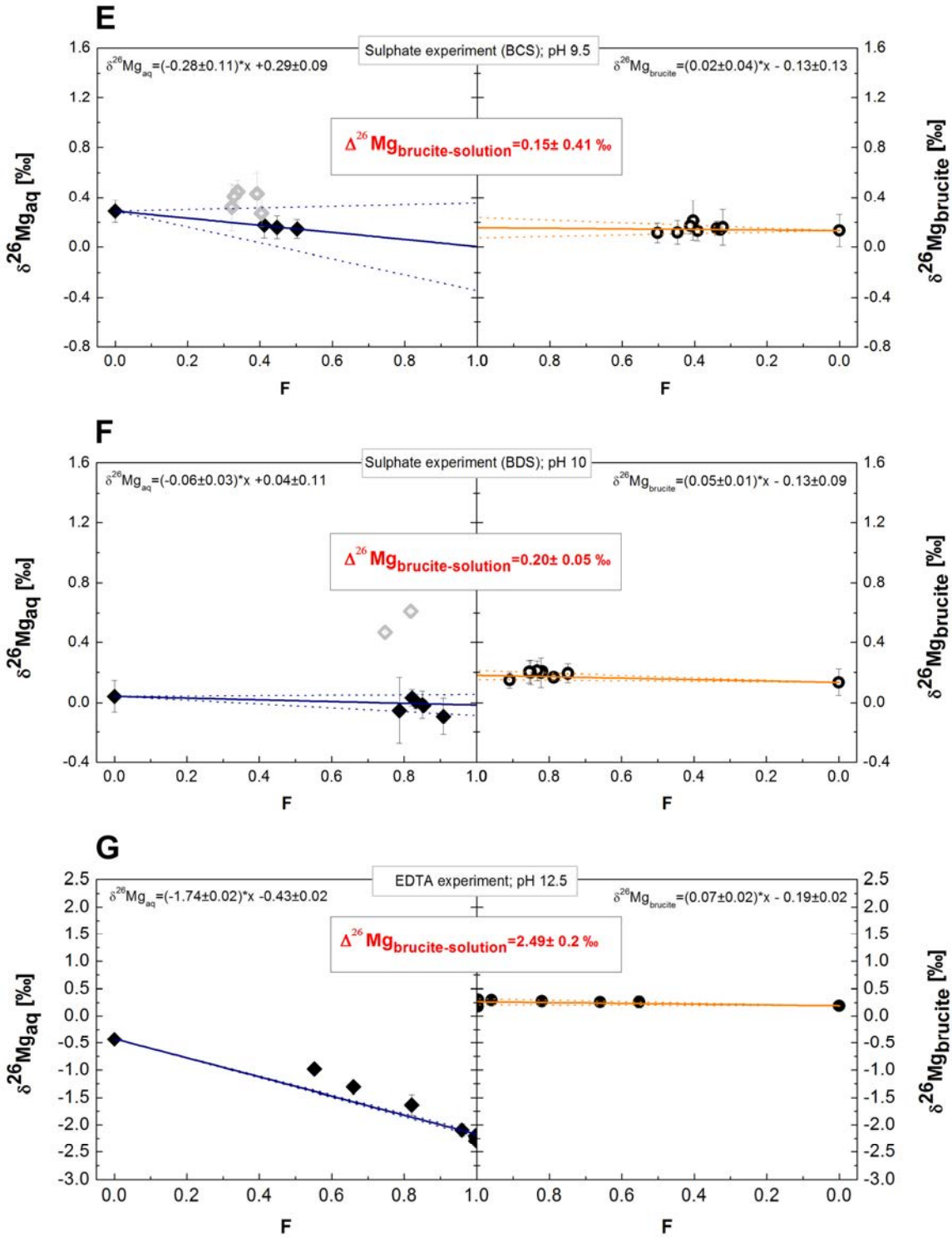

Figure 5.4 - Plots of the isotopic composition of the solid phase and solutions as a function of the degree of isotope exchange during the second stage of each experimental series. A. No inorganic or organic ligand (BB) , B: No inorganic or organic ligand (BABE) C. Mg citrate experiment using all isotopic data (BBC), D. Mg citrate experiment using only the two solutions of longest duration (BBC*), E. Mg sulphate experiment (BCS), F. Mg sulphate experiment (BDS), G. Mg EDTA experiment (BE-EDTA). Excluded data from the fit are shown by grey symbols – see section 5.3.2.

Table 5.6 - Average aqueous Mg-speciation during the second stage of each experimental series run in this study together with the resulting isotopic fractionation factors between brucite and solution, brucite and the Mg^{2+} species, and between Mg^{2+} and the different solutions species Mg (citrate)$^-$, $MgSO_4^o$, and $Mg(EDTA)^{2-}$ denoted as i.

Exp.	pH	Mg-conc. [mmol]	$\Delta^{26}Mg_{brucite-solution}$	err	Speciation							$\Delta^{26}Si_{brucite-Mg2+}$	err	$\Delta^{26}Si_{brucite-i}$	err	$\Delta^{26}Si_{Mg2+-i}$	err
			‰	‰	Mg^{2+} %	Mg(citrate)$^-$ %	$MgSO_4$ %	$MgEDTA^{2-}$ %	MgHEDTA$^-$ %	‰	‰	‰	‰	‰	‰	‰	‰
BB	9.3	85.2	-0.62	0.72	100.00					-0.36	0.38						
BABE	9.3	84.5	-0.09	0.21	100.00												
BBC	10.1	8.8	-0.07	0.21	49.35	50.65						0.21	0.21	-0.14	0.22		
BBC*	10.0	10.0	-0.17	0.10	55.55	44.45						0.06	0.19	-0.29	0.21		
BCS	9.4	70.4	0.15	0.41	64.72		35.28					1.08	0.28	0.72	0.23		
BDS	9.9	14.3	0.20	0.05	34.73		65.27					0.50	0.19	0.14	0.21		
BE-EDTA	12.0	83.6	2.43	0.20	0.00			98.98	1.02			2.43	0.20	2.08	0.21		

The equilibrium Mg isotope fractionation factors between brucite and aqueous sulphate solutions were determined to be 0.15 ± 0.41 ‰ and 0.20 ± 0.05 ‰ for a fraction of aqueous $MgSO_4^o$ complexes in solution equal to ~0.35 (Fig. 5.4 E) and 0.65 (Fig. 5.4 F), respectively. The value of $\Delta_{eq}{}^{26}Mg_{brucite\text{-}\ solution}$ measured in the presence of EDTA (~ 100% $Mg(EDTA)^{2-}$ in solution) (Fig. 5.4 G) is as high as +2.43 ± 0.20 ‰.

The average value of the equilibrium fractionation factor between brucite and Mg^{2+} determined in this study is $\Delta_{eq}{}^{26}Mg_{brucite\text{-}Mg^{2+}} = -0.36 \pm 0.38$ ‰. The values derived from Mg aqueous speciation using Eqn. (5.9) of the fractionation factors between brucite and the Mg aqueous complexes investigated in this study are listed in Table 5.6. The equilibrium fractionation factors between Mg^{2+} and the Mg aqueous complexes derived from these values and the equilibrium fractionation factor between brucite and Mg^{2+} are also reported in Table 5.6. The equilibrium fractionation factor between aqueous Mg^{2+} and $Mg(citrate)^-$ $\Delta_{eq}{}^{26}Mg_{Mg^{2+}\text{-}Mg(citrate)^-}$ was determined to be in the range between -0.14 ± 0.22 and -0.29 ± 0.21 ‰ and that between Mg^{2+} and $MgSO_4^o$ ranges between 0.72 ± 0.23 and 0.14 ± 0.21 ‰. The $\Delta_{eq}{}^{26}Mg$ between Mg^{2+} and $Mg(EDTA)^{2-}$ exhibits a significant positive fractionation of 2.08 ± 0.21 ‰.

5.3.4. Isotope exchange kinetics

The kinetics of isotopic exchange can be also quantified using the 'three-isotope method'. The rate with which isotopic equilibrium is attained helps define the mechanism of the isotopic equilibration. The degree of isotopic exchange (*F*) is plotted as a function of time in Fig. 5.5. The isotopic exchange rates of the experiments in this study were determined using (Cole and Chakraborty, 2001; Johnson et al., 2002):

$$\frac{-d(1-F)}{dt} = k_n(1-F)^n \tag{5.13}$$

where *k* is the rate constant and *n* the order of reaction. Isotope exchange rates follow either a first-order (*n*=1) or a second-order (*n*=2) rate law (Criss et al., 1987; Huang and Tsai, 1970; Johnson et al., 2002; Welch et al., 2003; Li et al., 2011; Zheng et al., 2016). A first-order reaction was assumed to be consistent with both Eqn. (5.11) and the brucite dissolution rates measured in the present study. The integrated form of Eqn. (5.13) can for a first order reaction be written as:

$$\ln(1-F) = -k_1 t. \tag{5.14}$$

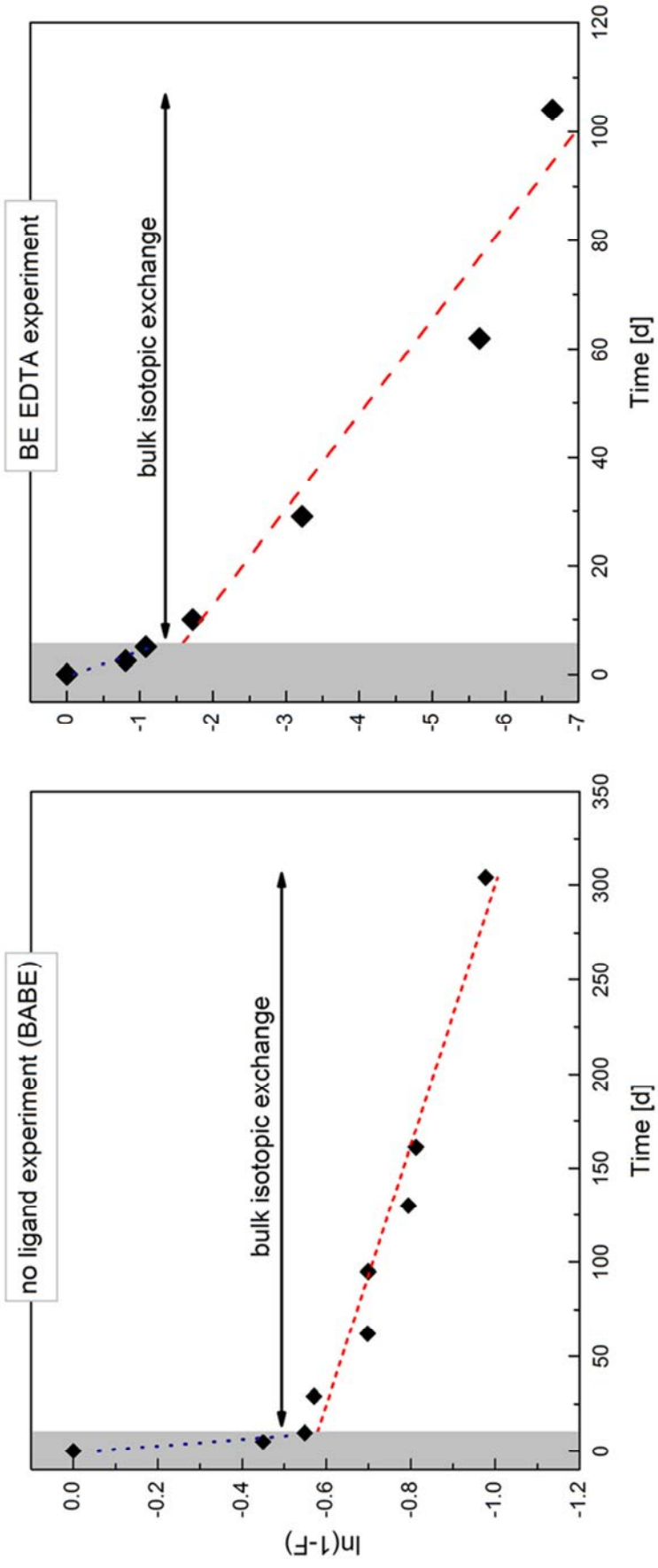

Figure 5.5 – Representative plots of the experiment without inorganic or organic ligands (BABE) and the experiment performed with aqueous EDTA in solution. The blue dotted lines denote the are used to determine the rate of the initial or surface exchange (grey area). The bulk isotope exchange rates are derived using the red dashed lines.

An example of the temporal evolution of the degree of ion exchange for the ligand free experiment (BABE) and the experiment in the presence of EDTA (BE EDTA) are shown in Fig 5.5. In both cases an initial fast isotope exchange rate is followed, after few days, by a much slower exchange rate in agreement with Eqn. (5.14), the first order rate law. Note that the isotope exchange rate constant derived from Eqn. (5.14) is 2.92×10^{-11} mol/m^2/s for the inorganic system but 4.54×10^{-13} mol/m^2/s in the presence of EDTA. Values of the initial and first-order rate constants ('bulk' rate constants) for isotope exchange are listed in Table 5.7 and compared to the values of brucite dissolution rate derived in the present study from Eqn. (5.11). It can be seen that the values of the initial rate constant for Mg isotope exchange are comparable (within one order of magnitude) to the bulk brucite dissolution rate constants generated during the first step of each experimental series. The longer-term rates, however are about 3 to 4 orders of magnitude slower than their corresponding bulk brucite dissolution rate constants except in the presence of EDTA. These results are shown in Figure 5.6 where the measured and calculated variation of the degree of isotopic exchange *F* are shown as a function of time.

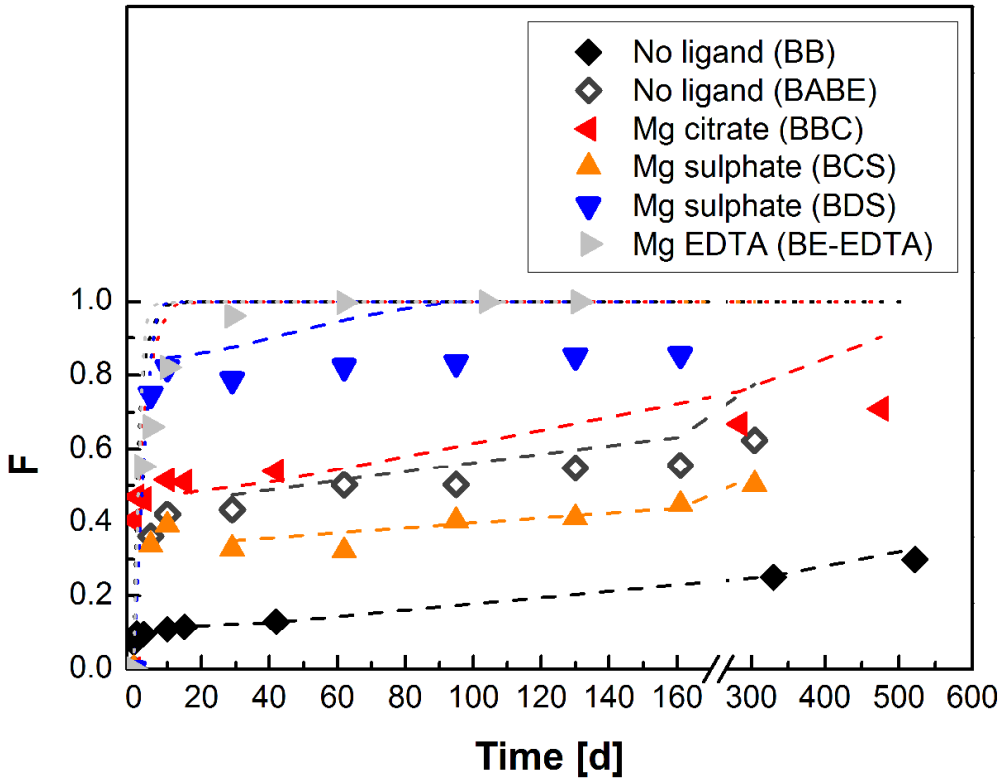

Figure 5.6 - The temporal evolution of the degree of isotopic exchange F during the six experimental series run this study. Dotted lines are generated assuming a first order rate law (Eqn. 5.14), using the dissolution rate constants from the brucite dissolution rate experiments (Table 5.4) performed as the first stage of each experimental series. Dashed lines are generated assuming first order rate law, using the bulk isotopic rate constants shown in Table 5.7

It can be seen that *F* calculated values using bulk brucite dissolution rates (doted lines) are much higher than the corresponding measured *F* values (they predict attainment of isotope equilibrium in about 15 days) but that the bulk dissolution rate constants provide a reasonable fit of *F* values (dashed lines) for reaction times ≥ 20 days.

5.4. Discussion

5.4.1. Magnesium isotope fractionation between brucite and Mg^{2+}

The average value at 25°C of the equilibrium Mg isotope fractionation factor between brucite and aqueous solution in the absence of aqueous organic and inorganic ligands is $\Delta_{eq}{}^{26}Mg_{brucite-\ solution}$= -0.36 ± 0.38‰. This value corresponds to the equilibrium isotope fractionation between brucite and aqueous Mg^{2+}, as 96% of dissolved Mg in these experiments is present as Mg^{2+} (see Table 5.6). This value is identical, within uncertainty, to that reported at 20 °C by Li et al. (2014) based on brucite recrystallization and synthesis experiments performed at brucite-aqueous solution chemical equilibrium using the three isotope method, $\Delta_{eq}{}^{26}Mg_{brucite-\ solution}$= -0.17 ± 0.07 ‰. The results of the present study and those reported by Li and co-workers (2014) indicate that light Mg is preferentially incorporated in brucite crystal lattice at temperatures from 20° to 40°C. This slight enrichment of the solid in light Mg isotopes can be attributed to the slightly shorter average Mg-O bond length in the octahedral Mg aquo ion (2.08/2.09 Å; Schott et al., 2016) compared to the corresponding average bond length in brucite octahedrons (2.100-2.093 Å; Catti et al., 1995; Chakoumakos et al., 1997). In contrast, Wimpenny et al. (2014) reported a $\Delta_{eq}{}^{26}Mg_{brucite\text{-}Mg^{2+}} \approx 0.5$ ‰ at 80°C based on brucite synthesis experiments similar to those of Li et al. (2014), which reflects the incorporation of heavy Mg into the brucite structure. Li et al. (2014) suggested, that this implies a reverse fractionation from positive to negative with decreasing temperature. As this type of behaviour was only previously observed for O, H, and C isotopes, it seems likely that the difference in the direction of Mg isotope fractionation with temperature could be due to kinetic factors, which might occur during the quenching of the experiment from 80°C to ambient temperature (Li et al., 2014).

The fractionation factors between brucite and aqueous Mg^{2+} determined by *ab initio* calculations suggest an enrichment of heavy Mg isotopes incorporated into brucite. The values of $\Delta_{eq}{}^{26}Mg_{brucite\text{-}Mg^{2+}}$ at 25°C recommended by Colla et al. (2018) and Gao et al. (2018) are equal to +3.14 ‰ and + 2.7/2.9 ‰, respectively. The large discrepancy between the values obtained in the present and other ambient temperature experimental studies and

the *ab initio* calculations remains unclear (Gao et al., 2018). It may originate in uncertainties associated with quantum chemistry calculations, for example Colla et al., (2018) noted that density functional theory (DFT) overestimates the Mg-O bond distances in the aqueous ion and therefore underestimates the reduced partition function ratio for aqueous Mg ions. Also, because of the very slow desolvation rate of the Mg aquo ion, it is possible that incorporation of hydrated Mg^{2+} into brucite during isotope exchange experiments at ambient temperature could affect the measured Mg isotope fractionation. In any case, because the mean Mg-O bond distances in the Mg aquo ion and in brucite are very close to each other, only a small degree of isotope fractionation between brucite and Mg^{2+}(aq) might be expected. This is consistent with preliminary *ab initio* calculations performed for this study, which suggest an equilibrium fractionation factor between brucite and aqueous Mg^{2+} of 0.8 ± 0.2 ‰ at 25 °C (pers. comm. Merlin Méheut). This is significantly smaller than the values recommended by Colla et al. (2018) and Gao et al. (2018), and closest to being consistent to the value suggested by Wimpenny et al. (2014).

5.4.2. Magnesium isotope fractionation between Mg^{2+} and aqueous Mg organic and inorganic complexes

The values of $\Delta_{eq}{}^{26}Mg_{Mg^{2+}\text{-}Mg(citrate)}$ determined in this study are – 0.14 ± 0.22 ‰ and -0.29 ± 0.21 ‰. These values are significantly smaller than that derived by Schott et al. (2016) from DFT calculations, who suggested that $\Delta_{eq}{}^{26}Mg_{Mg^{2+}\text{-}Mg(citrate)}$= -3 ‰. Although the values determined in this study are significantly smaller than the theoretically calculated values of Schott et al. (2016), they do suggest an enrichment of Mg^{2+} in ^{24}Mg isotopes, consistent with shorter Mg-O bonds in aqueous Mg citrate compared to the Mg aquo ion (Schott et al., 2016).

The average value of the equilibrium isotope fractionation factor between aqueous Mg^{2+} and aqueous $MgSO_4^o$ determined in this study is $\Delta_{eq}{}^{26}Mg_{Mg^{2+}\text{-}MgSO_4^o}$ = 0.43 ± 0.16 ‰. This value differs from the DFT estimates of Schott et al. (2016), who reported a $\Delta_{eq}{}^{26}Mg_{Mg^{2+}\text{-}MgSO_4^o}$ of -2.62 ‰. The value of Schott et al. (2016) suggests, unlike the value of this study, that Mg^{2+} would preferentially incorporate ^{24}Mg isotopes. Additional information on the isotope fractionation between Mg^{2+} and $MgSO_4^o$ could be obtained from the value of the fractionation factor between epsomite ($MgSO_4 \cdot 7H_2O$) and Mg^{2+}. Using the three-isotope method, Li et al. (2011) reported a value of Mg isotope fractionation factor between epsomite and an aqueous solution in equilibrium with this mineral, $\Delta_{eq}{}^{26}Mg_{epsomite\text{-}\ solution}$=

0.58 ± 0.16 ‰ at 20°C. PHREEQC speciation calculations show that in the solution equilibrated with epsomite 81 % of dissolved Mg is present as $MgSO_4^o$ and only 19% as Mg^{2+}. Using the values of $\Delta_{eq}{}^{26}Mg_{Mg^{2+}\text{-}MgSO_4^o}$ = -2.62 ‰ and + 0.43 ‰ reported by Schott et al. (2016) and in this study, respectively, values of $\Delta_{eq}{}^{26}Mg_{epsomite\text{-}Mg^{2+}}$ equal to + 2.7 and 0.3 ‰, respectively, can be calculated at 20°C. The strong fractionation between epsomite and Mg^{2+} implied by the $MgSO_4$° reduced partition function ratio reported by Schott et al. (2016) is unlikely because it is not consistent with the similar Mg-O bond lengths of the Mg aquo ion (2.08/2.09 Å) and epsomite (2.09 Å; Baur, 1964). In contrast, the weak fractionation between epsomite and Mg^{2+} (0.3 ‰) found in this study is consistent with these structural considerations. It should be noted that the value of the reduced partition function ratio reported by Schott et al. (2016) was based on a calculated optimized structure of $MgSO_4$° in which the sulphate ligand replaces a water molecule of the first coordination sphere in the Mg aquo ion, thus forming an inner-sphere complex with magnesium. The measured isotopic fractionation between sulphate-rich solutions and brucite and epsomite rather suggests that sulphate ions mostly form outer-sphere complexes with magnesium where sulphate replaces a water molecule of the second coordination sphere of the Mg aquo ion ($Mg(H_2O)_{18}{}^{2+}$) and/or double solvent separated ion pairs, which generate weaker Mg isotope fractionation. These results are in qualitative agreement with the detail dielectric relaxation spectroscopy investigation of aqueous solutions of $MgSO_4$ showing, for example, that in an aqueous 0.1 M $MgSO_4$ solution, the Mg-SO_4 inner-sphere complexes account for only 20% of the $MgSO_4$(aq) ion pairing (Buchner et al., 2004). Such uncertainties may also affect the structure of the Mg-citrate aqueous complexes and explained the observed difference between the calculated and measured value of $\Delta_{eq}{}^{26}Mg_{Mg^{2+}\text{-}Mg(citrate)}{}^{-}$.

Isotopic exchange experiments performed in the presence of aqueous EDTA yield a value of $\Delta_{eq}{}^{26}Mg_{brucite\text{-}EDTA}$ equal to + 2.43 ± 0.20 ‰ at 25°C. This value is in close agreement with corresponding results of Li et al. (2014), who reported a Mg isotope fractionation factor between brucite and aqueous EDTA at 22°C ≥ + 2.0 ‰. Taking account of the results reported above on the equilibrium isotope fractionation factor between Mg^{2+} and $MgEDTA^{2-}$, $\Delta_{eq}{}^{26}Mg_{Mg^{2+}\text{-}MgEDTA^{2-}}$ was determined to be 2.08 ± 0.21 ‰. This value is similar to the results of DFT calculations reported by Schott et al. (2016) who suggested $\Delta_{eq}{}^{26}Mg_{Mg^{2+}\text{-}MgEDTA^{2-}}$ = + 1.7 ‰. This result implies that Mg forms weaker bonds in $MgEDTA^{2-}$ than in Mg^{2+}, as Mg^{2+} is relatively enriched in heavy ^{26}Mg. This fractionation factor is consistent with the relative Mg-O bond lengths, with average Mg-O bond length in

the aqueous Mg-EDTA complex equal to 2.17 Å (Pozhidaev et al., 1974) and thus longer than the Mg-O bond length in brucite (2.08/2.09 Å; Schott et al., 2016).

The Mg isotope exchange experiments performed in this present study show that the Mg equilibrium isotope fractionation between a mineral and its co-existing aqueous solution is highly depending on Mg speciation in the aqueous phase. The results also show, that there are still significant disagreements between *ab initio* calculations and experimental determinations of equilibrium Mg isotope fractionation factors. Understanding and resolving these differences is crucial to precisely determine the Mg isotope fractionation in the presence of various inorganic and organic ligands and to accurately interpret the Mg isotopic signatures of minerals formed in natural environments.

5.4.3. Mg isotope exchange kinetics

The rates of isotopic equilibration determined in this study, as illustrated by Fig. 5.6, provide some insight into the processes controlling isotope exchange between brucite and solution. The dashed lines drawn through the data points in Fig 5.6, showing the variation of the degree of isotopic exchange (F) as a function of time, were calculated using the first order rate equation for isotope exchange (Eqn. 5.14), whereas the dotted curves were generated using the rate constants for brucite dissolution (Eq. 5.11). Within the first 5 to 10 days of each experimental series the, measured temporal evolution of the F values are consistent with the measured bulk brucite dissolution rates. This correspondence suggests that the rate of Mg isotopic exchange over this time period is controlled by the attachment and detachment of material at the brucite surface / fluid interface. Over these first 5 to 10 days, the degree of isotope exchange F for the experimental series run in the absence of aqueous ligands, and with aqueous citrate and sulphate reached values ranging from 0.15 to 0.8 depending on the nature of the ligand and the solid to solution ratio. After this fast initial isotopic exchange, the rate slows considerably, by about 2-3 orders of magnitude (Table 5.7). This suggests that the isotopic exchange during the later part of the experimental series is limited by a slower process, perhaps the slower transport of Mg within the solid.

Almost all experimental series performed in this study did not attain isotopic equilibrium within the series duration. The only exception is the experimental series performed in the presence of aqueous EDTA, which reaches Mg isotope equilibrium within 131 days. The rates of isotopic exchange, possibly catalysed by EDTA complexation at brucite surface, are close to the brucite dissolution rate (Table 5.7). This and the 53%

decrease of brucite specific area measured after 131 days of reaction strongly suggest a large degree of brucite recrystallization during the isotope exchange reaction.

Table 5.7 – Rate constants obtained in this study. Dissolution rate constants were calculated from the brucite dissolution experiments. Initial and bulk isotopic exchange rate constants were extracted using the first order rate law Eqn. 5.14.

		dissolution rate constants		*initial isotope exchange*		*bulk isotope exchange*	
Exp.	Mg-conc.	k'_{-}	k_{+}	$k_{initial}$	$k_{initial}$	k_{bulk}	k_{bulk}
	[mmol]	[1/s]	[mol/(m²s)]	[1/s]	[mol/(m²s)]	[1/s]	[mol/(m²s)]
BB	83.87	9.26×10^{-6}	3.87×10^{-9}	8.00×10^{-7}	1.11×10^{-10}	5.51×10^{-9}	5.83×10^{-13}
BABE	83.87	9.26×10^{-6}	3.87×10^{-9}	6.34×10^{-7}	1.67×10^{-11}	1.58×10^{-8}	4.52×10^{-13}
BBC	6.02	5.79×10^{-6}	1.87×10^{-10}	4.50×10^{-7}	6.34×10^{-12}	1.41×10^{-8}	1.63×10^{-13}
BCS	71.50	1.16×10^{-5}	4.70×10^{-9}	5.76×10^{-7}	1.56×10^{-11}	8.40×10^{-9}	2.55×10^{-13}
BDS	10.25	1.74×10^{-5}	1.08×10^{-9}	1.98×10^{-6}	1.00×10^{-11}	3.41×10^{-8}	1.54×10^{-13}
BE EDTA	75.63	2.89×10^{-6}	2.32×10^{-9}	2.499×10^{-6}	5.88×10^{-11}	6.59×10^{-7}	2.92×10^{-11}

5.4.3. Implications for natural systems

The fractionation factors obtained in this study show that the equilibrium Mg isotopic signatures of minerals depend on aqueous solution speciation. Many studies have shown that fluids originating from silicate weathering have a heavier Mg composition than their source rocks; surface waters tend to preferentially drain the light Mg isotopes from the source rocks (e.g. Tipper et al., 2006; Brenot et al., 2008; Opfergelt et al., 2012). In the present study, however, results demonstrate that the Mg in aqueous solutions in the absence of organic ligands preferentially retains light Mg isotopes when precipitating brucite. Other Mg bearing minerals, however, could preferentially incorporate light Mg. For example, dolomite appears to preferentially incorporate light Mg; Li et al. (2012) and Mavromatis et al. (2013) reported that Mg in dolomite is 2.5 to 3.5 ‰ lighter than its coexisting fluid. Indeed, Li et al. (2014) noted that isotope fractionation depends on both the aqueous bonding environment and the identity of the mineral precipitating in the system.

In the presence of organic and inorganic ligands, the equilibrium Mg isotopic fractionation between brucite and aqueous solutions depends strongly on aqueous speciation. Organically bound Mg in Mg-EDTA species exhibits a equilibrium Mg isotopic fractionation factor of > 2 ‰, suggesting that the water in organic-rich environments such as soils will tend to preferentially remove light Mg (Li et al., 2014). This observation can therefore explain the preferential uptake of heavy Mg isotopes into plants, as aqueous organic Mg complexes are generally neutral or negatively charged, so unavailable for plant

uptake (Li et al., 2014). Such enrichment can be seen in nature as well as in laboratory experiments (e.g. Bolou-Bi et al., 2010; Opfergelt et al., 2014).

5.5. Conclusion

The results of this study show that the aqueous speciation of Mg can have an significant influence on its equilibrium isotope fractionation. In the absence of organic or inorganic ligands $\Delta_{eq}{}^{26}Mg_{brucite\text{-}\,solution}$ is slightly negative with a fractionation of -0.36 ± 0.38 ‰. This value contrasts with past theoretical studies, which suggested that brucite should be enriched in heavy ^{26}Mg isotopes compared with this solution. Depending on the ligand present in the aqueous phase the equilibrium fractionation factor $\Delta_{eq}{}^{26}Mg_{brucite\text{-}solution}$ can change. For example in the presence of aqueous EDTA, $\Delta_{eq}{}^{26}Mg_{brucite\text{-}solution}$ was found to be 2.43 ± 0.20 ‰. This value is in close agreement with previous experimental and theoretical studies. Results obtained for citrate and sulphate bearing solutions, however, exhibit equilibrium Mg fractionation factors between -0.07 ± 0.21 and -0.17 ± 0.10 ‰ in the presence of citrate and an average equilibrium fractionation factor of 0.18 ± 0.21 ‰ in the presence of sulphate. These results differ significantly with the corresponding results of previously reported *ab initio* calculations.

The findings of this study demonstrate that the presence of organic ligands in natural systems can influence equilibrium Mg isotopic fractionation factors between minerals and aqueous solutions. As such the Mg isotope concentrations of precipitated minerals, could potentially be used as tracer to characterize the environment in which a mineral has formed. Note, however, that the results of this study differ significantly from those previously reported from *ab initio* calculations, suggesting that these need to be revised or further validated before they can be used with confidence as isotopic tracers of natural processes.

Chapter 6

Conclusions and outlook

6.1. General conclusions and outlook (English version)

This thesis determined the effects of aqueous speciation, notably the role of aqueous inorganic and organic complexation on the equilibrium fractionation factors of Si and Mg in the amorphous SiO_2 - aqueous solution and brucite ($Mg(OH)_2$)- aqueous solution systems. Isotopic exchange experiments at bulk chemical equilibrium were performed using the three-isotope method and compared to corresponding *ab initio* calculations. In addition to providing verified equilibrium fractionation factors, this method provides the rates of isotope exchange. Evaluation of these rates provides insight into the mechanism and the conditions at which mineral isotopic signatures are generated and preserved in nature.

Towards the quantitative application of Si isotopic signatures as a tracer for weathering, pH and marine paleo-temperature, the first part of this thesis determined the equilibrium Si isotope fractionation factors between amorphous silica (SiO_2•0.32 H_2O) and inorganic aqueous fluids at pH ranging from 5.8 to 9.9 at 25° and 75°C. Experimental results show that at 25 °C, the equilibrium fractionation factor between amorphous silica and the aqueous fluid, $\Delta_{eq}{}^{30}Si_{solid\text{-}fluid}$, increases from 0.45 ± 0.20 ‰ at pH 6.4 to 1.63 ± 0.23 ‰ at pH 9.9. These fractionation factors decrease with increasing temperature, and are equal to 0.07 ± 0.06 ‰ at pH 5.8 and 1.06 ± 0.13 ‰ at pH 9.1 at 75 °C. The value obtained for pH < 7 and 25°C is in good agreement with the experimental values obtained by Roerdink et al. (2015) and Oelze et al. (2015), and the decrease of isotopic fractionation with increasing temperature follows the relationship suggested in previous theoretical and experimental studies (e.g. Urey, 1947; Bigeleisen, 1965; Schauble, 2004; Shahar et al., 2011; Huang et al., 2014). Taking into account the pH dependence of aqueous Si speciation calculated with PHREEQC, the equilibrium Si isotope fractionation factors between the two major aqueous species $H_3SiO_4^-$ and $H_4SiO_4^o$, $\Delta_{eq}{}^{30}Si_{H_3SiO_4^- - H_4SiO_4^o}$, were determined. Retrieved $\Delta_{eq}{}^{30}Si_{H_3SiO_4^- - H_4SiO_4^o}$ at 25 ° and 75 °C were determined to be -2.34 ± 0.13 ‰, and -2.21± 0.05 ‰, respectively. These values are comparable with the results of ab initio calculations reported by Dupuis et al. (2015), showing that either experimental or theoretical calculations can be used to accurately model natural processes. The results obtained in the first part of this thesis indicate that Si isotopic signatures can potentially be used as paleo pH proxies in alkaline environments, and furthermore can provide insight into the temperature of mineral precipitation. The rate of isotopic exchange in these inorganic Si systems match closely the measured bulk dissolution rates of amorphous SiO_2, indicating that the dominant mechanism for isotopic exchange in this system is the detachment and reattachment of material at the amorphous SiO_2 surface, and

not the transport within the solid. This latter observation suggests that the original Si isotope compositions incorporated in minerals could potentially be altered over time through fluid-mineral interaction even when the system is at bulk chemical equilibrium.

In natural biogenic environments, dissolved Si can form strong aqueous complexes with various organic ligands. These complexes can change Si coordination from the usual four-coordinated aqueous silicic acid ($H_4SiO_4^o$) complex to a five- or six-coordinated aqueous Si complex if organic ligands are present. Such a change in aqueous complexation could change considerably mineral-fluid isotope fractionation. This possibility was evaluated in the second part of this thesis, where the equilibrium isotope fractional factors among amorphous silica and catechol ($C_6H_4(OH)_2$) bearing aqueous solutions were measured using the three-isotope method. It was shown that the equilibrium Si isotope fractionation factor between the Si-catechol complex and amorphous silica is about 20 ‰ lighter than the corresponding equilibrium Si isotope fractionation factor between silicic acid and amorphous silica. Measured equilibrium Si isotope fractionation factors were found to be in very close agreement with corresponding values obtained by ***ab initio*** calculations. Taken together, the results of this study demonstrate that the presence of aqueous organic ligands can have an important impact on the Si isotopic fractionation and might explain the strong negative fractionation found in naturally formed biological Si, such as sponges or diatoms.

The third part of this thesis measured the equilibrium Mg isotope fractionation factors between brucite and Mg bearing aqueous solutions in the absence/ presence of selected organic and inorganic ligands, notably citrate, EDTA (ethylenediaminetetraacetic acid), and sulphate. The isotopic fractionation factor determined in this study between brucite and solution, in the absence of inorganic and organic ligands, is in good agreement with the experimental data of Li et al. (2014) and theoretical calculations conducted recently in our laboratory. Similar to the results in the amorphous silica-aqueous fluid studies summarized above, the aqueous speciation of Mg was found to have an important influence on equilibrium Mg isotope fractionation. In the presence of aqueous EDTA, the equilibrium Mg isotope fractionation factor between brucite and solution, $\Delta_{eq}{}^{26}Mg_{brucite\text{-}solution}$, was found to be 2.43 ± 0.20 ‰, showing that brucite incorporates heavy Mg on the presence of this aqueous ligand. This is in close agreement with previous experimental and theoretical studies. Measured equilibrium Mg isotope fractionation factors determined in the presence of aqueous citrate and aqueous sulphate exhibit smaller equilibrium Mg isotopic fractionation factors ranging from -0.07 ± 0.21 to -0.17 ± 0.10 ‰ and 0.20 ± 0.05 to 0.15 ± 0.41 ‰, respectively. These values differ somewhat from previously reported ***ab initio*** calculations, suggesting that these

need to be revised or further validated before they can be used with confidence. These findings show that the presence of organic ligands and inorganic carbonate and hydrogen carbonate ligands, in natural systems have a significant impact on the equilibrium Mg isotopic fractionation factors between minerals and aqueous solutions. As such the Mg isotope concentrations of precipitated minerals might prove to be a useful tracer to characterize the environment in which a mineral has formed.

As with all these, this thesis both provides new insights but also opens the door to new future research projects. Results of this thesis show that the equilibrium isotope fractionation is highly dependent on the aqueous speciation. Therefore the aqueous composition can significantly influence the isotopic signatures of minerals and solutions in natural systems. Notably, in biological environments, the presence of aqueous organic ligands can alter significantly the isotopic signatures of precipitated minerals. Organic (or inorganic) ligands have two possible routes for impacting the isotopic composition of the solid, either by altering the isotopic composition of the free metal ion incorporated in the solid, or by participating directly in the incorporation of the metal into the solid phase in the form of an organometallic complex. In the latter case organic ligands drive the uptake and incorporation of Si and Mg into organisms such as sponges, diatoms, plants. In some instances, the biotic fluid within the organism provides the chemical drive to concentrate metals from solution to help make the skeletons or shells. An exciting new research direction would be to determine which inorganic and organic ligands take part in these biological and natural processes. The degree of isotopic fraction might aid in such studies. For example, as shown for Si in this thesis, organic ligands can change the coordination of Si in solution and therefore result in distinct Si isotope fractionation. Knowing the principles of isotopic fractionation in the presence of the organic and inorganic ligands it might also be possible to develop new isotopic tools to better constrain the biogeochemical cycles of Si and Mg, and the behaviour of these elements in natural processes.

This thesis additionally provides insight into the mechanisms of isotopic exchange, showing that the rate of isotopic exchange depends strongly on the system of interest, and its geometry, which can be controlled either by chemical reaction at the solid-liquid interface or by transport within the solid. A possible future research project could be focussed on identifying the rate of isotopic exchange for different mineral-solution systems to develop a general understanding of both the mechanism of isotope exchange as well as the degree to which mineral isotopic signatures are preserved over geological timescales.

Another important tool to model past and present natural processes are *ab initio* calculations. Therefore the accuracy of such calculation has to be verified. During this thesis it has been shown for the Si-catecholate system that *ab initio* calculations can accurately predict the equilibrium fractionation factor of this system or between silicic acid and its deprotonated form. However, experimental and theoretical results of the equilibrium isotope fractionation factors can also significantly differ from each other, as has been demonstrated in this thesis for the case of Mg. The cause of the differences are poorly understood, but might be caused by the difficulty of precisely modelling the structure of the weak complexes Mg forms with many inorganic and organic ligands. As such, one should be cautious applying the results of *ab initio* calculations to natural systems without validation. These observed discrepancies between experimental data and theoretical predictions should be addressed in future studies.

Ideally an extensive database of equilibrium isotopic fractionation factors among Si and Mg minerals and aqueous fluids, taking account of both experimental results and *ab initio* calculations, can be developed allowing the extensive use of mineral isotopic signals to interpret natural geochemical systems.

6.2. Conclusion générale et perspectives (Version française)

Cette thèse a permis de déterminer les effets de la spéciation aqueuse, notamment la formation de complexes aqueux inorganiques et organiques, sur les facteurs de fractionnement à l'équilibre du silicium et du magnésium dans les systèmes silice amorphe ($SiO_2(s)$) – solution et brucite ($Mg(OH)_2$) - solution. Les expériences d'échange isotopique ont été réalisées à l'équilibre chimique en utilisant la «méthode des trois isotopes» et les résultats ont été comparés à ceux de calculs *ab initio* correspondants aux mêmes systèmes. En plus de fournir des facteurs de fractionnement isotopique à l'équilibre, cette méthode permet de déterminer les vitesses d'échange isotopique et ainsi de mieux comprendre les mécanismes d'acquisition des signatures isotopiques des solides dans la nature et les conditions de leur préservation.

Afin d'appliquer quantitativement les signatures isotopiques de Si comme traceurs de l'altération continentale ou du pH et de la température passés des océans, la première partie de cette thèse a été consacrée à la détermination des facteurs de fractionnement isotopique de Si à l'équilibre entre la silice amorphe ($SiO_2 \bullet 0.32\ H_2O$) et des fluides aqueux inorganiques à pH variable de 5.8 à 9.9 à 25 et 75 °C. Les résultats expérimentaux montrent qu'à 25 °C, le facteur de fractionnement isotopique à l'équilibre entre silice amorphe et fluide aqueux, $\Delta_{eq}{}^{30}Si_{solide\text{-}fluide}$, augmente de 0.45 ± 0.20 ‰ à pH 6.4 à 1.13 ± 0.23 ‰ à pH 9.9. Avec l'augmentation de la température à 75 °C, ces facteurs de fractionnement diminuent jusqu'à 0.07 ± 0.6 ‰ à pH= 5.8 et 1.06 ± 0.13 ‰ à pH= 9.1. La valeur obtenue pour un pH < 7 et 25 °C est en bon accord avec les valeurs expérimentales obtenues par Roerdink et al. (2015) et Oelze et al. (2015) tandis que la diminution du fractionnement isotopique avec l'augmentation de la température suit la relation suggérée dans des études théoriques et expérimentales antérieures (par exemple, Urey, 1947; Bigeleisen, 1965; Schauble, 2004; Shahar et al., 2011; Huang et al., 2014). En tenant compte de la distribution en fonction du pH des espèces aqueuses de Si calculée avec PHREEQC, nous avons déterminé le facteur de fractionnement isotopique de Si à l'équilibre entre les deux espèces aqueuses majeures $H_3SiO_4^-$ et $H_4SiO_4^\circ$. Les valeurs $\Delta_{eq}{}^{30}Si_{H_3SiO_4^- - H_4SiO_4^\circ}$ obtenues à 25 et 75 °C sont respectivement égales à -2.34 ± 0.13 ‰ et à -2.21 ± 0.05 ‰. Ces valeurs sont comparables aux résultats des calculs *ab initio* rapportés par Dupuis et al. (2015), montrant que des calculs expérimentaux ou théoriques peuvent être utilisés pour modéliser avec précision les processus naturels de fractionnement isotopique du silicium. Les résultats obtenus dans la première partie de cette thèse indiquent que les signatures isotopiques de Si peuvent potentiellement être utilisées comme indicateurs de paléo pH dans des environnements alcalins et peuvent en

outre donner une idée de la température de formation de solides siliceux. La vitesse d'échange isotopique dans les systèmes inorganique SiO_2(am) - solution correspond à la vitesse de dissolution de la silice amorphe, ce qui montre que le mécanisme dominant d'échange isotopique dans ce système est l'attachement/ détachement de matière à l'interface solide-liquide et non pas le transport au sein du solide. Cette dernière observation suggère que les signaux isotopiques originaux du Si de la silice amorphe pourraient éventuellement être modifiés au fil du temps par le biais d'une interaction fluide-solide, même à l'équilibre chimique entre solution et silice amorphe.

Dans les environnements biogéniques naturels, la silice dissoute peut se complexer avec nombre de ligands organiques. La coordinence du silicium dissous peut ainsi passer de 4 à 5 ou 6 en présence de certains ligands organiques. De tels changements de coordinence sont susceptibles de considérablement modifier le fractionnement isotopique de Si lors des interactions solide-fluide. Cette possibilité a été évaluée dans la seconde partie de cette thèse en mesurant à l'aide de la méthode des trois isotopes les facteurs de fractionnement isotopiques à l'équilibre entre silice amorphe et solutions aqueuses contenant du catéchol ($C_6H_4(OH)_2$). Il a été montré que le facteur de fractionnement isotopique de Si à l'équilibre entre le complexe aqueux Si-catéchol et la silice amorphe est environ 20 ‰ plus négatif que le facteur de fractionnement isotopique de Si à l'équilibre entre l'acide silicique et la silice amorphe. Les facteurs de fractionnement isotopique de Si mesurés à l'équilibre sont en très bon accord avec les valeurs correspondantes obtenues par calculs *ab initio*. Ces résultats montrent que la présence de ligands organiques aqueux peut avoir un impact considérable sur le fractionnement isotopique du silicium et pourrait expliquer les signatures isotopiques fortement négatives de Si observées dans des biomatériaux naturels comme , les éponges ou les diatomées.

La troisième partie de cette thèse est dédiée à la mesure des facteurs de fractionnement isotopique du magnésium à l'équilibre entre la brucite et des solutions aqueuses contenant du Mg en présence ou non de ligands organiques et inorganiques sélectionnés, notamment le citrate, l'EDTA (acide éthylènediaminetétraacétique) et le sulfate. Le facteur de fractionnement isotopique déterminé dans cette étude entre brucite et solution, en l'absence de ligands inorganiques et organiques, est en bon accord avec les données expérimentales de Li et al. (2014) et les calculs théoriques conduits récemment dans notre laboratoire. Les résultats obtenus en présence de ligands présentent des similitudes avec ceux des échanges isotopiques entre fluide aqueux et silice amorphe rapportés ci-dessus. Il s'est avéré notamment que la spéciation aqueuse de Mg pouvait avoir une influence importante sur le fractionnement

isotopique de Mg à l'équilibre. En présence d'EDTA, nous avons mesuré un facteur de fractionnement isotopique de Mg à l'équilibre entre la brucite et la solution, $\Delta_{eq}{}^{26}Mg_{brucite\text{-}solution}$, égal à 2.43 ± 0.20 ‰, ce qui montre que la brucite incorpore préférentiellement les isotopes lourds du Mg en présence de ce ligand. Ceci est en accord avec les études expérimentales et théoriques existantes. Les facteurs de fractionnement isotopiques de Mg mesurés à l'équilibre en présence de citrate et de sulfate aqueux présentent des valeurs nettement plus faibles, respectivement égales à -0.04 ± 0.19 ‰ et 0.41 ± 0.14 ‰. Ces valeurs diffèrent quelque peu de celles déduites des calculs ab initio récemment publiées, ce qui suggère que ces calculs doivent être révisés ou davantage validés avant de pouvoir être utilisés avec confiance. Ces résultats montrent que la présence dans les systèmes naturels de certains ligands organiques, comme celle des ligands inorganiques carbonate et hydrogénocarbonate, peut avoir un impact significatif sur les facteurs de fractionnement isotopique du Mg à l'équilibre entre les minéraux porteurs de magnésium et les solutions aqueuses. La composition isotopique de Mg dans les minéraux magnésiens pourrait ainsi s'avérer être un traceur utile pour caractériser les environnements dans lesquels se sont formés ces minéraux.

Cette thèse fournit de nouvelles connaissances mais ouvre aussi la porte à de nouveaux projets de recherche. Nos résultats montrent que le fractionnement isotopique à l'équilibre peut fortement dépendre de la spéciation aqueuse de l'élément étudié. Par conséquent, la composition chimique aqueuse, notamment la présence de nombreux ligands, peut influencer de manière significative les signatures isotopiques des solides et des solutions dans les systèmes naturels. Dans les environnements biologiques, notamment, la présence de ligands organiques aqueux peut altérer de manière significative les signatures isotopiques des solides précipités. Les ligands organiques (ou inorganiques) ont deux voies possibles pour impacter la composition isotopique du solide, soit en altérant la composition isotopique de l'ion métallique libre incorporé dans le solide, soit en participant directement à l'incorporation du métal dans la phase solide sous forme de complexe organométallique. Dans ce dernier cas, les ligands organiques peuvent conduire le piégeage et l'incorporation d'éléments comme Si et Mg dans des organismes tels que les éponges, les diatomées et les plantes. Dans certains cas, le fluide biotique au sein de l'organisme fournit le vecteur chimique nécessaire pour concentrer les métaux de la solution afin d'aider à la fabrication des squelettes ou des coquilles. Une nouvelle direction de recherche prometteuse serait de déterminer quels sont les ligands inorganiques et organiques participant à ces processus biologiques naturels. La mise en œuvre des isotopes stables non traditionnels pourrait faciliter de telles études. Par exemple,

comme on l'a montré pour Si dans cette thèse, les ligands organiques peuvent modifier la coordination des métaux en solution et entraîner ainsi une composition isotopique distincte du métal. Connaissant les principes de fractionnement isotopique en présence des ligands organiques et inorganiques, il pourrait également être possible de développer de nouveaux outils isotopiques pour mieux contraindre les cycles biogéochimiques du silicium et du magnésium ainsi que le comportement de ces éléments dans les processus naturels.

Cette thèse fournit en outre un aperçu sur les mécanismes d'échange isotopique, montrant que la vitesse d'échange isotopique dépend fortement du système étudié et de sa géométrie, pouvant être contrôlée soit par réaction chimique à l'interface solide-liquide soit par transport au sein du solide. Un futur projet de recherche pourrait être centré sur la quantification des vitesses d'échange isotopique pour différents systèmes solide-solution afin de mieux caractériser les mécanisme d'échange isotopique ainsi que le degré de préservation des signatures isotopiques des solides à l'échelle des temps géologiques.

Les calculs *ab initio* sont un autre outil important pour modéliser les processus naturels passés et présents. Par conséquent, il est nécessaire de pouvoir vérifier la précision de ces calculs. Au cours de cette thèse, on a montré que les calculs *ab initio* pouvaient prédire avec précision le facteur de fractionnement à l'équilibre pour le système SiO_2-catecholate ou entre l'acide silicique et sa forme déprotonée. Cependant, les résultats des calculs expérimentaux et théoriques des facteurs de fractionnement isotopiques à l'équilibre peuvent également diverger comme nous l'avons montré dans le cas de Mg. L'origine de ces différences est encore mal connue mais elle peut résider dans la difficulté à modéliser précisément la structure des complexes assez faibles que forme le magnésium avec nombre de ligands inorganiques et organiques. Il convient donc de faire preuve de prudence en appliquant sans les valider les résultats des calculs *ab initio* à des systèmes naturels. Des études devront être conduites dans le futur afin de résoudre les divergences observées entre les données expérimentales et les prédictions théoriques.

Idéalement, une base de données exhaustive des facteurs de fractionnement isotopique à l'équilibre entre solides et espèces aqueuses de Si et de Mg, tenant compte des résultats expérimentaux et des calculs *ab initio*, pourrait être développée, permettant ainsi l'utilisation extensive des signatures isotopiques des solides pour interpréter les systèmes géochimiques naturels.

Bibliography

Aagaard, P., Helgeson, H.C., 1982. Thermodynamic and kinetic constraints on reaction rates among minerals and aqueous solutions; I, Theoretical considerations. Am. J. Sci. 282, 237–285. https://doi.org/10.2475/ajs.282.3.237

Alabaster, C.J., 1977. An occurrence of brucite at Merehead Quarry, Cranmore, Somerset. Mineral. Mag. 41, 406–408. https://doi.org/10.1180/minmag.1977.041.319.20

Allègre, C., Manhès, G., Lewin, É., 2001. Chemical composition of the Earth and the volatility control on planetary genetics. Earth Planet. Sci. Lett. 185, 49–69. https://doi.org/10.1016/S0012-821X(00)00359-9

Allenby, R.J., 1954. Determination of the isotopic ratios of silicon in rocks. Geochim. Cosmochim. Acta 5, 40–48. https://doi.org/10.1016/0016-7037(54)90060-5

Appelo, C.A.J., Postma, D., 2013. Geochemistry, groundwater and pollution, 2. ed., 10., corr. repr. ed. CRC Press [u.a.], Boca Raton.

Asael, D., Matthews, A., Oszczepalski, S., Bar-Matthews, M., Halicz, L., 2009. Fluid speciation controls of low temperature copper isotope fractionation applied to the Kupferschiefer and Timna ore deposits. Chem. Geol. 262, 147–158. https://doi.org/10.1016/j.chemgeo.2009.01.015

Bach, W., Paulick, H., Garrido, C.J., Ildefonse, B., Meurer, W.P., Humphris, S.E., 2006. Unraveling the sequence of serpentinization reactions: petrography, mineral chemistry, and petrophysics of serpentinites from MAR 15°N (ODP Leg 209, Site 1274). Geophys. Res. Lett. 33. https://doi.org/10.1029/2006GL025681

Balan, E., Noireaux, J., Mavromatis, V., Saldi, G.D., Montouillout, V., Blanchard, M., Pietrucci, F., Gervais, C., Rustad, J.R., Schott, J., Gaillardet, J., 2018. Theoretical isotopic fractionation between structural boron in carbonates and aqueous boric acid and borate ion. Geochim. Cosmochim. Acta 222, 117–129. https://doi.org/10.1016/j.gca.2017.10.017

Barnum, D.W., 1972. Reaction of catechol with colloidal silica and silicic acid in aqueous ammonia. Inorg. Chem. 11, 1424–1429. https://doi.org/10.1021/ic50112a052

Barnum, D.W., 1970. Catechol complexes with silicon. Inorg. Chem. 9, 1942–1943. https://doi.org/10.1021/ic50090a038

Baroni, S., de Gironcoli, S., Dal Corso, A., Giannozzi, P., 2001. Phonons and related crystal properties from density-functional perturbation theory. Rev. Af Mod. Phys. 73.

Basile-Doelsch, I., 2006. Si stable isotopes in the Earth's surface: A review. J. Geochem. Explor. 88, 252–256. https://doi.org/10.1016/j.gexplo.2005.08.050

Basile-Doelsch, I., Meunier, J.D., Parron, C., 2005. Another continental pool in the terrestrial silicon cycle. Nature 433, 399–402. https://doi.org/10.1038/nature03217

Baur, W.H., 1964. On the crystal chemistry of salt hydrates. IV. The refinement of the crystal structure of $MgSO_4 \cdot 7\ H_2O$ (epsomite). Acta Crystallogr. 17, 1361–1369. https://doi.org/10.1107/S0365110X64003449

Beard, B.L., Handler, R.M., Scherer, M.M., Wu, L., Czaja, A.D., Heimann, A., Johnson, C.M., 2010a. Iron isotope fractionation between aqueous ferrous iron and goethite. Earth Planet. Sci. Lett. 295, 241–250. https://doi.org/0.1016/j.epsl.2010.04.006

Beard, B.L., Handler, R.M., Scherer, M.M., Wu, L., Czaja, A.D., Heimann, A., Johnson, C.M., 2010b. Iron isotope fractionation between aqueous ferrous iron and goethite. Earth Planet. Sci. Lett. 295, 241–250. https://doi.org/10.1016/j.epsl.2010.04.006

Benner, K., Klüfers, P., Vogt, M., 2003. Hydrogen-Bonded Sugar-Alcohol Trimers as Hexadentate Silicon Chelators in Aqueous Solution. Angew. Chem. Int. Ed. 42, 1058–1062. https://doi.org/10.1002/anie.200390274

Bennett, P.C., 1991. Quartz dissolution in organic-rich aqueous systems. Geochim. Cosmochim. Acta 55, 1781–1797. https://doi.org/10.1016/0016-7037(91)90023-X

Bennett, P.C., Casey, W., 1994. Chemistry and Mechanisms of Low-Temperature Dissolution of Silicates by Organic Acids, in: Pittman, E.D., Lewan, M.D. (Eds.), Organic Acids in Geological Processes. Springer Berlin Heidelberg, Berlin, Heidelberg, pp. 162–200. https://doi.org/10.1007/978-3-642-78356-2_7

Bennett, P.C., Melcer, M.E., Siegel, D.I., Hassett, J.P., 1988. The dissolution of quartz in dilute aqueous solutions of organic acids at 25°C. Geochim. Cosmochim. Acta 52, 1521–1530. https://doi.org/10.1016/0016-7037(88)90222-0

Berger, G., Cadore, E., Schott, J., Dove, P.M., 1994. Dissolution rate of quartz in lead and sodium electrolyte solutions between 25 and 300°C: Effect of the nature of surface complexes and reaction affinity. Geochim. Cosmochim. Acta 58, 541–551. https://doi.org/10.1016/0016-7037(94)90487-1

Berglund, M., Wieser, M.E., 2011. Isotopic compositions of the elements 2009 (IUPAC Technical Report). Pure Appl. Chem. 83, 397–410. https://doi.org/10.1351/PAC-REP-10-06-02

Bigeleisen, J., 1965. Chemistry of Isotopes: Isotope chemistry has opened new areas of chemical physics, geochemistry, and molecular biology. Science 147, 463–471. https://doi.org/10.1126/science.147.3657.463

Bigeleisen, J., Mayer, M.G., 1947. Calculation of Equilibrium Constants for Isotopic Exchange Reactions. J. Chem. Phys. 15, 261–267. https://doi.org/10.1063/1.1746492

Birchall, J.D., 1995. The essentiality of silicon in biology. Chem. Soc. Rev. 24, 351. https://doi.org/10.1039/cs9952400351

Bolou-Bi, E.B., Poszwa, A., Leyval, C., Vigier, N., 2010. Experimental determination of magnesium isotope fractionation during higher plant growth. Geochim. Cosmochim. Acta 74, 2523–2537. https://doi.org/10.1016/j.gca.2010.02.010

Bolou-Bi, E.B., Vigier, N., Poszwa, A., Boudot, J.-P., Dambrine, E., 2012. Effects of biogeochemical processes on magnesium isotope variations in a forested catchment in the Vosges Mountains (France). Geochim. Cosmochim. Acta 87, 341–355. https://doi.org/10.1016/j.gca.2012.04.005

Boudin, A., Cerveau, G., Chuit, C., Corriu, R.J.P., Reye, C., 1988. Reactivity of dianionic hexacoordinated silicon complexes toward nucleophiles: a new route to organosilanes from silica. Organometallics 7, 1165–1171. https://doi.org/10.1021/om00095a023

Bouman, C., 2005. Stable isotope ratio measurements using the Finnigan NEPTUNE multicollector ICP-MS.

Box, G.F., Walsh, A., 1960. A simple atomic absorption spectrophotometer. Spectrochim. Acta 16, 255-E3. https://doi.org/10.1016/0371-1951(60)80088-4

Brady, P.V., Walther, J.V., 1989. Controls on silicate dissolution rates in neutral and basic pH solutions at 25°C. Geochim. Cosmochim. Acta 53, 2823–2830. https://doi.org/10.1016/0016-7037(89)90160-9

Brenot, A., Cloquet, C., Vigier, N., Carignan, J., France-Lanord, C., 2008. Magnesium isotope systematics of the lithologically varied Moselle river basin, France. Geochim. Cosmochim. Acta 72, 5070–5089. https://doi.org/10.1016/j.gca.2008.07.027

Brown, P.E., Bowman, J.R., Kelly, W.C., 1985. Petrologic and stable isotope constraints on the source and evolution of skarn-forming fluids at Pine Creek, California. Econ. Geol. 80, 72–95. https://doi.org/10.2113/gsecongeo.80.1.72

Brunauer, S., Emmett, P.H., Teller, E., 1938. Adsorption of Gases in Multimolecular Layers. J. Am. Chem. Soc. 60, 309–319. https://doi.org/10.1021/ja01269a023

Buchner, R., Chen, T., Hefter, G., 2004. Complexity in "Simple" Electrolyte Solutions: Ion Pairing in $MgSO_4$(aq). J. Phys. Chem. B 108, 2365–2375. https://doi.org/10.1021/jp034870p

Buffle, J., Chalmers, R.A., Masson, M.R., Midgley, D., 1988. Complexation reactions in aquatic systems: an analytical approach, Ellis Horwood series in analytical chemistry. E. Horwood ; Halsted Press [distributor], Chichester, West Sussex, England : New York.

Buster, N.A., Holmes, C.W., 2006. Magnesium content within the skeletal architecture of the coral Montastraea faveolata: locations of brucite precipitation and implications to fine-scale data fluctuations. Coral Reefs 25, 243–253. https://doi.org/10.1007/s00338-006-0092-y

Cardinal, D., Alleman, L.Y., de Jong, J., Ziegler, K., André, L., 2003. Isotopic composition of silicon measured by multicollector plasma source mass spectrometry in dry plasma mode. J. Anal. At. Spectrom. 18, 213–218. https://doi.org/10.1039/b210109b

Cardinal, D., Alleman, L.Y., Dehairs, F., Savoye, N., Trull, T.W., André, L., 2005. Relevance of silicon isotopes to Si-nutrient utilization and Si-source assessment in Antarctic waters: Silicon isotopes in arctic waters. Glob. Biogeochem. Cycles 19, n/a-n/a. https://doi.org/10.1029/2004GB002364

Catti, M., Ferraris, G., Hull, S., Pavese, A., 1995. Static compression and H disorder in brucite, Mg(OH)2, to 11 GPa: a powder neutron diffraction study. Phys. Chem. Miner. 22. https://doi.org/10.1007/BF00202300

Cella, J.A., Cargioli, J.D., Williams, E.A., 1980. 29Si NMR of five- and six-coordinate organosilicon complexes. J. Organomet. Chem. 186, 13–17. https://doi.org/10.1016/S0022-328X(00)93813-0

Chakoumakos, B.C., Loong, C.-K., Schultz, A.J., 1997. Low-Temperature Structure and Dynamics of Brucite. J. Phys. Chem. B 101, 9458–9462. https://doi.org/10.1021/jp972225a

Chakrabarti, R., Knoll, A.H., Jacobsen, S.B., Fischer, W.W., 2012. Si isotope variability in Proterozoic cherts. Geochim. Cosmochim. Acta 91, 187–201. https://doi.org/10.1016/j.gca.2012.05.025

Chang, V.T.-C., Makishima, A., Belshaw, N.S., O'Nions, R.K., 2003. Purification of Mg from low-Mg biogenic carbonates for isotope ratio determination using multiple collector ICP-MS. J. Anal. At. Spectrom. 18, 296–301. https://doi.org/10.1039/b210977h

Cole, D.R., Chakraborty, S., 2001. Rates and Mechanisms of Isotopic Exchange. Rev. Mineral. Geochem. 43, 83–223. https://doi.org/10.2138/gsrmg.43.1.83

Colla, C.A., Casey, W.H., Ohlin, C.A., 2018. Computational prediction of Mg-isotope fractionation between aqueous $[Mg(OH_2)_6]^{2+}$ and brucite. Geochim. Cosmochim. Acta 227, 64–74. https://doi.org/10.1016/j.gca.2018.02.005

Cornu, S., Lucas, Y., Lebon, E., Ambrosi, J.P., Luizão, F., Rouiller, J., Bonnay, M., Neal, C., 1999. Evidence of titanium mobility in soil profiles, Manaus, central Amazonia. Geoderma 91, 281–295. https://doi.org/10.1016/S0016-7061(99)00007-5

Criss, R.E., 1999. Principles of stable isotope distribution. Oxford University Press, New York.

Criss, R.E., Gregory, R.T., Taylor, H.P., 1987. Kinetic theory of oxygen isotopic exchange between minerals and water. Geochim. Cosmochim. Acta 51, 1099–1108. https://doi.org/10.1016/0016-7037(87)90203-1

Dal Corso, A., 2014. Pseudopotentials periodic table: From H to Pu. Comput. Mater. Sci. 95, 337–350.

Danielsson, S., Grenthe, I., Oskarsson, Å., 1976. A low-temperature apparatus for single-crystal diffractometry. The unit-cell dimension of α-quartz in the temperature range 86–298 K. J. Appl. Crystallogr. 9, 14–17. https://doi.org/10.1107/S0021889876010418

De Biévre, P., Taylor, P.D.P., 1993. Table of the isotopic compositions of the elements. Int. J. Mass Spectrom. Ion Process. 123, 149–166. https://doi.org/10.1016/0168-1176(93)87009-H

De La Rocha, C.L., 2003. Silicon isotope fractionation by marine sponges and the reconstruction of the silicon isotope composition of ancient deep water. Geology 31, 423. https://doi.org/10.1130/0091-7613(2003)031<0423:SIFBMS>2.0.CO;2

De La Rocha, C.L., 2002. Measurement of silicon stable isotope natural abundances via multicollector inductively coupled plasma mass spectrometry (MC-ICP-MS): SILICON STABLE ISOTOPE NATURAL ABUNDANCES. Geochem. Geophys. Geosystems 3, 1–8. https://doi.org/10.1029/2002GC000310

De La Rocha, C.L., Bescont, P., Croguennoc, A., Ponzevera, E., 2011. The silicon isotopic composition of surface waters in the Atlantic and Indian sectors of the Southern Ocean. Geochim. Cosmochim. Acta 75, 5283–5295. https://doi.org/10.1016/j.gca.2011.06.028

De La Rocha, C.L., Brzezinski, M.A., DeNiro, M.J., 2000. A first look at the distribution of the stable isotopes of silicon in natural waters. Geochim. Cosmochim. Acta 64, 2467–2477. https://doi.org/10.1016/S0016-7037(00)00373-2

De La Rocha, C.L., Brzezinski, M.A., DeNiro, M.J., Shemesh, A., 1998. Silicon-isotope composition of diatoms as an indicator of past oceanic change. Nature 395, 680–683. https://doi.org/10.1038/27174

Delstanche, S., Opfergelt, S., Cardinal, D., Elsass, F., André, L., Delvaux, B., 2009. Silicon isotopic fractionation during adsorption of aqueous monosilicic acid onto iron oxide. Geochim. Cosmochim. Acta 73, 923–934. https://doi.org/10.1016/j.gca.2008.11.014

Delvigne, C., Cardinal, D., Hofmann, A., André, L., 2012. Stratigraphic changes of Ge/Si, REE+Y and silicon isotopes as insights into the deposition of a Mesoarchaean banded iron formation. Earth Planet. Sci. Lett. 355–356, 109–118. https://doi.org/10.1016/j.epsl.2012.07.035

Delvigne, C., Opfergelt, S., Cardinal, D., Delvaux, B., André, L., 2009. Distinct silicon and germanium pathways in the soil-plant system: Evidence from banana and horsetail: distinct Si and Ge pathways in plants. J. Geophys. Res. Biogeosciences 114, n/a-n/a. https://doi.org/10.1029/2008JG000899

Demarest, M.S., Brzezinski, M.A., Beucher, C.P., 2009. Fractionation of silicon isotopes during biogenic silica dissolution. Geochim. Cosmochim. Acta 73, 5572–5583. https://doi.org/10.1016/j.gca.2009.06.019

Diedrich, T., Dybowska, A., Schott, J., Valsami-Jones, E., Oelkers, E.H., 2012. The Dissolution rates of SiO_2 nanoparticles as a function of particle size. Environ. Sci. Technol. 46, 4909–4915. https://doi.org/10.1021/es2045053

Dietzel, M., 2000. Dissolution of silicates and the stability of polysilicic acid. Geochim. Cosmochim. Acta 64, 3275–3281. https://doi.org/10.1016/S0016-7037(00)00426-9

Ding, T. (Ed.), 1996. Silicon isotope geochemistry. Geological Publ. House, Beijing, China.

Ding, T.P., Gao, J.F., Tian, S.H., Wang, H.B., Li, M., 2011. Silicon isotopic composition of dissolved silicon and suspended particulate matter in the Yellow River, China, with implications for the global silicon cycle. Geochim. Cosmochim. Acta 75, 6672–6689. https://doi.org/10.1016/j.gca.2011.07.040

Ding, T.P., Ma, G.R., Shui, M.X., Wan, D.F., Li, R.H., 2005. Silicon isotope study on rice plants from the Zhejiang province, China. Chem. Geol. 218, 41–50. https://doi.org/10.1016/j.chemgeo.2005.01.018

Ding, T.P., Tian, S.H., Sun, L., Wu, L.H., Zhou, J.X., Chen, Z.Y., 2008a. Silicon isotope fractionation between rice plants and nutrient solution and its significance to the study of the silicon cycle. Geochim. Cosmochim. Acta 72, 5600–5615. https://doi.org/10.1016/j.gca.2008.09.006

Ding, T.P., Zhou, J.X., Wan, D.F., Chen, Z.Y., Wang, C.Y., Zhang, F., 2008b. Silicon isotope fractionation in bamboo and its significance to the biogeochemical cycle of silicon. Geochim. Cosmochim. Acta 72, 1381–1395. https://doi.org/10.1016/j.gca.2008.01.008

Domagal-Goldman, S.D., Kubicki, J.D., 2008. Density functional theory predictions of equilibrium isotope fractionation of iron due to redox changes and organic complexation. Geochim. Cosmochim. Acta 72, 5201–5216. https://doi.org/10.1016/j.gca.2008.05.066

Douthitt, C.B., 1982. The geochemistry of the stable isotopes of silicon. Geochim. Cosmochim. Acta 46, 1449–1458. https://doi.org/10.1016/0016-7037(82)90278-2

Dupuis, R., Benoit, M., Nardin, E., Méheut, M., 2015. Fractionation of silicon isotopes in liquids: The importance of configurational disorder. Chem. Geol. 396, 239–254. https://doi.org/10.1016/j.chemgeo.2014.12.027

Engström, E., Rodushkin, I., Baxter, D.C., Öhlander, B., 2006. Chromatographic Purification for the Determination of Dissolved Silicon Isotopic Compositions in Natural Waters by High-Resolution Multicollector Inductively Coupled Plasma Mass Spectrometry. Anal. Chem. 78, 250–257. https://doi.org/10.1021/ac051246v

Estrada, C.F., Sverjensky, D.A., Pelletier, M., Razafitianamaharavo, A., Hazen, R.M., 2015. Interaction between l -aspartate and the brucite [Mg(OH) 2]–water interface. Geochim. Cosmochim. Acta 155, 172–186. https://doi.org/10.1016/j.gca.2015.02.002

Foster, G.L., Pogge von Strandmann, P.A.E., Rae, J.W.B., 2010. Boron and magnesium isotopic composition of seawater: DATA BRIEF. Geochem. Geophys. Geosystems 11, n/a-n/a. https://doi.org/10.1029/2010GC003201

Fraysse, F., Pokrovsky, O.S., Schott, J., Meunier, J.-D., 2006. Surface properties, solubility and dissolution kinetics of bamboo phytoliths. Geochim. Cosmochim. Acta 70, 1939–1951. https://doi.org/10.1016/j.gca.2005.12.025

Frierdich, A.J., Beard, B.L., Scherer, M.M., Johnson, C.M., 2014. Determination of the Fe(II)aq–magnetite equilibrium iron isotope fractionation factor using the three-isotope method and a multi-direction approach to equilibrium. Earth Planet. Sci. Lett. 391, 77–86. https://doi.org/10.1016/j.epsl.2014.01.032

Frings, P.J., Clymans, W., Fontorbe, G., Gray, W., Chakrapani, G.J., Conley, D.J., De La Rocha, C., 2015. Silicate weathering in the Ganges alluvial plain. Earth Planet. Sci. Lett. 427, 136–148. https://doi.org/10.1016/j.epsl.2015.06.049

Füger, A., Méheut, M., Mavromatis, V., Leis, A., Dietzel, M., 2018. Oxygen isotope fractionation during smithsonite formation from aqueous solutions. Chem. Geol. 495, 76–89. https://doi.org/10.1016/j.chemgeo.2018.08.005

Fujii, T., Moynier, F., Blichert-Toft, J., Albarède, F., 2014. Density functional theory estimation of isotope fractionation of Fe, Ni, Cu, and Zn among species relevant to geochemical and biological environments. Geochim. Cosmochim. Acta 140, 553–576. https://doi.org/10.1016/j.gca.2014.05.051

Fujii, T., Pringle, E.A., Chaussidon, M., Moynier, F., 2015. Isotope fractionation of Si in protonation/deprotonation reaction of silicic acid: A new pH proxy. Geochim. Cosmochim. Acta 168, 193–205. https://doi.org/10.1016/j.gca.2015.07.003

Galy, A., O'Nions, R.K., 2000. Is there a CHUR for Mg? Presented at the Goldschmidt Abstract, p. 424.

Galy, A., Yoffe, O., Janney, P.E., Williams, R.W., Cloquet, C., Alard, O., Halicz, L., Wadhwa, M., Hutcheon, I.D., Ramon, E., Carignan, J., 2003. Magnesium isotope heterogeneity of the isotopic standard SRM980 and new reference materials for magnesium-isotope-ratio measurements. J. Anal. At. Spectrom. 18, 1352. https://doi.org/10.1039/b309273a

Ganor, J., Reznik, I.J., Rosenberg, Y.O., 2009. Organics in Water-Rock Interactions. Rev. Mineral. Geochem. 70, 259–369. https://doi.org/10.2138/rmg.2009.70.7

Gao, C., Cao, X., Liu, Q., Yang, Y., Zhang, S., He, Y., Tang, M., Liu, Y., 2018. Theoretical calculation of equilibrium Mg isotope fractionations between minerals and aqueous solutions. Chem. Geol. 488, 62–75. https://doi.org/10.1016/j.chemgeo.2018.04.005

Gao, T., Ke, S., Teng, F.-Z., Chen, S., He, Y., Li, S.-G., 2016. Magnesium isotope fractionation during dolostone weathering. Chem. Geol. 445, 14–23. https://doi.org/10.1016/j.chemgeo.2016.07.012

Garrels, R.M., Christ, C.L., 1965. Solutions, minerals, and equilibria, A Harper International student reprint. Harper & Row Publ, New York.

Geilert, S., Vroon, P.Z., Roerdink, D.L., Van Cappellen, P., van Bergen, M.J., 2014. Silicon isotope fractionation during abiotic silica precipitation at low temperatures: Inferences from flow-through experiments. Geochim. Cosmochim. Acta 142, 95–114. https://doi.org/10.1016/j.gca.2014.07.003

Georg, R.B., 2006. Geochemistry of stable silicon isotopes measured by high-resolution multi-collector inductively-coupled-plasma mass-spectrometry (HR-MC-ICP-MS)

(Dissertation). Diss., Eidgenössische Technische Hochschule ETH Zürich, Nr. 16900, 2006, Zürich.

Georg, R.B., Reynolds, B.C., Frank, M., Halliday, A.N., 2006. New sample preparation techniques for the determination of Si isotopic compositions using MC-ICPMS. Chem. Geol. 235, 95–104. https://doi.org/10.1016/j.chemgeo.2006.06.006

Georg, R.B., Reynolds, B.C., West, A.J., Burton, K.W., Halliday, A.N., 2007. Silicon isotope variations accompanying basalt weathering in Iceland. Earth Planet. Sci. Lett. 261, 476–490. https://doi.org/10.1016/j.epsl.2007.07.004

Georg, R.B., Zhu, C., Reynolds, B.C., Halliday, A.N., 2009. Stable silicon isotopes of groundwater, feldspars, and clay coatings in the Navajo Sandstone aquifer, Black Mesa, Arizona, USA. Geochim. Cosmochim. Acta 73, 2229–2241. https://doi.org/10.1016/j.gca.2009.02.005

Giannozzi, P., Baroni, St., Bonini, N., Calandra, M., Car, R., Cavazzoni, C., Ceresoli, D., Chiarotti, G.L., Cococcioni, M., Dabo, I., Dal Corso, A., de Gironcoli, S., Fabris, S., Fratesi, G., Gebauer, R., Gerstmann, U., Gougoussis, C., Kokalj, A., Lazzeri, M., Martin-Samos, L., Marzari, N., Mauri, F., Mazzarello, R., Paolini, S., Pasquarello, A., Paulatto, L., Sbraccia, C., Scandolo, S., Sclauzero, G., Seitsonen, C., Smogunov, A., Umari, P., Wentzcovitch, R.M., 2009. QUANTUM ESPRESSO: a modular and open-source software project for quantum simulations of materials. J. Phys. Condens. Matter 21, 1–19. https://doi.org/10.1088/0953-8984/21/39/395502

Grasse, P., Ehlert, C., Frank, M., 2013. The influence of water mass mixing on the dissolved Si isotope composition in the Eastern Equatorial Pacific. Earth Planet. Sci. Lett. 380, 60–71. https://doi.org/10.1016/j.epsl.2013.07.033

Gulley-Stahl, H., Patrick A. Hogan, I.I., Schmidt, W.L., Wall, S.J., Buhrlage, A., Bullen, H.A., 2010. Surface Complexation of Catechol to Metal Oxides: An ATR-FTIR, Adsorption, and Dissolution Study. Environ. Sci. Technol. 44, 4116–4121. https://doi.org/10.1021/es902040u

Hahn, F.E., Keck, M., Raymond, K.N., 1995. Catecholate Complexes of Silicon: Synthesis and Molecular and Crystal Structures of [Si(cat)2].cntdot.2THF and Li2[Si(cat)3].cntdot.3.5dme (cat = Catecholate Dianion). Inorg. Chem. 34, 1402–1407. https://doi.org/10.1021/ic00110a018

He, H., Zhang, S., Zhu, C., Liu, Y., 2016. Equilibrium and kinetic Si isotope fractionation factors and their implications for Si isotope distributions in the Earth's surface environments. Acta Geochim. 35, 15–24. https://doi.org/10.1007/s11631-015-0079-x

Heck, P.R., Huberty, J.M., Kita, N.T., Ushikubo, T., Kozdon, R., Valley, J.W., 2011. SIMS analyses of silicon and oxygen isotope ratios for quartz from Archean and Paleoproterozoic banded iron formations. Geochim. Cosmochim. Acta 75, 5879–5891. https://doi.org/10.1016/j.gca.2011.07.023

Hemming, N.G., Hanson, G.N., 1992. Boron isotopic composition and concentration in modern marine carbonates. Geochim. Cosmochim. Acta 56, 537–543. https://doi.org/10.1016/0016-7037(92)90151-8

Hendry, K.R., Georg, R.B., Rickaby, R.E.M., Robinson, L.F., Halliday, A.N., 2010. Deep ocean nutrients during the Last Glacial Maximum deduced from sponge silicon isotopic compositions. Earth Planet. Sci. Lett. 292, 290–300. https://doi.org/10.1016/j.epsl.2010.02.005

Hendry, K.R., Leng, M.J., Robinson, L.F., Sloane, H.J., Blusztjan, J., Rickaby, R.E.M., Georg, R.B., Halliday, A.N., 2011. Silicon isotopes in Antarctic sponges: an interlaboratory comparison. Antarct. Sci. 23, 34–42. https://doi.org/10.1017/S0954102010000593

Hendry, K.R., Robinson, L.F., 2012. The relationship between silicon isotope fractionation in sponges and silicic acid concentration: Modern and core-top studies of biogenic opal. Geochim. Cosmochim. Acta 81, 1–12. https://doi.org/10.1016/j.gca.2011.12.010

Henrist, C., Mathieu, J.-P., Vogels, C., Rulmont, A., Cloots, R., 2003. Morphological study of magnesium hydroxide nanoparticles precipitated in dilute aqueous solution. J. Cryst. Growth 249, 321–330. https://doi.org/10.1016/S0022-0248(02)02068-7

Hippler, D., Buhl, D., Witbaard, R., Richter, D.K., Immenhauser, A., 2009. Towards a better understanding of magnesium-isotope ratios from marine skeletal carbonates. Geochim. Cosmochim. Acta 73, 6134–6146. https://doi.org/10.1016/j.gca.2009.07.031

Hoefs, J., 2009. Stable isotope geochemistry, Sixth edition. ed. Springer, Berlin.

Hohenberg, P., Kohn, W., 1964. Inhomogeneous Electron Gas. Phys. Rev. 136, 864–871.

Holloway, J.M., Nordstrom, D.K., Böhlke, J.K., McCleskey, R.B., Ball, J.W., 2011. Ammonium in thermal waters of Yellowstone National Park: Processes affecting speciation and isotope fractionation. Geochim. Cosmochim. Acta 75, 4611–4636. https://doi.org/10.1016/j.gca.2011.05.036

Hostetler, P.B., Coleman, R.G., Mumpton, F.A., Evans, B.W., 1966. Brucite in alpine serpentinites. Am. Mineral. 51, 75–98.

Huang, F., Wu, Z., Huang, S., Wu, F., 2014. First-principles calculations of equilibrium silicon isotope fractionation among mantle minerals. Geochim. Cosmochim. Acta 140, 509–520. https://doi.org/10.1016/j.gca.2014.05.035

Huang, T.-C., Tsai, F.-N., 1970. Kinetic studies on the isotopic exchange of calcium ion and calcium carbonate. J. Inorg. Nucl. Chem. 32, 17–31. https://doi.org/10.1016/0022-1902(70)80445-6

Icenhower, J.P., Dove, P.M., 2000. The dissolution kinetics of amorphous silica into sodium chloride solutions: effects of temperature and ionic strength. Geochim. Cosmochim. Acta 64, 4193–4203. https://doi.org/10.1016/S0016-7037(00)00487-7

Iler, R.K., 1979. The chemistry of silica: solubility, polymerization, colloid and surface properties, and biochemistry. Wiley, New York.

Immenhauser, A., Buhl, D., Richter, D., Niedermayr, A., Riechelmann, D., Dietzel, M., Schulte, U., 2010. Magnesium-isotope fractionation during low-Mg calcite precipitation in a limestone cave – Field study and experiments. Geochim. Cosmochim. Acta 74, 4346–4364. https://doi.org/10.1016/j.gca.2010.05.006

Jiskra, M., Wiederhold, J.G., Bourdon, B., Kretzschmar, R., 2012. Solution Speciation Controls Mercury Isotope Fractionation of Hg(II) Sorption to Goethite. Environ. Sci. Technol. 46, 6654–6662. https://doi.org/10.1021/es3008112

Johnson, C.M., Skulan, J.L., Beard, B.L., Sun, H., Nealson, K.H., Braterman, P.S., 2002. Isotopic fractionation between Fe(III) and Fe(II) in aqueous solutions. Earth Planet. Sci. Lett. 195, 141–153. https://doi.org/10.1016/S0012-821X(01)00581-7

Johnson, J., Anderson, G., Parkhurst, D.L., 2000. Database thermo.com.V8.R6.230. Livermore, California, USA.

Jugdaohsingh, R., Pedro, L.D., Watson, A., Powell, J.J., 2015. Silicon and boron differ in their localization and loading in bone. Bone Rep. 1, 9–15. https://doi.org/10.1016/j.bonr.2014.10.002

Kasemann, S.A., Pogge von Strandmann, P.A.E., Prave, A.R., Fallick, A.E., Elliott, T., Hoffmann, K.-H., 2014. Continental weathering following a Cryogenian glaciation: Evidence from calcium and magnesium isotopes. Earth Planet. Sci. Lett. 396, 66–77. https://doi.org/10.1016/j.epsl.2014.03.048

Kathrin Abraham, Opfergelt, S., Fripiat, F., Cavagna, A.-J., de Jong, J.T.M., Foley, S.F., André, L., Cardinal, D., 2008. δ^{30}Si and δ^{29}Si Determinations on USGS BHVO-1 and BHVO-2 Reference Materials with a New Configuration on a Nu Plasma Multi-

Collector ICP-MS. Geostand. Geoanalytical Res. 32, 193–202. https://doi.org/10.1111/j.1751-908X.2008.00879.x

Kinrade, S.D., 1999. Stable Five- and Six-Coordinated Silicate Anions in Aqueous Solution. Science 285, 1542–1545. https://doi.org/10.1126/science.285.5433.1542

Kinrade, S.D., Deguns, E.W., Gillson, A.-M.E., Knight, C.T.G., 2003. Complexes of pentaoxo and hexaoxo silicon with furanoidic vicinal cis-diols in aqueous solutionAs presented at the Second Silicon in Agriculture Conference, Tsuruoka, Japan, August 2002. Dalton Trans. 3713. https://doi.org/10.1039/b307510a

Kinrade, S.D., Gillson, A.-M.E., Knight, C.T.G., 2002. Silicon-29 NMR evidence of a transient hexavalent silicon complex in the diatom Navicula pelliculosa. J. Chem. Soc. Dalton Trans. 307–309. https://doi.org/10.1039/b105379p

Kinrade, S.D., Hamilton, R.J., Schach, A.S., Knight, C.T.G., 2001a. Aqueous hypervalent silicon complexes with aliphatic sugar acids. J. Chem. Soc. Dalton Trans. 961–963. https://doi.org/10.1039/b010111g

Kinrade, S.D., Schach, A.S., Hamilton, R.J., Knight, C.T.G., 2001b. NMR evidence of pentaoxo organosilicon complexes in dilute neutral aqueous silicate solutions. Chem. Commun. 1564–1565. https://doi.org/10.1039/b104713m

Kinrade, S.D., Swaddle, T.W., 2002. Silicon-29 NMR studies of aqueous silicate solutions. 1. Chemical shifts and equilibria.

Klochko, K., Cody, G.D., Tossell, J.A., Dera, P., Kaufman, A.J., 2009. Re-evaluating boron speciation in biogenic calcite and aragonite using 11B MAS NMR. Geochim. Cosmochim. Acta 73, 1890–1900. https://doi.org/10.1016/j.gca.2009.01.002

Klochko, K., Kaufman, A.J., Yao, W., Byrne, R.H., Tossell, J.A., 2006. Experimental measurement of boron isotope fractionation in seawater. Earth Planet. Sci. Lett. 248, 276–285. https://doi.org/10.1016/j.epsl.2006.05.034

Kohn, W., Sham, L.J., 1965. Self-Consistent Equations Including Exchange and Correlation Effects. Phys. Rev. 140, 1133–1138.

Kubicki, J.D., Heaney, P.J., 2003. Molecular orbital modeling of aqueous organosilicon complexes: implications for silica biomineralization. Geochim. Cosmochim. Acta 67, 4113–4121. https://doi.org/10.1016/S0016-7037(03)00093-0

Leng, M.J., Swann, G.E.A., Hodson, M.J., Tyler, J.J., Patwardhan, S.V., Sloane, H.J., 2009. The Potential use of Silicon Isotope Composition of Biogenic Silica as a Proxy for Environmental Change. Silicon 1, 65–77. https://doi.org/10.1007/s12633-009-9014-2

Li, W., Beard, B.L., Johnson, C.M., 2011. Exchange and fractionation of Mg isotopes between epsomite and saturated MgSO4 solution. Geochim. Cosmochim. Acta 75, 1814–1828. https://doi.org/10.1016/j.gca.2011.01.023

Li, W., Beard, B.L., Li, C., Johnson, C.M., 2014. Magnesium isotope fractionation between brucite [Mg(OH)2] and Mg aqueous species: Implications for silicate weathering and biogeochemical processes. Earth Planet. Sci. Lett. 394, 82–93. https://doi.org/10.1016/j.epsl.2014.03.022

Li, Y., Ding, T., Wan, D., 1995. Experimental study of silicon isotope dynamic fractionation and its application in geology. Chin. J. Geochem. 14, 212–219. https://doi.org/10.1007/BF02842044

Lincoln, S.F., Merbach, A., 1995. Substitution reactions of solvated metal ions, in: Advances in Inorganic Chemistry. A.G. Sykes Ed.

Ling, M.-X., Sedaghatpour, F., Teng, F.-Z., Hays, P.D., Strauss, J., Sun, W., 2011. Homogeneous magnesium isotopic composition of seawater: an excellent geostandard for Mg isotope analysis: Homogeneous magnesium isotopic composition of seawater. Rapid Commun. Mass Spectrom. 25, 2828–2836. https://doi.org/10.1002/rcm.5172

Liu, X.-M., Teng, F.-Z., Rudnick, R.L., McDonough, W.F., Cummings, M.L., 2014. Massive magnesium depletion and isotope fractionation in weathered basalts. Geochim. Cosmochim. Acta 135, 336–349. https://doi.org/10.1016/j.gca.2014.03.028

Lv, J., Qiu, L., Qu, B., 2004. Controlled growth of three morphological structures of magnesium hydroxide nanoparticles by wet precipitation method. J. Cryst. Growth 267, 676–684. https://doi.org/10.1016/j.jcrysgro.2004.04.034

Marin-Carbonne, J., Chaussidon, M., Robert, F., 2012. Micrometer-scale chemical and isotopic criteria (O and Si) on the origin and history of Precambrian cherts: Implications for paleo-temperature reconstructions. Geochim. Cosmochim. Acta 92, 129–147. https://doi.org/10.1016/j.gca.2012.05.040

Marin-Carbonne, J., Robert, F., Chaussidon, M., 2014. The silicon and oxygen isotope compositions of Precambrian cherts: A record of oceanic paleo-temperatures? Precambrian Res. 247, 223–234. https://doi.org/10.1016/j.precamres.2014.03.016

Martell, A.E., Hancock, R.D., 1996. Metal Complexes in Aqueous Solutions. Springer US, Boston, MA. https://doi.org/10.1007/978-1-4899-1486-6

Matsuhisa, Y., Goldsmith, J.R., Clayton, R.N., 1978. Mechanisms of hydrothermal crystallization of quartz at 250°C and 15 kbar. Geochim. Cosmochim. Acta 42, 173–182. https://doi.org/10.1016/0016-7037(78)90130-8

Matthews, A., Goldsmith, J.R., Clayton, R.N., 1983a. On the mechanisms and kinetics of oxygen isotope exchange in quartz and feldspars at elevated temperatures and pressures. Geol. Soc. Am. Bull. 94, 396. https://doi.org/10.1130/0016-7606(1983)94<396:OTMAKO>2.0.CO;2

Matthews, A., Goldsmith, J.R., Clayton, R.N., 1983b. Oxygen isotope fractionations involving pyroxenes: The calibration of mineral-pair geothermometers. Geochim. Cosmochim. Acta 47, 631–644. https://doi.org/10.1016/0016-7037(83)90284-3

Matthews, A., Goldsmith, J.R., Clayton, R.N., 1983c. Oxygen isotope fractionation between zoisite and water. Geochim. Cosmochim. Acta 47, 645–654. https://doi.org/10.1016/0016-7037(83)90285-5

Mavromatis, V., Gautier, Q., Bosc, O., Schott, J., 2013. Kinetics of Mg partition and Mg stable isotope fractionation during its incorporation in calcite. Geochim. Cosmochim. Acta 114, 188–203. https://doi.org/10.1016/j.gca.2013.03.024

Mavromatis, V., González, A.G., Dietzel, M., Schott, J., 2019. Zinc isotope fractionation during the inorganic precipitation of calcite – Towards a new pH proxy. Geochim. Cosmochim. Acta 244, 99–112. https://doi.org/10.1016/j.gca.2018.09.005

Mavromatis, V., Immenhauser, A., Buhl, D., Purgstaller, B., Baldermann, A., Dietzel, M., 2017. Effect of organic ligands on Mg partitioning and Mg isotope fractionation during low-temperature precipitation of calcite in the absence of growth rate effects. Geochim. Cosmochim. Acta 207, 139–153. https://doi.org/10.1016/j.gca.2017.03.020

Mavromatis, V., Meister, P., Oelkers, E.H., 2014a. Using stable Mg isotopes to distinguish dolomite formation mechanisms: A case study from the Peru Margin. Chem. Geol. 385, 84–91. https://doi.org/10.1016/j.chemgeo.2014.07.019

Mavromatis, V., Prokushkin, A.S., Pokrovsky, O.S., Viers, J., Korets, M.A., 2014b. Magnesium isotopes in permafrost-dominated Central Siberian larch forest watersheds. Geochim. Cosmochim. Acta 147, 76–89. https://doi.org/10.1016/j.gca.2014.10.009

Mavromatis, V., Rinder, T., Prokushkin, A.S., Pokrovsky, O.S., Korets, M.A., Chmeleff, J., Oelkers, E.H., 2016. The effect of permafrost, vegetation, and lithology on Mg and Si isotope composition of the Yenisey River and its tributaries at the end of the spring flood. Geochim. Cosmochim. Acta 191, 32–46. https://doi.org/10.1016/j.gca.2016.07.003

Méheut, M., Lazzeri, M., Balan, E., Mauri, F., 2007. Equilibrium isotopic fractionation in the kaolinite, quartz ,water system: Prediction from first-principles density-functional theory 71, 3170–3181. https://doi.org/10.1016/j.gca.2007.04.012

Mills, G.A., Urey, H.C., 1940. The Kinetics of Isotopic Exchange between Carbon Dioxide, Bicarbonate Ion, Carbonate Ion and Water [1]. J. Am. Chem. Soc. 62, 1019–1026. https://doi.org/10.1021/ja01862a010

Müller, W.E.G., Jinhe Li, Schröder, H.C., Li Qiao, Xiaohong Wang, 2007. The unique skeleton of siliceous sponges (Porifera; Hexactinellida and Demospongiae) that evolved first from the Urmetazoa during the Proterozoic: a review. Biogeosciences 4, 219–232. https://doi.org/10.5194/bg-4-219-2007

Neveu, M., Desch, S.J., Castillo-Rogez, J.C., 2017. Aqueous geochemistry in icy world interiors: Equilibrium fluid, rock, and gas compositions, and fate of antifreezes and radionuclides. Geochim. Cosmochim. Acta 212, 324–371. https://doi.org/10.1016/j.gca.2017.06.023

Noireaux, J., Mavromatis, V., Gaillardet, J., Schott, J., Montouillout, V., Louvat, P., Rollion-Bard, C., Neuville, D.R., 2015. Crystallographic control on the boron isotope paleo-pH proxy. Earth Planet. Sci. Lett. 430, 398–407. https://doi.org/10.1016/j.epsl.2015.07.063

Nothdurft, L.D., Webb, G.E., Buster, N.A., Holmes, C.W., Sorauf, J.E., Kloprogge, J.T., 2005. Brucite microbialites in living coral skeletons: Indicators of extreme microenvironments in shallow-marine settings. Geology 33, 169. https://doi.org/10.1130/G20932.1

Oelkers, E.H., 2001. General kinetic description of multioxide silicate mineral and glass dissolution. Geochim. Cosmochim. Acta 65, 3703–3719. https://doi.org/10.1016/S0016-7037(01)00710-4

Oelkers, E.H., Berninger, U.-N., Pérez-Fernàndez, A., Chmeleff, J., Mavromatis, V., 2018. The temporal evolution of magnesium isotope fractionation during hydromagnesite dissolution, precipitation, and at equilibrium. Geochim. Cosmochim. Acta 226, 36–49. https://doi.org/10.1016/j.gca.2017.11.004

Oelze, M., 2015. Silicon isotope fractionation at low temperatures in the presence of Aluminum: An experimental approach and application to different erent weathering regimes (Dissertation). Freie Universität Berlin, Berlin.

Oelze, M., von Blanckenburg, F., Bouchez, J., Hoellen, D., Dietzel, M., 2015. The effect of Al on Si isotope fractionation investigated by silica precipitation experiments. Chem. Geol. 397, 94–105. https://doi.org/10.1016/j.chemgeo.2015.01.002

Oelze, M., von Blanckenburg, F., Hoellen, D., Dietzel, M., Bouchez, J., 2014. Si stable isotope fractionation during adsorption and the competition between kinetic and

equilibrium isotope fractionation: Implications for weathering systems. Chem. Geol. 380, 161–171. https://doi.org/10.1016/j.chemgeo.2014.04.027

Opfergelt, S., Burton, K.W., Georg, R.B., West, A.J., Guicharnaud, R.A., Sigfusson, B., Siebert, C., Gislason, S.R., Halliday, A.N., 2014. Magnesium retention on the soil exchange complex controlling Mg isotope variations in soils, soil solutions and vegetation in volcanic soils, Iceland. Geochim. Cosmochim. Acta 125, 110–130. https://doi.org/10.1016/j.gca.2013.09.036

Opfergelt, S., Cardinal, D., André, L., Delvigne, C., Bremond, L., Delvaux, B., 2010. Variations of δ^{30}Si and Ge/Si with weathering and biogenic input in tropical basaltic ash soils under monoculture. Geochim. Cosmochim. Acta 74, 225–240. https://doi.org/10.1016/j.gca.2009.09.025

Opfergelt, S., Cardinal, D., Henriet, C., André, L., Delvaux, B., 2006a. Silicon isotope fractionation between plant parts in banana: In situ vs. in vitro. J. Geochem. Explor. 88, 224–227. https://doi.org/10.1016/j.gexplo.2005.08.044

Opfergelt, S., Cardinal, D., Henriet, C., Draye, X., André, L., Delvaux, B., 2006b. Silicon Isotopic Fractionation by Banana (Musa spp.) Grown in a Continuous Nutrient Flow Device. Plant Soil 285, 333–345. https://doi.org/10.1007/s11104-006-9019-1

Opfergelt, S., Delmelle, P., 2012. Silicon isotopes and continental weathering processes: Assessing controls on Si transfer to the ocean. Comptes Rendus Geosci. 344, 723–738. https://doi.org/10.1016/j.crte.2012.09.006

Opfergelt, S., Delvaux, B., André, L., Cardinal, D., 2008. Plant silicon isotopic signature might reflect soil weathering degree. Biogeochemistry 91, 163–175. https://doi.org/10.1007/s10533-008-9278-4

Opfergelt, S., Georg, R.B., Delvaux, B., Cabidoche, Y.-M., Burton, K.W., Halliday, A.N., 2012a. Mechanisms of magnesium isotope fractionation in volcanic soil weathering sequences, Guadeloupe. Earth Planet. Sci. Lett. 341–344, 176–185. https://doi.org/10.1016/j.epsl.2012.06.010

Opfergelt, S., Georg, R.B., Delvaux, B., Cabidoche, Y.-M., Burton, K.W., Halliday, A.N., 2012b. Silicon isotopes and the tracing of desilication in volcanic soil weathering sequences, Guadeloupe. Chem. Geol. 326–327, 113–122. https://doi.org/10.1016/j.chemgeo.2012.07.032

Opfergelt, S., Williams, H.M., Cornelis, J.T., Guicharnaud, R.A., Georg, R.B., Siebert, C., Gislason, S.R., Halliday, A.N., Burton, K.W., 2017. Iron and silicon isotope behaviour accompanying weathering in Icelandic soils, and the implications for iron export from

peatlands. Geochim. Cosmochim. Acta 217, 273–291. https://doi.org/10.1016/j.gca.2017.08.033

Pearce, C.R., Saldi, G.D., Schott, J., Oelkers, E.H., 2012. Isotopic fractionation during congruent dissolution, precipitation and at equilibrium: Evidence from Mg isotopes. Geochim. Cosmochim. Acta 92, 170–183. https://doi.org/10.1016/j.gca.2012.05.045

Peloquin, D.M., Schmedake, T.A., 2016. Recent advances in hexacoordinate silicon with pyridine-containing ligands: Chemistry and emerging applications. Coord. Chem. Rev. 323, 107–119. https://doi.org/10.1016/j.ccr.2016.02.005

Perdew, J.P., Burke, K., Ernzerhof, M., 1996. Generalized Gradient Approximation Made Simple. Phys. Rev. 77, 3865–3868.

Perry, C.C., 2003. Silicification: The Processes by Which Organisms Capture and Mineralize Silica. Rev. Mineral. Geochem. 54, 291–327. https://doi.org/10.2113/0540291

Pillar, E.A., Camm, R.C., Guzman, M.I., 2014. Catechol Oxidation by Ozone and Hydroxyl Radicals at the Air–Water Interface. Environ. Sci. Technol. 48, 14352–14360. https://doi.org/10.1021/es504094x

Pillar, E.A., Zhou, R., Guzman, M.I., 2015. Heterogeneous Oxidation of Catechol. J. Phys. Chem. A 119, 10349–10359. https://doi.org/10.1021/acs.jpca.5b07914

Pinilla, C., Blanchard, M., Balan, E., Natarajan, S.K., Vuilleumier, R., Mauri, F., 2015. Equilibrium magnesium isotope fractionation between aqueous Mg2+ and carbonate minerals: Insights from path integral molecular dynamics. Geochim. Cosmochim. Acta 163, 126–139. https://doi.org/10.1016/j.gca.2015.04.008

Platzner, I.T. (Itzhak T., Habfast, K., Walder, A.J., Goetz, A., 1997. Modern isotope ratio mass spectrometry, Chemical analysis. J. Wiley, Chichester ; New York.

Plettnick, S., Chou, L., Wollast, R., 1994. Kinetics and mechanisms of dissolution of silica at room temperature and pressure. Mineral. Mag. 58A.

Pogge von Strandmann, P.A.E., James, R.H., van Calsteren, P., Gíslason, S.R., Burton, K.W., 2008. Lithium, magnesium and uranium isotope behaviour in the estuarine environment of basaltic islands. Earth Planet. Sci. Lett. 274, 462–471. https://doi.org/10.1016/j.epsl.2008.07.041

Pogge von Strandmann, P.A.E., Opfergelt, S., Lai, Y.-J., Sigfússon, B., Gislason, S.R., Burton, K.W., 2012. Lithium, magnesium and silicon isotope behaviour accompanying weathering in a basaltic soil and pore water profile in Iceland. Earth Planet. Sci. Lett. 339–340, 11–23. https://doi.org/10.1016/j.epsl.2012.05.035

Poitrasson, F., 2017. Silicon Isotope Geochemistry. Rev. Mineral. Geochem. 82, 289–344. https://doi.org/10.2138/rmg.2017.82.8

Pokrovski, G.S., Schott, J., 1998. Experimental study of the complexation of silicon and germanium with aqueous organic species: implications for germanium and silicon transport and Ge/Si ratio in natural waters. Geochim. Cosmochim. Acta 62, 3413–3428. https://doi.org/10.1016/S0016-7037(98)00249-X

Pokrovsky, O.S., Galy, A., Schott, J., Pokrovski, G.S., Mantoura, S., 2014. Germanium isotope fractionation during Ge adsorption on goethite and its coprecipitation with Fe oxy(hydr)oxides. Geochim. Cosmochim. Acta 131, 138–149. https://doi.org/10.1016/j.gca.2014.01.023

Pokrovsky, O.S., Reynolds, B.C., Prokushkin, A.S., Schott, J., Viers, J., 2013. Silicon isotope variations in Central Siberian rivers during basalt weathering in permafrost-dominated larch forests. Chem. Geol.355, 103–116. https://doi.org/10.1016/j.chemgeo.2013.07.016

Pokrovsky, O.S., Schott, J., 2004. Experimental study of brucite dissolution and precipitation in aqueous solutions: surface speciation and chemical affinity control. Geochim. Cosmochim. Acta 68, 31–45. https://doi.org/10.1016/S0016-7037(03)00238-2

Pokrovsky, O.S., Schott, J., 2002. Surface Chemistry and Dissolution Kinetics of Divalent Metal Carbonates. Environ. Sci. Technol. 36, 426–432. https://doi.org/10.1021/es010925u

Pozhidaev, A.I., Polynova, T.N., Porai-Koshits, M.A., Dudakov, V.G., 1974. Crystal structure of disodium magnesium ethylenediaminetetraacetate tetrahydrate. J. Struct. Chem. 15, 149–150. https://doi.org/10.1007/BF00753807

Putnis, A., 1992. Introduction to mineral sciences. Cambridge University Press, Cambridge [England] ; New York.

Reddy, T.R., Frierdich, A.J., Beard, B.L., Johnson, C.M., 2015. The effect of pH on stable iron isotope exchange and fractionation between aqueous Fe(II) and goethite. Chem. Geol. 397, 118–127. https://doi.org/10.1016/j.chemgeo.2015.01.018

Reynolds, B., Frank, M., Halliday, A., 2006. Silicon isotope fractionation during nutrient utilization in the North Pacific. Earth Planet. Sci. Lett. 244, 431–443. https://doi.org/10.1016/j.epsl.2006.02.002

Reynolds, J.H., Verhoogen, J., 1953. Natural variations in the isotopic constitution of silicon. Geochim. Cosmochim. Acta 3, 224–234. https://doi.org/10.1016/0016-7037(53)90041-6

Rimstidt, J.D., Barnes, H.L., 1980. The kinetics of silica-water reactions. Geochim. Cosmochim. Acta 44, 1683–1699. https://doi.org/10.1016/0016-7037(80)90220-3

Riotte, J., Meunier, J.-D., Zambardi, T., Audry, S., Barboni, D., Anupama, K., Prasad, S., Chmeleff, J., Poitrasson, F., Sekhar, M., Braun, J.-J., 2018a. Processes controlling silicon isotopic fractionation in a forested tropical watershed: Mule Hole Critical Zone Observatory (Southern India). Geochim. Cosmochim. Acta 228, 301–319. https://doi.org/10.1016/j.gca.2018.02.046

Riotte, J., Sandhya, K., Prakash, N.B., Audry, S., Zambardi, T., Chmeleff, J., Buvaneshwari, S., Meunier, J.-D., 2018b. Origin of silica in rice plants and contribution of diatom Earth fertilization: insights from isotopic Si mass balance in a paddy field. Plant Soil 423, 481–501. https://doi.org/10.1007/s11104-017-3535-z

Roerdink, D.L., van den Boorn, S.H.J.M., Geilert, S., Vroon, P.Z., van Bergen, M.J., 2015. Experimental constraints on kinetic and equilibrium silicon isotope fractionation during the formation of non-biogenic chert deposits. Chem. Geol. 402, 40–51. https://doi.org/10.1016/j.chemgeo.2015.02.038

Rosenheim, A., Raibmann, B., Schendel, G., 1931. Über innerkomplexe Brenzcatechinate vierwertiger Elemente. Z. für Anorg. Allg. Chem. 196, 160–176. https://doi.org/10.1002/zaac.19311960117

Russell, B.J., Shelton, J.P., Walsh, A., 1957. An atomic-absorption spectrophotometer and its application to the analysis of solutions. Spectrochim. Acta 8, 317–328. https://doi.org/10.1016/0371-1951(57)80193-3

Russell, W.A., Papanastassiou, D.A., Tombrello, T.A., 1978. Ca isotope fractionation on the Earth and other solar system materials. Geochim. Cosmochim. Acta 42, 1075–1090. https://doi.org/10.1016/0016-7037(78)90105-9

Rustad, J.R., Casey, W.H., Yin, Q.-Z., Bylaska, E.J., Felmy, A.R., Bogatko, S.A., Jackson, V.E., Dixon, D.A., 2010. Isotopic fractionation of Mg^{2+}(aq), Ca^{2+}(aq), and Fe^{2+}(aq) with carbonate minerals. Geochim. Cosmochim. Acta 74, 6301–6323. https://doi.org/10.1016/j.gca.2010.08.018

Ryan, B.M., Kirby, J.K., Degryse, F., Harris, H., McLaughlin, M.J., Scheiderich, K., 2013. Copper speciation and isotopic fractionation in plants: uptake and translocation mechanisms. New Phytol. 199, 367–378. https://doi.org/10.1111/nph.12276

Saenger, C., Wang, Z., 2014. Magnesium isotope fractionation in biogenic and abiogenic carbonates: implications for paleoenvironmental proxies. Quat. Sci. Rev. 90, 1–21. https://doi.org/10.1016/j.quascirev.2014.01.014

Saldi, G.D., Noireaux, J., Louvat, P., Faure, L., Balan, E., Schott, J., Gaillardet, J., 2018. Boron isotopic fractionation during adsorption by calcite – Implication for the seawater

pH proxy. Geochim. Cosmochim. Acta 240, 255–273. https://doi.org/10.1016/j.gca.2018.08.025

Savage, P.S., Armytage, R.M.G., Georg, R.B., Halliday, A.N., 2014. High temperature silicon isotope geochemistry. Lithos 190–191, 500–519. https://doi.org/10.1016/j.lithos.2014.01.003

Savage, P.S., Georg, R.B., Williams, H.M., Halliday, A.N., 2013. The silicon isotope composition of the upper continental crust. Geochim. Cosmochim. Acta 109, 384–399. https://doi.org/10.1016/j.gca.2013.02.004

Savin, S.M., Douglas, R.G., 1973. Stable Isotope and Magnesium Geochemistry of Recent Planktonic Foraminifera from the South Pacific. Geol. Soc. Am. Bull. 84, 2327. https://doi.org/10.1130/0016-7606(1973)84<2327:SIAMGO>2.0.CO;2

Schauble, E.A., 2011. First-principles estimates of equilibrium magnesium isotope fractionation in silicate, oxide, carbonate and hexaaquamagnesium(2+) crystals. Geochim. Cosmochim. Acta 75, 844–869. https://doi.org/10.1016/j.gca.2010.09.044

Schauble, E.A., 2004. Applying Stable Isotope Fractionation Theory to New Systems. Rev. Mineral. Geochem. 55, 65–111. https://doi.org/10.2138/gsrmg.55.1.65

Schindelin, J., Arganda-Carreras, I., Frise, E., Kaynig, V., Longair, M., Pietzsch, T., Preibisch, S., Rueden, C., Saalfeld, S., Schmid, B., Tinevez, J.-Y., White, D.J., Hartenstein, V., Eliceiri, K., Tomancak, P., Cardona, A., 2012. Fiji: an open-source platform for biological-image analysis. Nat. Methods 9, 676–682. https://doi.org/10.1038/nmeth.2019

Schott, J., Mavromatis, V., Fujii, T., Pearce, C.R., Oelkers, E.H., 2016. The control of carbonate mineral Mg isotope composition by aqueous speciation: Theoretical and experimental modeling. Chem. Geol. 445, 120–134. https://doi.org/10.1016/j.chemgeo.2016.03.011

Schott, J., Pokrovsky, O.S., Oelkers, E.H., 2009. The Link Between Mineral Dissolution/Precipitation Kinetics and Solution Chemistry. Rev. Mineral. Geochem. 70, 207–258. https://doi.org/10.2138/rmg.2009.70.6

Schuessler, J.A., von Blanckenburg, F., 2014. Testing the limits of micro-scale analyses of Si stable isotopes by femtosecond laser ablation multicollector inductively coupled plasma mass spectrometry with application to rock weathering. Spectrochim. Acta Part B At. Spectrosc. 98, 1–18. https://doi.org/10.1016/j.sab.2014.05.002

Sedaghatpour, F., Teng, F.-Z., Liu, Y., Sears, D.W.G., Taylor, L.A., 2013. Magnesium isotopic composition of the Moon. Geochim. Cosmochim. Acta 120, 1–16. https://doi.org/10.1016/j.gca.2013.06.026

Sedeh, I.F., Öhman, L.-O., Sjöberg, S., Frimpong-Manso, S., Springborg, J., Wang, D.-N., Christensen, S.B., 1992. Equilibrium and Structural Studies of Silicon(IV) and Aluminium(III) in Aqueous Solution. 30. Aqueous Complexation between Silicic Acid and Some ortho-Di- and Triphenolic Compounds. Acta Chem. Scand. 46, 933–940. https://doi.org/10.3891/acta.chem.scand.46-0933

Sedeh, I.F., Sjöberg, S., Öhman, L.-O., 1993. Equilibrium and structural studies of silicon(IV) and aluminum(III) in aqueous solution. 31. Aqueous complexation between silicic acid and the catecholamines dopamine and L-DOPA. J. Inorg. Biochem. 50, 119–132. https://doi.org/10.1016/0162-0134(93)80019-6

Shahar, A., Elardo, S.M., Macris, C.A., 2017. Equilibrium Fractionation of Non-traditional Stable Isotopes: an Experimental Perspective. Rev. Mineral. Geochem. 82, 65–83. https://doi.org/10.2138/rmg.2017.82.3

Shahar, A., Hillgren, V.J., Young, E.D., Fei, Y., Macris, C.A., Deng, L., 2011. High-temperature Si isotope fractionation between iron metal and silicate. Geochim. Cosmochim. Acta 75, 7688–7697. https://doi.org/10.1016/j.gca.2011.09.038

Shahar, A., Young, E.D., Manning, C.E., 2008. Equilibrium high-temperature Fe isotope fractionation between fayalite and magnetite: An experimental calibration. Earth Planet. Sci. Lett. 268, 330–338. https://doi.org/10.1016/j.epsl.2008.01.026

Sikdar, J., Rai, V.K., 2017. Simultaneous chromatographic purification of Si and Mg for isotopic analyses using MC-ICPMS. J. Anal. At. Spectrom. 32, 822–833. https://doi.org/10.1039/C6JA00426A

Sillen, L.G., Martell, A.E., 1971. Stability Constants of Metal-Ion Complexes., Suppl. Chemical Society.

Sjöberg, S., Ingri, N., Nenner, A.-M., Öhman, L.-O., 1985. Equilibrium and structural studies of silicon(IV) and aluminium(III) in aqueous solution. 12. A potentiometric and ^{29}Si-NMR study of silicon tropolonates. J. Inorg. Biochem. 24, 267–277. https://doi.org/10.1016/0162-0134(85)85055-8

Stamm, F.M., Zambardi, T., Chmeleff, J., Schott, J., von Blanckenburg, F., Oelkers, E.H., 2019. The experimental determination of equilibrium Si isotope fractionation factors among $H_4SiO_4^o$, $H_3SiO_4^-$ and amorphous silica ($SiO_2 \cdot 0.32\ H_2O$) at 25 ° and 75 °C using

the three-isotope method. Geochim. Cosmochim. Acta 255, 49–68. https://doi.org/10.1016/j.gca.2019.03.035

Steinhoefel, G., von Blanckenburg, F., Horn, I., Konhauser, K.O., Beukes, N.J., Gutzmer, J., 2010. Deciphering formation processes of banded iron formations from the Transvaal and the Hamersley successions by combined Si and Fe isotope analysis using UV femtosecond laser ablation. Geochim. Cosmochim. Acta 74, 2677–2696. https://doi.org/10.1016/j.gca.2010.01.028

Strickland, J.D.H., 1952. The Preparation and Properties of Silicomolybdic Acid. II. The Preparation and Properties of β-Silicomolybdic Acid. J. Am. Chem. Soc. 74, 868–871. https://doi.org/10.1021/ja01124a003

Sun, L., Wu, L.H., Ding, T.P., Tian, S.H., 2008. Silicon isotope fractionation in rice plants, an experimental study on rice growth under hydroponic conditions. Plant Soil 304, 291–300. https://doi.org/10.1007/s11104-008-9552-1

Sun, X., Olofsson, M., Andersson, P.S., Fry, B., Legrand, C., Humborg, C., Mörth, C.-M., 2014. Effects of growth and dissolution on the fractionation of silicon isotopes by estuarine diatoms. Geochim. Cosmochim. Acta 130, 156–166. https://doi.org/10.1016/j.gca.2014.01.024

Sutton, J.N., Varela, D.E., Brzezinski, M.A., Beucher, C.P., 2013. Species-dependent silicon isotope fractionation by marine diatoms. Geochim. Cosmochim. Acta 104, 300–309. https://doi.org/10.1016/j.gca.2012.10.057

Sverjensky, D.A., Shock, E.L., Helgeson, H.C., 1997. Prediction of the thermodynamic properties of aqueous metal complexes to 1000°C and 5 kb. Geochim. Cosmochim. Acta 61, 1359–1412. https://doi.org/10.1016/S0016-7037(97)00009-4

Taylor, H.P., Epstein, S., 1973. Oxygen and silicon isotope ratios of the Luna 20 soil. Geochim. Cosmochim. Acta 37, 1107–1109. https://doi.org/10.1016/0016-7037(73)90204-4

Teng, F.-Z., 2017. Magnesium Isotope Geochemistry. Rev. Mineral. Geochem. 82, 219–287. https://doi.org/10.2138/rmg.2017.82.7

Teng, F.-Z., Wadhwa, M., Helz, R.T., 2007. Investigation of magnesium isotope fractionation during basalt differentiation: Implications for a chondritic composition of the terrestrial mantle. Earth Planet. Sci. Lett. 261, 84–92. https://doi.org/10.1016/j.epsl.2007.06.004

Tesson, B., Gaillard, C., Martin-Jézéquel, V., 2008. Brucite formation mediated by the diatom Phaeodactylum tricornutum. Mar. Chem. 109, 60–76. https://doi.org/10.1016/j.marchem.2007.12.005

Tilles, D., 1961. Natural variations in isotopic abundances of silicon. J. Geophys. Res. 66, 3003–3013. https://doi.org/10.1029/JZ066i009p03003

Tipper, E., Galy, A., Bickle, M., 2006a. Riverine evidence for a fractionated reservoir of Ca and Mg on the continents: Implications for the oceanic Ca cycle. Earth Planet. Sci. Lett. 247, 267–279. https://doi.org/10.1016/j.epsl.2006.04.033

Tipper, E., Galy, A., Gaillardet, J., Bickle, M., Elderfield, H., Carder, E., 2006b. The magnesium isotope budget of the modern ocean: Constraints from riverine magnesium isotope ratios. Earth Planet. Sci. Lett. 250, 241–253. https://doi.org/10.1016/j.epsl.2006.07.037

Tipper, E.T., Calmels, D., Gaillardet, J., Louvat, P., Capmas, F., Dubacq, B., 2012a. Positive correlation between Li and Mg isotope ratios in the river waters of the Mackenzie Basin challenges the interpretation of apparent isotopic fractionation during weathering. Earth Planet. Sci. Lett. 333–334, 35–45. https://doi.org/10.1016/j.epsl.2012.04.023

Tipper, E.T., Lemarchand, E., Hindshaw, R.S., Reynolds, B.C., Bourdon, B., 2012b. Seasonal sensitivity of weathering processes: Hints from magnesium isotopes in a glacial stream. Chem. Geol. 312–313, 80–92. https://doi.org/10.1016/j.chemgeo.2012.04.002

Tréguer, P., Le Corre, P., 1975. Manuel d'analyses automatiques des sels nutritifs dans l'eau de mer. Utilisation de l'Auto-Analyzer II Technicon. Universite´ de Bretagne occidentale, France.

Truesdale, V.W., LeCorre, P., 1975. Manuel d'analyse des sels nuritifs dans l'eau de mer: Utilisation de L'autoanalyzer II technicon (r). Université de Bretagne occiendtale, France.

Urey, H.C., 1947. The thermodynamic properties of isotopic substances. J. Chem. Soc. Resumed 562. https://doi.org/10.1039/jr9470000562

Uriz, M.-J., Turon, X., Becerro, M.A., Agell, G., 2003. Siliceous spicules and skeleton frameworks in sponges: Origin, diversity, ultrastructural patterns, and biological functions. Microsc. Res. Tech. 62, 279–299. https://doi.org/10.1002/jemt.10395

van den Boorn, S.H.J.M., van Bergen, M.J., Vroon, P.Z., de Vries, S.T., Nijman, W., 2010. Silicon isotope and trace element constraints on the origin of ~3.5Ga cherts: Implications for Early Archaean marine environments. Geochim. Cosmochim. Acta 74, 1077–1103. https://doi.org/10.1016/j.gca.2009.09.009

Varela, D.E., Pride, C.J., Brzezinski, M.A., 2004. Biological fractionation of silicon isotopes in Southern Ocean surface waters: BIOLOGICAL FRACTIONATION OF SILICON. Glob. Biogeochem. Cycles 18, n/a-n/a. https://doi.org/10.1029/2003GB002140

Walsh, A., 1955. The application of atomic absorption spectra to chemical analysis. Spectrochim. Acta 7, 108–117. https://doi.org/10.1016/0371-1951(55)80013-6

Wang, W., Wei, H.-Z., Jiang, S.-Y., Eastoe, C.J., Guo, Q., Lin, Y.-B., 2016. Adsorption Behavior of Metasilicate on N−Methyl D−Glucamine Functional Groups and Associated Silicon Isotope Fractionation. Langmuir 32, 8872–8881. https://doi.org/10.1021/acs.langmuir.6b02388

Weber, J.N., Kaufman, J.W., 1965. Brucite in the Calcareous Alga Goniolithon. Science 149, 996–997. https://doi.org/10.1126/science.149.3687.996

Weiss, A., Harvey, D.R., 1964. Wasserbeständige, kationische Siliciumkomplexe mit 1-Hydroxypyridin-N-oxyd. Angew. Chem. 76, 818–818. https://doi.org/10.1002/ange.19640761908

Welch, S.A., Beard, B.L., Johnson, C.M., Braterman, P.S., 2003. Kinetic and equilibrium Fe isotope fractionation between aqueous Fe(II) and Fe(III). Geochim. Cosmochim. Acta 67, 4231–4250. https://doi.org/10.1016/S0016-7037(03)00266-7

Weyer, S., Schwieters, J.B., 2003. High precision Fe isotope measurements with high mass resolution MC-ICPMS. Int. J. Mass Spectrom. 226, 355–368. https://doi.org/10.1016/S1387-3806(03)00078-2

White, W.M., 2013. Geochemistry. John Wiley & Sons Inc, Hoboken, NJ.

Wiederhold, J.G., Kraemer, S.M., Teutsch, N., Borer, P.M., Halliday, A.N., Kretzschmar, R., 2006. Iron Isotope Fractionation during Proton-Promoted, Ligand-Controlled, and Reductive Dissolution of Goethite. Environ. Sci. Technol. 40, 3787–3793. https://doi.org/10.1021/es052228y

Wille, M., Sutton, J., Ellwood, M.J., Sambridge, M., Maher, W., Eggins, S., Kelly, M., 2010. Silicon isotopic fractionation in marine sponges: A new model for understanding silicon isotopic variations in sponges. Earth Planet. Sci. Lett. 292, 281–289. https://doi.org/10.1016/j.epsl.2010.01.036

Wimpenny, J., Burton, K.W., James, R.H., Gannoun, A., Mokadem, F., Gíslason, S.R., 2011. The behaviour of magnesium and its isotopes during glacial weathering in an ancient shield terrain in West Greenland. Earth Planet. Sci. Lett. 304, 260–269. https://doi.org/10.1016/j.epsl.2011.02.008

Wimpenny, J., Colla, C.A., Yin, Q.-Z., Rustad, J.R., Casey, W.H., 2014. Investigating the behaviour of Mg isotopes during the formation of clay minerals. Geochim. Cosmochim. Acta 128, 178–194. https://doi.org/10.1016/j.gca.2013.12.012

Wischmeyer, A.G., De La Rocha, C.L., Maier-Reimer, E., Wolf-Gladrow, D.A., 2003. Control mechanisms for the oceanic distribution of silicon isotopes. Glob. Biogeochem. Cycles 17, n/a-n/a. https://doi.org/10.1029/2002GB002022

Wombacher, F., Eisenhauer, A., Heuser, A., Weyer, S., 2009. Separation of Mg, Ca and Fe from geological reference materials for stable isotope ratio analyses by MC-ICP-MS and double-spike TIMS. J. Anal. At. Spectrom. 24, 627–636. https://doi.org/10.1039/b820154d

Wu, L., Percak-Dennett, E.M., Beard, B.L., Roden, E.E., Johnson, C.M., 2012. Stable iron isotope fractionation between aqueous Fe(II) and model Archean ocean Fe–Si coprecipitates and implications for iron isotope variations in the ancient rock record. Geochim. Cosmochim. Acta 84, 14–28. https://doi.org/10.1016/j.gca.2012.01.007

Yeh, H.W., Epstein, S., 1978. 29Si/28Si and 30Si/28Si of Meteorites and Allende Inclusions. Lunar Planet Sci. 9, 1289–1291.

Yin, R., Feng, X., Wang, J., Li, P., Liu, J., Zhang, Y., Chen, J., Zheng, L., Hu, T., 2013. Mercury speciation and mercury isotope fractionation during ore roasting process and their implication to source identification of downstream sediment in the Wanshan mercury mining area SW China. Chem. Geol. 336, 72–79. https://doi.org/10.1016/j.chemgeo.2012.04.030

Young, E.D., Galy, A., Nagahara, H., 2002. Kinetic and equilibrium mass-dependent isotope fractionation laws in nature and their geochemical and cosmochemical significance. Geochim. Cosmochim. Acta 66, 1095–1104. https://doi.org/10.1016/S0016-7037(01)00832-8

Zambardi, T., 2011. Recherche de marqueurs de processus de formation des planètes à travers les isotopes stables de masse moyenne (Dissertation). Université Paul Sabatier, Toulouse III, Toulouse.

Zambardi, T., Poitrasson, F., 2011. Precise Determination of Silicon Isotopes in Silicate Rock Reference Materials by MC-ICP-MS. Geostand. Geoanalytical Res. 35, 89–99. https://doi.org/10.1111/j.1751-908X.2010.00067.x

Zeebe, R.E., 2005. Stable boron isotope fractionation between dissolved $B(OH)_3$ and $B(OH)_4^-$. Geochim. Cosmochim. Acta 69, 2753–2766. https://doi.org/10.1016/j.gca.2004.12.011

Zhang, J., Quay, P.D., Wilbur, D.O., 1995. Carbon isotope fractionation during gas-water exchange and dissolution of CO2. Geochim. Cosmochim. Acta 59, 107–114. https://doi.org/10.1016/0016-7037(95)91550-D

Zheng, X.-Y., Beard, B.L., Reddy, T.R., Roden, E.E., Johnson, C.M., 2016. Abiologic silicon isotope fractionation between aqueous Si and Fe(III)–Si gel in simulated Archean seawater: Implications for Si isotope records in Precambrian sedimentary rocks. Geochim. Cosmochim. Acta 187, 102–122. https://doi.org/10.1016/j.gca.2016.05.012

Ziegler, K., Chadwick, O.A., Brzezinski, M.A., Kelly, E.F., 2005a. Natural variations of δ30Si ratios during progressive basalt weathering, Hawaiian Islands. Geochim. Cosmochim. Acta 69, 4597–4610. https://doi.org/10.1016/j.gca.2005.05.008

Ziegler, K., Chadwick, O.A., White, A.F., Brzezinski, M.A., 2005b. δ30Si systematics in a granitic saprolite, Puerto Rico. Geology 33, 817. https://doi.org/10.1130/G21707.1

Annex

Annex I: Electronic supplement of chapter 3

Table A: Temporal evolution of dissolved Si concentration and pH during equilibration of the initial Si-free reactive fluids with the pre-treated amorphous silica.

Exp.	Temperature [°C]	Time [d]	pH	Si-conc. [ppm]	Si-conc. [mmol/kg]
SibA:					
	25	0	8.7	0.0	0.0
	25	1	5.5	2.7	0.1
	25	4	6.6	14.8	0.5
	25	7	6.0	23.1	0.8
	25	13	6.8	32.8	1.2
	25	19	6.6	39.0	1.4
	25	27	6.7	44.2	1.6
	25	37	6.4	46.7	1.7
	25	47	6.2	44.4	1.6
SicB:					
	25	0	10.2	0.0	0.0
	25	1	10.2	58.2	2.1
	25	4	10.2	104.1	3.7
	25	8	10.2	115.0	4.1
	25	16	10.2	154.3	5.5
	25	26	10.1	141.1	5.0
	25	50	10.2	114.7	4.1
	25	66	10.1	118.7	4.2
Sig75A:					
	75	0	5.9	0.0	0.0
	75	1	6.4	41.1	1.5
	75	4	6.5	87.7	3.1
	75	19	5.8	108.0	3.9
	75	23	5.7	107.1	3.8
	75	29	5.8	115.1	4.1
	75	33	5.7	114.9	4.1
	75	41	5.7	116.7	4.2
	75	69	5.7	117.4	4.2
Sik75B:					
	75	0	9.25	0.00	0.0
	75	1	10.02	148.7	5.3
	75	3	9.4	236.2	8.4
	75	8	9.9	231.4	8.2
	75	14	9.3	264.2	9.4
	75	22	9.3	257.9	9.2
	75	37	9.3	257.4	9.2

Table B: Summary of the measured characteristics of the reacted solids collected after the longest duration experiment for the experiments at 25°C and pH 5.8 at 75°C. Longest reacted powder available at time of analysis at pH 9.1 and 75°C after 33 days.

sample	Temp. [°C]	run time [d]	S_{BET} [m^2/g]	grain size [nm]	m_{H2O} [wt %]	chemical formula
SibA 8	25	351	137.1	20.86	9.4	$SiO_2 \cdot 0.33\ H_2O$
SicB 8	25	385	164.1	20.69	8.6	$SiO_2 \cdot 0.34\ H_2O$
Sig75A 8	75	55	171.7	19.60	8.1	$SiO_2 \cdot 0.28\ H_2O$
Sik75B 6	75	33	119.0	n.a.	7.5	$SiO_2 \cdot 0.32\ H_2O$

Annex II: Electronic supplement of chapter 4

Table A: Temporal evolution of dissolved Si concentration and pH during equilibration of the initial Si-free reactive fluids containing 0.05 mol/kg (SigC0.05), and 0.08 mol/kg catechol (SigC0.08) with the pre-treated amorphous silica.

Exp.	Temperature [°C]	Time [d]	pH	Si-conc. [ppm]	Si-conc. [mmol/kg]
SigC0.05:					
	25	0	9.0	0.0	0.0
	25	1	9.2	158.2	5.6
	25	4	8.9	299.8	10.7
	25	9	9.0	354.3	12.6
	25	10	9.0	343.2	12.2
SigC0.08:					
	25	0	9.1	0.0	0.0
	25	1	9.0	219.5	7.8
	25	4	9.0	331.5	11.8
	25	7	9.0	537.3	19.1
	25	10	8.9	610.9	21.8

Annex III: Electronic supplement of chapter 5

Table A: Species and dissociation constant added to the PHREEQC core10 database to perform speciation calculations.

Reaction	log K	Source
$Mg(OH)_2 + 2H^+ = 2\ H_2O + Mg^{2+}$	17.209	this study
Sulphate		
$SO_4^{2-} + Mg^{2+} \leftrightarrow MgSO_4$	2.41	McCollom & Shock (1997)
Citrate		
$Citrate^{3-} + H^+ \leftrightarrow HCitrate^{2-}$	6.40	Bénézeth et al. (1997)
$HCitrate^{2-} + H^+ \leftrightarrow H_2Citrate^-$	4.76	Bénézeth et al. (1997)
$H_2Citrate^- + H^+ \leftrightarrow H_3Citrate^{2-}$	3.13	Bénézeth et al. (1997)
$Mg^{2+} + Citrate^{3-} \leftrightarrow Mg(Citrate)^-$	5.00	Covingron & Danish (2009)
$Mg^{2+} + HCitrate^{2-} \leftrightarrow MgHCitrate$	2.59	Covingron & Danish (2009)
$Mg^{2+} + H_2Citrate^- \leftrightarrow MgH_2Citrate^+$	1.00	Covingron & Danish (2009)
$Mg^{2+} + 2Citrate^{3-} \leftrightarrow Mg(Citrate)_2^{4-}$	5.49	Covingron & Danish (2009)
EDTA		
$EDTA^{4-} + H^+ \leftrightarrow HEDTA^{3-}$	10.95	Carini & Martell (1953)
$EDTA^{4-} + 2\ H^+ \leftrightarrow H_2EDTA^{2-}$	17.22	Carini & Martell (1953)
$EDTA^{4-} + 3\ H^+ \leftrightarrow H_3EDTA^-$	20.37	Hummel (2005)
$EDTA^{4-} + 4\ H^+ \leftrightarrow H_4EDTA$	22.60	Hummel (2005)
$EDTA^{4-} + 5\ H^+ \leftrightarrow H_5EDTA^+$	23.90	Hummel (2005)
$Mg^{2+}\ EDTA^{4-} \leftrightarrow MgEDTA^{2-}$	10.45	Gautier (2013)
$Mg^{2+}\ EDTA^{4-} + H^+ \leftrightarrow MgHEDTA^-$	20.87	Hummel (2005)
$Na^+\ EDTA^{4-} + H^+ \leftrightarrow NaEDTA^{3-}$	2.7	Felmy & Mason (2003)

Table B: Temporal evolution of dissolved Mg concentration and pH during equilibration of the initial Mg-free reactive fluids with the synthesized brucite.

Exp.	Time [d]	pH	Si-conc. [ppm]	Si-conc. [mmol/kg]
BB/BABE:				
	0	9.6	0.0	0.0
	1	9.7	971.9	40.0
	3	9.4	1836.9	75.6
	10	9.4	1854.5	76.3
	15	9.5	1875.3	77.2
	21	9.4	1863.4	76.7
	30	9.5	1901.0	78.2
	36	9.4	2008.7	82.6
	46	9.4	2043.3	84.1
	57	9.4	2038.9	83.9
BBC:				
	0	11.1	0.0	0.0
	1	10.9	70.5	2.9
	4	10.4	124.5	5.1
	7	10.2	139.9	5.8
	13	10.2	144.1	5.9
	19	10.3	149.7	6.2
	27	10.0	150.8	6.2
	37	10.0	149.7	6.2
	47	10.1	146.4	6.0
BCS:				
	0	-	0.0	0.0
	1	9.2	1619.7	66.6
	3	9.1	1380.9	56.8
	12	9.3	1651.5	67.9
	17	9.2	1628.5	67.0
	34	9.0	1717.7	70.7
	43	9.2	1738.2	71.5
BDS:				
	0	-	0.0	0.0
	2	9.56	267.1	11.0
	11	9.8	266.1	10.9
	18	9.8	264.3	10.9
	23	10.0	259.1	10.7
	30	9.8	256.2	10.5
	35	10.0	262.1	10.8
	36	9.9	249.1	10.2
BE EDTA:				
	0	-	0.0	0.0
	2	9.1	636.5	26.2
	6	11.3	1398.0	57.5
	11	12.4	1633.3	67.2
	15	12.5	1770.3	72.8
	22	12.4	1690.4	69.5
	24	12.5	1715.2	70.6
	28	12.5	1682.7	69.2
	57	12.4	1838.5	75.6